

**Rare-Earth-Containing Chalcogenides and Intermetallics**

by

Dundappa Mumbaraddi

A thesis submitted in partial fulfillment of the requirements for the degree of  
Doctor of Philosophy

Department of Chemistry

University of Alberta

© Dundappa Mumbaraddi, 2023

## Abstract

This thesis describes the synthesis, structures, and properties of two broad classes of inorganic solids, chalcogenides and intermetallics, with the common theme that they contain rare-earth (*RE*) elements, which belong to the set of critical minerals essential for many technological applications.

Quaternary rare-earth chalcogenides  $RE-M-Ch-X$  ( $M$  = d- or p-block metal or metalloid,  $Ch$  = chalcogen,  $X$  = halogen) represent a growing family of mixed-anion compounds, which remain relatively scarce compared to conventional “single-anion” compounds such as oxides, but offer the possibility of greater control over physical properties. Several series of compounds  $RE_3Tt_2Ch_8I$  ( $RE$  = La, Ce, Pr;  $Tt$  = Si, Ge;  $Ch$  = S, Se) were prepared by direct combination of the elements at high temperatures. By gradual substitution of different proportions of  $Tt$  or  $Ch$  components in solid solutions of these semiconducting compounds, the band gap can be tuned within a range of 1.9 to 3.6 eV. The Ce-containing members exhibit blue luminescence, making them suitable candidates for applications in phosphor-converted white light emitting diodes. The emission behaviour can be controlled by changing the crystal field environment of  $Ch$  vs. I anions around the luminescent  $Ce^{3+}$  centres within these compounds.

Ternary rare-earth intermetallics  $RE-M-X$  ( $M$  = d-block metal;  $X$  = p-block metal or metalloid) have long been a rich source of quantum materials with exotic electrical and magnetic properties. Nevertheless, many aspects of their chemistry, including synthesis, phase stability, crystal structures, and chemical bonding remain poorly systematized and understood. Because reliable physical measurements depend on the availability of large single crystals or pure phase samples, efforts were made to apply flux methods for crystal growth of these compounds. In

particular, ternary gallides  $RE-M-Ga$  ( $RE = La, Ce, Yb$ ) were prepared in a gallium self-flux, and they were examined against a previously proposed stability diagram which predicts formation of ternary intermetallic phases. The new compound  $YbCu_3Ga_8$  was discovered in this process, and the structure of  $YbNi_3Ga_9$  was redetermined to resolve ambiguities in the literature. As examples of polar intermetallics, these compounds were confirmed by electronic structure calculations to exhibit multicenter covalent bonding within the anionic Ga networks. Similarly, crystal growth of ternary germanides  $RE-M-Ge$  ( $RE = Ce, Eu, Yb$ ) was attempted in an indium flux to test a classification model. Crystals of  $RECo_2Ge_2$  and  $CeIr_2Ge_2$  were obtained, the latter exhibiting polymorphism with structures in two different space groups. The Yb-containing compounds  $Yb_5Ir_4Ge_{10}$  and  $Yb_4Ir_7Ge_6$  were also identified from the Yb–Ir–In–Ge reaction.

## Preface

This thesis summarizes the research work performed in the laboratory of Prof. Arthur Mar in the Department of Chemistry at the University of Alberta from September 2017 to April 2023. My contributions and those of others are summarized below.

Chapter 2 was published as Mumbaraddi, D.; Iyer, A. K.; Üzer, E.; Mishra, V.; Oliynyk, A. O.; Nilges, T.; Mar, A. Synthesis, structure, and properties of rare-earth germanium sulfide iodides  $RE_3Ge_2S_8I$  ( $RE = La, Ce, Pr$ ). *J. Solid State Chem.* **2019**, *274*, 162–167. My contribution includes synthesis, data collection, analysis, characterization, and writing of the initial draft. Dr. A. K. Iyer and Dr. E. Üzer assisted with synthesis, Dr. V. Mishra assisted with DFT calculations, Dr. A. O. Oliynyk assisted with magnetic measurement, Dr. T Nilges assisted with manuscript corrections, Dr. A. Mar revised and submitted the manuscript.

Chapter 3 is under preparation as a manuscript for publication, as Mumbaraddi, D.; Mishra, V.; Jomaa, M.; Liu, X.; Karmakar, A.; Thirupurasanthiran, S.; Meldrum, A, Grosvenor, A. P, Michaelis, V. K, Mar, A. Controlling the Luminescence of Rare-Earth Chalcogenide Iodides  $RE_3(Ge_{1-x}Si_x)_2S_8I$  ( $RE = La, Ce, Pr$ ) and  $Ce_3Si_2(S_{1-y}Se_y)_8I$ . My contribution includes synthesis, data collection, analysis, characterization, and writing of the initial draft. Dr. V. Mishra assisted with DFT calculations, Dr. M. Jomaa and S. Thirupurasanthiran assisted with synthesis and characterization. Dr. A. Karmakar assisted with initial PL measurements and Dr. V. K. Michaelis helped with manuscript corrections, X. Liu, and Dr. A. Meldrum assisted with photoluminescence measurements and analysis; Dr. A. P. Grosvenor performed the XPS measurements. Dr. A. Mar will revise and submit the manuscript.

Chapter 4 was published as Mumbaraddi, D.; Mishra, V.; Lidin, S.; Mar, A. Minority report: Structure and bonding of  $\text{YbNi}_3\text{Ga}_9$  and  $\text{YbCu}_3\text{Ga}_8$  obtained in gallium flux. *J. Solid State Chem.* **2022**, *311*, 123157. My contribution includes synthesis, data collection, analysis, characterization, and writing of the initial draft. Dr. V. Mishra assisted with DFT calculations. Dr. S. Lidin assisted with the structure determination. Dr. A. Mar revised and submitted the manuscript.

Chapter 5 is under preparation as a manuscript for publication, as Mumbaraddi, D.; Mishra, V.; Sikdar, R.; Mar, A. Metal flux single crystal growth of Ce, Eu, and Yb-based intermetallic compounds. My contribution includes synthesis, data collection, analysis, characterization, and writing of the initial draft. Dr. V. Mishra and R. Sikdar assisted with synthesis and characterization. Dr. A. Mar will revise and submit the manuscript.

## Acknowledgements

I want to express my sincere gratitude to Prof. Arthur Mar, my supervisor, teacher, and mentor. He is the one who inspired me, guided me, and assisted me through my studies at University of Alberta. I am so glad to have such a wise, hard-working, and understanding supervisor. Arthur inspires every student in his research group as a true researcher and incredible scientist.

Special thanks go to my committee members: Prof. Rylan Lundgren and Prof. Vladimir Michaelis, who agreed readily to serve starting in my first year of studies. I thank Prof. Siobhan A. (Sasha) Wilson, Prof. Lingzi Sang, and Prof. Mariusz Klobukowski for their assistance with my candidacy exam. I am also obligated to my collaborators Prof. Vladimir Michaelis, Prof. Tom Nilges, Prof. Sven Lidin, Prof. Alkiviathes Meldrum, and Prof. Andrew P. Grosvenor for their scientific support. I express my gratitude to Dr. Yoram Apelblat, my teaching assistant coordinator. I appreciate his mentoring, which enabled me to develop my teaching skills. I want to thank the faculty and staff in the Chemistry Department. I am also thankful to Dr. Michael J. Ferguson, Dr. Wayne Moffat, Dr. Guibin Ma, Jennifer Jones, and Rebecca Funk for the fruitful scientific discussion. I am also thankful for all my groupmates: Dr. Abishek, K. Iyer, Dr. Vidyanshu Mishra, Dr. Amit Bhattacharya, Dr. Mohammed Jomaa, Alex, Dong, Fuwei, Arkadii, Ritobroto, Trinanjan, Viktor, Allison, Pritam, Dr. Anton Oliynyk, Dr. Lawrence Adutwum, Dr. Frank Stegemann, Dr. Balaranjan Selvaratnam, Dr. Brett Duell, Dr. Volodymyr Gvozdetskyi, Dr. Maxwell Wallace, Dr. Dmitry Vrublevskiy.

I also wish to acknowledge my parents and my family members.

I want to thank Prof. K. B. Gudasi for allowing me to work in his research lab to complete my M. Sc dissertation work. I thank Prof. S. P. Marudar, Prof. G. V. Shanbag and Poornaprajna institute of scientific research faculty for allowing me to work as a project assistant. I thank Prof. S. C. Peter and research group that inspired me to work in solid state chemistry at Jawaharlal Nehru centre for advanced scientific research, Bengaluru. I thank Dr. Sumanta Sarkar and Dr. Udumula Subbarao for teaching me solid state reactions and characterizations. I sincerely thank Dr. Sudhindra Rayaprol and Prof. S. M. Shivaprasad for their encouragement. Words will fall short for me to thank the following people who have been with me through this journey: Special thanks to Vidyanshu, Girish, Mahantesh, Gururaj, Sachin, Praveen, Yamanappa, Mahadev, Mohan, and Iranna. I am grateful to my housemates (Ramesh, Vijay, Felix, and Abhi) for being kind and helpful. I thank Shaivya and Hima for making good food and hospitality.

I thank Department of Chemistry for teaching assistantship appointments, Future Energy Systems, Natural Sciences and Engineering Research Council of Canada, Doctoral Recruitment Scholarship, Alberta graduate excellence scholarship, and J Gordin Kaplan graduate student award for the financial support.

I am sure I forgot to mention everyone on this acknowledgement page, but I am very thankful to everyone I have met.

## Table of Contents

Abstract.....	ii
Preface.....	iv
Acknowledgements.....	vi
Table of Contents.....	viii
List of Tables .....	xii
List of Figures.....	xv
List of symbols and abbreviations .....	xxi
<b>Chapter 1. Introduction.....</b>	<b>1</b>
1.1. Rare earth compounds .....	1
1.2. Mixed anion compounds.....	1
1.1 Chalcogenides.....	3
1.2 Structures of quaternary rare-earth-containing chalcogenides .....	7
1.2.1 CuZrSiAs- or LaAgSO-type .....	7
1.2.2 CeBiS <sub>2</sub> O type.....	8
1.2.3 Misfit layered compounds.....	9
1.2.4 Ce <sub>2</sub> SbS <sub>5</sub> Br-type.....	10
1.2.5 Sm <sub>3</sub> SiS <sub>6</sub> Cl-type.....	11
1.3 Intermetallic compounds.....	12
1.3.1 Rare-earth intermetallics.....	14
1.3.2 Crystal growth.....	15
1.4 Synthesis .....	17
1.4.1 Direct reaction.....	18

1.4.2	Arc melting .....	19
1.4.3	Induction heating .....	20
1.4.4	Metal flux growth .....	20
1.5	Characterization .....	21
1.5.1	X-ray diffraction .....	21
1.5.2	Scanning electron microscopy .....	25
1.5.3	Diffuse reflectance spectroscopy .....	27
1.6	Band structure calculations .....	28
1.7	Physical properties .....	30
1.7.1	Photoluminescence .....	30
1.7.2	Magnetic properties .....	33
1.8	Objectives .....	34
1.9	References.....	36
 <b>Chapter 2. Synthesis, structure, and properties of rare-earth germanium sulfide iodides</b>		
	<b><i>RE</i><sub>3</sub>Ge<sub>2</sub>S<sub>8</sub>I (<i>RE</i> = La, Ce, Pr).....</b>	<b>44</b>
2.1.	Introduction.....	44
2.2.	Experimental.....	45
2.2.1.	Synthesis .....	45
2.2.2.	Structure determination.....	48
2.2.3.	Electronic structure calculations .....	51
2.2.4.	Diffuse reflectance spectroscopy .....	52
2.2.5.	Magnetic susceptibility measurements .....	52
2.3.	Results and discussion .....	52

2.4. Conclusions.....	59
2.5. References.....	60

### **Chapter 3. Controlling the Luminescence of Rare-Earth Chalcogenide Iodides**

<b><math>RE_3(Ge_{1-x}Si_x)_2S_8I</math> (<math>RE = La, Ce, Pr</math>) and <math>Ce_3Si_2(S_{1-y}Se_y)_8I</math> .....</b>	<b>62</b>
3.1. Introduction.....	62
3.2. Experimental Section.....	63
3.2.1. Synthesis .....	63
3.2.2. Structure Determination.....	65
3.2.3. Property Measurements .....	69
3.2.4. Electronic Structure Calculations .....	70
3.3. Results and Discussion .....	71
3.3.1. Solid Solutions.....	71
3.3.2. Optical Band Gaps .....	77
3.3.3. Electronic Structure .....	79
3.3.4. Photoluminescence .....	82
3.4. Conclusions.....	90
3.4.1. References.....	92

### **Chapter 4. Minority report: Structure and bonding of $YbNi_3Ga_9$ and $YbCu_3Ga_8$**

<b>obtained in gallium flux.....</b>	<b>95</b>
4.1. Introduction.....	95
4.2. Experimental.....	97
4.2.1. Synthesis .....	97
4.2.2. Structure determination.....	98

4.2.3.	Electronic structure calculations .....	101
4.3.	Results and discussion .....	102
4.3.1.	Flux growth.....	102
4.3.2.	YbNi <sub>3</sub> Ga <sub>9</sub> .....	106
4.3.3.	YbCu <sub>3</sub> Ga <sub>8</sub> .....	109
4.3.4.	Electronic structure .....	111
4.4.	Conclusions.....	116
4.5.	References.....	117
<b>Chapter 5.</b>	<b>Crystal growth of Ce, Eu, and Yb-containing germanides in metal flux ....</b>	<b>121</b>
5.1.	Introduction.....	121
5.2.	Experimental .....	122
5.2.1.	Synthesis .....	122
5.2.2.	Structure determination.....	123
5.3.	Results and discussion .....	124
5.3.1.	Flux growth.....	124
5.3.2.	Structures .....	126
5.4.	Conclusions.....	131
5.5.	References.....	132
<b>Chapter 6.</b>	<b>Conclusions.....</b>	<b>135</b>
<b>Bibliography</b>	<b>.....</b>	<b>138</b>
<b>Appendix 1.</b>	<b>Supplementary Data for Chapter 3 .....</b>	<b>156</b>
<b>Appendix 2.</b>	<b>Supplementary Data for Chapter 4 .....</b>	<b>183</b>
<b>Appendix 3</b>	<b>Supplementary Data for Chapter 5.....</b>	<b>196</b>

## List of Tables

<b>Table 1-1.</b> Previously reported quaternary chalcogenides (parent structure types are in blue). ....	4
<b>Table 1-2.</b> Quaternary rare-earth-containing chalcogenides. ....	7
<b>Table 2-1.</b> Crystallographic data for $RE_3Ge_2S_8I$ . ....	49
<b>Table 2-2.</b> Atomic coordinates and equivalent isotropic displacement parameters ( $\text{\AA}^2$ ) <sup>a</sup> for $RE_3Ge_2S_8I$ . ....	50
<b>Table 2-3.</b> Interatomic distances ( $\text{\AA}$ ) in $RE_3Ge_2S_8I$ . ....	51
<b>Table 2-4.</b> Bond valence sums in $RE_3Ge_2S_8I$ . ....	53
<b>Table 3-1.</b> Abbreviated Crystallographic Data for $RE_3(Ge_{1-x}Si_x)_2S_8I$ and $Ce_3Si_2(S_{1-y}Se_y)_8I$ . <sup>a</sup> ....	67
<b>Table 3-2.</b> Ranges of Interatomic Distances ( $\text{\AA}$ ) for $RE_3(Ge_{1-x}Si_x)_2S_8I$ and $Ce_3Si_2(S_{1-y}Se_y)_8I$ . ...	68
<b>Table 4-1.</b> Crystallographic data for $YbNi_3Ga_9$ and $YbCu_3Ga_8$ . ....	99
<b>Table 4-2.</b> Atomic coordinates and equivalent isotropic displacement parameters for $YbNi_3Ga_9$ and $YbCu_3Ga_8$ . ....	100
<b>Table 4-3.</b> Interatomic distances ( $\text{\AA}$ ) in $YbNi_3Ga_9$ and $YbCu_3Ga_8$ . ....	101
<b>Table 4-4.</b> Compositions, as determined by EDX analyses, of crystals obtained in Ga flux reactions. ....	103
<b>Table 5-1.</b> Compositions of crystals obtained in indium flux reactions. ....	124
<b>Table A1-1.</b> Cell Parameters and Refinement Agreement Factors for $RE_3(Ge_{1-x}Si_x)_2S_8I$ and $Ce_3Si_2(S_{1-y}Se_y)_8I$ . ....	156
<b>Table A1-2.</b> EDX Analyses (mol. %) for $RE_3(Ge_{1-x}Si_x)_2S_8I$ and $Ce_3Si_2(S_{1-y}Se_y)_8I$ . ....	157
<b>Table A1-3.</b> Crystallographic Data for $RE_3(Ge_{1-x}Si_x)_2S_8I$ and $Ce_3Si_2(S_{1-y}Se_y)_8I$ . ....	159
<b>Table A1-4.</b> Atomic Coordinates and Equivalent Isotropic Displacement Parameters for $RE_3(Ge_{1-x}Si_x)_2S_8I$ and $Ce_3Si_2(S_{1-y}Se_y)_8I$ . ....	162
<b>Table A1-5.</b> Interatomic Distances ( $\text{\AA}$ ) for $RE_3(Ge_{1-x}Si_x)_2S_8I$ and $Ce_3Si_2(S_{1-y}Se_y)_8I$ . ....	165

<b>Table A1-6.</b> Optical Band Gaps (eV) for $RE_3(\text{Ge}_{1-x}\text{Si}_x)_2\text{S}_8\text{I}$ and $\text{Ce}_3\text{Si}_2(\text{S}_{1-y}\text{Se}_y)_8\text{I}$ .	168
<b>Table A1-7.</b> Integrated COBI (eV/bond) for Bonding Interactions in $\text{Ce}_3(\text{Ge}_{1-x}\text{Si}_x)_2\text{S}_8\text{I}$ and $\text{Ce}_3\text{Si}_2(\text{S}_{1-y}\text{Se}_y)_8\text{I}$ .	169
<b>Table A1-8.</b> CIE Coordinates for $\text{Ce}_3(\text{Ge}_{1-x}\text{Si}_x)_2\text{S}_8\text{I}$ and $\text{Ce}_3\text{Si}_2(\text{S}_{1-y}\text{Se}_y)_8\text{I}$ .	170
<b>Table A1-9.</b> Fitting Parameters for Photoluminescent Decay for $\text{Ce}_3(\text{Ge}_{1-x}\text{Si}_x)_2\text{S}_8\text{I}$ and $\text{Ce}_3\text{Si}_2(\text{S}_{1-y}\text{Se}_y)_8\text{I}$ <sup>a</sup> .	170
<b>Table A1-10.</b> XPS peak position and % area.	171
<b>Table A2-1.</b> Crystallographic data for $\text{YbNi}_3\text{Ga}_9$ .	187
<b>Table A2-2.</b> Atomic coordinates and equivalent isotropic displacement parameters for $\text{YbNi}_3\text{Ga}_9$ .	188
<b>Table A2-3.</b> Interatomic distances (Å) in $\text{YbNi}_3\text{Ga}_9$ .	189
<b>Table A2-4.</b> Crystallographic data for $\text{YbCu}_3\text{Ga}_8$ .	190
<b>Table A2-5.</b> Atomic coordinates and equivalent isotropic displacement parameters for $\text{YbCu}_3\text{Ga}_8$ <sup>a</sup> .	191
<b>Table A2-6.</b> Interatomic distances (Å) in $\text{YbCu}_3\text{Ga}_8$ .	192
<b>Table A2-7.</b> Cell parameters for $\text{YbNi}_3\text{Ga}_9$ at different temperatures.	192
<b>Table A3-1.</b> Ternary germanides with $\text{U}_4\text{Re}_7\text{Ge}_6$ -type structure.	196
<b>Table A3-2.</b> Ternary germanides with $\text{Sc}_5\text{Co}_4\text{Si}_{10}$ -type structure.	197
<b>Table A3-3.</b> Crystallographic data for $\text{EuCo}_2\text{Ge}_2$ .	198
<b>Table A3-4.</b> Crystallographic data for $\text{YbCo}_2\text{Ge}_2$ .	199
<b>Table A3-5.</b> Crystallographic data for $\text{CeTGe}_2$ ( $T = \text{Co}, \text{Ir}$ ).	200
<b>Table A3-6.</b> Crystallographic data for $\text{CeIrGe}_2$ .	201
<b>Table A3-7.</b> Crystallographic data for $\text{Yb}_4\text{Ir}_7\text{Ge}_6$ .	202
<b>Table A3-8.</b> Crystallographic data for $\text{Yb}_5\text{Ir}_4\text{Ge}_{10}$ .	203
<b>Table A3-9.</b> Atomic coordinates and equivalent isotropic displacement parameters (Å <sup>2</sup> ) <sup>a</sup> for $R\text{Co}_2\text{Ge}_2$ ( $R = \text{Eu}, \text{Yb}$ ), $\text{CeCoGe}_2$ and $\text{CeIrGe}_2$ ( $Cmcm$ ).	204
<b>Table A3-10.</b> Atomic coordinates and equivalent isotropic displacement parameters (Å <sup>2</sup> ) for $\text{CeIrGe}_2$ ( $Immm$ ), $\text{Yb}_4\text{Ir}_7\text{Ge}_6$ .	205
<b>Table A3-11.</b> Atomic coordinates and equivalent isotropic displacement parameters (Å <sup>2</sup> ) for $\text{Yb}_5\text{Ir}_4\text{Ge}_{10}$ .	206

**Table A3-12.** Interatomic distances (Å) for  $RCo_2Ge_2$  ( $R = Eu, Yb$ ),  $CeTGe_2$  ( $T = Co, Ir$ )..... 207

**Table A3-13.** Interatomic distances (Å) for  $CeIrGe_2$  ( $Immm$ ),  $Yb_4Ir_7Ge_6$  and  $Yb_5Ir_4Ge_{10}$ . ..... 208

## List of Figures

<b>Figure 1-1.</b> Unique entries of reported mixed anion compounds. ....	2
<b>Figure 1-2.</b> Structure of $REMChF$ ( $RE$ = Rare-earth; $M$ = Cu, Ag; $Ch$ = S, Se, Te). ....	8
<b>Figure 1-3.</b> Structures of (a) $EuBiS_2F$ and (b) $Eu_3Bi_2S_4F_4$ . ....	9
<b>Figure 1-4.</b> Structure of $RE_8CrTe_{13}Cl$ ( $RE$ = Sm, Gd, Tb).....	10
<b>Figure 1-5.</b> Structure of $RE_2SbS_5Br$ ( $RE$ = La, Ce). ....	11
<b>Figure 1-6.</b> Structure of $RE_3SiS_6Cl$ ( $RE$ = Nd, Sm) containing isolated $SiS_4$ tetrahedra.....	12
<b>Figure 1-7.</b> Formation of intermetallic compounds. ....	13
<b>Figure 1-8.</b> Reported ternary $RE-T-X$ intermetallic compounds.....	15
<b>Figure 1-9.</b> Synthetic methods: (a) direct reaction, (b) arc melting, (c) induction heating, and (d) metal flux growth.....	18
<b>Figure 1-10.</b> (a) Generation of X-rays, (b) emission spectrum, and (c) electronic transitions responsible for characteristic X-rays. ....	21
<b>Figure 1-11.</b> (a) Laue equations for a 1D row of atoms and for a 3D crystal and (b) Bragg's law. ....	22
<b>Figure 1-12.</b> Precession image of $YbCu_3Ga_8$ .....	23
<b>Figure 1-13.</b> Experimental and simulated powder XRD patterns for $YbNi_3Ga_9$ . ....	25
<b>Figure 1-14.</b> (a) Interactions of incident electron beam on a sample. (b) Secondary electrons, (c) backscattered electrons, and (d) characteristic X-rays produced in an electron microscope. ....	26
<b>Figure 1-15.</b> EDX spectrum for $YbPtGe$ crystal and a secondary electron image (inset). ....	27
<b>Figure 1-16.</b> (a) UV-Vis-NIR spectrometer with light reflected by a rough sample surface. (b) diffuse reflectance spectra collected on powder sample of $Ce_3Ge_2S_8I$ .....	28

<b>Figure 1-17.</b> (a) Chain of atoms with orbitals $\chi_n$ , taken to be s-orbitals, (b) band dispersion diagram, (c) density of states, and (d) crystal orbital Hamilton population. ....	29
<b>Figure 1-18.</b> Mechanisms for fluorescence and phosphorescence.....	32
<b>Figure 1-19.</b> (a) Temperature dependence of magnetic susceptibility, and (b) Inverse magnetic susceptibility vs temperature.....	34
<b>Figure 2-1.</b> Powder XRD patterns (with Pawley fittings) and SEM images of typical crystals (insets) for $RE_3Ge_2S_8I$ .....	47
<b>Figure 2-2.</b> Structure of $RE_3Ge_2S_8I$ ( $RE = La, Ce, Pr$ ) (a) viewed down the $c$ -direction revealing tunnels occupied by I atoms, (b) highlighting a slice parallel to the $ac$ -plane containing isolated $GeS_4$ tetrahedra, and (c) showing the coordination environments around $RE$ atoms. ....	54
<b>Figure 2-3.</b> (a) Density of states (DOS) (b) atomic projections, and (c) crystal orbital Hamilton population ( $-COHP$ ) curves for $La_3Ge_2S_8I$ .....	56
<b>Figure 2-4.</b> Optical absorption spectra, converted from the diffuse reflectance spectra, for (a) $La_3Ge_2S_8I$ , (b) $Ce_3Ge_2S_8I$ , and (c) $Pr_3Ge_2S_8I$ .....	57
<b>Figure 2-5.</b> Magnetic susceptibility and its inverse (inset) for $RE_3Ge_2S_8I$ ( $RE = Ce, Pr$ ).....	59
<b>Figure 3-1.</b> Evolution of unit cell volume for (a) complete solid solutions $RE_3(Ge_{1-x}Si_x)_2S_8I$ ( $RE = La, Ce, Pr$ ) and (b) partial solid solution $Ce_3Si_2(S_{1-y}Se_y)_8I$ . ....	73
<b>Figure 3-2.</b> (a) Structure of $RE_3(Ge_{1-x}Si_x)_2S_8I$ ( $RE = La, Ce, Pr$ ) and $Ce_3Si_2(S_{1-y}Se_y)_8I$ viewed down the $c$ -direction (upper panel) and highlighting a slice parallel to the $ac$ -plane (lower panel). (b) Coordination environments around $RE$ atoms, consisting of $Ch$ and I atoms at distances up to 3.5 Å, and $Tt$ atoms at distances up to 3.9 Å. ....	75

**Figure 3-3.** Bond length ranges within the solid solutions  $RE_3(Ge_{1-x}Si_x)_2S_8I$  ( $RE = La, Ce, Pr$ ) and  $Ce_3Si_2(S_{1-y}Se_y)_8I$ . Data for the end-members were taken from previous reports. 76

**Figure 3-4.** Normalized UV-Vis-near IR absorption spectra extracted from diffuse reflectance spectra for selected members of solid solutions  $RE_3(Ge_{1-x}Si_x)_2S_8I$  ( $RE = La, Ce, Pr$ ) and  $Ce_3Si_2(S_{1-y}Se_y)_8I$ ..... 78

**Figure 3-5.** Optical band gaps for (a) complete solid solutions  $RE_3(Ge_{1-x}Si_x)_2S_8I$  ( $RE = La, Ce, Pr$ ) and (b) partial solid solution  $Ce_3Si_2(S_{1-y}Se_y)_8I$ . .... 79

**Figure 3-6.** Band dispersion for (a)  $Ce_3(Ge_{1-x}Si_x)_2S_8I$  and (b)  $Ce_3Si_2(S_{1-y}Se_y)_8I$ . .... 81

**Figure 3-7.** Photoluminescence emission spectra for (a)  $Ce_3(Ge_{1-x}Si_x)_2S_8I$  (with filters applied to sharpen the peaks) and (b)  $Ce_3Si_2(S_{1-y}Se_y)_8I$ . Normalized spectra are shown in the insets. .... 83

**Figure 3-8.** CIE 1931 colour coordinates for various members of (a)  $Ce_3(Ge_{1-x}Si_x)_2S_8I$  and (b)  $Ce_3Si_2(S_{1-y}Se_y)_8I$ . The samples were exposed to ultraviolet light with wavelength of 365 nm. .... 85

**Figure 3-9.** Photoluminescence decay curve ( $\lambda_{ex} = 405$  nm) for (a)  $Ce_3(Ge_{1-x}Si_x)_2S_8I$  and (b)  $Ce_3Si_2(S_{1-y}Se_y)_8I$ . .... 86

**Figure 3-10.** (a) Temperature-dependent photoluminescence emission spectra ( $\lambda_{ex} = 365$  nm) for  $Ce_3Si_2S_8I$ . (b) Plot of relative integrated intensity of emission peaks. The inset shows an Arrhenius fitting to extract the activation energy. .... 88

**Figure 3-11.** High-resolution cerium XPS spectra for various members of  $Ce_3(Ge_{1-x}Si_x)_2S_8I$ . .. 90

<b>Figure 4-1.</b> SEM images: (a) YbCu <sub>3</sub> Ga <sub>8</sub> crystals (circled) within a larger collection of mostly Yb(Cu,Ga) <sub>12</sub> crystals grown in gallium flux. (b) Single crystals of YbNi <sub>3</sub> Ga <sub>9</sub> and YbCu <sub>3</sub> Ga <sub>8</sub> .....	103
<b>Figure 4-2.</b> Powder XRD patterns of ground crystals of (a) YbNi <sub>3</sub> Ga <sub>9</sub> and (b) YbCu <sub>3</sub> Ga <sub>8</sub> grown by gallium flux.....	104
<b>Figure 4-3.</b> Stability diagram showing the crystal growth of ternary, quasi-ternary, or binary phases as promoted by metal fluxes within intermetallic systems A–B–C, with new results overlaid on the plot previously reported by Westerveld et al.....	105
<b>Figure 4-4.</b> Structure of YbNi <sub>3</sub> Ga <sub>9</sub> in terms of nets.....	107
<b>Figure 4-5.</b> Cell parameters of YbNi <sub>3</sub> Ga <sub>9</sub> as a function of temperature. ....	109
<b>Figure 4-6.</b> Structure of YbCu <sub>3</sub> Ga <sub>8</sub> in terms of polyhedra. The Cu and Ga atoms are disordered within sites labelled X. ....	110
<b>Figure 4-7.</b> Density of states (DOS), projected crystal orbital Hamilton population (–pCOHP), and crystal orbital bond index (COBI) for (a) YbNi <sub>3</sub> Ga <sub>9</sub> and (b) ordered model of YbCu <sub>3</sub> Ga <sub>8</sub> .....	113
<b>Figure 4-8.</b> ELF plots and Löwdin charges for (a) YbNi <sub>3</sub> Ga <sub>9</sub> (projected parallel to (001) plane at $z = 0, 1/12,$ and $5/6$ ) and (b) ordered model of YbCu <sub>3</sub> Ga <sub>8</sub> projected on (110) plane. ....	115
<b>Figure 5-1.</b> SEM images of single crystals obtained from In flux. ....	125
<b>Figure 5-2.</b> Structure map of RE–M–Ge phases based on radius ratios $r_{RE}/r_M$ .....	126
<b>Figure 5-3.</b> Structure of RECo <sub>2</sub> Ge <sub>2</sub> (RE = Eu, Yb).....	127
<b>Figure 5-4.</b> Structures of $\alpha$ - and $\beta$ -CeIrGe <sub>2</sub> . ....	128
<b>Figure 5-5.</b> Conceptual structural conversion between $\alpha$ - and $\beta$ -CeIrGe <sub>2</sub> . ....	129

<b>Figure 5-6.</b> Structure of $\text{Yb}_5\text{Ir}_4\text{Ge}_{10}$ , with tunnels propagating along the $c$ -direction. ....	130
<b>Figure A1-1.</b> Powder XRD patterns for $\text{La}_3(\text{Ge}_{1-x}\text{Si}_x)_2\text{S}_8\text{I}$ . ....	172
<b>Figure A1-2.</b> Powder XRD patterns for $\text{Ce}_3(\text{Ge}_{1-x}\text{Si}_x)_2\text{S}_8\text{I}$ . ....	173
<b>Figure A1-3.</b> Powder XRD patterns for $\text{Ce}_3\text{Si}_2(\text{S}_{1-y}\text{Se}_y)_8\text{I}$ . ....	174
<b>Figure A1-4.</b> Powder XRD patterns for $\text{Pr}_3(\text{Ge}_{1-x}\text{Si}_x)_2\text{S}_8\text{I}$ . ....	175
<b>Figure A1-5.</b> EDX elemental mapping for $\text{Ce}_3\text{Si}_2\text{S}_8\text{I}$ sample. ....	176
<b>Figure A1-6.</b> TGA analysis for sample of $\text{Ce}_3\text{Si}_{1.5}\text{Ge}_{0.5}\text{S}_8\text{I}$ . ....	176
<b>Figure A1-7.</b> Normalized diffuse reflectance spectra for $\text{La}_3(\text{Ge}_{1-x}\text{Si}_x)_2\text{S}_8\text{I}$ , showing fittings to extract band gaps. ....	177
<b>Figure A1-8.</b> Density of states (DOS), projected crystal orbital Hamilton populations (pCOHP), and crystal orbital bond index (COBI) for models within the solid solution $\text{Ce}_3(\text{Ge}_{1-x}\text{Si}_x)_2\text{S}_8\text{I}$ . ....	178
<b>Figure A1-9.</b> Density of states (DOS), projected crystal orbital Hamilton populations (pCOHP), and crystal orbital bond index (COBI) for models within the solid solution $\text{Ce}_3\text{Si}_2(\text{S}_{1-y}\text{Se}_y)_8\text{I}$ (up to $y = 0.25$ ). ....	179
<b>Figure A1-10.</b> Electron localization function (ELF) plots, taken as slices parallel to (001), for (a) $\text{Ce}_3(\text{Ge}_{1-x}\text{Si}_x)_2\text{S}_8\text{I}$ and (b) $\text{Ce}_3\text{Si}_2(\text{S}_{1-y}\text{Se}_y)_8\text{I}$ . Bader charges are shown on selected atoms. ....	180
<b>Figure A1-11.</b> Excitation and emission spectra for Si-rich members of $\text{Ce}_3(\text{Ge}_{1-x}\text{Si}_x)_2\text{S}_8\text{I}$ , measured on a Horiba PTI QM-8075-11 fluorescence system. The grey arrow shows quenching of the luminescence with lower Si concentrations. ....	181
<b>Figure A1-12.</b> Emission spectrum of $\text{Ce}_3\text{Si}_2\text{S}_8\text{I}$ , measured with an 365+351-nm Ar-ion laser source. The profile was fit to two sets of Gaussian peaks centred at 453 and 501 nm for the first sets (blue line) and 489 nm and 536 nm for the second set (green line). ....	181
<b>Figure A1-13.</b> Powder XRD patterns of $\text{Ce}_3\text{Si}_2\text{S}_8\text{I}$ sample before and after photoluminescence measurements made with a laser source. ....	182

<b>Figure A1-14.</b> High-resolution cerium XPS spectra for (a) $\text{Ce}_3\text{Si}_2\text{S}_8\text{I}$ , (b) $\text{Ce}_3\text{Ge}_{0.25}\text{Si}_{1.75}\text{S}_8\text{I}$ , (c) $\text{Ce}_3\text{Ge}_{0.50}\text{Si}_{1.50}\text{S}_8\text{I}$ , (d) $\text{Ce}_3\text{Si}_2\text{S}_{7.75}\text{Se}_{0.25}\text{I}$ and (e) $\text{Ce}_3\text{Si}_2\text{S}_{6.50}\text{Se}_{1.50}\text{I}$ . .....	182
<b>Figure A2-1.</b> Reciprocal lattice section of $\text{YbNi}_3\text{Ga}_9$ viewed on the $hhl$ plane. Note how the reciprocal space diagonals go through the most prominent parts of the diffuse scattering. ....	183
<b>Figure A2-2.</b> Note the twin maxima of electron density (blue arrows). The locus of their barycentres (red arrow) is the origin of the unit cell. The axes in the image are $a$ (horizontal) and $c$ (vertical). .....	184
<b>Figure A2-3.</b> Electron density from the model in $R\text{-}3m$ . The section is the $ab$ -plane and the $a$ -axis is horizontal. The centre of the hexagon of electron density is at $\frac{2}{3}, \frac{1}{3}, 0$ .....	185
<b>Figure A2-4.</b> SEM images of crystals grown in gallium flux.....	193
<b>Figure A2-5.</b> Powder XRD patterns of ground crystals grown in gallium flux.....	194
<b>Figure A2-6.</b> Coordination polyhedra around Yb (blue), Ni (green), and Ga (red) atoms in $\text{YbNi}_3\text{Ga}_9$ . .....	195
<b>Figure A3-1.</b> Powder X-ray diffraction patterns compared with simulated patterns.....	209
<b>Figure A3-2.</b> Powder X-ray diffraction patterns compared with simulated patterns.....	209
<b>Figure A3-3.</b> (a) Cell length of $\text{RE}_4\text{T}_7\text{Ge}_6$ ( $T = \text{Rh}, \text{Ir}$ ) compounds, and (b) $c/a$ ratio of $\text{RE}_5\text{T}_4\text{Ge}_{10}$ ( $T = \text{Rh}, \text{Ir}$ ) compounds.....	210

## List of symbols and abbreviations

$\theta$	angle of reflection
$\mu$	absorption coefficient
$Z$	atomic number
$Ae$	alkali metal or alkaline-earth metals
$E_g$	bandgap
$V$	cell volume
$Ch$	chalcogenide
$T_c$	critical temperature
COHP	crystal orbital Hamilton population
$M$	$d$ -block elements
$\rho$	density
DFT	density functional theory
DOS	density of states
$d_{hkl}$	$d$ -spacing
$e^-$	electron
EDX	energy dispersive X-ray spectroscopy
$E_f$	Fermi level
FWHM	full width half maxima
$S$	goodness-of-fit
LASER	light amplification by stimulated emission of radiation
LED	light emitting diodes
LMTO	linear muffin-tin orbital
LDA	local density approximation
$hkl$	Miller indices
$T_N$	Néel temperature
1D, 2D, 3D	one-, two-, three-dimensional
$l$	orbital angular momentum
PPMS	physical property measurement system

<i>RE</i>	rare earth
SEM	scanning electron microscope
$F_{hkl}$	structure factor
<i>T</i>	temperature
<i>Tt</i>	tetrel (Group 14 element)
TGA	thermogravimetric analysis
TB	tight-binding
<i>j</i>	total angular momentum
<i>Tr</i>	triel (Group 13 element)
UV	ultraviolet
$a, b, c, \alpha, \beta, \gamma$	unit cell parameters
$\lambda$	wavelength
<i>k</i>	wavevector
XRD	X-ray diffraction

# Chapter 1.

## Introduction

### 1.1. Rare earth compounds

Rare earth metals comprise the lanthanides (La–Lu) as well as Sc and Y. Compounds containing these elements exhibit varied electronic, magnetic, and optical properties exploited in many applications for consumers, industry, and national security. The strongest permanent magnets are  $\text{Nd}_2\text{Fe}_{14}\text{B}$ ,  $\text{SmCo}_5$ , and  $\text{Sm}_2\text{Co}_{17}$ , which are found in generators, electric motors, microphones, loudspeakers, and hard drives.<sup>1</sup> Solid state lasers in which rare-earth elements are doped in yttrium aluminum garnet, such as  $\text{Nd}:\text{Y}_3\text{Al}_5\text{O}_{12}$ , are used for industrial cutting and welding, medical treatment, and military surveillance.<sup>2</sup> Phosphors doped with rare earth elements such as europium and cerium are used in light-emitting diodes and medical imaging.<sup>3,4</sup> Yellow  $\text{Ca}_{1-x}\text{Eu}_x\text{ZrO}_3$  and the new vibrant blue compound  $\text{YMn}_{1-x}\text{In}_x\text{O}_3$  used as inorganic pigments.<sup>5,6</sup>

Given these widespread applications and their increasing demand, rare earth elements have garnered geopolitical importance. In recent years, there have been serious concerns about most of the world's rare-earth mineral resources being controlled by China, so that Western governments wishing to develop their own resources must develop their own domestic markets for such extraction to be economically viable. Many rare-earth compounds remain to be discovered, which may open the door to new applications.

### 1.2. Mixed anion compounds

Many inorganic solids, such as oxides and halides, consist of a single type of anion. The structures and properties of these compounds are then frequently modified by introducing mixed

cations. A similar idea could be proposed that mixed anions confer additional flexibility to design new materials.<sup>7</sup> In practice, this is harder to achieve because the properties of non-metallic elements, such as ionic radii, electronegativity, and polarizability, vary more drastically than they do for metallic elements. Although mixed-anion compounds have not been as well studied as single anion compounds, there is no fundamental reason that limits their formation or existence. After all, they can be commonly found as minerals such as dadsonite ( $\text{Pb}_{23}\text{Sb}_{25}\text{S}_{60}\text{Cl}$ ), mutnovskite ( $\text{Pb}_2\text{AsS}_3(\text{I}, \text{Cl}, \text{Br})$ ), and pillaitite  $\text{Pb}_9\text{Sb}_{10}\text{S}_{23}\text{ClO}_{0.5}$ .<sup>8</sup> In recent years, a growing number of mixed-anion compounds have now been discovered, including oxypnictides, oxynitrides, oxychalcogenides, oxyhalides, oxyfluorides, oxyhydrides, and chalcocohalides (**Figure 1-1**). (A comment about nomenclature: Some researchers have advocated alternative terminology, such as pnictide oxides in lieu of oxypnictides, to emphasize that two distinct anionic species are present, to avoid confusion with compounds that contain polyatomic anions built from these elements, such as phosphate oxyanions,  $\text{PO}_4^{3-}$ ). Some classes of mixed-anion compounds have experienced bouts of popularity, such as iron-based oxypnictide superconductors  $\text{LaFeAsO}$  and transparent p-type oxychalcogenide semiconductors  $\text{LaCuSO}$ , but others remain relatively neglected.<sup>9,10</sup>

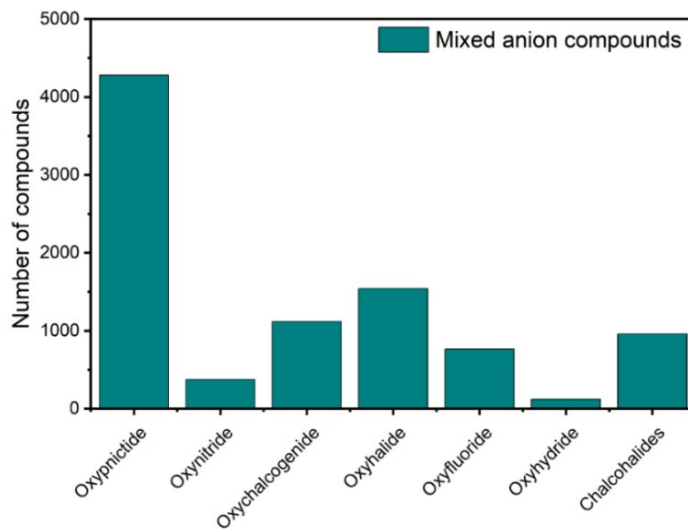


**Figure 1-1.** Unique entries of reported mixed anion compounds.<sup>11</sup>

## 1.1 Chalcogenides

The term chalcogenides generally refers to compounds of the heavier group-16 elements, because their lower electronegativities (Pauling values of 2.5 for S, 2.4 for Se, and 2.1 for Te) lead to greater covalent bonding character, making them distinct from oxides (Pauling electronegativity of 3.5 for O). Many metal chalcogenides are semiconductors, with smaller band gaps than found in oxides. If anions of the highly electronegative halogens ( $X = \text{F, Cl, Br, I}$ ) are introduced, there is the possibility of forming compounds containing both  $Ch$  and  $X$  anions, called chalcogenides, whose structures may be built from networks different from those found in parent chalcogenides or halides. A frequently proposed hypothesis is that band gaps of chalcogenides will be intermediate between those of chalcogenides and halides, because the bonding character will also be intermediate between covalent and ionic, but this expectation may be too simplistic without knowing details of the actual structures.<sup>12</sup>

Compared to other classes of mixed-anion compounds, chalcogenides remain far underrepresented. Ternary chalcogenides number around 560, and structure determinations have been performed for about 400 of them.<sup>11</sup> Very few quaternary chalcogenides have been reported. Some chalcogenides have been identified for potential applications, including  $\text{Tl}_6\text{SeI}_4$  for hard radiation detection,<sup>12</sup>  $\text{Li}_6\text{PS}_5\text{I}$  for lithium ion batteries,<sup>13</sup>  $\text{Sn}_2\text{SbS}_2\text{I}_3$  for solar cells,<sup>14</sup>  $\text{BiTeI}$  for low thermal conductivity materials,<sup>15</sup>  $\text{Ba}_4\text{Ge}_3\text{S}_9\text{Cl}_2$  for nonlinear optical materials,<sup>16</sup> and  $\text{BiTeBr}$  for thermoelectric materials.<sup>15</sup> Because quaternary chalcogenides offer substantial flexibility in accommodating not only mixed anions, but also mixed cations, they may be attractive candidates to enable further tuning of materials properties. A survey of previously reported quaternary chalcogenides is worthwhile (**Table 1-1**).

**Table 1-1.** Previously reported quaternary chalcogenides (parent structure types are in blue).<sup>11</sup>

Multiple entries	Three entries
<p><i>AeMChF</i> (<i>Ae</i> = Sr, Ba; <i>M</i> = Cu, Ag; <i>Ch</i> = S, Se, Te), BaMn<sub>0.5</sub>TeF,</p> <p>MnSbSe<sub>2</sub>I, MnSbS<sub>2</sub>Br, CdBiS<sub>2</sub>Br, MnBiS<sub>2</sub>Br, CdBiSe<sub>2</sub>I, MnBiSe<sub>2</sub>I, CdSbS<sub>2</sub>Br</p> <p>Ag<sub>7</sub>SiS<sub>5</sub>I, Ag<sub>7</sub>GeCh<sub>5</sub>I (<i>Ch</i> = S, Se), Ag<sub>6.69</sub>GeSe<sub>5</sub>I<sub>0.69</sub></p> <p>Ba<sub>3</sub>GaS<sub>4</sub>Cl, Ba<sub>3</sub>AlCh<sub>4</sub>X (<i>Ch</i> = S, Se; <i>X</i> = Br, Te), Ba<sub>3</sub>FeS<sub>4</sub>Br, Ba<sub>3</sub>GaS<sub>4</sub>Br, Ba<sub>3</sub>GaSe<sub>4</sub>Cl</p> <p>AlBiS<sub>2</sub>Cl<sub>4</sub>, AlBiTeX<sub>4</sub>, (<i>X</i> = Cl, Br), AlBiSeCl<sub>4</sub></p> <p>Ba<sub>2</sub>AsCh<sub>3</sub>X (<i>Ch</i> = S, Se; <i>X</i> = Cl, Br, I), Pb<sub>2</sub>AsS<sub>3</sub>I, Ba<sub>2</sub>SbS<sub>3</sub>I</p> <p>Cu<sub>6</sub>PS<sub>5</sub>Br, Cu<sub>6</sub>AsS<sub>5</sub>I, Cu<sub>6</sub>PS<sub>5</sub>I, Cu<sub>7</sub>GeS<sub>5</sub>I, Cu<sub>6</sub>PSe<sub>5</sub>I, Cu<sub>7</sub>SiS<sub>5</sub>I, Li<sub>6</sub>PS<sub>5</sub>I, Li<sub>6</sub>SbS<sub>5</sub>I</p> <p>Ba<sub>2</sub>SnCh<sub>3</sub>F<sub>2</sub> (<i>Ch</i> = S, Se), Sr<sub>2</sub>SnCh<sub>3</sub>F<sub>2</sub> (<i>Ch</i> = S, Se)<sup>62</sup></p> <p>MnSbS<sub>2</sub>Cl, CdBiSe<sub>2</sub>Br, MnBiSe<sub>2</sub>Br, CdBiS<sub>2</sub>Cl, MnBiS<sub>2</sub>Cl, MnSbSe<sub>2</sub>Br, CdSbS<sub>2</sub>Cl</p> <p>CdSb<sub>2</sub>Se<sub>3</sub>Br<sub>2</sub>, InBi<sub>2</sub>Se<sub>4</sub>Br, InSb<sub>2</sub>Ch<sub>4</sub>Br (<i>Ch</i> = S, Se), InSb<sub>2</sub>S<sub>4</sub>Cl</p> <p>Hg<sub>3</sub>ZrS<sub>2</sub>Cl<sub>6</sub>, Hg<sub>3</sub>ZrCh<sub>2</sub>Br<sub>6</sub> (<i>Ch</i> = S, Se), Hg<sub>3</sub>HfCh<sub>2</sub>Cl<sub>6</sub> (<i>Ch</i> = S, Se), Hg<sub>3</sub>ZrSe<sub>2</sub>Cl<sub>6</sub>, Hg<sub>3</sub>UTe<sub>2</sub>Cl<sub>6</sub></p> <p>Hg<sub>2</sub>Mg<sub>2</sub>SF<sub>6</sub>, Hg<sub>2</sub>Mn<sub>2</sub>SF<sub>6</sub>, Hg<sub>2</sub>Co<sub>2</sub>SF<sub>6</sub>, Hg<sub>2</sub>Ni<sub>2</sub>SF<sub>6</sub>, Hg<sub>2</sub>Cu<sub>2</sub>SF<sub>6</sub>, Hg<sub>2</sub>Zn<sub>2</sub>SF<sub>6</sub></p> <p>Sn<sub>2</sub>SbS<sub>2</sub>I<sub>3</sub>, Sn<sub>2</sub>SbSe<sub>2</sub>I<sub>3</sub>, Sn<sub>2</sub>BiS<sub>2</sub>I<sub>3</sub>, Pb<sub>2</sub>SbS<sub>2</sub>I<sub>3</sub>, Pb<sub>2</sub>BiS<sub>2</sub>I<sub>3</sub></p>	<p>Ag<sub>6</sub>SnS<sub>4</sub>Br<sub>2</sub>, Ag<sub>6</sub>GeS<sub>4</sub>X<sub>2</sub> (<i>X</i> = Cl, Br)</p> <p>Hg<sub>3</sub>AsS<sub>4</sub>Cl, Hg<sub>3</sub>AsSe<sub>4</sub>X (<i>X</i> = Br, I)</p> <p>Li<sub>6</sub>PS<sub>5</sub>Cl, Li<sub>6</sub>AsCh<sub>5</sub>I (<i>Ch</i> = S, Se)</p> <p>Ba<sub>4</sub>Ge<sub>3</sub>S<sub>9</sub>Cl<sub>2</sub>, Ba<sub>4</sub>Ge<sub>3</sub>Se<sub>9</sub>Cl<sub>2</sub>, Ba<sub>4</sub>Si<sub>3</sub>Se<sub>9</sub>Cl<sub>2</sub></p> <p>Tl<sub>5</sub>Re<sub>6</sub>Se<sub>8</sub>Cl<sub>7</sub>, Cs<sub>5</sub>Re<sub>6</sub>S<sub>8</sub>Br<sub>7</sub> (<i>X</i> = Cl, Br)</p> <p>CuHgS<sub>2</sub>Cl, CuHgSBr, CuHgSeCl</p> <p>TlIn<sub>4</sub>Se<sub>5</sub>Br, TlIn<sub>4</sub>Ch<sub>5</sub>Cl (<i>Ch</i> = S, Se)</p> <p>CuHgSeBr, AgHgSX (<i>X</i> = Br, I)</p>
	Two entries
	<p>CuBiS<sub>2</sub>Cl<sub>2</sub>, AgBiS<sub>2</sub>Cl<sub>2</sub></p> <p>AgBi<sub>2</sub>S<sub>3</sub>Cl, AgBi<sub>2</sub>Se<sub>3</sub>Cl</p> <p>Cs<sub>2</sub>Re<sub>6</sub>Se<sub>8</sub>Br<sub>4</sub>, Cs<sub>2</sub>Re<sub>6</sub>S<sub>8</sub>Br<sub>4</sub></p> <p>Ag<sub>15</sub>P<sub>4</sub>S<sub>16</sub>Cl<sub>3</sub>, Li<sub>15</sub>P<sub>4</sub>S<sub>16</sub>Cl<sub>3</sub></p> <p>Ba<sub>3</sub>InCh<sub>4</sub>Cl (<i>Ch</i> = S, Se)</p> <p>Ba<sub>2</sub>Fe<sub>1.98</sub>S<sub>3</sub>F<sub>2</sub>, Ba<sub>2</sub>Fe<sub>1.78</sub>Se<sub>3</sub>F<sub>2</sub></p> <p>Cu<sub>3</sub>Bi<sub>2</sub>S<sub>4</sub>Cl, Cu<sub>3</sub>Bi<sub>2</sub>S<sub>4</sub>Br</p> <p>InBi<sub>2</sub>S<sub>4</sub>Cl, InBi<sub>2</sub>S<sub>4</sub>Br</p> <p>GaBi<sub>2</sub>Te<sub>2</sub>Cl<sub>5</sub>, GaBi<sub>2</sub>Se<sub>2</sub>Cl<sub>5</sub></p> <p>SrBiS<sub>2</sub>F, SrSbSe<sub>2</sub>F</p> <p>Tl<sub>3</sub>Nb<sub>6</sub>SBr<sub>17</sub>, Cs<sub>3</sub>Nb<sub>6</sub>SBr<sub>17</sub></p> <p>CsRe<sub>6</sub>Se<sub>8</sub>I<sub>3</sub>, CsRe<sub>6</sub>S<sub>8</sub>Br<sub>3</sub></p> <p>CsRe<sub>3</sub>S<sub>4</sub>Br<sub>2</sub>, CsRe<sub>3</sub>Se<sub>4</sub>Br<sub>2</sub></p> <p>TlHg<sub>6</sub>S<sub>4</sub>Br<sub>5</sub>, TlHg<sub>6</sub>Se<sub>4</sub>Br<sub>5</sub></p> <p>K<sub>3</sub>Nb<sub>6</sub>SBr<sub>17</sub>, Rb<sub>3</sub>Nb<sub>6</sub>SBr<sub>17</sub></p> <p>Hg<sub>3</sub>TS<sub>2</sub>Cl<sub>4</sub>, (<i>T</i> = Fe, Co)</p> <p>Cs<sub>3</sub>Mo<sub>6</sub>Se<sub>1.2</sub>I<sub>2.8</sub>, Cs<sub>3</sub>Mo<sub>6</sub>Se<sub>1.5</sub>I<sub>2.5</sub></p>
One entry	
<p>AgBi<sub>2</sub>S<sub>2</sub>Cl<sub>3</sub>, Ag<sub>7</sub>SiS<sub>5</sub>Br, Ba<sub>7</sub>In<sub>2</sub>Se<sub>6</sub>F<sub>8</sub>, Cu<sub>6</sub>AsS<sub>5</sub>Br, Cu<sub>6</sub>PS<sub>5</sub>I, β-AgHgSI, Ag<sub>5</sub>PS<sub>4</sub>Cl<sub>2</sub>, AlP<sub>3</sub>Se<sub>4</sub>Cl<sub>4</sub>, AlSb<sub>2</sub>Te<sub>2</sub>I<sub>5</sub>, Cu<sub>2</sub>Ga<sub>2</sub>Se<sub>7</sub>Cl<sub>8</sub>, Ba<sub>2</sub>Sb<sub>2</sub>Se<sub>4</sub>F<sub>2</sub>, Sr<sub>2</sub>Sb<sub>2</sub>Se<sub>4</sub>F<sub>2</sub>, Ag<sub>3</sub>Ge<sub>2</sub>S<sub>3</sub>Br, Ag<sub>2</sub>Bi<sub>2</sub>S<sub>3</sub>Cl<sub>2</sub>, Ag<sub>1.2</sub>Bi<sub>17.6</sub>S<sub>23</sub>Cl<sub>8</sub>, Ag<sub>4.1</sub>Mo<sub>9</sub>Se<sub>11</sub>Cl, Ag<sub>2</sub>HgSI<sub>2</sub>, α-AgHgSI, Ag<sub>5</sub>SbS<sub>3</sub>I<sub>2</sub>, Al<sub>2</sub>Sb<sub>5</sub>Se<sub>6</sub>Br<sub>9</sub>, Li<sub>6</sub>PS<sub>5</sub>I, Hg<sub>5</sub>AsS<sub>2</sub>I<sub>3</sub>, Li<sub>6</sub>AsS<sub>5</sub>I, Ba<sub>4</sub>Sb<sub>3</sub>S<sub>8</sub>Cl, Ba<sub>4</sub>Fe<sub>3</sub>S<sub>6</sub>F<sub>4</sub>, Ba<sub>2</sub>Fe<sub>1.72</sub>S<sub>3</sub>F<sub>2</sub>, Ba<sub>2</sub>Fe<sub>1.96</sub>S<sub>3</sub>F<sub>2</sub>, Ba<sub>2</sub>Fe<sub>1.5</sub>Se<sub>3</sub>F<sub>2</sub>, Ba<sub>4</sub>Fe<sub>3</sub>Se<sub>6</sub>F<sub>4</sub>, Ba<sub>18</sub>In<sub>8</sub>S<sub>21</sub>F<sub>18</sub>, Ba<sub>9</sub>In<sub>4</sub>S<sub>10</sub>F<sub>10</sub>, Ba<sub>3</sub>MnSe<sub>3</sub>F<sub>2</sub>, BaSbSe<sub>2</sub>F, Ba<sub>4</sub>Fe<sub>2</sub>S<sub>4</sub>I<sub>5</sub>, Ba<sub>3</sub>GaS<sub>4</sub>I, Cu<sub>1.49</sub>Bi<sub>2.64</sub>S<sub>3.42</sub>Br<sub>2.58</sub>, Cu<sub>1.57</sub>Bi<sub>4.69</sub>Se<sub>7.64</sub>I<sub>0.36</sub>, Cu<sub>1.5</sub>Bi<sub>2.64</sub>S<sub>3.42</sub>Br<sub>2.58</sub>, Cu<sub>1.57</sub>Bi<sub>2.37</sub>Se<sub>2.68</sub>Br<sub>3.32</sub>, Cu<sub>3</sub>Bi<sub>2</sub>S<sub>3</sub>Br<sub>2</sub>, Cu<sub>3</sub>Bi<sub>2</sub>Br<sub>2</sub>, Cu<sub>7</sub>Bi<sub>6</sub>S<sub>10</sub>Cl<sub>5</sub>, Cu<sub>7.4</sub>Bi<sub>6</sub>Se<sub>12</sub>Cl<sub>7</sub>, Cu<sub>9</sub>Bi<sub>9</sub>S<sub>16</sub>Cl<sub>8</sub>, Cu<sub>22</sub>Bi<sub>12</sub>S<sub>21</sub>Cl<sub>16</sub>, Cu<sub>3.32</sub>Bi<sub>2</sub>S<sub>3.33</sub>I<sub>2.67</sub>, Cu<sub>3.58</sub>Bi<sub>4.42</sub>Se<sub>6.84</sub>Cl<sub>3.16</sub>, Ga<sub>5</sub>Bi<sub>3</sub>S<sub>5</sub>Cl<sub>14</sub>(S<sub>8</sub>)<sub>0.5</sub>, Hg<sub>3</sub>Bi<sub>2</sub>S<sub>2</sub>Cl<sub>8</sub>, Hg<sub>3</sub>Bi<sub>2</sub>Te<sub>2</sub>Cl<sub>8</sub>, Cu<sub>3</sub>Bi<sub>6</sub>S<sub>10</sub>I, CuBi<sub>2</sub>Se<sub>3</sub>I, Cu<sub>3</sub>Bi<sub>2</sub>S<sub>3</sub>I<sub>3</sub>, In<sub>2</sub>Bi<sub>3</sub>Se<sub>7</sub>I, In<sub>2</sub>BiSe<sub>4</sub>I, Ni<sub>8</sub>Bi<sub>8</sub>SI<sub>2</sub>, CdHgSBr, Na<sub>5</sub>Co<sub>2</sub>S<sub>4</sub>Br, CsNb<sub>3</sub>SBr<sub>7</sub>, CsRe<sub>3</sub>S<sub>3</sub>Br<sub>4</sub>, Cs<sub>4</sub>Re<sub>6</sub>S<sub>8</sub>Br<sub>6</sub>, Cs<sub>4</sub>Re<sub>6</sub>Se<sub>8</sub>I<sub>6</sub>, Cs<sub>5</sub>Tc<sub>6</sub>S<sub>8</sub>Br<sub>7</sub>, CsTc<sub>3</sub>Se<sub>4</sub>Br<sub>2</sub>, Cu<sub>3</sub>P<sub>4</sub>Se<sub>4</sub>Br<sub>3</sub>, Hg<sub>2</sub>SnS<sub>2</sub>Br<sub>2</sub>, CdSb<sub>6</sub>S<sub>8</sub>I<sub>4</sub>, Cs<sub>13</sub>Ga<sub>17.67</sub>Se<sub>32</sub>Cl<sub>2</sub>, Cs<sub>2.32</sub>Mo<sub>4.21</sub>S<sub>4</sub>Cl<sub>8.22</sub>, Cu<sub>6</sub>PS<sub>5</sub>Cl, Ga<sub>2</sub>P<sub>3</sub>Se<sub>4</sub>Cl<sub>7</sub>, GaSb<sub>2</sub>Te<sub>2</sub>Cl<sub>4</sub>, GaSb<sub>3</sub>Te<sub>4</sub>Cl<sub>4</sub>, Ga<sub>7</sub>Sb<sub>7</sub>Te<sub>8</sub>Cl<sub>26</sub>, Ga<sub>8</sub>Sb<sub>7</sub>Te<sub>8</sub>Cl<sub>29</sub>, Ga<sub>2</sub>SbTe<sub>4</sub>Cl<sub>7</sub>, Hg<sub>7</sub>InS<sub>6</sub>Cl<sub>5</sub>, Hg<sub>3</sub>ZnS<sub>2</sub>Cl<sub>4</sub>, Pb<sub>3.45</sub>Sb<sub>2.55</sub>S<sub>6.55</sub>Cl<sub>1.45</sub>, Pb<sub>10.38</sub>Sb<sub>9.68</sub>S<sub>23</sub>Cl<sub>4</sub>, Pb<sub>12.65</sub>Sb<sub>11.35</sub>S<sub>28.35</sub>Cl<sub>2.65</sub>, TlRe<sub>3</sub>S<sub>4</sub>Cl<sub>2</sub>, TlRe<sub>3</sub>Se<sub>4</sub>Cl<sub>2</sub>, TlRe<sub>6</sub>Se<sub>8</sub>Cl<sub>3</sub>, Cs<sub>3</sub>Re<sub>3</sub>S<sub>4</sub>I<sub>4</sub>, Cs<sub>2</sub>Re<sub>3</sub>Se<sub>4</sub>I<sub>3</sub>, CuHgSI, Cu<sub>5</sub>SbS<sub>3</sub>I<sub>2</sub>, Cu<sub>5</sub>TeS<sub>3</sub>I<sub>3</sub>, Hg<sub>3</sub>SiS<sub>2</sub>F<sub>6</sub>, Hg<sub>2</sub>PbS<sub>2</sub>I<sub>2</sub>, Li<sub>4</sub>PS<sub>4</sub>I, Li<sub>5</sub>SbS<sub>3</sub>I<sub>2</sub>, Pb<sub>2</sub>SbS<sub>2</sub>I<sub>3</sub>, Pb<sub>2</sub>SbS<sub>2</sub>I<sub>3</sub>, Ta<sub>4</sub>PfTe<sub>16</sub>I<sub>8</sub>, U<sub>4</sub>Ta<sub>7</sub>Se<sub>28</sub>I<sub>20</sub>, Sn<sub>2</sub>BiSI<sub>5</sub>,</p>	

The first quaternary chalcogenide,  $\text{Hg}_3\text{SiS}_2\text{F}_6$ , was synthesized in 1969; the derivatives  $\text{Hg}_3\text{SiSe}_2\text{F}_6$  and  $\text{Hg}_3\text{SiTe}_2\text{F}_6$  were also mentioned but no further characterization has appeared.<sup>17</sup> Several chalcogenides containing mobile monovalent Li, Cu, or Ag ions have been of interest for their ionic conductivity.  $\text{Li}_5\text{SbS}_3\text{I}_2$ ,  $\text{Cu}_5\text{SbS}_3\text{I}_2$ , and  $\text{Ag}_5\text{SbS}_3\text{I}_2$  have closely related structures but the arrangement of Li atoms is different from those of Cu and Ag atoms, which appear to be mobile.<sup>18–20</sup>  $\text{Cu}_{22}\text{Bi}_{12}\text{S}_{21}\text{Cl}_{16}$  also shows high mobility of Cu ions.<sup>21</sup> The argyrodites  $\text{Li}_6\text{PS}_5\text{X}$  ( $\text{X} = \text{Cl, Br, I}$ ) are derived by replacing one of the sulfur atoms in the mineral  $\text{Ag}_8\text{GeS}_6$  by a halogen atom and then reducing the number of Li atoms per formula unit for charge balance.<sup>13</sup> Other well known ionic conductors are the related argyrodite-type compounds  $\text{Ag}_7\text{GeCh}_5\text{I}$  ( $\text{Ch} = \text{S, Se}$ ),<sup>22</sup> and  $\text{AgHgSX}$  ( $\text{X} = \text{Br, I}$ ),<sup>23</sup> and the Li-containing compounds  $\text{Li}_4\text{PS}_4\text{I}^{24}$  and  $\text{Li}_{15}\text{P}_4\text{S}_{16}\text{Cl}_3$ .<sup>25</sup>

Characteristic motifs reminiscent of simpler structures emerge in some quaternary chalcogenides, depending on the size and electronegativities of the constituent anions. For example,  $\text{MnSbS}_2\text{Cl}$  and  $\text{MnSbSe}_2\text{I}$  adopt different structures despite having the same composition,<sup>26,27</sup> whereas  $\text{In}_2\text{BiSe}_4\text{I}$  and  $\text{In}_2\text{Bi}_2\text{Se}_7\text{I}$  contain similar structural motifs (distorted rocksalt-type and  $\text{CdI}_2$ -type strands) despite having different compositions.<sup>28</sup> From simple electronic and geometric considerations, 2D building blocks can be envisioned which stack alternately to build new structures for  $\text{BaFCl}$  (containing fluorite-type blocks  $[\text{Ba}_2\text{F}_2]$ ) and  $\text{La}_2\text{O}_2\text{SnS}_3$  (containing  $[\text{SnS}_3]$  blocks), following analogous concepts of so-called “crystal engineering” in supramolecular chemistry and aided by electronic structure calculations. Combining this approach with the concept of phase homologies offers a way to “design” solid state compounds, as illustrated by the series  $\text{Ae}_2\text{SnCh}_3\text{F}_2$  ( $\text{Ae} = \text{Sr, Ba}$ ;  $\text{Ch} = \text{S, Se}$ ), built from fluorite  $[\text{Ae}_2\text{F}_2]$  and distorted rock salt  $[\text{SnCh}_3]$  blocks, and a new homologous series  $\text{Ae}_2\text{M}_{1+n}\text{Ch}_{3+n}\text{F}_2$  ( $\text{Ae} = \text{Sr, Ba}$ ;  $\text{M} = \text{main group metal}$ ;  $n = \text{integer}$ ).<sup>29</sup>

Peculiar structural effects occur in some quaternary chalcogenides.  $\text{Ag}_{15}(\text{PS}_4)_4\text{Cl}_3$  can be considered to be derived from  $\text{Ag}_3\text{PS}_4$  (or  $\text{Ag}_{15}(\text{PS}_4)_5$  if the formula unit is multiplied by five) with one of the  $\text{PS}_4^{3-}$  anions replaced by three  $\text{Cl}^-$  ions. The structure contains not only  $\text{AgS}_4$  and  $\text{PS}_4$  tetrahedra, but also  $\text{AgS}_3\text{Cl}$  tetrahedra.<sup>30</sup>  $\text{Cs}_4\text{Re}_6\text{S}_8\text{Br}_6$  and  $\text{Cs}_2\text{Re}_6\text{S}_8\text{Br}_4$  compounds contain  $\text{Re}_6$  clusters like those found in Chevrel phases.<sup>31</sup> The magnetic properties of  $\text{Ba}_2\text{Fe}_{2-x}\text{Ch}_3\text{F}_2$  ( $\text{Ch} = \text{S}, \text{Se}$ ) were varied by controlling the level of Fe defects.<sup>32</sup>  $\text{Cs}_{13}\text{Ga}_{17.67}\text{Se}_{32}\text{Cl}_2$  consists of a very long stacking sequence of  $[\text{Ga}_{53}\text{Se}_{96}]^{33-}$  layers built from  $[\text{Ga}_2\text{Se}_6]^{6-}$  dimers.<sup>33</sup> Partial substitution of divalent S atoms by monovalent halogen atoms occurs in various known and hypothetical members of the homologous  $\text{Ag-Bi-Ch-X}$  series.<sup>34</sup>  $\text{Ag}_{1.2}\text{Bi}_{17.6}\text{S}_{23}\text{Cl}_8$  is built by intergrowth of layers containing complex units.<sup>35</sup>

Incorporating rare-earth metals into quaternary chalcogenides gives rise to diverse crystal structures and further opportunities to vary physical properties. Given the large atomic sizes and similar electronegativities, they can often be substituted for each other and are found in a wide variety of coordination geometries with high CN. The optical and magnetic properties of these compounds depend on the presence of unpaired electrons in highly localized f orbitals. Most rare-earth elements are trivalent, but a few can exhibit other oxidation states (e.g.,  $\text{Ce}^{4+}$ ,  $\text{Eu}^{2+}$ ,  $\text{Yb}^{2+}$ ). Chalcogenides containing two or more metal cations are generally challenging to prepare because they may compete with thermodynamically more stable mixtures of binary and ternary phases.

An important principle governing the structures of mixed-anion compounds is that the more electropositive metal atoms will tend to form ionic bonds with the more electronegative nonmetal atoms, while less electropositive metal atoms will tend to form more covalent bonds with the less electronegative nonmetal atoms. Rare-earth-containing chalcogenides  $\text{RE-M-Ch-X}$  are still scarce, with about 50 compounds reported to date (**Table 1-2**), but they generally conform to

this principle. These structures encompass the usual range of 3D networks, 2D layers, 1D chains, and isolated molecular units.

**Table 1-2.** Quaternary rare-earth-containing chalcogenides.

Compounds	Structure type	Space group
EuAgSeF, EuCuChF ( <i>Ch</i> = S, Se, Te)	CuZrSiAs	<i>P4/nmm</i>
EuAg <sub>0.949</sub> TeF, SmCuSeF <sup>36-38</sup>	(or LaAgSO)	
Pr <sub>3</sub> AsS <sub>5</sub> Cl <sub>2</sub> <sup>39</sup>	Pr <sub>3</sub> AsS <sub>5</sub> Cl <sub>2</sub>	<i>Cc</i>
EuBiS <sub>2</sub> F <sup>40</sup>	CeBiS <sub>2</sub> O	<i>P4/nmm</i>
Eu <sub>3</sub> Bi <sub>2</sub> S <sub>4</sub> F <sub>4</sub> <sup>41-42</sup>	Eu <sub>3</sub> Bi <sub>2</sub> S <sub>4</sub> F <sub>4</sub>	<i>I4/mmm</i>
RESbS <sub>2</sub> Br <sub>2</sub> ( <i>RE</i> = La, Ce) <sup>43</sup>	CeSbS <sub>2</sub> Br <sub>2</sub>	<i>P2<sub>1</sub>/c</i>
RE <sub>2</sub> SbS <sub>5</sub> Br ( <i>RE</i> = La, Ce) <sup>44</sup>	Ce <sub>2</sub> SbS <sub>5</sub> Br	<i>Pnma</i>
Ce <sub>17.67</sub> Fe <sub>4</sub> S <sub>30</sub> X ( <i>X</i> = Cl, Br, I) <sup>45</sup>	Ce <sub>17.67</sub> Fe <sub>4</sub> S <sub>30</sub> Cl	<i>R<math>\bar{3}m</math></i>
La <sub>17.67</sub> Fe <sub>4</sub> S <sub>30</sub> Br <sup>46</sup>	La <sub>17.67</sub> Fe <sub>4</sub> S <sub>30</sub> Br	<i>R<math>\bar{3}m</math></i>
La <sub>17.67</sub> Fe <sub>4</sub> S <sub>30</sub> Cl <sup>46</sup>	La <sub>17.67</sub> Fe <sub>4</sub> S <sub>30</sub> Cl	<i>R<math>\bar{3}m</math></i>
La <sub>17.67</sub> Fe <sub>4</sub> S <sub>30</sub> I <sup>46</sup>	La <sub>17.67</sub> Fe <sub>4</sub> S <sub>30</sub> I	<i>R<math>\bar{3}m</math></i>
RE <sub>8</sub> CrTe <sub>13</sub> Cl ( <i>RE</i> = Sm, Gd, Tb) <sup>47</sup>	Sm <sub>8</sub> CrTe <sub>13</sub> Cl	<i>Cmc2<sub>1</sub></i>
Cs <sub>6</sub> RE <sub>21</sub> Ch <sub>34</sub> Cl ( <i>RE</i> = Ho, Dy; <i>Ch</i> = S, Se, Te) <sup>48</sup>	Cs <sub>6</sub> Dy <sub>21</sub> S <sub>34</sub> Cl	<i>C2/m</i>
RE <sub>3</sub> Si <sub>6</sub> Cl ( <i>RE</i> = Sm, Nd) <sup>49-50</sup>	Sm <sub>3</sub> Si <sub>6</sub> Cl	<i>Pnma</i>
RE <sub>3</sub> Si <sub>2</sub> S <sub>8</sub> X ( <i>RE</i> = La, Ce, Pr; <i>X</i> = Cl, Br, I), RE <sub>3</sub> Si <sub>2</sub> S <sub>8</sub> X ( <i>RE</i> = Nd, Sm; <i>X</i> = Br, I), Tb <sub>3</sub> Si <sub>2</sub> S <sub>8</sub> I, Gd <sub>3</sub> Si <sub>2</sub> S <sub>8</sub> Br, RE <sub>3</sub> Ge <sub>2</sub> S <sub>8</sub> I ( <i>RE</i> = La, Ce, Pr) <sup>51-57</sup>	La <sub>3</sub> [SiO <sub>4</sub> ] <sub>2</sub> Cl	<i>C2/c</i>

## 1.2 Structures of quaternary rare-earth-containing chalcogenides

### 1.2.1 CuZrSiAs- or LaAgSO-type

The compounds *REMChF* (*RE* = Eu, Sm; *M* = Cu, Ag; *Ch* = S, Se, Te) crystallize in the well known tetragonal CuZrSiAs-type structure (also called LaAgSO-type) in space group *P4/nmm*, characterized by [*RE*<sub>2</sub>F<sub>2</sub>]<sup>2+</sup> and [*M*<sub>2</sub>Ch<sub>2</sub>]<sup>2-</sup> layers (**Figure 1-2**).<sup>36-38</sup> These layers consist of edge-sharing tetrahedra, either F atoms surrounded by *RE* atoms, or *M* atoms surrounded by *Ch* atoms. The *RE* atoms are divalent, which is common for Eu but unusual for Sm. Thus it is no surprise that there exist related compounds in which these *RE* atoms are substituted by alkaline-

earth atoms: BaAgChF ( $Ch = S, Se, Te$ ), SrAgChF ( $Ch = S, Se, Te$ ), BaCuChF ( $Ch = S, Se, Te$ ), BaMn<sub>0.5</sub>TeF, and SrCuChF ( $Ch = S, Se, Te$ ).<sup>58–61</sup> These compounds are semiconductors with band gaps of 1.7 to 3.0 eV.

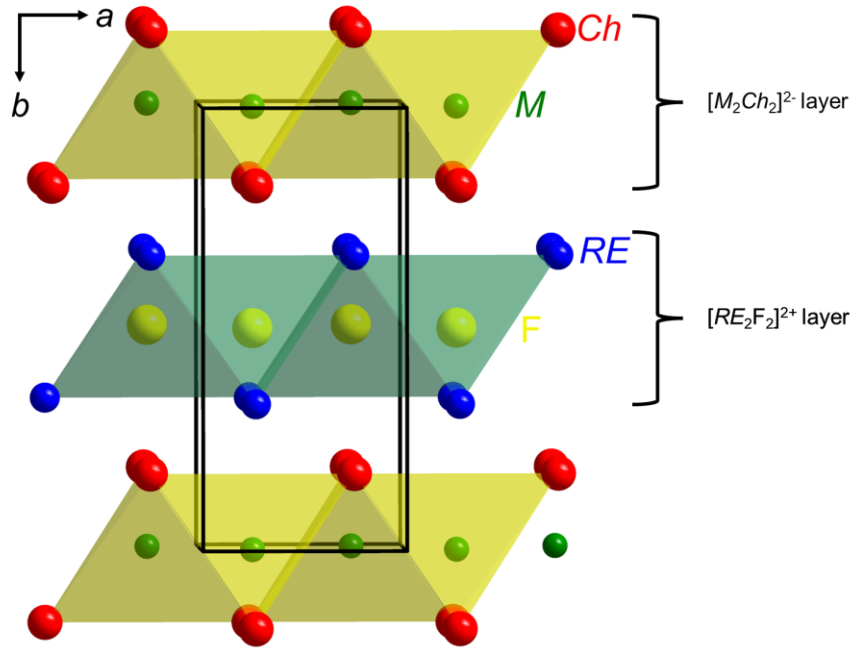


**Figure 1-2.** Structure of  $REMChF$  ( $RE =$  Rare-earth;  $M = Cu, Ag$ ;  $Ch = S, Se, Te$ ).

### 1.2.2 CeBiS<sub>2</sub>O type

Closely related to the LaAgSO-type discussed above, EuBiS<sub>2</sub>F adopts the tetragonal CeBiS<sub>2</sub>O-type structure in space group  $P4/nmm$ , with  $[Eu_2F_2]$  and  $[BiS_2]$  layers (**Figure 1-3a**).<sup>40</sup> The related compound Sr<sub>0.5</sub>La<sub>0.5</sub>BiS<sub>2</sub>F undergoes a superconducting transition at 2.8 K, through tuning of the electron concentration within the conducting  $[BiS_2]$  layers. Eu<sub>3</sub>Bi<sub>2</sub>S<sub>4</sub>F<sub>4</sub> is derived by doubling the thicknesses of the layers (**Figure 1-3b**), with evidence for mixed valence of the Eu atoms.<sup>41,42</sup>

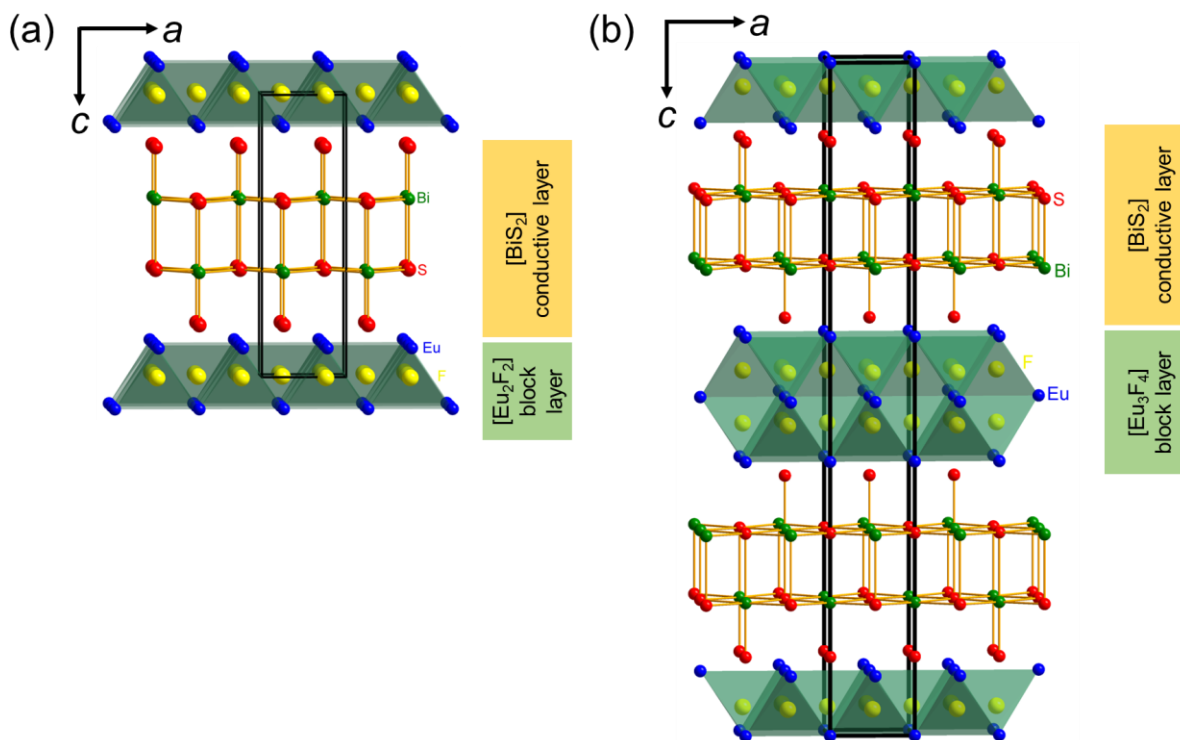


**Figure 1-3.** Structures of (a) EuBiS<sub>2</sub>F and (b) Eu<sub>3</sub>Bi<sub>2</sub>S<sub>4</sub>F<sub>4</sub>.

### 1.2.3 Misfit layered compounds

Several rare-earth chalcogenides adopt misfit layered structures, which are built from independent layers whose periodicities do not align in registry. The compounds  $RE_8CrTe_{13}Cl$  ( $RE = Sm, Gd, Tb$ ) consist of double rock-salt-type layers  $[RE_6Te_5Cl]$  alternating with CdI<sub>2</sub>-type layers  $[RE_2CrTe_6]$  in monoclinic space group  $Cmc2_1$  (**Figure 1-4**). The  $RE$  atoms are surrounded by Te and Cl atoms, whereas the Cr atoms are surrounded by only Te atoms.<sup>47</sup>

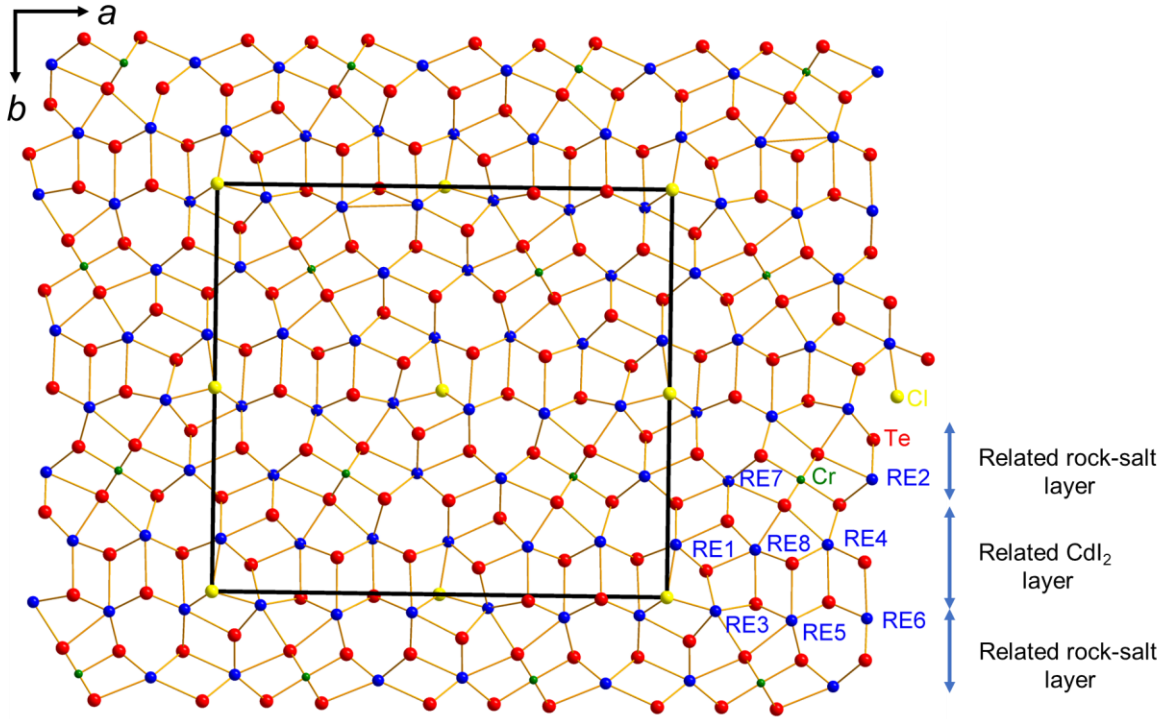


**Figure 1-4.** Structure of  $RE_8CrTe_{13}Cl$  ( $RE = Sm, Gd, Tb$ ).

### 1.2.4 $Ce_2SbS_5Br$ -type

$RE_2SbS_5Br$  ( $RE = La, Ce$ ) crystallize in an orthorhombic structure in space group  $Pnma$  containing  $[RE_2S_{10}Br_2]$  and  $[RE_2S_8Br_2]$  layers, which are connected to form a 3D framework defining tunnels that run along the  $a$ -direction (**Figure 1-5**). The  $RE$  atoms are surrounded by S and Br atoms, whereas the Sb atoms are surrounded only by S atoms.<sup>44</sup>  $RESbS_2Br_2$  ( $RE = La, Ce$ ) are closely related but crystallize in a monoclinic structure in space group  $P2_1/c$  containing  $[RE_2S_6Br_8]$  chains aligned along the  $b$ -direction.<sup>43</sup> These chains are then linked to form corrugated  $[RE_2S_4Br_4]$  layers which stack along the  $c$ -direction. The optical band gaps are 2.1 eV for  $RE_2SbS_5Br$  ( $RE = La, Ce$ ) and 2.4–2.7 eV for  $RESbS_2Br_2$  ( $RE = La, Ce$ ).

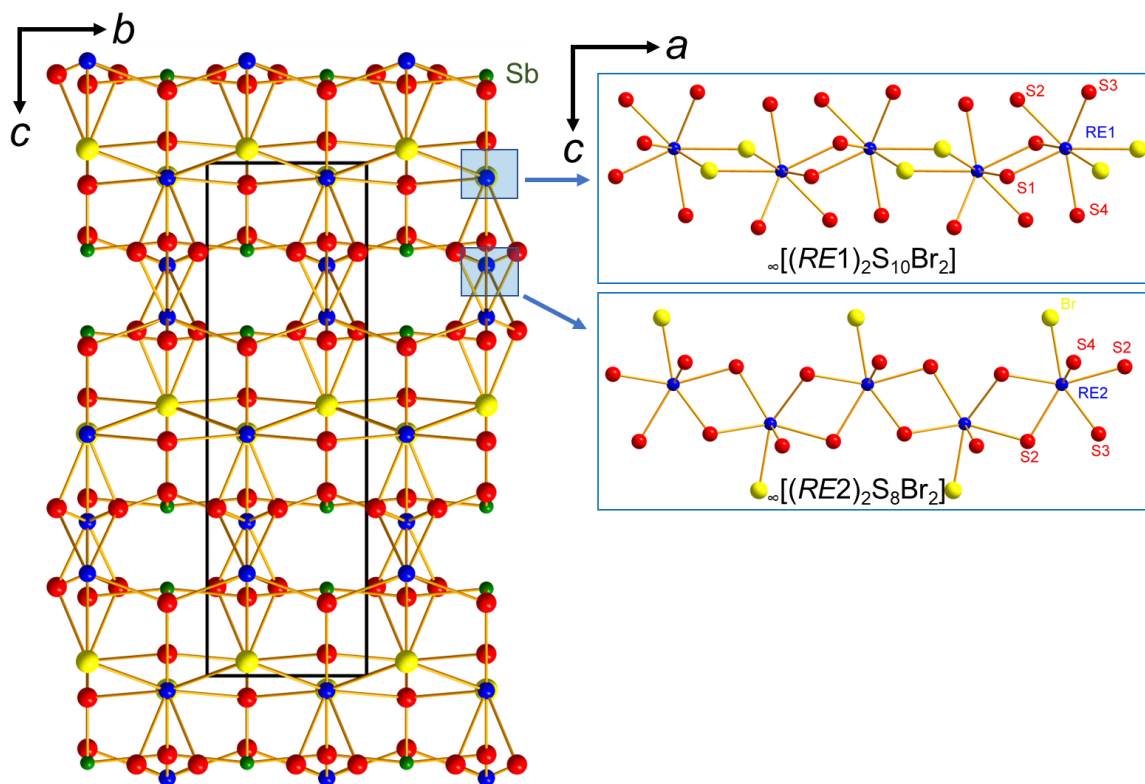


**Figure 1-5.** Structure of  $RE_2SbS_5Br$  ( $RE = La, Ce$ ).

### 1.2.5 $Sm_3SiS_6Cl$ -type

$RE_3SiS_6Cl$  ( $RE = Nd, Sm$ ) was obtained in attempts to prepare heavier  $RE$  homologues of  $RE_3[SiS_4]_2Cl$  ( $RE = La-Pr$ ). They crystallize in the orthorhombic  $Sm_3SiS_6Cl$ -type structure in space group  $Pnma$  (**Figure 1-6**).<sup>49,50</sup> Both types of structures contain isolated tetrahedral thiosilicate groups  $SiS_4$ , and infinite chains of Cl ions. The  $RE$  atoms are surrounded by S and Cl atoms.  $Nd_3SiS_6Cl$  exhibits antiferromagnetic interactions between the Nd atoms.

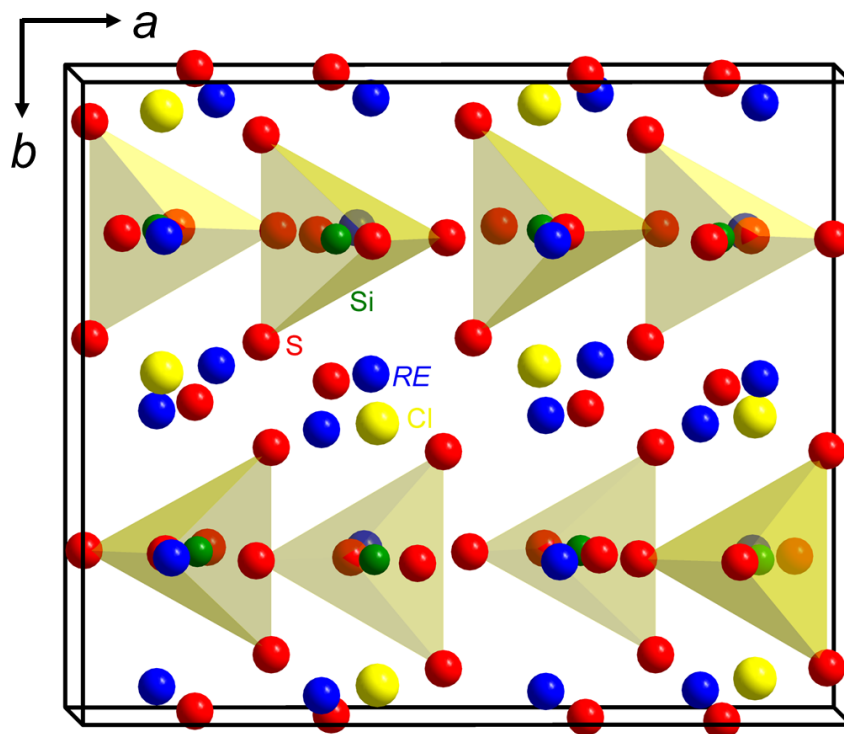


**Figure 1-6.** Structure of  $RE_3SiS_6Cl$  ( $RE = Nd, Sm$ ) containing isolated  $SiS_4$  tetrahedra.

### 1.3 Intermetallic compounds

Intermetallic compounds consist of two or more metals or metalloids bonded together, with definite structures and compositions that may vary slightly. It is unfortunate that, to this day, many chemists still cling to the misguided notion, propagated by Dalton but valiantly disputed by Berthollet, that compounds must conform to the law of definite proportions, meaning that their compositions are fixed; some of them may find it inconceivable that intermetallic compounds are legitimate compounds or, even more preposterously, they may dismiss them as being “non-chemical.” In fact, many everyday inorganic solids, such as lithium-containing oxides in batteries or carbon steels in structural materials, owe their useful properties precisely to the occurrence of variable compositions. Aluminides and silicides are often strong and heat resistant, such as  $Ni_3Al$  (jet engines),  $TiAl$  (turbines), and  $MoSi_2$  (heating elements).<sup>62</sup> Lead-free solders such as stannides

$\text{Cu}_6\text{Sn}_5$ ,  $\text{Cu}_3\text{Sn}$ , and  $\text{Ni}_3\text{Sn}_4$  are used to join copper pipes.<sup>63</sup> NMR spectrometers and magnetic resonance imaging would not be possible without superconducting  $\text{Nb}_3\text{Sn}$  used in high-field magnets.<sup>64</sup>

Intermetallic compounds are generally distinguished from alloys in that their structures are different from the component elements, and their phase compositions vary less or are fixed (in which case they are called “line phases” because they are represented as vertical lines in phase diagrams) (**Figure 1-7**). Like alloys, however, intermetallic compounds may still exhibit some degree of disorder. Notwithstanding their name, intermetallic compounds exhibit bonding character that can combine metallic, ionic, and covalent interactions.<sup>65</sup>

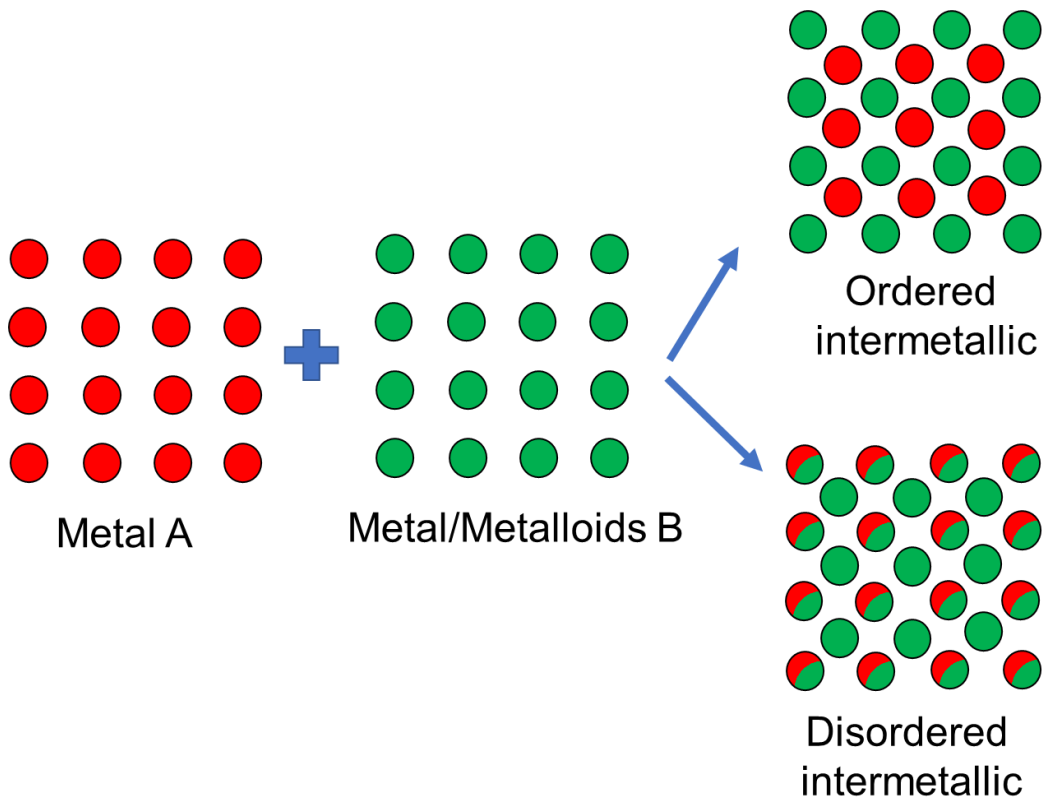


**Figure 1-7.** Formation of intermetallic compounds.

### 1.3.1 Rare-earth intermetallics

Given the major use of rare-earth compounds as magnetic materials (such as  $\text{SmCo}_5$  and  $\text{Nd}_2\text{Fe}_{14}\text{B}$ ), it is not a surprise that intermetallics containing rare-earth metals remain an attractive area of research. For crystallographers, they are interesting because they show a great variety of compositions and structures that enable systematic patterns to be revealed. For condensed matter physicists, they are a source of “quantum materials” exhibiting unusual magnetic and transport properties arising from the interactions of localized f-electrons with delocalized conduction electrons. For materials scientists, they enable control of properties through gradual changes in atomic sizes and electron counts. In addition to existing rare-earth intermetallics already used in applications, many binary rare-earth transition-metal compounds such as  $\text{LaNi}_5$  are promising as hydrogen storage materials,<sup>66</sup> and ternary intermetallics such as  $\text{Gd}_5\text{Si}_2\text{Ge}_2$  may be useful as magnetocaloric materials for magnetic refrigeration.<sup>67</sup>

Among ternary intermetallics  $RE-M-X$  (where  $M$  = transition metal and  $X$  = main-group metal or metalloid), those that contain Ce, Eu, and Yb are unusual because they are prone to valence fluctuation or mixed valence; they are often studied in connection to exotic phenomena such as superconductivity, charge density waves, itinerant ferromagnetism, quantum criticality, heavy fermion behaviour, and Kondo effect. There are many Ce-containing compounds, but relatively fewer Eu- and Yb-containing compounds (**Figure 1-8**).<sup>11</sup> One reason might be that there are special problems in synthesizing intermetallics containing Eu and Yb. These metals are difficult to handle using conventional synthetic methods such as arc-melting because they have high vapour pressures and they react with many container materials.

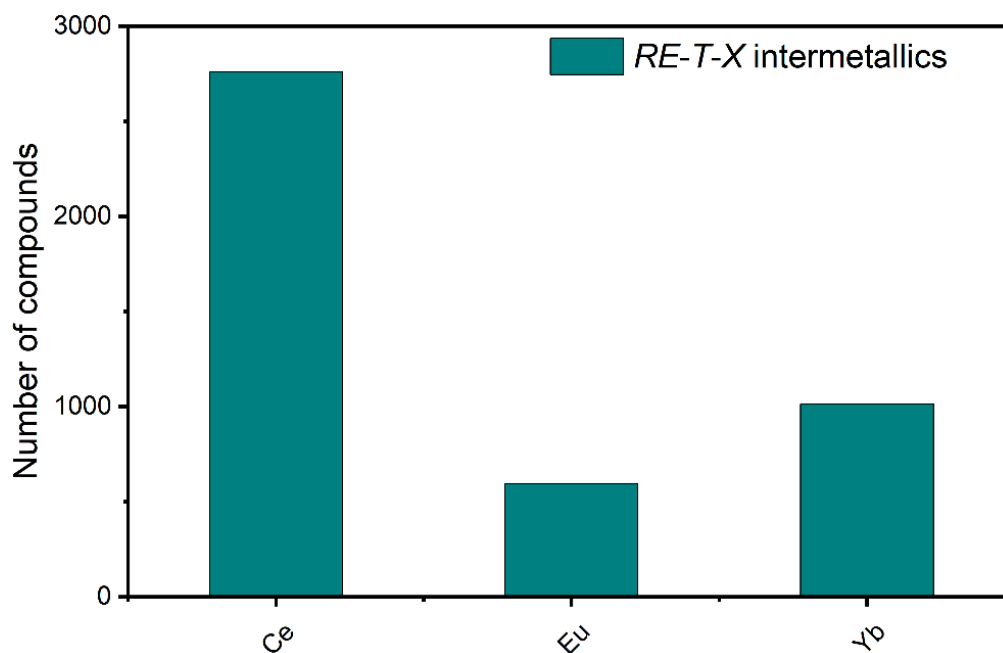


**Figure 1-8.** Reported ternary  $RE-T-X$  intermetallic compounds.

### 1.3.2 Crystal growth

Given their high melting points, intermetallic compounds have been synthesized by methods such as arc melting, induction heating, and direct reactions at high temperatures. These methods normally lead to polycrystalline samples. It is often desirable to obtain large single crystals for X-ray diffraction experiments and physical property measurements. Many rare-earth intermetallic compounds are quantum materials whose properties depend on orientation, such as topological materials, for which complete characterization depends on the availability of high quality single crystals.<sup>68</sup> Because Bridgman and Czochralski methods require investment in specialized equipment, which requires considerable experience to maintain and operate, there has been interest in developing crystal growth methods that are simpler to apply in a laboratory setting.<sup>69</sup> Molten salts have long been effective for single crystal growth of oxides, chalcogenides, oxychalcogenides, and some pnictides, but they generally do not work well for intermetallics.

Instead, low-melting metal fluxes have been found to be highly suitable for single crystal growth of many intermetallics. The purpose of the flux is to dissolve the components at lower temperatures than would normally be accessible, enhancing diffusion rates to promote growth of crystals.

The history of metal fluxes can be traced to as early as Moissan's failed attempts to prepare diamond crystals in the presence of molten iron, resulting in crystals of SiC (carborundum) instead. His colleague Lebeau grew transition metal silicides in a copper flux, a technique which is now used to prepare many borides and carbides as well. The most commonly used fluxes have low melting points and remain molten over a wide range of temperatures, including Al (660 °C), Ga (30 °C), In (157 °C), Sn (232 °C), Pb (328 °C), Sb (631 °C), and Bi (271 °C). Usually they are present in large excess, and the reaction mixture is slowly cooled to promote growth of large crystals. However, there is no guarantee of success: multiple phases can result from these processes, the crystals may not be particularly large, and metastable or kinetically stable products may also be formed. It may also not be straightforward to separate crystals from the flux. Crystal growth remains, as it has for centuries, as much an art as a science, depending sensitively on the vicissitudes of reaction conditions. These conditions include loading compositions, reaction temperatures, heating and cooling rates, and perhaps many other factors that we may still be unaware about.<sup>70</sup>

The group-13 elements Al, Ga, and In have been used frequently to prepare many rare-earth intermetallics, often acting as reactive fluxes in which these elements are also incorporated into the final product. Various aluminides have been prepared in this way:  $\text{Sm}_2\text{Ni}(\text{Ni}_x\text{Si}_{1-x})\text{Al}_4\text{Si}_6$ ,<sup>71</sup>  $\text{REFe}_4\text{Al}_9\text{Si}_6$  ( $\text{RE} = \text{Tb}, \text{Er}$ ),<sup>72</sup>  $\text{RE}_8\text{Ru}_{12}\text{Al}_9\text{Si}_9(\text{Al}_x\text{Si}_{12-x})$  ( $\text{RE} = \text{Pr}, \text{Sm}$ ),<sup>73</sup> and  $\text{RE}_6\text{M}_4\text{Al}_{43}$  ( $\text{RE} = \text{Gd}, \text{Yb}$ ;  $\text{M} = \text{Cr}, \text{Mo}, \text{W}$ ).<sup>74</sup> However, one drawback is that aluminum is

incompatible with fused-silica tubing, which is the most frequently used container in solid state reactions. Many gallides and germanides have been obtained in the presence of gallium and indium fluxes, which can be separated by filtration or chemical dissolution. Gallium flux was used to grow crystals of  $\text{GdCo}_{1-x}\text{Ga}_3\text{Ge}$ ,<sup>75</sup>  $\text{REAg}_x\text{Ga}_{4-x}$  ( $\text{RE} = \text{La-Nd, Sm, Eu, Yb}$ ),<sup>76</sup> and  $\text{Yb}_6(\text{CuGa})_{50}$ .<sup>77</sup> Because In forms no binary phases with Ge, it is an appropriate nonreactive flux for many germanides, including  $\text{RE}_2\text{Ru}_3\text{Ge}_5$  ( $\text{RE} = \text{La, Ce, Nd, Gd, Tb}$ ),<sup>78</sup>  $\text{Yb}_2\text{CuGe}_6$ ,<sup>79</sup>  $\text{EuCu}_2\text{Ge}_2$ ,<sup>80</sup> and  $\text{RE}_4\text{TGe}_8$  ( $\text{RE} = \text{Gd, Yb}$ ;  $\text{T} = \text{Cr-Ni, Ag}$ ),<sup>81</sup> although in some cases, it does act as a reactive flux, to form  $\text{Eu}_3\text{Ag}_2\text{In}_9$ ,<sup>80</sup>  $\text{EuIr}_4\text{In}_2\text{Ge}_4$ ,<sup>82</sup>  $\text{RE}_7\text{M}_4\text{InGe}_{12}$  ( $\text{RE} = \text{Y, Yb}$ ;  $\text{M} = \text{Co, Ni, Ru}$ ),<sup>83-85</sup> and  $\text{Yb}_3\text{AuGe}_2\text{In}_3$ .<sup>86</sup> The other elements Sn, Pb, Sb, and Bi are also commonly encountered fluxes. Sn has been frequently used to prepare many pnictides, especially phosphides.  $\text{LaPd}_{1-x}\text{Bi}_2$  and  $\text{Ce}_2\text{Rh}_3\text{Ge}_5$  were obtained in Bi flux,<sup>87</sup> and  $\text{Ce}_2\text{Ru}_{12}\text{P}_7$  and  $\text{Eu}_4\text{Ir}_8\text{As}_7$  were obtained in the Pb flux.<sup>88-89</sup>

## 1.4 Synthesis

The special challenges of crystal growth of intermetallics were explained above, but it is worthwhile to review the standard techniques for synthesis of solid state compounds and to describe the experimental procedures in more detail, as they pertain to the preparation of chalcogenides and intermetallics (**Figure 1-9**). To prepare rare-earth chalcogenides, direct reactions were performed. To prepare rare-earth intermetallics, arc melting and induction heating were used to prepare bulk polycrystalline samples, and metal fluxes were used to grow single crystals.

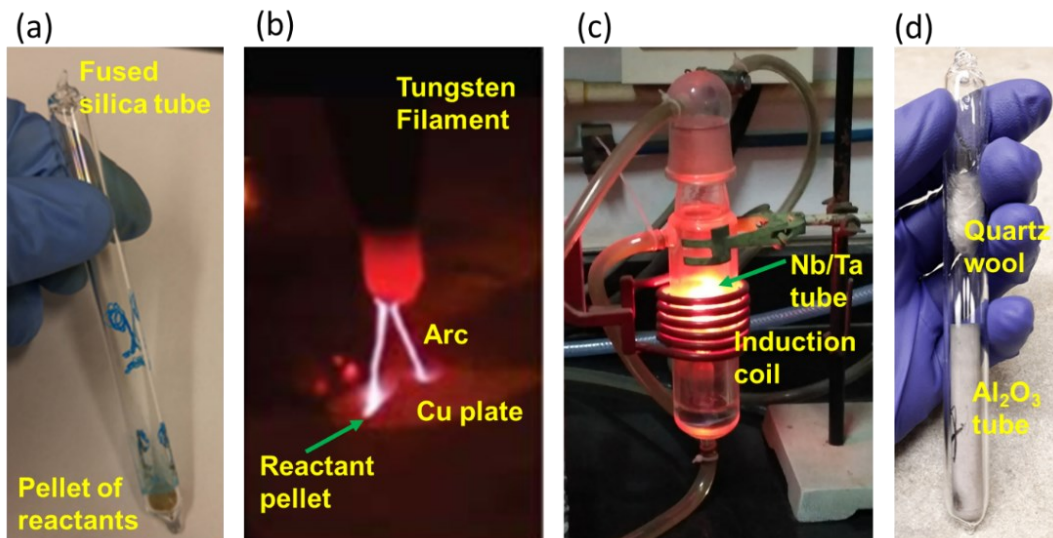


**Figure 1-9.** Synthetic methods: (a) direct reaction, (b) arc melting, (c) induction heating, and (d) metal flux growth.

### 1.4.1 Direct reaction

The reactants are typically the constituent elements, which are ground into fine powders to increase surface area and pressed into pellets to improve contact between particles, and then placed into suitable containers, depending on their compatibility with the reactants. In most cases, fused silica tubes, with dimensions of 12-mm diameter and 15-cm length, are appropriate for the small scale (a few hundred mg) of the reactions performed. Although there is a risk that rare-earth elements will react with fused silica, they usually react faster with the other elements (e.g., S, Se, Si, Ge, Sn) within the pressed pellets. The tubes are then evacuated, sealed, and heated to high temperatures within resistance furnaces (up to 1000 °C). A common question that neophytes pose is how to choose appropriate heating (and cooling) profiles. Many of these details are considered on a case-by-case basis, with knowledge of properties and reactivities of the elements. For example, when highly volatile elements such as sulfur or iodine are present, the tubes are heated gradually to avoid volatilization losses and to prevent catastrophic failure of the tubes caused by a

sudden increase in pressure. In other cases, optimized conditions reported in the literature for related compounds are used without shame or embarrassment. Of course, this does not excuse the need for analysis of the products, followed by rational adjustment of conditions to improve phase purity. It is no different from the tedious work that molecular chemists do to try different solvents, temperatures, reagents, and other adjustments. In situ monitoring of solid state reactions through X-ray diffraction experiments could help optimize reaction conditions more rapidly, but this remains a specialized technique that is not always easy to carry out.

### **1.4.2 Arc melting**

When reactants are unreactive at the typical temperatures attainable in a resistance furnace, they can be melted in an electric arc generated by high potentials under an inert atmosphere. To ensure that traces of oxygen gas are removed from the chamber, the arc is briefly directed to a metal ingot (typically a Ti pellet), which is melted and acts as a getter. Then the arc is directed to the reactants (usually, but not always, combined in a pressed pellet). Again, careful consideration must be made of the relative melting (and boiling) points of the constituent elements; if they are too dissimilar, one reactant may volatilize before it has a chance to react. This is especially problematic for elements such as Eu, Yb, Zn, and others. Weighing the pellet before and after arc melting is good practice to monitor any mass losses. If mass losses are unavoidable, then they can be compensated by adding an appropriate excess of the volatile element. Typically, the ingots are flipped and arc melted two or more times to achieve homogeneity. Then, the arc-melted ingots can be further annealed within fused silica tubes at different temperatures to attain equilibrium conditions.

### **1.4.3 Induction heating**

When container compatibility is a problem, induction heating can be a valuable synthetic method. The precursors are loaded into metal tubes (typically Nb or Ta), which are welded shut by arc-melting under inert atmosphere. These tubes are then placed within an induction coil, which generates an alternating electromagnetic field and heats the sample extremely rapidly (within seconds) through eddy currents. The reaction temperature can be measured using an optical pyrometer, but caution should be exercised because the readings depend on its position to the coil and the position of the sample being heated.

### **1.4.4 Metal flux growth**

Constituent elements as well as the metal flux are loaded into crucibles (alumina, zirconia, or graphite) or metal tubes (Nb, Ta). Where possible, alumina crucibles are used because they are the least expensive. The crucibles are then enclosed within fused silica tubes, which are evacuated and sealed. A small piece of quartz wool is placed above the crucible to act as a filter for removing the flux at a subsequent stage. The tubes are heated at high temperatures, followed by slow cooling to promote crystal growth. Different heating profiles and loading ratios are investigated to optimize the crystal growth. The tubes are then inverted and centrifuged to remove excess flux while molten by filtering through the quartz wool, leaving crystals within the crucible. The resulting crystals can then be further cleaned by etching the surface with appropriate solvents, such as a dilute solution of HCl to remove Ga or In flux.

## 1.5 Characterization

### 1.5.1 X-ray diffraction

The most important technique for determining the crystal structures of inorganic solids is X-ray diffraction, either on single crystals or powder samples. Single-crystal X-ray diffraction is generally used for complete structure determination, whereas powder X-ray diffraction is used to assess phase compositions and degree of crystallinity.

X-rays are produced when electrons generated by thermionic emission strike a metal target (e.g., Cu, Mo) (**Figure 1-10**). The X-ray emission spectrum consists of intense lines superimposed on a continuum of white radiation. The characteristic X-rays are emitted when outer shell electrons relax to fill the hole created when core electrons of the target atoms are ejected, the most prominent being the  $K\alpha$  ( $2p \rightarrow 1s$ ) and  $K\beta$  ( $3p \rightarrow 1s$ ) lines. (Each of these lines is further split into a doublet due to spin-orbit coupling). Diffraction experiments are performed with the intense  $K\alpha$  X-rays, monochromatized by applying filters to remove the background and  $K\beta$  radiation, or by using a single-crystal monochromator (e.g., graphite).

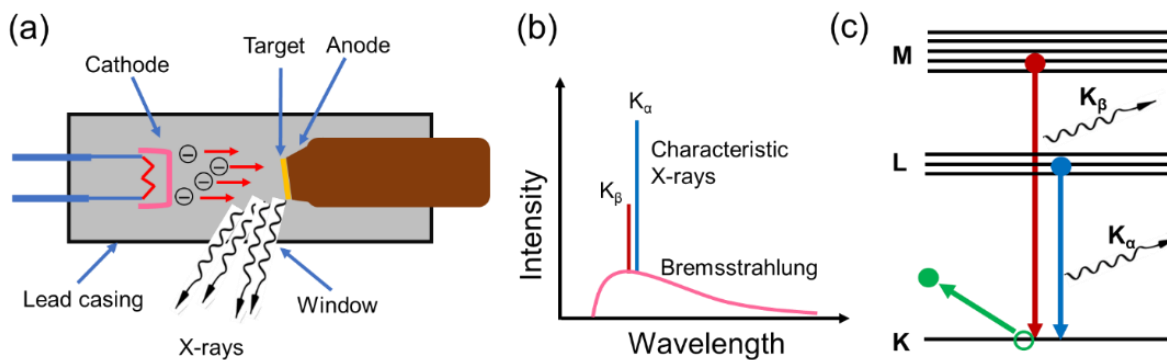


**Figure 1-10.** (a) Generation of X-rays, (b) emission spectrum, and (c) electronic transitions responsible for characteristic X-rays.

X-rays are scattered by the periodic arrangement of atoms in a crystal, and they undergo constructive and destructive interference to form a diffraction pattern, from which the structure can be deduced. The repeat pattern of the crystal is represented by its lattice, a set of points that define various parallel lattice planes ( $hkl$ ), separated by a constant spacing  $d_{hkl}$ . The condition for constructive interference can be expressed in terms of intersecting cones of scattered X-rays, oriented at angles relative to each of the unit cell axes (Laue equations), or in terms of “reflections” by lattice planes (Bragg’s law) (**Figure 1-11**).

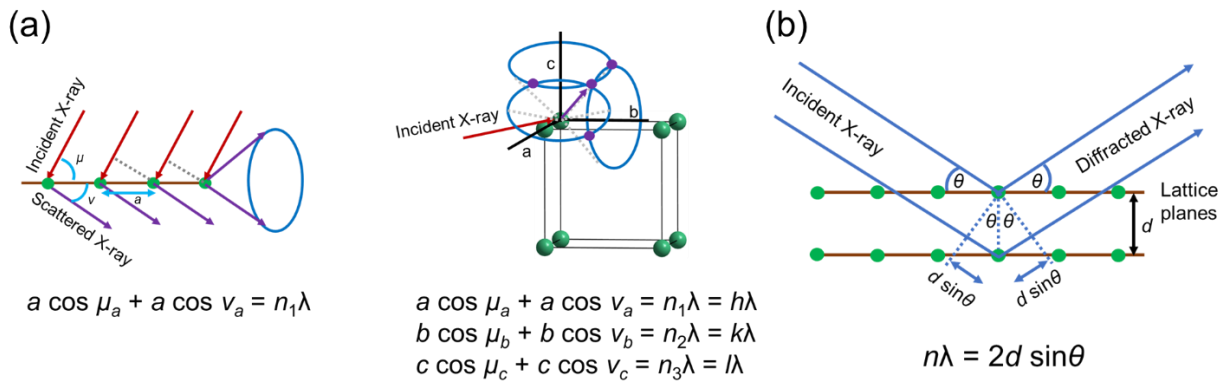


**Figure 1-11.** (a) Laue equations for a 1D row of atoms and for a 3D crystal and (b) Bragg’s law.

For single-crystal X-ray diffraction, a typical procedure can be described. A suitable crystal, with typical dimensions ranging from 0.5 to 0.01 mm, is mounted on a glass fibre and placed on a goniometer. In this thesis, a Bruker PLATFORM diffractometer equipped with a SMART APEX II CCD area detector and a Mo  $K\alpha$  X-ray source was used routinely, whereas a Bruker D8 Advance diffractometer was used for temperature-dependent studies. The crystal quality is screened by collecting a few frames of intensity data, and ensuring that the reflections are singular and strong (**Figure 1-12**). If the crystal is judged to be adequate, a full set of intensity

data is obtained, each frame being collected at different orientations  $(\omega, \chi, \phi)$  of the crystal, with exposure times of about 10–15 s.

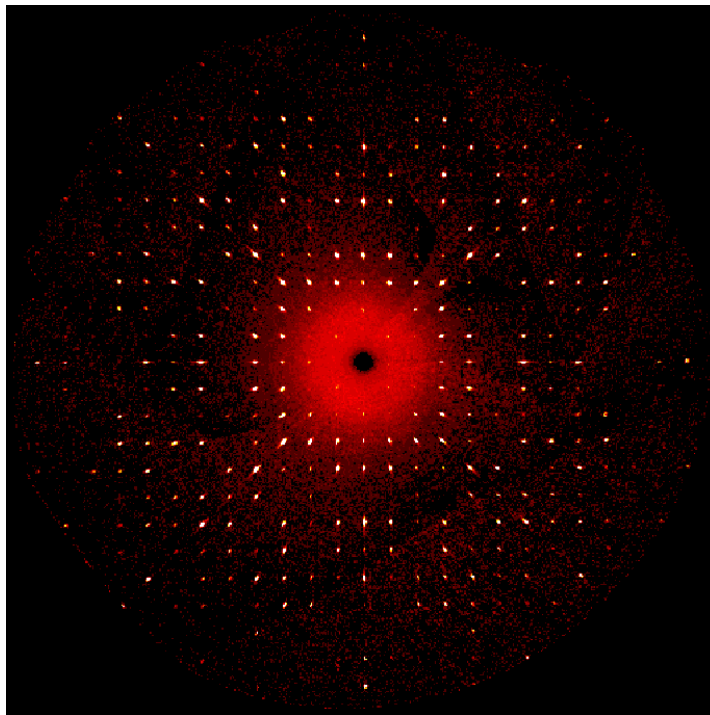


**Figure 1-12.** Precession image of  $\text{YbCu}_3\text{Ga}_8$ .

The data set consists of a large number of intensities  $I_{hkl}$ , from which the magnitude of the structure factor can be obtained,  $|F_{hkl}| \propto \sqrt{I_{hkl}}$ . Various standard corrections are applied at this data reduction stage, performed using the program SAINT. For crystals containing many heavy atoms, as is the case here, absorption corrections are essential, performed using the program SADABS. The structure factor is interpreted as the superposition of the waves scattered by atoms within the unit cell, with respect to a set of lattice planes  $(hkl)$ . In principle, it should be possible to locate the positions of atoms (i.e., the crystal structure), which is equivalent to determining the electron density function by performing a Fourier transform of the structure factors  $F_{hkl}$ , through the summation:  $\rho_{(x,y,z)} = \frac{1}{V} \sum_{hkl} F_{hkl} \cdot e^{-i2\pi(hx+ky+lz)}$ , where  $V$  is the unit cell volume.

Unfortunately, these structure factors are complex-valued, but only their magnitudes (and not their phases, or orientations within the complex number plane) can be obtained in the X-ray diffraction experiment. It is a testament to modern crystallography that statistical methods to determine these phases are now so routine and quick that users barely give a thought to how powerful they are. Crystal structures are solved and refined using the program package SHELXTL. The goal is to minimize the differences between the observed and calculated structure factors based on a structural model, to attain reasonable agreement (as assessed by a conventional  $R$ -factor, generally being less than 0.10, and a goodness-of-fit value being close to unity). Besides atomic positions, other features of the structural model that can be considered include displacement parameters that measure the vibrational motion of atoms and site occupancies that may need to be refined if atomic disorder occurs.

For powder X-ray diffraction, a sample is ground to a fine powder and placed on a rotating sample holder. The instruments used were either an Inel powder diffractometer with a curved position-sensitive detector, or a Bruker D8 Advance powder diffractometer, both operated with a  $\text{Cu K}\alpha_1$  radiation source. The powder XRD pattern is measured over a range of angles, usually between 5 and 90° in  $2\theta$ . To determine the phase composition of the sample, the experimental pattern is compared with simulated patterns for known phases, with crystallographic information available from Pearson's Crystal Database (**Figure 1-13**).<sup>90</sup> If a new phase is discovered, its powder XRD pattern can be indexed and its cell parameters can be refined. These patterns were analyzed with the programs in the TOPAS package.

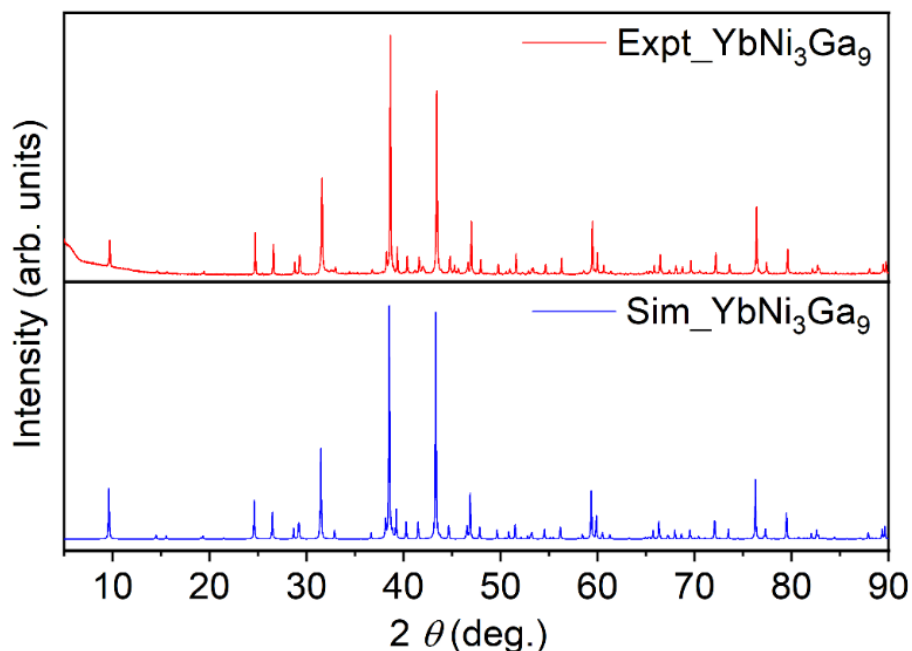


**Figure 1-13.** Experimental and simulated powder XRD patterns for  $\text{YbNi}_3\text{Ga}_9$ .

### 1.5.2 Scanning electron microscopy

Chemical compositions of inorganic solids can be determined on a scanning electron microscope. A focused beam of electrons undergoes many possible interactions with atoms at the surface of a sample (**Figure 1-14**). The primary electrons can undergo inelastic collisions with atoms near the surface of the sample to become secondary electrons with reduced energy, which are mainly used for imaging. Alternatively, the primary electrons can undergo elastic collisions with atoms over a larger interaction volume to become backscattered electrons. Because heavier atoms cause more scattering, the number of backscattered electrons is sensitive to the type of element and can be used to convey information about chemical composition, so that brighter parts of an image correspond to phases containing heavier elements. Perhaps most useful, when the primary electrons cause core electrons to be ejected, characteristic X-rays are produced by the electronic transitions to fill the hole. The energies of these X-rays are specific to the elements

present in the sample, so that the intensities of peaks in the energy-dispersive X-ray (EDX) spectrum give quantitative information about chemical composition, in terms of mass or atomic percentages (**Figure 1-15**). The precision of EDX analysis is typically about 2 to 5%, depending on factors such as the type of element, peak overlap, surface topography, and other effects such as fluorescence and absorption. In this thesis, the instrument used was a JEOL JSM-6010LA InTouchScope scanning electron microscope or a Zeiss Sigma 300 VP field emission scanning electron microscope.

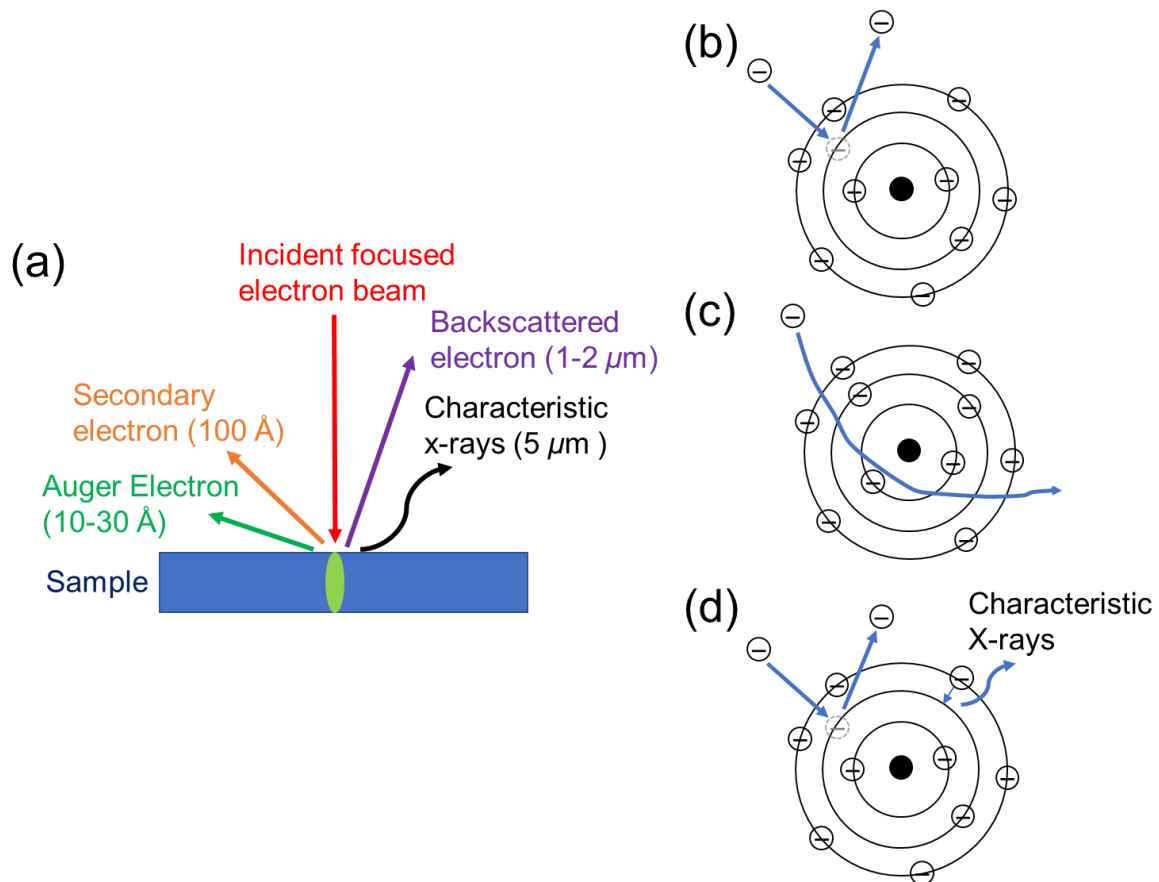


**Figure 1-14.** (a) Interactions of incident electron beam on a sample. (b) Secondary electrons, (c) backscattered electrons, and (d) characteristic X-rays produced in an electron microscope.

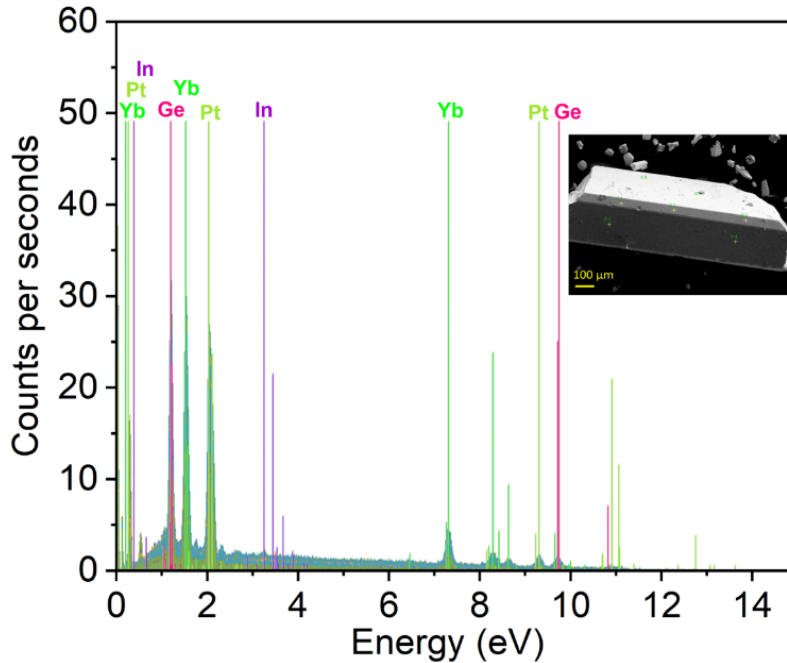


**Figure 1-15.** EDX spectrum for YbPtGe crystal and a secondary electron image (inset). A small amount of indium flux was observed on the surface of crystal.

### 1.5.3 Diffuse reflectance spectroscopy

Optical diffuse reflectance spectroscopy is used to determine the band gap of a solid. Reflection of light can be specular, with scattering occurring at the same angle to the normal as the incident beam, as occurs on a smooth surface such as a polished sample or a single crystal; or it can be diffuse, with scattering occurring at many angles, as occurs on a rough surface such as a microcrystalline sample. The scattered light originates from many processes (reflection, refraction, and diffraction) which are hard to separate. The diffuse reflectance spectrum can be converted to an absorption spectrum through a relationship called the Kubelka-Munk function:

$$F(R_{\infty}) = \frac{K}{S} = \frac{(1 - R_{\infty})^2}{2R_{\infty}}$$

where  $K$  is the absorption coefficient,  $S$  is the scattering coefficient, and  $R_\infty$  is the reflectance assuming an infinitely thick layer.<sup>91,92</sup> The instrument used was a Cary 5000 UV-Vis-NIR spectrophotometer equipped with a diffuse reflectance accessory (**Figure 1-16a**). An optical polytetrafluoroethylene disc with >98% reflectivity or a compacted pellet of BaSO<sub>4</sub> was used as a reflectance standard over the range from 200 nm (6.2 eV) to 2500 nm (0.5 eV). The optical band gap was estimated by extrapolating the absorption edge to the baseline (**Figure 1-16b**).

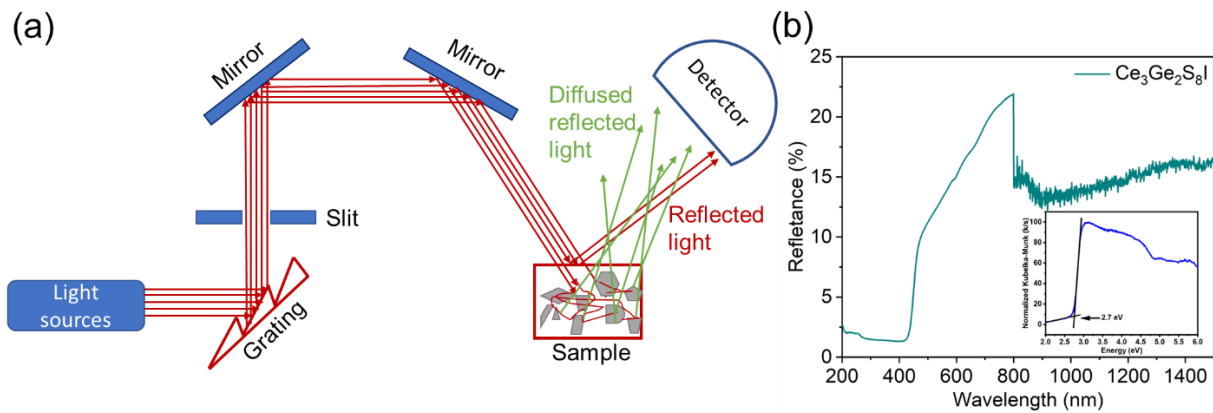


**Figure 1-16.** (a) UV-Vis-NIR spectrometer with light reflected by a rough sample surface. (b) diffuse reflectance spectra collected on powder sample of Ce<sub>3</sub>Ge<sub>2</sub>S<sub>8</sub>I.

## 1.6 Band structure calculations

The electronic structure of extended solids can be calculated from first principles.<sup>93</sup> The appropriate electronic wavefunctions are taken as linear combinations of atomic orbitals  $\chi_n$ , adapted to the translational symmetry of the crystal structure. For the simple case of a chain of atoms with unit cell repeat  $a$ , these symmetry-adapted wavefunctions, called Bloch functions, are of the form:

$$\psi_k = \sum_n e^{ikna} \chi_n$$

where  $k$  is the wavevector and is restricted to quantized values within a repeat in reciprocal space called the first Brillouin zone,  $-\pi/a \leq k \leq \pi/a$ . If the chain consists of s-orbitals on each atom, these Bloch functions and their energies, obtained through the Schrödinger equation, can be understood (Figure 1-17). The most bonding combination, with all orbitals in phase, is found at lowest energy at  $k = 0$ , and the most antibonding combination, with all orbitals out of phase, is found at highest energy at  $k = \pi/a$ . A band dispersion diagram shows how these energies vary as a function of  $k$ . These curves are quasi-continuous, with many energy levels so closely spaced that it is convenient to portray the density of states within infinitesimal energy intervals. The states are filled with electrons up to the highest energy, called the Fermi level  $E_f$ .

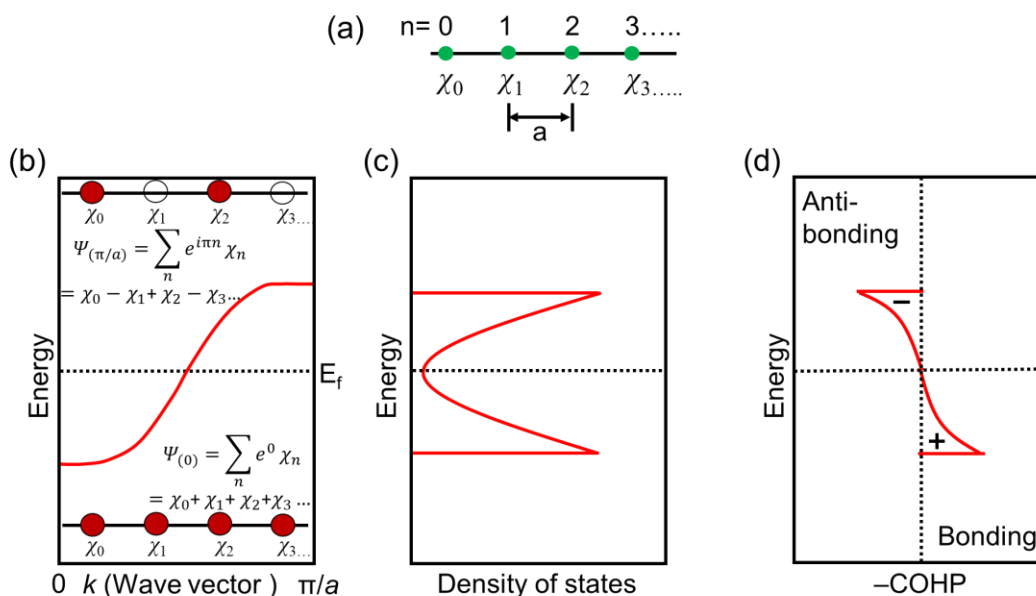


**Figure 1-17.** (a) Chain of atoms with orbitals  $\chi_n$ , taken to be s-orbitals, (b) band dispersion diagram, (c) density of states, and (d) crystal orbital Hamilton population.

Electronic structure calculations allow conclusions to be inferred about bonding in the crystal structure. The crystal orbital Hamilton populations (COHP) are obtained by weighting the DOS by the Hamiltonian matrix elements and serve to classify interactions between specified pairs

of atoms to be bonding or antibonding at different energies. The integrated values of the COHP up to the Fermi level can be interpreted as a measure of the bond strength. Borrowed from an old concept by Wiberg and Mayer, the crystal orbital bond index (COBI) has been recently developed as a way to quantify the degree of covalent vs. ionic character within specified bonds.

The calculations performed here have made use of widely available programs, such as TB-LMTO (tight-binding linear muffin tin orbital program) and VASP (Vienna ab initio simulation package). The program LOBSTER makes use of the results from these calculations to extract COHP and COBI values.

## **1.7 Physical properties**

The properties of potential interest investigated in this thesis are the photoluminescence and magnetic properties of rare-earth chalcogenides.

### **1.7.1 Photoluminescence**

Modern emissive displays, fluorescent lamps, and light emitting diodes (LEDs) owe their operation to photoluminescent materials. LEDs are more energy efficient, longer lasting, and less costly to maintain than incandescent bulbs. The most common method to generate white light in an LED is by combining a blue InGaN chip with a yellow emitting phosphor such as  $\text{Ce}^{3+}:\text{Y}_3\text{Al}_5\text{O}_{12}$ .<sup>94</sup> However, this type of LED emits a small amount of blue light, which disturbs the human sleep cycle.<sup>95</sup> An alternative method to produce white light is to combine red, green, and blue emitting phosphors that are excited by a UV-LED. Mixing three phosphors gives access to a wider gamut to produce tunable colours, but to reduce spectral overlap, these phosphors must give narrow emission peaks with high efficiency. Some of the currently used phosphor materials

in LEDs are  $\text{CaAlSiN}_3:\text{Eu}^{2+}$  (red),  $\text{SrS}:\text{Eu}^{2+}$  (red),  $\text{SrGa}_2\text{S}_4:\text{Eu}^{2+}$  (green)  $\beta\text{-SiAlON}$  ( $\text{Si}_{6-z}\text{Al}_z\text{O}_z\text{N}_{8-z}:\text{Eu}^{2+}$ ) (green) and  $\text{BaMgAl}_{10}\text{O}_{17}:\text{Eu}^{2+}$  (blue).<sup>96–98</sup>

Inorganic phosphors consist of an insulating or semiconducting host (oxides, oxyhalides, chalcogenides, oxychalcogenides) and an activator (rare earth or transition metal ion). Activators are responsible for light emission, which occurs through several possible radiative decay mechanisms upon absorption of incident radiation (**Figure 1-18**). The mechanisms involve either fluorescence (electrons relaxing to the ground state by emitting photons) or phosphorescence (electrons undergoing intersystem crossing from singlet to triplet excited states). The excited electron could also undergo vibrational relaxation or internal conversion. The emission and temperature-dependent optical properties are strongly influenced by the coordination environment around the activator ions. Phosphors can degrade over time because they undergo chemical reactions or are thermally unstable. The market for white LEDs is highly lucrative, and many scientists are involved in searching for new phosphors or improving existing ones.

Although chalcogenides have not been well investigated as photoluminescent materials, a few have been previously identified.  $\text{Re}_6\text{S}_8\text{I}_2$  and  $\text{Re}_6\text{Se}_8\text{I}_2$  exhibit photoluminescence in a broad region from red to near infrared regions.<sup>99</sup>  $\text{Ba}_2\text{SbS}_3\text{I}$  emits at 350 and 468 nm.<sup>100</sup>  $\text{Ba}_3\text{AGa}_5\text{Se}_{10}\text{Cl}_2$  ( $A = \text{Cs, Rb, K}$ ) emits at 711–831 nm without metal activators.<sup>101</sup> When photoluminescence occurs in the absence of activators, it arises because there are defect levels lying within the band gap.

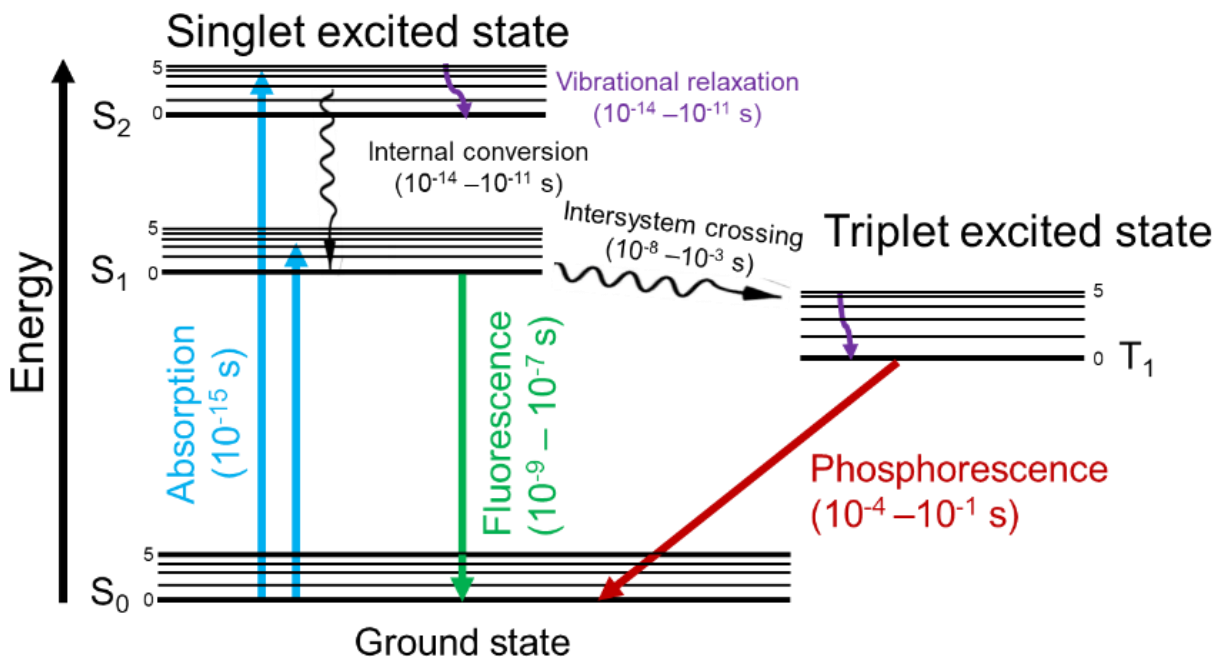


**Figure 1-18.** Mechanisms for fluorescence and phosphorescence.

There exists a small family of rare-earth chalcogenides  $RE_3(\text{SiS}_4)_2X$  that were briefly investigated in the past for their photoluminescent properties. The series  $\text{Ce}_3(\text{SiS}_4)_2X$  ( $X = \text{Cl}, \text{Br}, \text{I}$ ) were found to show strong blue luminescence, with a shift to shorter emission wavelengths upon substitution with larger halogens (478 nm for Cl, 468 nm for Br, 465 nm for I).<sup>52</sup>  $\text{La}_3\text{Br}(\text{SiS}_4)_2:\text{Ce}^{3+}$  emits in the cyan region (466 nm), and  $\text{La}_3\text{Br}(\text{SiS}_4)_2:\text{Eu}^{2+}$  emits in the red-orange region (640 nm), and they have been demonstrated for use in white light-emitting diodes.<sup>102</sup> There appears to be many unexplored opportunities to examine the impact of both cation and anion substitutions on these photoluminescent properties.

### 1.7.2 Magnetic properties

Magnetic properties are characterized by applying an external magnetic field  $H$  to a sample and measuring the resulting magnetization  $M$ , which can be divided by the field to give the magnetic susceptibility  $\chi$ . The temperature dependence of the magnetic susceptibility ( $\chi$  vs  $T$ ) and the field dependence of the magnetization ( $M$  vs  $H$ ) are routinely measured to infer the arrangement of magnetic moments in the solid (**Figure 1-19**). In a paramagnetic substance, the magnetic moments are randomly arranged but tend to align with the applied magnetic field at lower temperatures, in accordance with the Curie law,  $\chi = C/T$ . In a ferromagnetic substance, there is a spontaneous parallel alignment of magnetic moments below a critical temperature called the Curie temperature  $T_C$ . In an antiferromagnetic substance, the magnetic moments align antiparallel to each other below the Neel temperature  $T_N$ . Plots of the inverse magnetic susceptibility vs temperature can suggest the type of magnetic coupling interactions that are taking place. If the linear portion of this curve (the paramagnetic regime at high temperature) is extrapolated to the abscissa, the intercept can be related to the Weiss constant, for which a positive sign suggests ferromagnetic and a negative sign suggests antiferromagnetic coupling. Typical measurements are made on powder samples with mass of 20–100 mg, on a Quantum Design 9T-PPMS instrument, with an applied magnetic field of 0.5 T and between temperatures of 2 to 300 K.

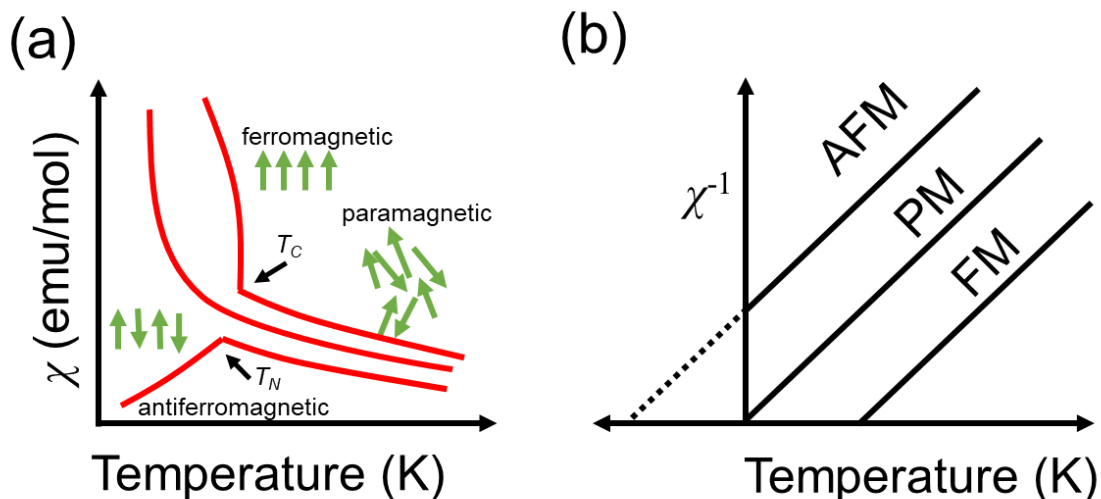


**Figure 1-19.** (a) Temperature dependence of magnetic susceptibility, and (b) Inverse magnetic susceptibility vs temperature.

Rare-earth compounds exhibit a wide range of magnetic behaviour, ranging from mundane to exotic. Among rare-earth intermetallics, those that adopt  $\text{Th}_2\text{Zn}_{17}$ ,  $\text{ThMn}_{12}$ ,  $\text{CaCo}_5$ , and  $\text{BaAl}_4$ -type structures are prone to exhibit orientation-dependent magnetization. Materials with high magnetic anisotropy are of interest to condensed matter physicists, but measurements require the availability of large, high-quality single crystals.

## 1.8 Objectives

The common theme of this thesis is the investigation of rare-earth-containing compounds, including their synthesis, structures, and physical properties. As surveyed above, quaternary rare-earth chalcogenides are an underrepresented class of compounds that could offer new possibilities for structural diversity by introducing both mixed cations and mixed anions. These compounds are expected to behave as semiconductors. The long term vision would be to enable control of physical properties by choosing an appropriate combination of these components. Perhaps the

biggest challenge is that multicomponent phases tend to be hard to synthesize because they compete with more stable binary and ternary phases. This thesis focuses on an interesting series of rare-earth chalcogenides  $RE_3Tt_2Ch_8I$  for which substitution of the  $RE$ ,  $Tt$ , and  $Ch$  components is systematically investigated. The approach is to prepare solid solutions from different end members to examine how band gaps are affected, and subsequently to control the emission colour for photoluminescence applications such as white LEDs. Characterization methods include detailed structure determinations, extensive optical measurements, and first-principles calculations.

Rare-earth transition-metal intermetallics are an extremely diverse class that have been implicated as quantum materials because the interplay of f- and d-electrons can lead to complex magnetic behaviour. Although this research area has long been investigated by condensed matter physicists, there is an important need to develop more systematic ways to synthesize these compounds, particularly in the form of large single crystals. This thesis examines the use of metal fluxes to promote crystal growth of ternary gallides and germanides. In many cases, the crystal growth of known ternary intermetallics can be frustratingly difficult. The relative stability of the  $RET_2Ge_2$  compounds was evaluated by conducting reactions in indium as a nonreactive flux.

## 1.9 References

- (1) Ma, Z.; Mohapatra, J.; Wei, K.; Liu, J. P.; Sun, S. *Chem. Rev.* **2021**, *in Press*.
- (2) Geusic, J. E.; Marcos, H. M.; Van Uitert, L. G. *Appl. Phys. Lett.* **1964**, *4*, 182–184.
- (3) Zheng, B.; Fan, J.; Chen, B.; Qin, X.; Wang, J.; Wang, F.; Deng, R.; Liu, X. *Chem. Rev.* **2022**, *122*, 5519–5603.
- (4) Fang, M.-H.; Bao, Z.; Huang, W.-T.; Liu, R.-S. *Chem. Rev.* **2022**, *122*, 11474–11513.
- (5) Minagawa, K.; Nishiguchi, Y.; Oka, R.; Masui, T. *ACS Omega* **2021**, *6*, 3411–3417.
- (6) Smith, A. E.; Mizoguchi, H.; Delaney, K.; Spaldin, N. A.; Sleight, A. W.; Subramanian, M. A. *J. Am. Chem. Soc.* **2009**, *131*, 17084–17086.
- (7) Kageyama, H.; Hayashi, K.; Maeda, K.; Attfield, J. P.; Hiroi, Z.; Rondinelli, J. M.; Poeppelmeier, K. R. *Nat. Commun.* **2018**, *9*, 772-1–772-15.
- (8) Doussier, C.; Moëlo, Y.; Meerschaut, A.; Léone, P.; Guillot-Deudon, C. *J. Solid State Chem.* **2008**, *181*, 920–934.
- (9) Kumar, R. S.; Hamlin, J. J.; Maple, M. B.; Zhang, Y.; Chen, C.; Baker, J.; Cornelius, A. L.; Zhao, Y.; Xiao, Y.; Sinogeikin, S.; Chow, P. *Appl. Phys. Lett.* **2014**, *105*, 251902.
- (10) Yang, X.; Li, Y.; Shen, C.; Si, B.; Sun, Y.; Tao, Q.; Cao, G.; Xu, Z.; Zhang, F. *Appl. Phys. Lett.* **2013**, *103*, 022410.
- (11) Villars, P.; Cenzual, K., *Pearson's Crystal Data – Crystal Structure Database for Inorganic Compounds*. Release 2022/23, ASM International, Materials Park: Ohio, USA,.
- (12) Johnsen, S.; Liu, Z.; Peters, J. A.; Song, J.-H.; Nguyen, S.; Malliakas, C. D.; Jin, H.; Freeman, A. J.; Wessels, B. W.; Kanatzidis, M. G. *J. Am. Chem. Soc.* **2011**, *133*, 10030–10033.

- (13) Minafra, N.; Kraft, M. A.; Bernges, T.; Li, C.; Schlem, R.; Morgan, B. J.; Zeier, W. G. *Inorg. Chem.* **2020**, *59*, 11009–11019.
- (14) Kavanagh, S. R.; Savory, C. N.; Scanlon, D. O.; Walsh, A. *Mater. Horiz.* **2021**, *8*, 2709–2716.
- (15) Kulbachinskii, V. A.; Kytin, V. G.; Kudryashov, A. A.; Kuznetsov, A. N.; Shevelkov, A. *V. J Solid State Chem.* **2012**, *193*, 154–160.
- (16) Liu, P. -F.; Li, Y. -Y.; Zheng, Y. -J.; Yu, J. -S.; Duan, R. -H.; Chen, H.; Lin, H.; Chen, L.; Wu, L. -M. *Dalton Trans.* **2017**, *46*, 2715–2721.
- (17) Puff, H.; Lorbacher, G.; Heine, D. *Naturwissenschaften* **1969**, *56*, 461.
- (18) Pfitzner, A.; Preitschaft, C.; Rau, F. *Z. Anorg. Allg. Chem.* **2004**, *630*, 75–79.
- (19) Pfitzner, A. *Chem. Eur. J.* **1997**, *3*, 2032–2038.
- (20) Nilges, T.; Reiser, S.; Hong, J. H.; Gaudin, E.; Pfitzner, A. *Phys. Chem. Chem. Phys.* **2002**, *4*, 5888–5894.
- (21) Heerwig, A.; Merkle, R.; Maier, J.; Ruck, M. *J. Solid State Chem.* **2011**, *184*, 191–198.
- (22) Belin, R.; Aldon, L.; Zerouale, A.; Belin, C.; Ribes, M. *Solid State Sci.* **2001**, *3*, 251–265.
- (23) Moro'oka, M.; Ohki, H.; Yamada, K.; Okuda, T. *Bull. Chem. Soc. Jpn.* **2004**, *77*, 975–980.
- (24) Sedlmaier, S. J.; Indris, S.; Dietrich, C.; Yavuz, M.; Dräger, C.; Seggern, F. V.; Sommer, H.; Janek, J. *Chem. Mater.* **2017**, *29*, 1830–1835.
- (25) Liu, Z.; Zinkevich, T.; Indris, S.; He, X.; Liu, J.; Xu, W.; Bai, J.; Xiong, S.; Mo, Y.; Chen, H. *Inorg. Chem.* **2020**, *59*, 226–234.
- (26) Tougait, O.; Ibers, J. A.; Mar, A. *Acta Crystallogr. C* **2003**, *59*, i77–i78.
- (27) Doussier, C.; Léone, P.; Moëlo, Y. *Solid State Sci.* **2004**, *6*, 1387–1391.

- (28) Rosenthal, T.; Döblinger, M.; Wagatha, P.; Gold, C.; Scheidt, E. -W.; Scherer, W.; Oeckler, O. *Z. Anorg. Allg. Chem* **2011**, *637*, 2239–2245.
- (29) Kabbour, H.; Cario, L.; Danot, M.; Meerschaut, A. *Inorg. Chem.* **2006**, *45*, 917–922.
- (30) Jörgens, S.; Mewis, A. *Solid State Sci.* **2007**, *9*, 213–217.
- (31) Pilet, G.; Perrin, A. *Solid State Sci* **2004**, *6*, 109–116.
- (32) Sturza, M.; Allred, J. M.; Malliakas, C. D.; Bugaris, D. E.; Han, F.; Chung, D. Y.; Kanatzidis, M. G. *Chem. Mater.* **2015**, *27*, 3280–3290.
- (33) Lin, H.; Chen, H.; Lin, Z. -X.; Zhao, H. -J.; Liu, P. -F.; Yu, J. -S.; Chen, L. *Inorg. Chem.* **2016**, *55*, 1014–1016.
- (34) Poudeu, P. F.; Söhnle, T.; Ruck, M. *Z. Anorg. Allg. Chem.* **2004**, *630*, 1276–1285.
- (35) Poudeu, P. F.; Ruck, M. *J. Solid State Chem.* **2006**, *179*, 3636–3644.
- (36) Motomitsu, E.; Yanagi, H.; Kamiya, T.; Hirano, M.; Hosono, H. *J. Solid State Chem.* **2006**, *179*, 1668–1673.
- (37) Janka, O.; Schleid, T. *Z. Anorg. Allg. Chem.* **2008**, *634*, 2048.
- (38) Grossholz, H.; Schleid, T. *Z. Anorg. Allg. Chem.* **2002**, *628*, 2169.
- (39) Kang, D. -H.; Ledderboge, F.; Kleinke, H.; Schleid, T. *Z. Anorg. Allg. Chem.* **2015**, *641*, 322–326.
- (40) Sugimoto, T.; Paris, E.; Terashima, K.; Barinov, A.; Giampietri, A.; Wakita, T.; Yokoya, T.; Kajitani, J.; Higashinaka, R.; Matsuda, T. D.; Aoki, Y.; Mizokawa, T.; Saini, N. L. *Phys. Rev. B* **2019**, *100*, 064520.
- (41) Higashinaka, R.; Endo, H.; Kajitani, J.; Matsuda, T. D.; Aoki, Y. *Physica. B Condens.Matter* **2018**, *536*, 824–826.

- (42) Zhai, H. -F.; Zhang, P.; Wu, S. -Q.; He, C. -Y.; Tang, Z. -T.; Jiang, H.; Sun, Y. -L.; Bao, J. -K.; Nowik, I.; Felner, I.; Zeng, Y. -W.; Li, Y. -K.; Xu, X. -F.; Tao, Q.; Xu, Z. -A.; Cao, G. H. *J. Am. Chem. Soc.* **2014**, *136*, 15386–15393.
- (43) Gout, D.; Jobic, S.; Evain, M.; Brec, R. *J. Solid State Chem.* **2001**, *158*, 218–226.
- (44) Gout, D.; Jobic, S.; Evain, M.; Brec, R. *Solid State Sci.* **2001**, *3*, 223–234.
- (45) Mills, A. M.; Ruck, M. *Inorg. Chem.* **2006**, *45*, 5172–5178.
- (46) Bräunling, D.; Leoni, S.; Mills, A. M.; Ruck, M. *Z. Anorg. Allg. Chem.* **2008**, *634*, 107–114.
- (47) Tougait, O.; Ibers, J. A. *Inorg. Chem.* **2000**, *39*, 6136–6138.
- (48) Lin, H.; Li, L. H.; Chen, L. *Inorg. Chem.* **2012**, *51*, 4588–4596.
- (49) Hatscher, S. T.; Umland, W. *Mater. Res. Bull.* **2003**, *38*, 99–112.
- (50) Hatscher, S. T.; Umland, W. *Acta Crystallogr., Sect. E , Struct. Rep. Online* **2002**, *58*, i124–i126.
- (51) Hatscher, S. T.; Umland, W. *Z. Anorg. Allg. Chem.* **2002**, *628*, 608–611.
- (52) Riccardi, R.; Gout, D.; Gauthier, G.; Guillen, F.; Jobic, S.; Garcia, A.; Huguenin, D.; Macaudière, P.; Fouassier, C.; Brec, R. *J. Solid State Chem.* **1999**, *147*, 259–268.
- (53) Mumbaraddi, D.; Iyer, A. K.; Üzer, E.; Mishra, V.; Oliynyk, A. O.; Nilges, T.; Mar, A. *J. Solid State Chem.* **2019**, *274*, 162–167.
- (54) Gauthier, G.; Kawasaki, S.; Jobic, S.; Macaudière, P.; Brec, R.; Rouxel, J. *J. Alloys Compd.* **1998**, *275–277*, 46–49.
- (55) Gauthier, G.; Kawasaki, S.; Jobic, S.; Macaudière, P.; Brec, R.; Rouxel, J. *J. Mater. Chem.* **1998**, *8*, 179–186.

- (56) Hatscher, S. T.; Umland, W. *Acta Crystallogr., Sect. E, Struct. Rep. Online* **2002**, *58*, i100–i102.
- (57) Hatscher, S. T.; Umland, W. *Z. Anorg. Allg. Chem.* **2001**, *627*, 2198–2200.
- (58) Charkin, D. O.; Urmanov, A. V.; Kazakov, S. M. *J. Alloys Compd.* **2012**, *516*, 134–138.
- (59) Zhu, W. J.; Huang, Y. Z.; Wu, F.; Dong, C.; Chen, H.; Zhao, Z. X. *Mater. Res. Bull.* **1994**, *29*, 505–508.
- (60) Park, C. -H.; Kykyneshi, R.; Yokochi, A.; Tate, J.; Keszler, D. A. *J. Solid State Chem.* **2007**, *180*, 1672–1677.
- (61) Chen, H.; McClain, R.; He, J.; Zhang, C.; Olding, J. N.; Reis, R.; Bao, J. -K.; Hadar, I.; Spanopoulos, I.; Malliakas, C. D.; He, Y.; Chung, D. Y.; Kwok, W. -K.; Weiss, E. A.; Dravid, V. P.; Wolverton, C.; Kanatzidis, M. G. *J. Am. Chem. Soc.* **2019**, *141*, 17421–17430.
- (62) Stoloff, N. S.; Liu, C. T.; Deevi, S. C. *Intermetallics* **2000**, *8*, 1313–1320.
- (63) Lee, H. -T.; Chen, M. -H. *Mater. Sci. Eng. A* **2002**, *333*, 24–34.
- (64) Pantsyrny, V.; Shikov, A.; Vorobieva, A. *Cryogenics* **2008**, *48*, 354–370.
- (65) Sauthoff, G., *Intermetallics*. VCH: Weinheim, New York, 1995.
- (66) Lys, A.; Fadonougbo, J. O.; Faisal, M.; Suh, J. -Y.; Lee, Y. -S.; Shim, J. -H.; Park, J.; Cho, Y. W. *Hydrogen* **2020**, *1*, 38–63.
- (67) Belo, J. H.; Pereira, A. M.; Ventura, J.; Oliveira, G. N. P.; Araújo, J. P.; Tavares, P. B.; Fernandes, L.; Algarabel, P. A.; Magen, C.; Morellon, L.; Ibarra, M. R. *J. Alloys Compd.* **2012**, *529*, 89–95.
- (68) Kumar, N.; Guin, S. N.; Manna, K.; Shekhar, C.; Felser, C. *Chem. Rev.* **2021**, *121*, 2780–2815.

- (69) Gille, P.; Grin, Y., *Crystal Growth of Intermetallics*. Walter de Gruyter: Berlin, 2019.
- (70) Kanatzidis, M. G.; Pöttgen, R.; Jeitschko, W. *Angew. Chem. Int. Ed.* **2005**, *44*, 6996–7023.
- (71) Chen, X. Z.; Sportouch, S.; Sieve, B.; Brazis, P.; Kannewurf, C. R.; Cowen, J. A.; Patschke, R.; Kanatzidis, M. G. *Chem. Mater.* **1998**, *10*, 3202–3211.
- (72) Sieve, B.; Gray, D. L.; Henning, R.; Bakas, T.; Schultz, A. J.; Kanatzidis, M. G. *Chem. Mater.* **2008**, *20*, 6107–6115.
- (73) Sieve, B.; Chen, X. Z.; Henning, R.; Brazis, P.; Kannewurf, C. R.; Cowen, J. A.; Schultz, A. J.; Kanatzidis, M. G. *J. Am. Chem. Soc.* **2001**, *123*, 7040–7047.
- (74) Kangas, M. J.; Treadwell, L. J.; Haldolaarachchige, N.; McAlpin, J. D.; Young, D. P.; Chan, J. Y. *J. Solid State Chem.* **2013**, *197*, 523–531.
- (75) Zhuravleva, M. A.; Evain, M.; Petricek, V.; Kanatzidis, M. G. *J. Am. Chem. Soc.* **2007**, *129*, 3082–3083.
- (76) Mishra, V.; Subbarao, U.; Roy, S.; Sarma, S. Ch.; Mumbaraddi, D.; Sarkar, S.; Peter, S. *C. Inorg. Chem.* **2018**, *57*, 12576–12587.
- (77) Mishra, V.; Oliynyk, A. O.; Subbarao, U.; Sarma, S. Ch.; Mumbaraddi, D.; Roy, S.; Peter, S. C. *Cryst. Growth Des.* **2018**, *18*, 6091–6099.
- (78) Bugaris, D. E.; Malliakas, C. D.; Bud'ko, S. L.; Calta, N. P.; Chung, D. Y.; Kanatzidis, M. G. *Inorg. Chem.* **2017**, *56*, 14584–14595.
- (79) Peter, S. C.; Subbarao, U.; Sarkar, S.; Vaitheeswaran, G.; Svane, A.; Kanatzidis, M. G. *J. Alloys Compds.* **2014**, *589*, 405–411.
- (80) Subbarao, U.; Roy, S.; Sarma, S. Ch.; Sarkar, S.; Mishra, V.; Khulbe, Y.; Peter, S. C. *Inorg. Chem.* **2016**, *55*, 10351–10360.

- (81) Peter, S. C.; Chondroudi, M.; Malliakas, C. D.; Balasubramanian, M.; Kanatzidis, M. G. *J. Am. Chem. Soc.* **2011**, *133*, 13840–13843.
- (82) Calta, N. P.; Im, J.; Rodriguez, A. P.; Fang, L.; Bugaris, D. E.; Chasapis, T. C.; Freeman, A. J.; Kanatzidis, M. G. *Angew. Chem. Int. Ed.* **2015**, *54*, 9186–9191.
- (83) Bao, J.-K.; Bugaris, D. E.; Zheng, H.; Willa, K.; Welp, U.; Chung, D. Y.; Kanatzidis, M. G. *Phys. Rev. Materials* **2019**, *3*, 024802.
- (84) Chondroudi, M.; Balasubramanian, M.; Welp, U.; Kwok, W. -K.; Kanatzidis, M. G. *Chem. Mater.* **2007**, *19*, 4769–4775.
- (85) Subbarao, U.; Jana, R.; Chondroudi, M.; Balasubramanian, M.; Kanatzidis, M. G.; Peter, S. C. *Dalton Trans.* **2015**, *44*, 5797–5804.
- (86) Chondroudi, M.; Peter, S. C.; Malliakas, C. D.; Balasubramanian, M.; Li, Q.; Kanatzidis, M. G. *Inorg. Chem.* **2011**, *50*, 1184–1193.
- (87) Han, F.; Malliakas, C. D.; Stoumpos, C. C.; Sturza, M.; Claus, H.; Chung, D. Y.; Kanatzidis, M. G. *Phys. Rev. B Condens. Matter* **2013**, *88*, 144511.
- (88) Pfannenschmidt, U.; Pöttgen, R. *Z. Naturforsch.* **2013**, *68b*, 1185–1190.
- (89) Niehaus, O.; Hoffmann, R.-D.; Pöttgen, R. *Z. Naturforsch.* **2016**, *71(8)b*, 919–923.
- (90) Mumbaraddi, D.; Mishra, V.; Lidin, S.; Mar, A. *J. Solid State Chem.* **2022**, *311*, 123157.
- (91) Kubelka, P.; Munk, F., *Z. Tech. Phys* **1931**, *12*, 259–274.
- (92) Makuła, P.; Pacia, M.; Macyk, W. *J. Phys. Chem. Lett.* **2018**, *9*, 6814–6817.
- (93) Hoffmann, R. *Angew. Chem., Int. Ed. Engl.* **1987**, *26*, 846–878.
- (94) Blasse, G.; Brill, A. *Appl. Phys. Lett.* **1967**, *11*, 53–55.
- (95) Hariyani, S.; Brgoch, J. *ACS Appl. Mater. Interfaces* **2021**, *13*, 16669–16676.

- (96) Uheda, K.; Hirosaki, N.; Yamamoto, Y.; Naito, A.; Nakajima, T.; Yamamoto, H. *Electrochem. Solid-State Lett.* **2006**, *9*, H22–H25.
- (97) Kominami, H.; Mjakin, S. V.; Sychov, M. M.; Korsakov, V. G.; Bakhmetjev, V. V.; Sidorova, A. A.; Sosnov, E. A.; Nakanishi, Y.; Hara, K.; Mimura, H. *Opt. Mater.* **2013**, *35*, 1109–1111.
- (98) Yin, L. -J.; Dong, J.; Wang, Y.; Zhang, B.; Zhou, Z. -Y.; Jian, X.; Wu, M.; Xu, X.; Ommen, J. R.; Hintzen, H. T. *J. Phys. Chem. C* **2016**, *120*, 2355–2361.
- (99) Laing, C. C.; Shen, J.; Chica, D. G.; Cuthriell, S. A.; Schaller, R. D.; Wolverton, C.; Kanatzidis, M. G. *Chem. Mater.* **2021**, *33*, 5780–5789.
- (100) Wang, R.; Zhang, X.; He, J.; Bu, K.; Zheng, C.; Lin, J.; Huang, F. *Inorg. Chem.* **2018**, *57*, 1449–1454.
- (101) Yu, P.; Zhou, L.-J.; Chen, L. *J. Am. Chem. Soc.* **2012**, *134*, 2227–2235.
- (102) Lee, S. -P.; Liu, S. -D.; Chan, T. -S.; Chen, T. -M. *ACS Appl. Mater. Interfaces* **2016**, *8*, 9218–9223.

## Chapter 2.

### Synthesis, structure, and properties of rare-earth germanium sulfide iodides $RE_3Ge_2S_8I$ ( $RE = La, Ce, Pr$ )

*A version of this chapter has been published. Mumbaraddi, D.; Iyer, A. K.; Mishra, V.; Oliynyk, A. O.; Nilges, T.; Mar. A. J. Solid State Chem. 2019, 274, 162–167. Copyright (2019) by Elsevier.*

#### 2.1. Introduction

Mixed-anion compounds, which contain more than one type of anion, offer ways to control the structures and properties of solids that are not accessible in single-anion or mixed-cation compounds.<sup>1</sup> The local environment around cations can be changed to create coordination polyhedra with different symmetries, the bonding character can be adjusted by introducing intermediate degrees of electron transfer, and the band gap can be varied to desired magnitudes. Well-known examples of mixed-anion compounds typically contain oxide with fluoride (e.g.,  $LiFeSO_4F$  as cathode materials in batteries),<sup>2</sup> other chalcogenide (e.g.,  $LaCuChO$  ( $Ch = S, Se$ ) as transparent conductors),<sup>3</sup> and pnictide ions (e.g.,  $Ca_{1-x}La_xTaO_{2-x}N_{1+x}$  as inorganic pigments,<sup>4</sup>  $LaFeAsO$  as superconductors).<sup>5</sup> Mixed-anion compounds containing heavier chalcogenide and halide ions are less common,<sup>6</sup> but they have also emerged as attractive candidates for various applications (e.g.,  $Ag_5Te_2Cl$  as ionic conductors,<sup>7</sup>  $BiSI$  and  $BiSeI$  as photovoltaic materials,<sup>8</sup>  $Ba_4ZnGa_4Se_{10}Cl_2$  as infrared nonlinear optical materials,<sup>9</sup> and  $Tl_6SI_4$  as hard radiation detectors).<sup>10</sup>

Chalcogenide halides containing rare-earth metals are relatively scarce but may be interesting because of their potential as optical and magnetic materials.<sup>6</sup> Narrow-band optical spectra and large magnetic moments may be expected from the presence of unpaired electrons in highly localized f-orbitals. Within the systems  $RE-Tt-Ch-X$  ( $RE =$  rare-earth metal;  $Tt = Si, Ge,$

Sn (tetrel),  $Ch = S, Se, Te$ ;  $X = F, Cl, Br, I$ ), the only known quaternary phases so far are  $RE_3Si_2S_8X$  ( $RE =$  early rare-earth metals;  $X = Cl, Br, I$ )<sup>11-17</sup> and  $RE_3Si_6Cl$  ( $RE = Nd, Sm$ ),<sup>18,19</sup> first discovered nearly 20 years ago. The compound  $Ce_3Si_2S_8I$  luminesces in the blue region and may be useful in electroluminescent devices.<sup>13</sup>

As part of our ongoing investigations of chalcogenides as optical materials, we examine these  $RE-Tl-Ch-X$  systems to ascertain if other quaternary phases can be found. In particular, we hypothesize that the Ge-substituted analogues of  $RE_3Si_2S_8X$  may be viable targets to prepare. The existence of  $Ce_3Ge_2S_8I$  has been mentioned, but no publication has been forthcoming.<sup>13</sup> Here, we present the synthesis and complete structural characterization of the Ge-containing members  $RE_3Ge_2S_8I$ , their electronic band structure, and their optical and magnetic properties.

## 2.2. Experimental

### 2.2.1. Synthesis

Starting materials were freshly filed rare-earth metal pieces ( $RE = La, Ce, Pr$ ; 99.9%, Hefa), germanium powder (99.999%, Sigma-Aldrich), sulfur flakes (99.998%, Sigma-Aldrich), and iodine crystals (99.8%, Anachemia). The elements were combined in stoichiometric ratios on a 0.5-g scale to target the composition  $RE_3Ge_2S_8I$ , with a 10% excess (by weight) of  $I_2$  added. The mixtures were finely ground, cold-pressed into pellets, and loaded into fused-silica tubes (12 mm diameter and 15 cm length), which were evacuated to  $10^{-3}$  mbar and sealed. To minimize volatilization losses of sulfur and iodine and to avoid catastrophic failure of the tubes, the samples were heated slowly at  $2\text{ }^\circ\text{C}/\text{min}$  to  $300\text{ }^\circ\text{C}$ , held there for 2 d, heated at  $2\text{ }^\circ\text{C}/\text{min}$  to  $900\text{ }^\circ\text{C}$ , held there for 7 d, and then cooled to room temperature over 2 d. The targeted compounds formed as powders, with excess  $I_2$  deposited at the other end of the tubes.

Products were analyzed by powder X-ray diffraction (XRD) performed on an Inel powder diffractometer equipped with a curved position-sensitive detector (CPS 120) and a Cu  $K\alpha_1$  radiation source operated at 40 kV and 20 mA. The XRD patterns were analyzed with the use of the TOPAS Academic software package.<sup>20</sup> The background was modelled by a six-term polynomial function, and a Pawley fit was applied (**Figure 2-1**).

Small irregularly shaped crystals (light yellow or nearly colourless  $\text{La}_3\text{Ge}_2\text{S}_8\text{I}$ , yellow  $\text{Ce}_3\text{Ge}_2\text{S}_8\text{I}$ , and green  $\text{Pr}_3\text{Ge}_2\text{S}_8\text{I}$ ) were found within the products which were examined on a JEOL JSM-6010LA InTouchScope scanning electron microscope, operated with an accelerating voltage of 15 kV. Energy-dispersive X-ray (EDX) analyses performed with acquisition times of 120 s on several points of multiple crystals (insets of **Figure 2-1**) gave compositions of 19–25% RE, 10–16% Ge, 50–58% S, and 8–13% I, in reasonable agreement with expectations (21% RE, 14% Ge, 57% S, 7% I). The high I content is attributed to the surface deposition of some excess iodine which can be removed by washing the crystals with DMF.

Attempts were made to extend the RE substitution beyond Pr (e.g., RE = Nd, Sm, Eu, Gd, Tb, Dy, Ho, Er) and to prepare the analogous selenide series  $\text{RE}_3\text{Ge}_2\text{SeI}$ , using the same preparative conditions as indicated above, but these generally led to the formation of ternary phases  $\text{RE}_3\text{Ge}_{1+x}\text{S}_7$  or  $\text{RE}_3\text{Ge}_{1+x}\text{Se}_7$ . Attempts were also made to prepare the Cl or Br analogues through the use of binary halide starting materials, but these were unsuccessful and led to complex multiphase mixtures.

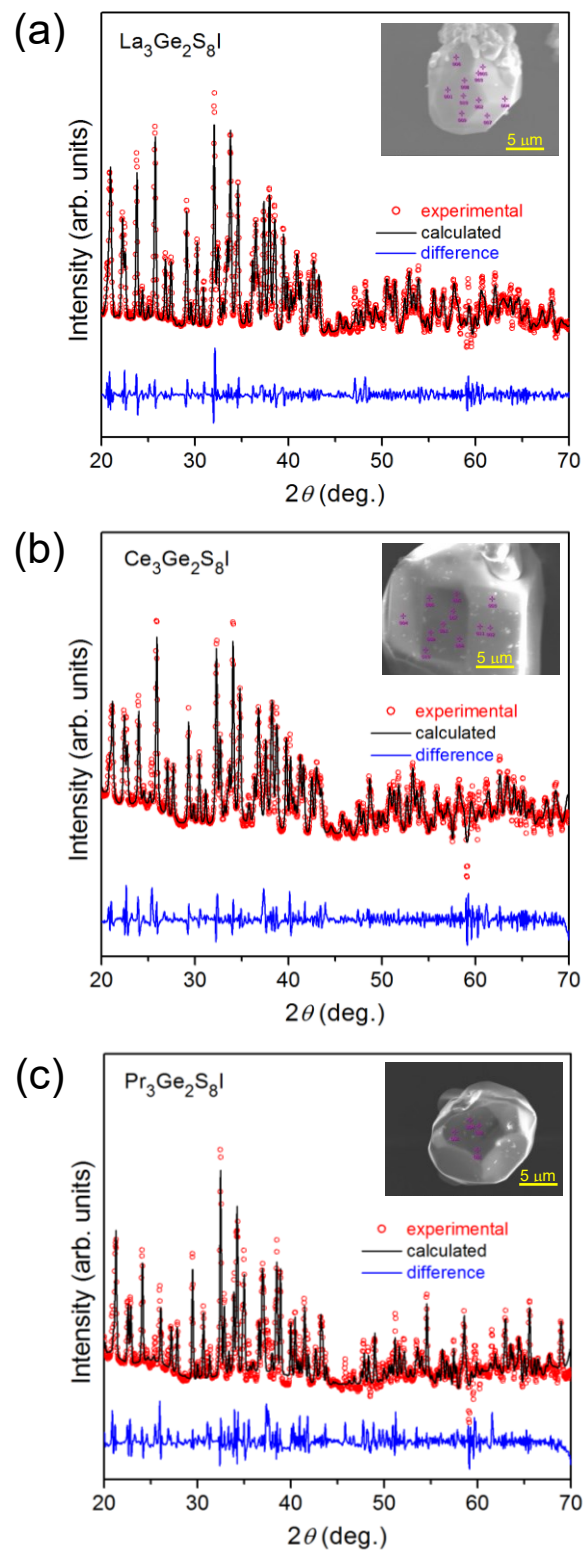


**Figure 2-1.** Powder XRD patterns (with Pawley fittings) and SEM images of typical crystals (insets) for  $\text{RE}_3\text{Ge}_2\text{S}_8\text{I}$ .

### 2.2.2. Structure determination

Intensity data for  $RE_3Ge_2S_8I$  ( $RE = La, Ce, Pr$ ) were collected at room temperature on a Bruker PLATFORM diffractometer equipped with a SMART APEX II CCD area detector and a graphite-monochromated Mo  $K\alpha$  radiation source, using  $\omega$  scans at 7–8 different  $\phi$  angles with a frame width of  $0.3^\circ$  and an exposure time of 10–12 s per frame. Face-indexed numerical absorption corrections were applied. Structure solution and refinement were carried out with the use of the SHELXTL (version 6.12) program package.<sup>21</sup> The centrosymmetric monoclinic space group  $C2/c$  was chosen on the basis of Laue symmetry and intensity statistics. Initial positions of all atoms were easily found by direct methods, and structure refinement proceeded in a straightforward fashion. All sites were confirmed to be fully occupied when occupancies were refined. The displacement parameters for the I atom are slightly elevated compared to those of the other atoms, but this appears to be a recurring characteristic in related  $RE_3Si_2S_6X$  structures associated with its location within a large tunnel and its relatively weak bonding to only three neighbouring  $RE$  atoms.<sup>11–17</sup> Atomic positions were standardized with the program STRUCTURE TIDY.<sup>22</sup> **Table 2-1** lists crystal data, **Table 2-2** lists atomic and displacement parameters, and **Table 2-3** lists interatomic distances. CCDC 1890620–1890622 contains the supplementary crystallographic data for this paper. These data can be obtained free of charge from the Cambridge Crystallographic Data Centre via [www.ccdc.cam.ac.uk/structures](http://www.ccdc.cam.ac.uk/structures).

**Table 2-1.** Crystallographic data for  $RE_3Ge_2S_8I$ .

formula	La <sub>3</sub> Ge <sub>2</sub> S <sub>8</sub> I	Ce <sub>3</sub> Ge <sub>2</sub> S <sub>8</sub> I	Pr <sub>3</sub> Ge <sub>2</sub> S <sub>8</sub> I
formula mass (amu)	945.29	948.92	951.29
space group	<i>C2/c</i> (No. 15)	<i>C2/c</i> (No. 15)	<i>C2/c</i> (No. 15)
<i>a</i> (Å)	16.156(4)	16.054(2)	15.9760(9)
<i>b</i> (Å)	7.9776(18)	7.9233(11)	7.8786(5)
<i>c</i> (Å)	11.018(3)	10.9624(15)	10.9281(6)
$\beta$ (°)	98.192(5)	98.262(3)	98.4525(10)
<i>V</i> (Å <sup>3</sup> )	1405.6(6)	1379.9(3)	1360.56(14)
<i>Z</i>	4	4	4
<i>T</i> (K)	296(2)	296(2)	296(2)
$\rho_{\text{calcd}}$ (g cm <sup>-3</sup> )	4.467	4.568	4.644
crystal dimensions (mm)	0.05 × 0.04 × 0.04	0.07 × 0.05 × 0.04	0.05 × 0.04 × 0.04
$\mu$ (Mo <i>K</i> α) (mm <sup>-1</sup> )	16.49	17.41	18.36
transmission factors	0.511–0.558	0.331–0.531	0.471–0.553
2θ limits	5.09–66.33°	5.13–66.56°	5.16–66.54°
data collected	–24 ≤ <i>h</i> ≤ 24, –12 ≤ <i>k</i> ≤ 12, –16 ≤ <i>l</i> ≤ 16	–24 ≤ <i>h</i> ≤ 24, –12 ≤ <i>k</i> ≤ 12, –16 ≤ <i>l</i> ≤ 16	–24 ≤ <i>h</i> ≤ 24, –12 ≤ <i>k</i> ≤ 12, –16 ≤ <i>l</i> ≤ 16
no. of data collected	9974	9823	9815
no. of unique data, including $F_o^2 < 0$	2654	2634	2605
no. of unique data, with $F_o^2 > 2\sigma(F_o^2)$	1767	1874	1946
no. of variables	65	65	65
$R(F)$ for $F_o^2 > 2\sigma(F_o^2)$	0.048	0.043	0.041
<sup>a</sup>			
$R_w(F_o^2)$ <sup>b</sup>	0.128	0.108	0.104
goodness of fit	1.02	1.02	1.07
( $\Delta\rho$ ) <sub>max</sub> , ( $\Delta\rho$ ) <sub>min</sub> (e Å <sup>-3</sup> )	3.70, –2.52	3.13, –2.08	3.47, –2.21

<sup>a</sup>  $R(F) = \sum ||F_o| - |F_c|| / \sum |F_o|$ . <sup>b</sup>  $R_w(F_o^2) = [\sum [w(F_o^2 - F_c^2)^2] / \sum wF_o^4]^{1/2}$ ;  $w^{-1} = [\sigma^2(F_o^2) + (Ap)^2 + Bp]$ , where  $p = [\max(F_o^2, 0) + 2F_c^2] / 3$ .

**Table 2-2.** Atomic coordinates and equivalent isotropic displacement parameters ( $\text{\AA}^2$ ) <sup>a</sup> for  $RE_3Ge_2S_8I$ .

Atom	Wyckoff position	$x$	$y$	$z$	$U_{eq}$ ( $\text{\AA}^2$ ) <sup>a</sup>
<b>La<sub>3</sub>Ge<sub>2</sub>S<sub>8</sub>I</b>					
La1	8 <i>f</i>	0.30365(3)	0.12072(6)	0.32098(4)	0.0144(1)
La2	4 <i>e</i>	0	0.10242(9)	1/4	0.0166(2)
Ge	8 <i>f</i>	0.15867(6)	0.03916(11)	0.02736(8)	0.0139(2)
S1	8 <i>f</i>	0.0650(1)	0.1575(3)	0.5404(2)	0.0163(4)
S2	8 <i>f</i>	0.1446(1)	0.2501(3)	0.1496(2)	0.0166(4)
S3	8 <i>f</i>	0.2160(1)	0.4296(3)	0.4133(2)	0.0155(4)
S4	8 <i>f</i>	0.3507(1)	0.4014(3)	0.1684(2)	0.0153(4)
I	4 <i>e</i>	0	0.5186(1)	1/4	0.0273(2)
<b>Ce<sub>3</sub>Ge<sub>2</sub>S<sub>8</sub>I</b>					
Ce1	8 <i>f</i>	0.30319(3)	0.12132(5)	0.32094(4)	0.0147(1)
Ce2	4 <i>e</i>	0	0.10510(8)	1/4	0.0173(1)
Ge	8 <i>f</i>	0.15843(5)	0.03936(10)	0.02651(7)	0.0143(2)
S1	8 <i>f</i>	0.0649(1)	0.1602(2)	0.5395(2)	0.0187(4)
S2	8 <i>f</i>	0.1445(1)	0.2522(2)	0.1496(2)	0.0179(4)
S3	8 <i>f</i>	0.2152(1)	0.4299(2)	0.4133(2)	0.0162(3)
S4	8 <i>f</i>	0.3510(1)	0.4020(2)	0.1703(2)	0.0163(3)
I	4 <i>e</i>	0	0.5193(1)	1/4	0.0267(2)
<b>Pr<sub>3</sub>Ge<sub>2</sub>S<sub>8</sub>I</b>					
Pr1	8 <i>f</i>	0.30270(2)	0.12199(4)	0.32111(3)	0.0131(1)
Pr2	4 <i>e</i>	0	0.10822(7)	1/4	0.0156(1)
Ge	8 <i>f</i>	0.15808(4)	0.03975(9)	0.02567(6)	0.0125(2)
S1	8 <i>f</i>	0.0647(1)	0.1618(2)	0.5380(2)	0.0165(3)
S2	8 <i>f</i>	0.1441(1)	0.2534(2)	0.1490(2)	0.0160(3)
S3	8 <i>f</i>	0.2151(1)	0.4306(2)	0.4131(2)	0.0147(3)
S4	8 <i>f</i>	0.3516(1)	0.4019(2)	0.1723(2)	0.0145(3)
I	4 <i>e</i>	0	0.5203(1)	1/4	0.0241(2)

<sup>a</sup>  $U_{eq}$  is defined as one-third of the trace of the orthogonalized  $U_{ij}$  tensor.

**Table 2-3.** Interatomic distances (Å) in  $RE_3Ge_2S_8I$ .

	$La_3Ge_2S_8I$	$Ce_3Ge_2S_8I$	$Pr_3Ge_2S_8I$
<i>RE1</i> –S4	2.963(2)	2.937(2)	2.914(2)
<i>RE1</i> –S3	2.976(2)	2.960(2)	2.948(2)
<i>RE1</i> –S1	3.007(2)	2.982(2)	2.967(2)
<i>RE1</i> –S3	3.016(2)	2.998(2)	2.988(2)
<i>RE1</i> –S4	3.062(2)	3.038(2)	3.024(2)
<i>RE1</i> –S2	3.077(2)	3.047(2)	3.030(2)
<i>RE1</i> –S3	3.086(2)	3.068(2)	3.049(2)
<i>RE1</i> –S2	3.139(2)	3.117(2)	3.103(2)
<i>RE1</i> –I	3.4708(9)	3.4565(6)	3.4499(4)
<i>RE2</i> –S4 (×2)	2.930(2)	2.910(2)	2.896(2)
<i>RE2</i> –S2 (×2)	2.967(2)	2.947(2)	2.928(2)
<i>RE2</i> –S1 (×2)	3.252(2)	3.224(2)	3.193(2)
<i>RE2</i> –S1 (×2)	3.381(2)	3.394(2)	3.415(2)
<i>RE2</i> –I	3.3190(14)	3.282(1)	3.246(1)
Ge–S2	2.187(2)	2.191(2)	2.188(2)
Ge–S4	2.192(2)	2.191(2)	2.195(2)
Ge–S1	2.199(2)	2.200(2)	2.197(2)
Ge–S3	2.217(2)	2.218(2)	2.212(2)

### 2.2.3. Electronic structure calculations

Tight-binding linear muffin-tin orbital (TB-LMTO) band structure calculations were performed within the local density and atomic-spheres approximation with the use of the Stuttgart TB-LMTO program.<sup>23</sup> The basis set consisted of La 6s/6p/5d/4f, Ge 4s/4p/4d, S 3s/3p/3d, and I 5s/5p/4d/4f orbitals, with the La 6p, Ge 4d, S 3d, and I 4d/4f orbitals being downfolded. Integrations in reciprocal space were carried out with an improved tetrahedron method over 78 irreducible  $k$  points within the first Brillouin zone. Crystal orbital Hamilton populations (COHP) were evaluated to analyze bonding interactions.<sup>24</sup>

#### 2.2.4. Diffuse reflectance spectroscopy

Optical diffuse reflectance spectra for all three compounds were measured from 200 nm (6.2 eV) to 2500 nm (0.50 eV) on a Cary 5000 UV-vis-NIR spectrophotometer equipped with a diffuse reflectance accessory, with a compacted pellet of BaSO<sub>4</sub> used as a 100% reflectance standard. These reflectance spectra were converted to optical absorption spectra using the Kubelka-Munk function,  $F(R) = \alpha/S = (1-R)^2/2R$ , where  $\alpha$  is the Kubelka–Munk absorption coefficient,  $S$  is the scattering coefficient, and  $R$  is the reflectance.<sup>25</sup>

#### 2.2.5. Magnetic susceptibility measurements

Zero-field-cooled dc magnetic susceptibility measurements were made on  $RE_3Ge_2S_8I$  ( $RE = Ce, Pr$ ) between 2 and 300 K under an applied magnetic field of 0.5 T on a Quantum Design 9T–PPMS magnetometer. Susceptibility values were corrected for contributions from the holder and sample diamagnetism.

### 2.3. Results and discussion

The sulfide iodides  $RE_3Ge_2S_8I$  were successfully prepared by reactions of the elements at 900 °C. They are the first quaternary phases found in the  $RE$ –Ge–S–I systems. As in the corresponding Si-containing compounds  $RE_3Si_2S_8X$  ( $X = Cl, Br, I$ ),<sup>11–17</sup> the range of  $RE$  substitution in  $RE_3Ge_2S_8I$  is limited to the lighter members ( $RE = La, Ce, Pr$ ). The formula could also be written as  $RE_3(GeS_4)_2I$  to emphasize the presence of thiogermanate groups, in analogy to the orthosilicate groups found in the  $La_3(SiO_4)_2Cl$ -type structure to which these compounds are isostructural.<sup>26</sup> The monoclinic structure (space group  $C2/c$ ) consists of discrete anionic  $[GeS_4]^{4-}$  tetrahedra arranged in stacks along the  $c$ -direction and separated by  $RE^{3+}$  cations; these stacks outline large tunnels occupied by  $I^-$  anions (**Figure 2-2a**, and **b**). The Ge-centred tetrahedra are

quite regular, with nearly equidistant Ge–S bonds (2.18–2.22 Å) that fall within the usual range (2.1–2.3 Å) found in other Ge-containing sulfides.<sup>27</sup> The two types of *RE* sites are each surrounded by one I and eight S atoms in roughly tricapped trigonal prismatic geometry, but the coordination environment around *RE2* is quite irregular (**Figure 2-2c**). These environments are asymmetric as a result of the presence of the two different kinds of ions, S<sup>2-</sup> and I<sup>-</sup>, around the *RE*<sup>3+</sup> cations. The distances to the S atoms are shorter (La–S, 2.96–3.14 Å; Ce–S, 2.94–3.12 Å; Pr–S, 2.91–3.10 Å) than to the I atoms (La–I, 3.47 Å; Ce–I, 3.28 Å; Pr–I, 3.25 Å), and agree well with the sum of Shannon ionic radii (La<sup>3+</sup>, 1.16 Å; Ce<sup>3+</sup>, 1.14 Å; Pr<sup>3+</sup>, 1.13 Å; S<sup>2-</sup>, 1.84 Å; I<sup>-</sup>, 2.20 Å).<sup>28</sup> Bond valence sums (**Table 2-4**) support the simple charge-balanced ionic formulation (*RE*<sup>3+</sup>)<sub>3</sub>(Ge<sup>4+</sup>)<sub>2</sub>(S<sup>2-</sup>)<sub>8</sub>(I<sup>-</sup>).<sup>29</sup>

**Table 2-4.** Bond valence sums in *RE*<sub>3</sub>Ge<sub>2</sub>S<sub>8</sub>I.

	La <sub>3</sub> Ge <sub>2</sub> S <sub>8</sub> I	Ce <sub>3</sub> Ge <sub>2</sub> S <sub>8</sub> I	Pr <sub>3</sub> Ge <sub>2</sub> S <sub>8</sub> I
<i>RE1</i>	2.97	2.99	2.94
<i>RE2</i>	2.74	2.75	2.73
Ge	4.24	4.22	4.25
S1	1.76	1.75	1.75
S2	2.07	2.07	2.07
S3	2.07	2.06	2.06
S4	2.27	2.29	2.26
I	0.81	0.84	0.82

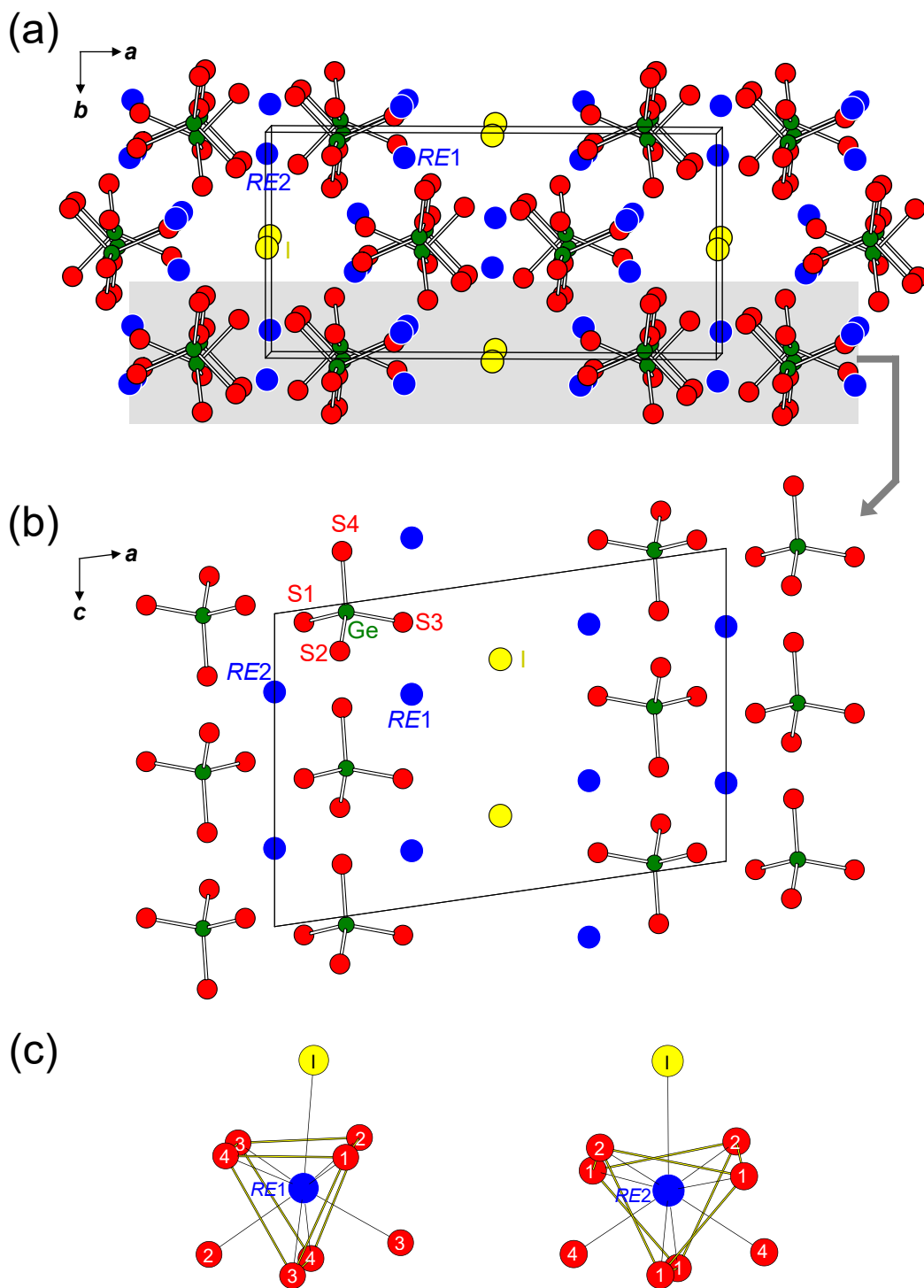


**Figure 2-2.** Structure of  $RE_3Ge_2S_8I$  ( $RE = La, Ce, Pr$ ) (a) viewed down the  $c$ -direction revealing tunnels occupied by  $I$  atoms, (b) highlighting a slice parallel to the  $ac$ -plane containing isolated  $GeS_4$  tetrahedra, and (c) showing the coordination environments around  $RE$  atoms.

Electronic structure calculations were performed on  $\text{La}_3\text{Ge}_2\text{S}_8\text{I}$ , whose closed-shell electron configurations for all atoms imply the presence of a band gap. The density of states (DOS) curve shows a gap between filled states below the Fermi level at 0 eV and empty states above 1.0 eV (**Figure 2-3a**). The gap is a direct one at the Brillouin zone centre  $\Gamma$ , as revealed in a band dispersion diagram (not shown). The valence band results from the mixing of Ge 4p (from  $-6.0$  to  $-1.2$  eV), I 5p states (from  $-0.9$  to 0 eV), and S 3p states as indicated by the atomic projections of the DOS curve (**Figure 2-3b**). The normal expectation is that the band gap is controlled by the strongest covalent interactions in the structure, namely that it would correspond to the separation of filled Ge–S bonding and empty Ge–S antibonding levels. As seen in the crystal orbital Hamilton population (–COHP) curves (**Figure 2-3c**), this is indeed the case, but the band gap is considerably narrowed by the presence of the I-based states that lie higher in energy than the Ge-based states in the valence band. This feature was also observed in the electronic structure of  $\text{Ce}_3\text{Si}_2\text{S}_8\text{I}$ .<sup>12</sup> Notwithstanding the ionic formulation indicated earlier, both La–S and La–I interactions bring important contributions to the covalent bonding stabilization of the structure. The integrated COHP values (–ICOHP) are 15.5 eV/cell for Ge–S, 14.0 eV/cell for La–S, and 1.5 eV/cell for La–I interactions.

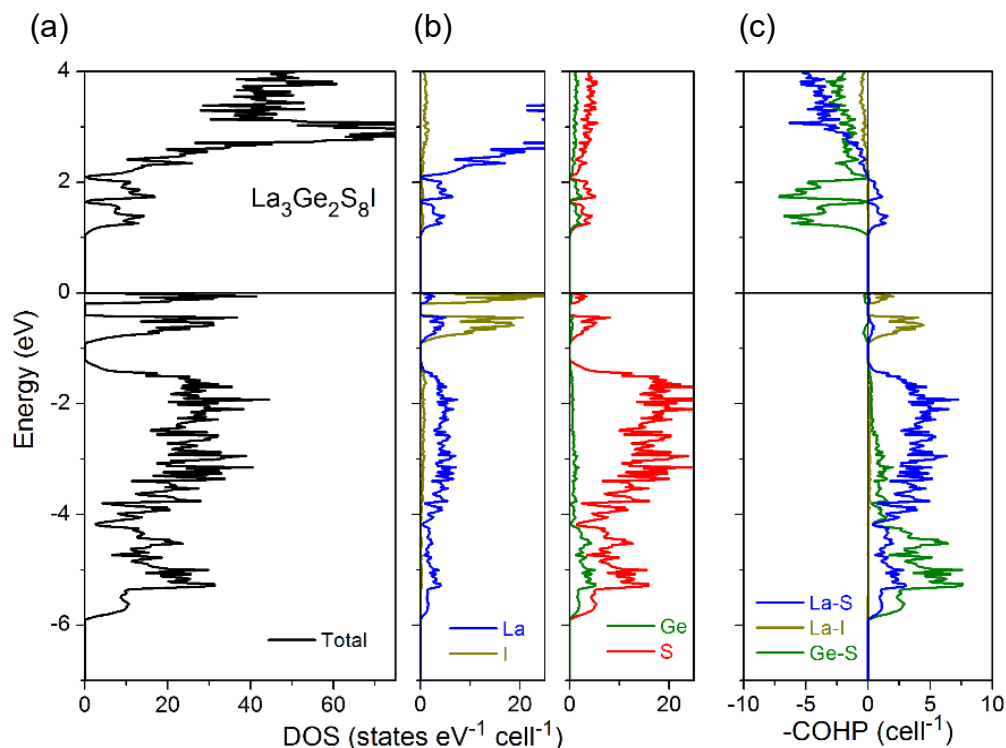


**Figure 2-3.** (a) Density of states (DOS) (b) atomic projections, and (c) crystal orbital Hamilton population ( $-COHP$ ) curves for  $La_3Ge_2S_8I$ .

The optical band gaps are 3.1 eV for  $La_3Ge_2S_8I$ , 2.7 eV for  $Ce_3Ge_2S_8I$ , and 2.9 eV for  $Pr_3Ge_2S_8I$ , as extrapolated from the absorption edges of the UV-vis-NIR diffuse reflectance spectra, converted to absorption spectra (**Figure 2-4**). For  $La_3Ge_2S_8I$ , the observed band gap is significantly larger than found in the electronic structure calculated from the LMTO method (with a discrepancy of similar magnitude as found for  $Ce_3Si_2S_8I$ ),<sup>12</sup> which tends to underestimate the gap, but it is consistent with the nearly colourless appearance of crystals of  $La_3Ge_2S_8I$ . For comparison, the experimental band gap of the Si-containing analogues are larger, 3.9 eV for  $La_3Si_2S_8I$  and 2.9 eV for  $Ce_3Si_2S_8I$ .<sup>13</sup>

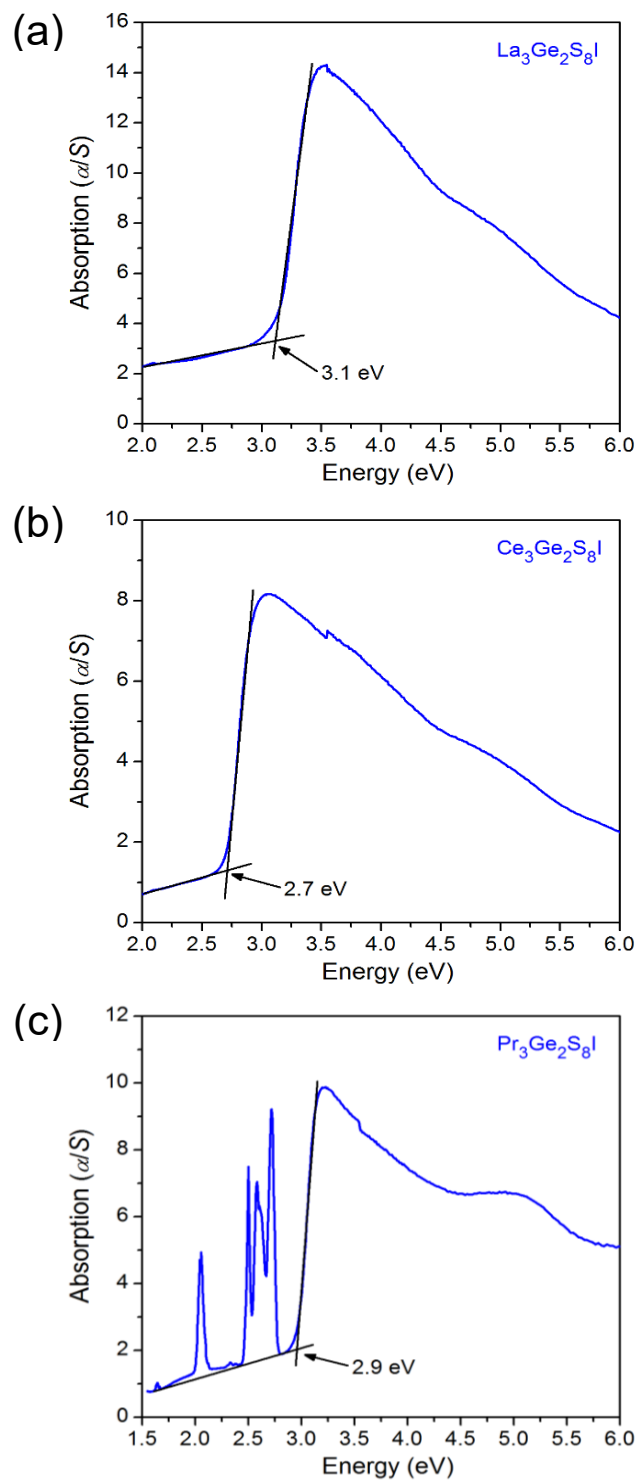


**Figure 2-4.** Optical absorption spectra, converted from the diffuse reflectance spectra, for (a)  $\text{La}_3\text{Ge}_2\text{S}_8\text{I}$ , (b)  $\text{Ce}_3\text{Ge}_2\text{S}_8\text{I}$ , and (c)  $\text{Pr}_3\text{Ge}_2\text{S}_8\text{I}$ .

Magnetic susceptibility measurements made on  $\text{Ce}_3\text{Ge}_2\text{S}_8\text{I}$  and  $\text{Pr}_3\text{Ge}_2\text{S}_8\text{I}$ , which contain  $RE$  components with unpaired  $f$  electrons, reveal simple paramagnetism with no obvious transitions down to 2 K (**Figure 2-5**). The linear portions of the inverse magnetic susceptibility (over the entire temperature range for  $\text{Ce}_3\text{Ge}_2\text{S}_8\text{I}$  and above  $\sim 20$  K for  $\text{Pr}_3\text{Ge}_2\text{S}_8\text{I}$ ) were fit to the Curie-Weiss law,  $\chi = C / (T - \theta_p)$ . The effective magnetic moments evaluated from the Curie constant, through  $\mu_{\text{eff}} = (8C)^{1/2}$ , were  $4.51(1) \mu_B/\text{f.u.}$  for  $\text{Ce}_3\text{Ge}_2\text{S}_8\text{I}$  and  $6.20(1) \mu_B/\text{f.u.}$  for  $\text{Pr}_3\text{Ge}_2\text{S}_8\text{I}$ . If the  $RE$  atoms are assumed to be the only contribution to the effective magnetic moment, according to  $\mu_{\text{eff}} = (3\mu_{RE}^2)^{1/2}$ , the values of  $\mu_{RE}$  are  $2.60(1) \mu_B/\text{Ce}$  for  $\text{Ce}_3\text{Ge}_2\text{S}_8\text{I}$  and  $3.63(1) \mu_B/\text{Pr}$  for  $\text{Pr}_3\text{Ge}_2\text{S}_8\text{I}$ , in good agreement with the theoretical free-ion values of  $2.54 \mu_B$  for  $\text{Ce}^{3+}$  and  $3.58 \mu_B$  for  $\text{Pr}^{3+}$ . The paramagnetic Weiss constants are  $0(1)$  K for  $\text{Ce}_3\text{Ge}_2\text{S}_8\text{I}$  and  $9(1)$  K for  $\text{Pr}_3\text{Ge}_2\text{S}_8\text{I}$ , implying little to no magnetic coupling of the  $RE$  atoms, which are quite far apart ( $4.5 \text{ \AA}$ ) from each other. In comparison,  $\text{Ce}_3\text{Si}_2\text{S}_8\text{I}$  also follows the Curie-Weiss law with  $\mu_{\text{eff}} = 2.45(2) \mu_B/\text{Ce}$  and  $\theta_p = -4.7(3) \text{ K}$ .<sup>12</sup>

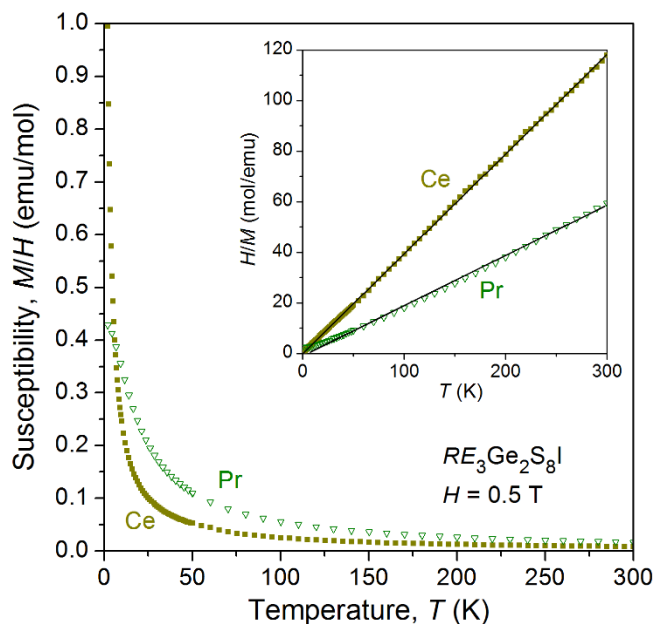


**Figure 2-5.** Magnetic susceptibility and its inverse (inset) for  $RE_3Ge_2S_8I$  ( $RE = Ce, Pr$ ).

## 2.4. Conclusions

The Ge-substituted analogues of  $RE_3Si_2S_8I$  ( $RE = La-Nd, Sm, Tb$ ) have been successfully prepared, but the range of  $RE$  substitution is even more limited to just the largest components,  $RE_3Ge_2S_8I$  ( $RE = La-Pr$ ). The structures can be viewed as consisting of isolated  $[GeS_4]^{4-}$  units in combination with monoatomic  $RE^{3+}$  and  $I^-$  ions. Preliminary experiments in which powders of these samples were exposed to a handheld UV light source showed no visibly detectable luminescence.

## 2.5. References

- (1) Kageyama, H.; Hayashi, K.; Maeda, K.; Attfield, J. P.; Hiroi, Z.; Rondinelli, J. M.; Poeppelmeier, K. R. *Nat. Commun.* **2018**, *9*, 772-1–772-15.
- (2) Recham, N.; Chotard, J.-N.; Dupont, L.; Delacourt, C.; Walker, W.; Armand, M.; Tarascon, J.-M. *Nat. Mater.* **2010**, *9*, 68–74.
- (3) Ueda, K.; Inoue, S.; Hirose, S.; Kawazoe, H.; Hosono, H. *Appl. Phys. Lett.* **2000**, *77*, 2701–2703.
- (4) Jansen, M.; Letschert, H. P. *Nature* **2000**, *404*, 980–982.
- (5) Kamihara, Y.; Watanabe, T.; Hirano, M.; Hosono, H. *J. Am. Chem. Soc.* **2008**, *130*, 3296–3297.
- (6) Xiao, J.-R.; Yang, S.-H.; Feng, F.; Xue, H.-G.; Guo, S.-P. *Coord. Chem. Rev.* **2017**, *347*, 23–47.
- (7) Nilges, T.; Nilges, S.; Pfitzner, A.; Doert, T.; Böttcher, P. *Chem. Mater.* **2004**, *16*, 806–812.
- (8) Shi, H.; Ming, W.; Du, M.-H. *Phys. Rev. B* **2016**, *93*, 104108-1–104108-7.
- (9) Li, Y.-Y.; Liu, P.-F.; Hu, L.; Chen, L.; Lin, H.; Zhou, L.-J.; Wu, L.-M. *Adv. Opt. Mater.* **2015**, *3*, 957–966.
- (10) Gauthier, G.; Kawasaki, S.; Jobic, S.; Macaudière, P.; Brec, R.; Rouxel, J. *J. Alloys Compd.* **1998**, *275–277*, 46–49.
- (11) Gauthier, G.; Kawasaki, S.; Jobic, S.; Macaudière, P.; Brec, R.; Rouxel, J. *J. Mater. Chem.* **1998**, *8*, 179–186.
- (12) Riccardi, R.; Gout, D.; Gauthier, G.; Guillen, F.; Jobic, S.; Garcia, A.; Huguenin, D.; Macaudière, P.; Fouassier, C.; Brec, R. *J. Solid State Chem.* **1999**, *147*, 259–268.

- (13) Hatscher, S. T.; Umland, W. *Z. Anorg. Allg. Chem.* **2001**, *627*, 2198–2200.
- (14) Hatscher, S. T.; Umland, W. *Acta Crystallogr., Sect. E, Struct. Rep. Online* **2002**, *58*, i100–i102.
- (15) Hatscher, S. T.; Umland, W. *Z. Anorg. Allg. Chem.* **2002**, *628*, 608–611.
- (16) Hatscher, S. T.; Umland, W. *Mater. Res. Bull.* **2002**, *37*, 1239–1247.
- (17) Hatscher, S. T.; Umland, W. *Acta Crystallogr., Sect. E, Struct. Rep. Online* **2002**, *58*, i124–i126.
- (18) Hatscher, S. T.; Umland, W. *Mater. Res. Bull.* **2003**, *38*, 99–112.
- (19) Coelho, A. A. TOPAS-Academic, version 6, Coelho Software, Brisbane, Australia, 2007.
- (20) Sheldrick, G. M. SHELXTL, version 6.12, Bruker AXS Inc., Madison, WI, 2001.
- (21) Gelato, L. M.; Parthé, E. *J. Appl. Crystallogr.* **1987**, *20*, 139–143.
- (22) Tank, R.; Jepsen, O.; Burkhardt, A.; Andersen, O. K. TB-LMTO-ASA Program, version 4.7, Max Planck Institut für Festkörperforschung, Stuttgart, Germany, 1998.
- (23) Dronskowski, R.; Blöchl, P. E. *J. Phys. Chem.* **1993**, *97*, 8617–8624.
- (24) Kortüm, G. *Reflectance Spectroscopy*, Springer, New York, 1969.
- (25) Gravereau, P.; Es-Sakhi, B.; Fouassier, C. *Acta Crystallogr., Sect. C: Cryst. Struct. Commun.* **1988**, *44*, 1884–1887.
- (26) Villars, P.; Cenzual, K. *Pearson's Crystal Data – Crystal Structure Database for Inorganic Compounds (on DVD)*, Release 2016/17, ASM International, Materials Park, OH, USA.
- (27) Shannon, R. D. *Acta Crystallogr., Sect. A: Cryst. Phys., Diffr., Theor. Gen. Crystallogr.* **1976**, *32*, 751–767.
- (28) Brese, N. E. O'Keeffe, M. *Acta Crystallogr., Sect. B: Struct. Sci.* **1991**, *47*, 192–197.

## Chapter 3.

### Controlling the Luminescence of Rare-Earth Chalcogenide Iodides $RE_3(\text{Ge}_{1-x}\text{Si}_x)_2\text{S}_8\text{I}$ ( $RE = \text{La}, \text{Ce}, \text{Pr}$ ) and $\text{Ce}_3\text{Si}_2(\text{S}_{1-y}\text{Se}_y)_8\text{I}$

#### 3.1. Introduction

Mixed-anion compounds, which contain more than one type of nonmetal anion, offer additional flexibility to control the structures and properties of an inorganic solid beyond what could be accomplished by the conventional approach of varying the metal cations alone. The challenge is that the atomic features (e.g., size, electronegativity, charge) for multiple nonmetals vary more significantly than for metals, so that it is not obvious that simple substitution strategies will succeed. Nevertheless, many promising materials for applications such as batteries, thermoelectrics, ferroelectrics, and optical materials have now been identified, especially among oxyhalides, oxychalcogenides, and oxypnictides.<sup>1-6</sup>

Chalcogenide halides (or “chalcahalides”) form a class of mixed-anion compounds that have recently gained popularity as energy materials, on the assumption that a combination of chalcogenide (*Ch*) and halide ions offers further ability to tune properties.<sup>7</sup> Among these compounds, those containing rare-earth (*RE*) metals could exhibit interesting magnetic and optical properties arising from the localized f-electrons of the *RE* cations, but they remain relatively rare, numbering around 50.<sup>8</sup> Within the family of quaternary sulfide halides  $RE_3\text{Si}_2\text{S}_8X$  (*RE* = early rare-earth metals; *X* = Cl, Br, I), the Ce-containing members were first reported to exhibit strong luminescence in the blue region.<sup>9-15</sup> Subsequently,  $\text{La}_3\text{Si}_2\text{S}_8\text{Br}$  was exploited as a host to prepare phosphors that give broadband emission in the cyan region when doped with  $\text{Ce}^{3+}$  or in the red-orange region when doped with  $\text{Eu}^{2+}$ , demonstrating promise for applications in phosphor-converted white light emitting diodes.<sup>16</sup> Luminescent materials based on sulfides provide

advantages over oxides because their greater covalency tends to shift the emission wavelengths toward the visible region; thus, SrS, ZnS, and SrGa<sub>2</sub>S<sub>4</sub> are well known to act as hosts in electroluminescent devices.<sup>17-19</sup> On the other hand, these sulfides tend to be less stable and require encapsulation. There remains a pressing need for other sulfides that could act as hosts for phosphors, especially with the ability to tune the emission wavelength.

Expanding the palette of compositions for these quaternary sulfide halides  $RE_3Si_2S_8X$ , we recently prepared the Ge-containing analogues  $RE_3Ge_2S_8I$ .<sup>20</sup> The environment around the two types of  $RE$  atoms in the structure of all  $RE_3Tt_2S_8X$  [ $Tt$  (tetrel) = Si, Ge] compounds is highly heterogeneous, consisting of S and  $X$  atoms in the first coordination sphere and  $Tt$  atoms in the second coordination sphere, all within 4 Å. Given that the emission of light in the original  $Ce_3Si_2S_8X$  series results from transitions between 4f and 5d states of the cerium ions, it can be hypothesized that the centroid shift and crystal field effects on the d-orbitals are strongly influenced by changing the environment around them, thereby enabling control of the emission properties.<sup>16</sup> To investigate these effects, we attempt the preparation of solid solutions  $RE_3(Ge_{1-x}Si_x)_2S_8I$ , in which the tetrel cations are mixed, and  $Ce_3Si_2(S_{1-y}Se_y)_8I$ , in which the chalcogen anions are mixed. Their luminescence properties were measured and related to changes in the crystal and electronic structures.

## 3.2. Experimental Section

### 3.2.1. Synthesis

Starting materials were freshly filed rare-earth metal pieces ( $RE = La, Ce, Pr$ ; 99.9%, Hefa), germanium powder (99.999%, Alfa Aesar), silicon lumps (99.9999%, Alfa Aesar), sulfur flakes (99.998%, Sigma-Aldrich), selenium powder (99.99%, Onyxmet), and iodine crystals (99.8%,

Anachemia). Various members of the solid solutions  $RE_3(Ge_{1-x}Si_x)_2S_8I$  and  $Ce_3Si_2(S_{1-y}Se_y)_8I$  were targeted by combining the elements in stoichiometric ratios on a 0.5-g scale, with a 10 wt. % excess of  $I_2$  added. The mixtures were cold-pressed into pellets (10 mm diameter) and placed into fused-silica tubes, which were evacuated to  $10^{-3}$  mbar and sealed (12 mm diameter and 15 cm length). The tubes were heated to 300 °C, at a slow ramp rate at 2 °C/min to minimize volatilization losses of sulfur and iodine, held at that temperature for 2 d, heated 2 °C/min to 900 °C, held there for 7 d, and then cooled to room temperature over 2 d. Most of the excess  $I_2$  was found to be deposited at the other end of the tubes. The resulting products were ground and stored in vials under ambient conditions.

Powder X-ray diffraction (XRD) patterns of the samples were collected on a Bruker D8 Advance diffractometer equipped with a  $Cu K\alpha_1$  radiation source operated at 40 kV and 40 mA. Rietveld refinements of these patterns were carried out using the TOPAS Academic software package, with the background modeled by a 12-term polynomial function (**Figure A1-1** to **Figure A1-4**).<sup>21</sup> Refined cell parameters were extracted from these patterns (**Table A1-1**).

Energy-dispersive X-ray (EDX) analyses were performed on a Zeiss Sigma 300 VP field emission scanning electron microscope operated with an accelerating voltage of 15 kV and equipped with a Bruker Quantax 600 system with dual X-Flash 6/60 detectors. A representative elemental map for  $Ce_3Si_2S_8I$  confirms a homogeneous distribution of all elements (**Figure A1-5**). The elemental compositions were determined from area analysis of the powder samples and multiple point analyses of several single crystals for each sample, with acquisition times of 120 s (**Table A1-2**). These compositions agree reasonably well with expectations, although in some

cases, deposition of excess iodine was noted, as evidenced by dark coloration on the surface of crystals. These samples can be easily cleaned by washing with organic solvents such as hexane.

### 3.2.2. Structure Determination

Single-crystal X-ray diffraction experiments for various members of the solid solutions  $RE_3(Ge_{1-x}Si_x)_2S_8I$  and  $Ce_3Si_2(S_{1-y}Se_y)_8I$  were carried out on a Bruker PLATFORM diffractometer equipped with a graphite monochromated Mo  $K\alpha$  radiation source and a SMART APEX II CCD detector. Intensity data were collected at room temperature using  $\omega$  scans at eight different  $\phi$  angles with a frame width of  $0.3^\circ$  and exposure times of 10 s per frame. Face-indexed numerical absorption corrections were applied to all data sets. Structure solution and refinement were carried out using the SHELXTL program package.<sup>22</sup>

Based on the Laue symmetry, intensity statistics, and systematic absences, the monoclinic space group  $C2/c$  was chosen. Direct methods confirmed the  $La_3Si_2O_8Cl$ -type structure expected for these compounds.<sup>23</sup> To treat disorder of Ge and Si atoms in  $RE_3(Ge_{1-x}Si_x)_2S_8I$ , the sum of the occupancies of these atoms in the sole tetrel site was constrained to unity and their displacement parameters were fixed to be equal. Similarly, to treat disorder of S and Se atoms in  $Ce_3Si_2(S_{1-y}Se_y)_8I$ , each of the four chalcogen sites was first examined individually, by allowing them to be fully occupied by a mixture of these atoms. Then, the refinement was relaxed with the occupancies of all four sites being freed simultaneously, with no constraint imposed on the sum of the occupancies over these sites. The refinements were stable, and the occupancies converged to reasonable values, leading to chemical formulas that agree well with the nominally loaded compositions in the syntheses.

Atomic positions were standardized using the program STRUCTURE TIDY.<sup>24</sup> No additional symmetry was detected by the ADDSYM routine in PLATON.<sup>25</sup> Full information about the structure refinement results, atomic coordinates, displacement parameters, and interatomic distances are provided in **Table A1-3 to Table A1-5**. Abbreviated crystal data and ranges of interatomic distances are listed in **Table 3-1 to Table 3-2**.

**Table 3-1.** Abbreviated Crystallographic Data for  $RE_3(\text{Ge}_{1-x}\text{Si}_x)_2\text{S}_8\text{I}$  and  $\text{Ce}_3\text{Si}_2(\text{S}_{1-y}\text{Se}_y)_8\text{I}$ . <sup>a</sup>

	$\text{La}_3\text{Ge}_{1.5}\text{Si}_{0.5}\text{S}_8\text{I}$	$\text{La}_3\text{GeSiS}_8\text{I}$	$\text{La}_3\text{Ge}_{0.5}\text{Si}_{1.5}\text{S}_8\text{I}$	$\text{Ce}_3\text{Ge}_{1.5}\text{Si}_{0.5}\text{S}_8\text{I}$	$\text{Ce}_3\text{GeSiS}_8\text{I}$
refined composition	$\text{La}_3\text{Ge}_{1.55(1)}\text{Si}_{0.45(1)}\text{S}_8\text{I}$	$\text{La}_3\text{Ge}_{0.98(2)}\text{Si}_{1.02(2)}\text{S}_8\text{I}$	$\text{La}_3\text{Ge}_{0.52(1)}\text{Si}_{1.48(1)}\text{S}_8\text{I}$	$\text{Ce}_3\text{Ge}_{1.55(1)}\text{Si}_{0.45(1)}\text{S}_8\text{I}$	$\text{Ce}_3\text{Ge}_{0.96(2)}\text{Si}_{1.04(2)}\text{S}_8\text{I}$
fw (amu)	923.04	900.79	878.54	926.67	908.42
$a$ (Å)	16.1274(13)	16.127(2)	16.137(16)	16.0237(10)	16.014(2)
$b$ (Å)	7.9621(6)	7.9458(11)	7.921(8)	7.8998(5)	7.8845(11)
$c$ (Å)	10.9988(9)	10.9756(15)	10.959(11)	10.9439(7)	10.9249(15)
$\beta$ (deg.)	98.0961(15)	98.019(3)	97.957(18)	98.1716(10)	98.063(3)
$V$ (Å <sup>3</sup> )	1398.26(19)	1392.7(3)	1387(2)	1371.26(15)	1365.8(3)
$\rho_c$ (g cm <sup>-3</sup> )	4.385	4.296	4.206	4.489	4.398
$\mu$ (mm <sup>-1</sup> )	15.56	14.61	13.65	16.48	15.52
$R(F)$ for $F_o^2 > 2\sigma(F_o^2)$ <sup>b</sup>	0.037	0.052	0.044	0.026	0.047
$R_w(F_o^2)$ <sup>c</sup>	0.084	0.141	0.113	0.054	0.124
	$\text{Ce}_3\text{Ge}_{0.5}\text{Si}_{1.5}\text{S}_8\text{I}$	$\text{Ce}_3\text{Si}_2\text{S}_{7.5}\text{Se}_{0.5}\text{I}$	$\text{Ce}_3\text{Si}_2\text{S}_7\text{SeI}$	$\text{Pr}_3\text{GeSiS}_8\text{I}$	
refined composition	$\text{Ce}_3\text{Ge}_{0.43(1)}\text{Si}_{1.57(1)}\text{S}_8\text{I}$	$\text{Ce}_3\text{Si}_2\text{S}_{7.55(1)}\text{Se}_{0.45(1)}\text{I}$	$\text{Ce}_3\text{Si}_2\text{S}_{7.00(2)}\text{Se}_{1.00(2)}\text{I}$	$\text{Pr}_3\text{Ge}_{1.01(2)}\text{Si}_{0.99(2)}\text{S}_8\text{I}$	
fw (amu)	882.17	883.37	906.82	906.79	
$a$ (Å)	15.9844(11)	15.9941(12)	16.046(2)	15.908(4)	
$b$ (Å)	7.8676(6)	7.8706(6)	7.8872(11)	7.8343(19)	
$c$ (Å)	10.8912(8)	10.8909(8)	10.9161(16)	10.864(3)	
$\beta$ (deg.)	98.0066(14)	97.8085(13)	97.689(3)	98.191(5)	
$V$ (Å <sup>3</sup> )	1356.31(17)	1358.27(18)	1369.1(3)	1340.1(6)	
$\rho_c$ (g cm <sup>-3</sup> )	4.320	4.320	4.399	4.494	
$\mu$ (mm <sup>-1</sup> )	14.58	14.78	15.92	16.53	
$R(F)$ for $F_o^2 > 2\sigma(F_o^2)$ <sup>b</sup>	0.040	0.025	0.055	0.042	
$R_w(F_o^2)$ <sup>c</sup>	0.098	0.052	0.155	0.108	

<sup>a</sup> For all structures, space group  $C2/c$  (no. 15),  $Z = 4$ ,  $T = 296(2)$  K,  $\lambda = 0.71073$  Å. <sup>b</sup>  $R_w(F_o^2) = [\sum[w(F_o^2 - F_c^2)^2] / \sum wF_o^4]^{1/2}$ ;  $w^{-1} = [\sigma^2(F_o^2) + (Ap)^2 + Bp]$ , where  $p = [\max(F_o^2, 0) + 2F_c^2] / 3$ .

**Table 3-2.** Ranges of Interatomic Distances (Å) for  $RE_3(\text{Ge}_{1-x}\text{Si}_x)_2\text{S}_8\text{I}$  and  $\text{Ce}_3\text{Si}_2(\text{S}_{1-y}\text{Se}_y)_8\text{I}$ .

	$\text{La}_3\text{Ge}_{1.5}\text{Si}_{0.5}\text{S}_8\text{I}$	$\text{La}_3\text{GeSiS}_8\text{I}$	$\text{La}_3\text{Ge}_{0.5}\text{Si}_{1.5}\text{S}_8\text{I}$	$\text{Ce}_3\text{Ge}_{1.5}\text{Si}_{0.5}\text{S}_8\text{I}$	$\text{Ce}_3\text{GeSiS}_8\text{I}$	$\text{Ce}_3\text{Ge}_{0.5}\text{Si}_{1.5}\text{S}_8\text{I}$
<i>RE1-Ch</i>	2.966(2)–3.131(2)	2.960(3)–3.131(3)	2.957(3)–3.129(3)	2.9368(12)–3.1118(13)	2.942(3)–3.110(3)	2.9341(17)–3.0982(18)
<i>RE1-I</i>	3.4636(5)	3.4610(8)	3.462(3)	3.4489(3)	3.4457(7)	3.4379(5)
<i>RE2-Ch</i>	2.928(2)–3.362(2)	2.931(3)–3.334(3)	2.933(3)–3.316(3)	2.9069(12)–3.3661(13)	2.909(3)–3.334(3)	2.9068(17)–3.3051(18)
<i>RE2-I</i>	3.3206(11)	3.3227(14)	3.322(3)	3.2820(6)	3.2852(13)	3.2910(9)
<i>Tt-Ch</i>	2.169(2)–2.199(2)	2.150(3)–2.172(3)	2.125(3)–2.157(3)	2.1686(13)–2.1958(13)	2.140(3)–2.170(3)	2.120(2)–2.149(2)
	$\text{Ce}_3\text{Si}_2\text{S}_{7.5}\text{Se}_{0.5}\text{I}$	$\text{Ce}_3\text{Si}_2\text{S}_7\text{SeI}$	$\text{Ce}_3\text{Si}_2\text{S}_4\text{Se}_4\text{I}$	$\text{Ce}_3\text{Si}_2\text{S}_7\text{SeI}$	$\text{Pr}_3\text{GeSiS}_8\text{I}$	
<i>RE1-Ch</i>	2.9263(12)–3.0958(12)	2.929(3)–3.104(3)	2.9717(5)–3.1498(5)	3.0508(11)–3.2124(12)	2.919(3)–3.090(3)	
<i>RE1-I</i>	3.4418(4)	3.4567(9)	3.5103(2)	3.6007(7)	3.4306(9)	
<i>RE2-Ch</i>	2.9126(12)–3.2972(10)	2.922(3)–3.304(2)	2.9438(6)–3.3601(4)	3.0084(11)–3.5157(11)	2.891(3)–3.342(3)	
<i>RE2-I</i>	3.2944(7)	3.2948(17)	3.3109(4)	3.2830(13)	3.2513(16)	
<i>Tt-Ch</i>	2.1085(17)–2.1552(16)	2.108(4)–2.182(4)	2.1483(10)–2.2453(9)	2.245(3)–2.272(3)	2.139(3)–2.169(3)	

### 3.2.3. Property Measurements

Thermogravimetric analysis (TGA) was performed on a Perkin Elmer Pyris 1 instrument. The samples were heated under an Ar atmosphere at a rate of 10 °C/min from 25 to 950 °C.

Optical diffuse reflectance spectra were measured from 200 nm (6.2 eV) to 2500 nm (0.50 eV) on a Cary 5000 UV-vis-NIR spectrophotometer equipped with a diffuse reflectance accessory. An optical polytetrafluoroethylene disc with >98% reflectivity was used as a reflectance standard. The absorption spectra were converted from the optical reflectance data using the Kubelka-Munk function,  $F(R) = \alpha/S = (1-R)^2/2R$ , where  $\alpha$  is the Kubelka-Munk absorption coefficient,  $S$  is the scattering coefficient, and  $R$  is the reflectance.<sup>26</sup>

Excitation and emission spectra were obtained on a Horiba PTI QM-8075-11 fluorescence system with a 75 W Xenon arc lamp as an excitation source and equipped with an integrated sphere. The steady-state photoluminescence (PL) was excited with a 364+352-nm (combined UV lines) Ar-ion laser source operated at a power of 2 mW. Photoluminescence spectra were collected using an intensity-calibrated Ocean Optics USB2000+ miniature spectrometer with a 375-nm long-pass filter to block the scattered laser light. Time-resolved PL employed an Alphas picopower 405-nm diode laser (nominally 25-ps pulses) at a repetition rate of 4.1 MHz to excite the sample and a Becker-Hickl HPM100-50 hybrid single photon counting detector with a measured instrument response time of ~400 ps. Data collection was performed using a single photon counting module (SPM-130-EMN) from Becker-Hickl.

X-ray photoelectron spectra (XPS) for several members of  $\text{Ce}_3(\text{Ge}_{1-x}\text{Si}_x)_2\text{S}_8\text{I}$  and  $\text{Ce}_3\text{Si}_2(\text{S}_{1-y}\text{Se}_y)_8\text{I}$  were collected using a Kratos AXIS Supra XPS instrument equipped with a monochromatic Al  $K\alpha$  X-ray source (1487 eV) operating under high vacuum in the analytical

chamber. All samples were sputter-cleaned for nearly 1 h with an Ar<sup>+</sup>-ion beam (4 kV, 10 mA) to remove surface oxide contaminants, down to a level of ~5 to 6 at. % oxygen. Survey spectra confirmed the presence of all expected elements. High-resolution Ce 3d spectra were then collected with energy envelopes in the range of 60 to 20 eV, step size of 0.05 eV, and pass energy of 20 eV. The spectra were calibrated by setting the C 1s binding energy (BE) of adventitious carbon to 289.8 eV. The XPS spectra were analyzed using the CasaXPS software program.<sup>27</sup>

### 3.2.4. Electronic Structure Calculations

Ordered models for various members of the solid solutions Ce<sub>3</sub>(Ge<sub>1-x</sub>Si<sub>x</sub>)<sub>2</sub>S<sub>8</sub>I and Ce<sub>3</sub>Si<sub>2</sub>(S<sub>1-y</sub>Se<sub>y</sub>)<sub>8</sub>I were generated using the program Supercell (version 2.0).<sup>28</sup> The electronic structure and density of states (DOS) were determined by first-principles calculations using the projected augmented wave (PAW) method as implemented in the Vienna ab initio simulation package (VASP, version 5.4.4).<sup>29</sup> Exchange and correlation were treated in this density functional theory (DFT) method by the generalized gradient approximation, as parameterized by Perdew, Burke, and Ernzerhof.<sup>30</sup> PAW potentials (Ce\_3, Si, Ge\_d, S, Se, I) were used, with the plane-wave basis cutoff energy set to 450 eV. To contend with the difficulties inherent in DFT of describing f-electrons, the Ce\_3 potential was chosen in which the f-electrons in trivalent cerium are treated as core states. The first Brillouin zone was sampled by a gamma-centred 6 × 13 × 9 *k*-point mesh for DOS calculations. The convergence criteria were set to 10<sup>-6</sup> eV for electronic optimization and |−2 × 10<sup>-2</sup>| eV for ionic relaxation. Electron localization functions (ELF) were plotted using VESTA, and Bader charges were evaluated.<sup>31-33</sup> Projected crystal orbital Hamilton populations (−pCOHP) and crystal orbital bond indices (COBI) were determined using the program LOBSTER (version 4.1.0).<sup>34-36</sup>

### 3.3. Results and Discussion

#### 3.3.1. Solid Solutions

Several solid solutions derived from  $RE_3Ge_2S_8I$  ( $RE = La, Ce, Pr$ ) were targeted by reactions of the elements at 900 °C. Substitution of Ge with Si led to the complete solid solutions  $RE_3(Ge_{1-x}Si_x)_2S_8I$  ( $0 \leq x \leq 1$ ) with all samples being phase pure, as confirmed by powder XRD patterns, and having elemental compositions in agreement with expectations, as confirmed by EDX analyses. They appear light yellow or nearly colourless for  $La_3(Ge_{1-x}Si_x)_2S_8I$ , yellow for  $Ce_3(Ge_{1-x}Si_x)_2S_8I$ , and green for  $Pr_3(Ge_{1-x}Si_x)_2S_8I$ , with no visibly discernible difference in colours among members within each series. The unit cell volumes, as determined from the monoclinic cell parameters refined from the powder XRD patterns, shrink as the Si content ( $x$ ) increases, following a nearly linear dependence in accordance with Vegard's law (**Figure 3-1(a)**). Other attempts were made to prepare solid solutions with different combinations of tetrel atoms, but they were unsuccessful. For example, when members of  $Ce_3(Si_{1-z}Sn_z)_2S_8I$  were targeted, complex mixtures containing  $Ce_3Si_2S_8I$ ,  $Ce_2SnS_5$ ,  $SnI_4$ , and other phases were obtained instead. These results are understandable in terms of the classical Hume-Rothery rules for the formation of substitutional solid solutions. The solid solutions  $RE_3(Ge_{1-x}Si_x)_2S_8I$  are feasible because the atomic radii (on whatever scale) for Ge and Si are not too different, but more importantly, the end members  $RE_3Ge_2S_8I$  and  $RE_2Si_2S_8I$  exist and adopt the same crystal structure. In contrast, it is not surprising that solid solutions  $Ce_3(Si_{1-z}Sn_z)_2S_8I$  do not form, even with very low Sn content, because the atomic radii are too disparate (or near the limits of formability of solid solutions for Ge and Sn, with a ~14% difference in covalent radii) and the end member “ $Ce_3Sn_2S_8I$ ” does not exist.

It is not so obvious if mixing of the chalcogen anions would be achievable. Solid solutions derived from  $Ce_3Si_2S_8I$  were targeted in which S was gradually substituted by Se. Initially, members of the solid solution  $Ce_3Si_2(S_{1-y}Se_y)_8I$  were only prepared and characterized up to a partial substitution level of  $y = 0.19$ , because the photoluminescence (presented later) had already rapidly quenched up to this point, so no attempts were made to synthesize Se-richer members. Upon close inspection of the literature, the existence of  $Ce_3Si_2Se_8I$  has been implied but no publication has been forthcoming.<sup>11</sup> For completeness of this study, all remaining members of the solid solution  $Ce_3Si_2(S_{1-y}Se_y)_8I$ , including the all-selenium end-member  $Ce_3Si_2Se_8I$ , were subsequently targeted. They could be successfully prepared under the same experimental conditions as before. Pure phases of the complete solid solution  $Ce_3Si_2(S_{1-y}Se_y)_8I$  were obtained, with their cell volumes generally expanding as the Se content ( $y$ ) increases (**Figure 3-1(b)**).

Single-crystal X-ray diffraction studies for several members of these solid solutions were conducted to examine the detailed structural changes taking place (**Table 3-1** and **Table 3-2**). The monoclinic crystal structure ( $La_3Si_2O_8Cl$ -type, space group  $C2/c$ )<sup>23</sup> of these compounds consists of two *RE*, one *Tt*, four *Ch*, and one I site (**Figure 3-2(a)**). This structure type is known so far for  $RE_3Si_2O_8Cl$ ,<sup>23,37,38</sup>  $RE_3Si_2S_8X$  ( $X = Cl, Br, I$ ),<sup>9-16</sup> and  $RE_3Ge_2S_8I$ ,<sup>20</sup> with *RE* restricted to the early rare-earth metals. Isolated *TtCh*<sub>4</sub> tetrahedra are arranged in one-dimensional stacks, which are grouped in opposite-pointing pairs aligned along the *c*-direction. The three-dimensional packing of these stacks leads to large tunnels that are occupied by the I anions. The two types of *RE* atoms lie in the intervening spaces between the *TtCh*<sub>4</sub> tetrahedra. The coordination environment around each of these *RE* atoms consists of one I and eight *Ch* atoms in what could be approximated as tricapped trigonal prismatic geometry, but highly distorted, at distances up to 3.5 Å (**Figure 3-2(b)**). There are also *Tt* atoms slightly farther away, at distances up to 3.9 Å, three around *RE1* and four around *RE2*.

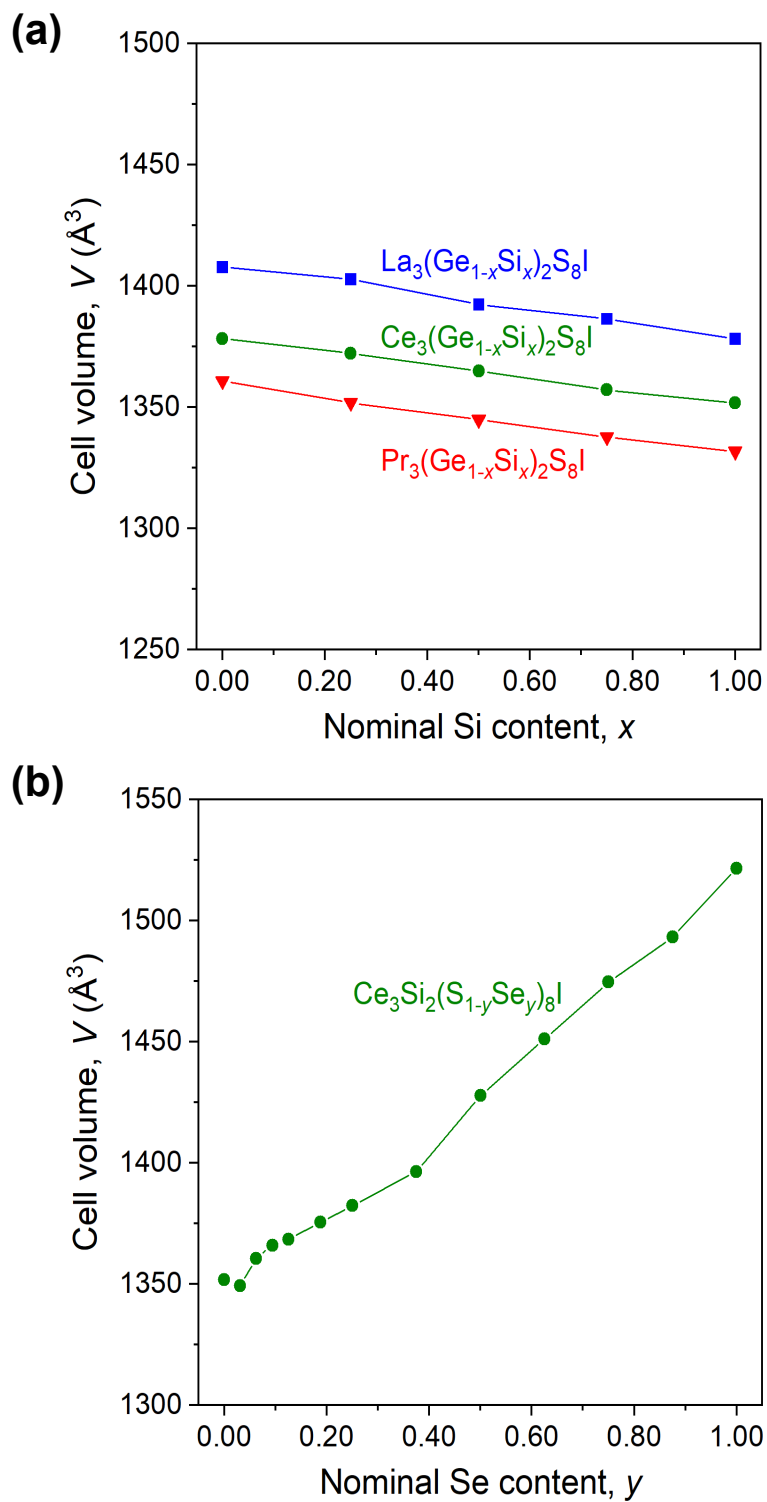


**Figure 3-1.** Evolution of unit cell volume for (a)  $RE_3(\text{Ge}_{1-x}\text{Si}_x)_2\text{S}_8\text{I}$  ( $RE = \text{La, Ce, Pr}$ ) and (b)  $\text{Ce}_3\text{Si}_2(\text{S}_{1-y}\text{Se}_y)_8\text{I}$ .

The *RE–Ch*, *RE–I*, and *Tt–Ch* interatomic distances in these compounds are generally consistent with the sum of ionic radii (IR values of 1.22 Å for La<sup>3+</sup> (CN9), 1.20 Å for Ce<sup>3+</sup> (CN9), 1.18 Å for Pr<sup>3+</sup> (CN9), 0.39 Å for Ge<sup>4+</sup> (CN4), 0.26 Å for Si<sup>4+</sup> (CN4), 1.84 Å for S<sup>2–</sup> (CN6), 1.98 Å for Se<sup>2–</sup> (CN6), and 2.20 Å for I<sup>–</sup> (CN6))<sup>39</sup> (**Table 3-2**). Plots of these distances for different members of the solid solutions show the trends more clearly (**Figure 3-3**). Within the mixed-tetrel solid solutions *RE*<sub>3</sub>(Ge<sub>1–*x*</sub>Si<sub>*x*</sub>)<sub>2</sub>S<sub>8</sub>I (*RE* = La, Ce, Pr), the main effects of substituting Si for Ge are to shorten the *Tt–S* bonds regularly, while the other distances remain relatively constant within a given series, and to result in a slightly less distorted coordination environment around the *RE2* atoms. For example, for Ce<sub>3</sub>(Ge<sub>1–*x*</sub>Si<sub>*x*</sub>)<sub>2</sub>S<sub>8</sub>I, the *Tt–S* distances decrease from 2.19–2.22 Å to 2.10–2.13 Å, and the Ce<sub>2</sub>–S distances change from 2.91–3.39 Å to 2.90–3.28 Å on proceeding from Ce<sub>3</sub>Ge<sub>2</sub>S<sub>8</sub>I to Ce<sub>3</sub>Si<sub>2</sub>S<sub>8</sub>I.

For the mixed-chalcogen solid solution Ce<sub>3</sub>Si<sub>2</sub>(S<sub>1–*y*</sub>Se<sub>*y*</sub>)<sub>8</sub>I, structure refinements were initially performed on Ce<sub>3</sub>Si<sub>2</sub>S<sub>7.5</sub>Se<sub>0.5</sub>I and Ce<sub>3</sub>Si<sub>2</sub>S<sub>7</sub>SeI, which revealed evidence for site preference as Se substitutes for S. Only one of four *Ch* sites (labeled as *Ch1*) permits mixing of S and Se atoms, whereas the remaining three are almost exclusively occupied by S atoms (**Table A1-4**). In view of this interesting result, additional experiments were later conducted to determine the detailed structures of Se-richer members Ce<sub>3</sub>Si<sub>2</sub>S<sub>4</sub>Se<sub>4</sub>I and Ce<sub>3</sub>Si<sub>2</sub>Se<sub>8</sub>I. At the midpoint of the solid solution, the Se atoms prefer to occupy the sites following the order *Ch1* > *Ch3*, *Ch2* > *Ch4*. This sequence correlates strongly with the bonds to the Si atoms, with the more distant *Ch* sites being preferentially occupied by larger Se atoms. With increasing Se substitution, the Si*Ch*<sub>4</sub> tetrahedra become more distorted, as the Si–*Ch* distances change from 2.10–2.13 Å in Ce<sub>3</sub>Si<sub>2</sub>S<sub>8</sub>I<sup>9–11</sup> to 2.15–2.25 Å in Ce<sub>3</sub>Si<sub>2</sub>S<sub>4</sub>Se<sub>4</sub>I, and then they become more regular again, with Si–Se distances of 2.25–2.27 Å in Ce<sub>3</sub>Si<sub>2</sub>Se<sub>8</sub>I.

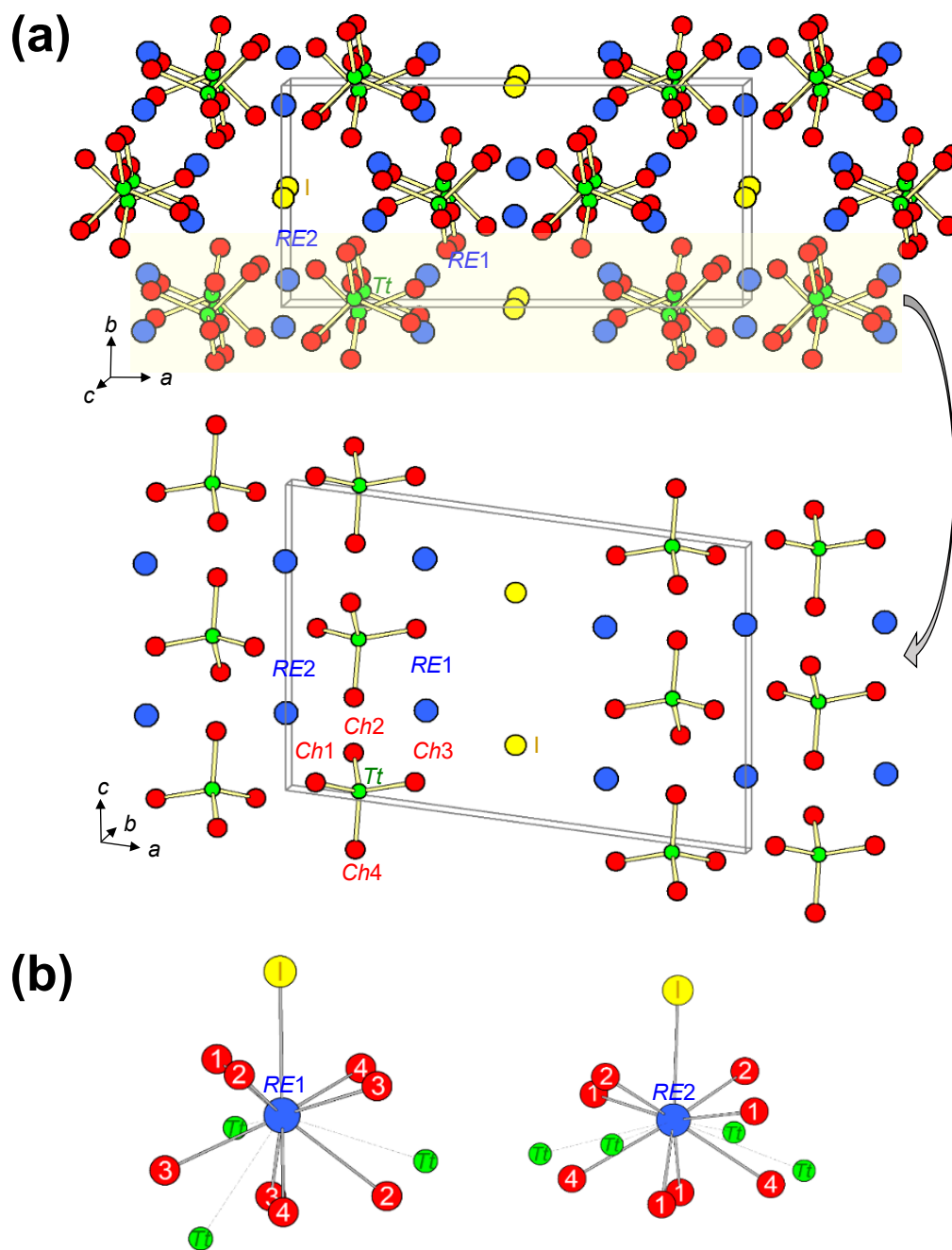


**Figure 3-2.** (a) Structure of  $RE_3(Ge_{1-x}Si_x)_2S_8I$  ( $RE = La, Ce, Pr$ ) and  $Ce_3Si_2(S_{1-y}Se_y)_8I$  viewed down the  $c$ -direction (upper panel) and highlighting a slice parallel to the  $ac$ -plane (lower panel). (b) Coordination environments around  $RE$  atoms, consisting of  $Ch$  and  $I$  atoms at distances up to 3.5 Å, and  $Tt$  atoms at distances up to 3.9 Å.

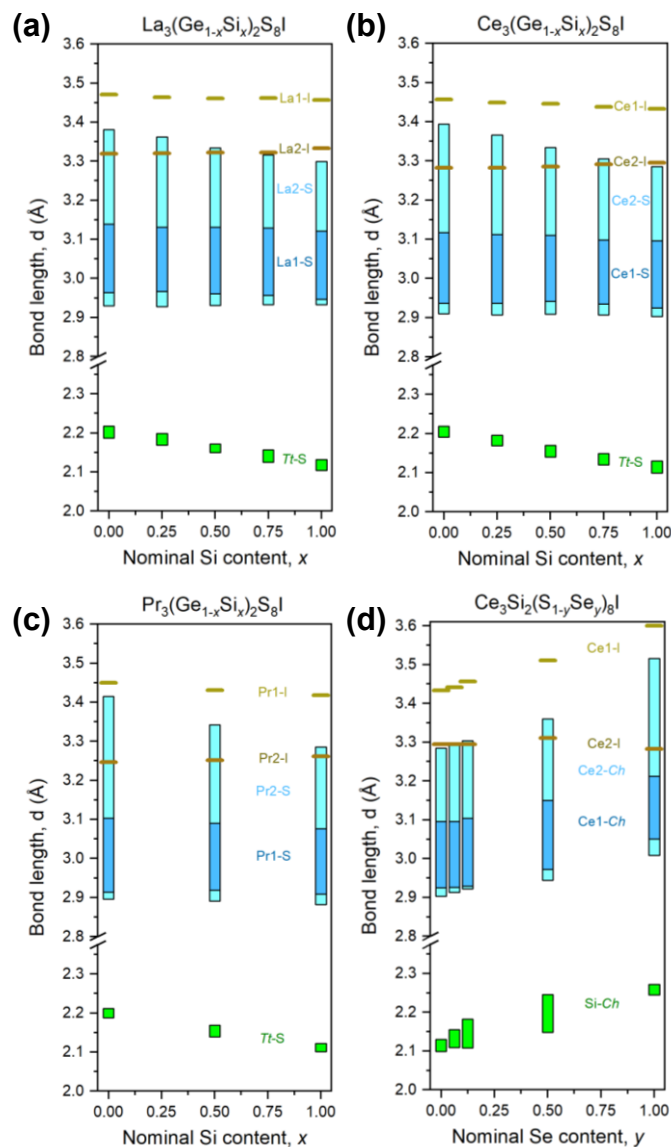


**Figure 3-3.** Bond length ranges within the solid solutions  $RE_3(Ge_{1-x}Si_x)_2S_8I$  ( $RE = La, Ce, Pr$ ) and  $Ce_3Si_2(S_{1-y}Se_y)_8I$ . Data for the end-members of  $RE_3(Ge_{1-x}Si_x)_2S_8I$  were taken from previous reports.

All of the  $RE_3(Ge_{1-x}Si_x)_2S_8I$  and  $Ce_3Si_2(S_{1-y}Se_y)_8I$  samples were stable and suffered no degradation upon exposure to ambient conditions. For example, the powder XRD patterns of samples of  $RE_3Ge_2S_8I$ , which were stored with no special precautions, remained unchanged after four years. The thermal stability of one compound,  $Ce_3Si_{1.5}Ge_{0.5}S_8I$ , was tested by a TGA experiment (**Figure A1-6**). A small weight loss (4.5%) occurs during heating from room temperature to 200 °C, and then

significant weight loss takes place at 750 °C, presumably upon formation of volatile sulfur- and iodine-containing species, as the sample decomposes rapidly. (*Caution: The platinum crucible serving as the sample holder becomes embrittled after this experiment, resulting in temporary banishment from the analysis facility.*)

### 3.3.2. Optical Band Gaps

The optical diffuse reflectance spectra, which were converted through the Kubelka-Munk function to absorption spectra and normalized (**Figure 3-4**). These spectra show strong absorption edges, from which optical band gaps were determined (representative examples of fittings are shown for  $\text{La}_3(\text{Ge}_{1-x}\text{Si}_x)_2\text{S}_8\text{I}$  in **Figure A1-7**) and plotted (**Table A1-6 and Figure 3-5**). The spectra are similar for  $\text{La}_3(\text{Ge}_{1-x}\text{Si}_x)_2\text{S}_8\text{I}$  and  $\text{Pr}_3(\text{Ge}_{1-x}\text{Si}_x)_2\text{S}_8\text{I}$ , except that localized f-f transitions from the unpaired electrons of rare-earth ions give rise to sharp peaks in the latter, appearing at energies lower than the absorption arising from the band gap transition (valence to conduction bands). For these two series, the band gaps shift to higher energy upon greater substitution of Ge by Si, from 3.0 to 3.6 eV for the La-containing series, or from 3.0 to 3.4 eV for the Pr-containing series. The shift progresses fairly smoothly over most of the range but is more marked over the last increment, from  $\text{RE}_3\text{Ge}_{0.2}\text{Si}_{1.8}\text{S}_8\text{I}$  to  $\text{RE}_3\text{Si}_2\text{S}_8\text{I}$ .

The spectra for the Ce-containing series  $\text{Ce}_3(\text{Ge}_{1-x}\text{Si}_x)_2\text{S}_8\text{I}$  and  $\text{Ce}_3\text{Si}_2(\text{S}_{1-y}\text{Se}_y)_8\text{I}$  show absorption edges that are assigned to transitions from localized mid-gap cerium 4f states to the bottom of the conduction band, which has contributions from cerium 5d states. Although the spectra are not identical within  $\text{Ce}_3(\text{Ge}_{1-x}\text{Si}_x)_2\text{S}_8\text{I}$ , the energy shifts are quite small and lie in a range of 2.7–2.8 eV.<sup>11,</sup>

<sup>20</sup> The profile of the absorption edge also becomes less sharp for  $\text{Ce}_3\text{Si}_2\text{S}_8\text{I}$ ; this smearing is typically attributed to additional defect states found below the conduction band. For  $\text{Ce}_3\text{Si}_2(\text{S}_{1-y}\text{Se}_y)_8\text{I}$ ,

substitution of Se for S causes the energy gap to decrease gradually from 2.8 eV (at  $y = 0$ ) to 1.9 eV (at  $y = 1.0$ ). Most of the general trends in band gap energy are understandable in terms of changes to the bonding character upon substitution. Greater covalent character would be imparted by the presence of Ge instead of Si atoms, or by Se instead of S atoms, leading to smaller gaps for compounds containing more of these substituents.

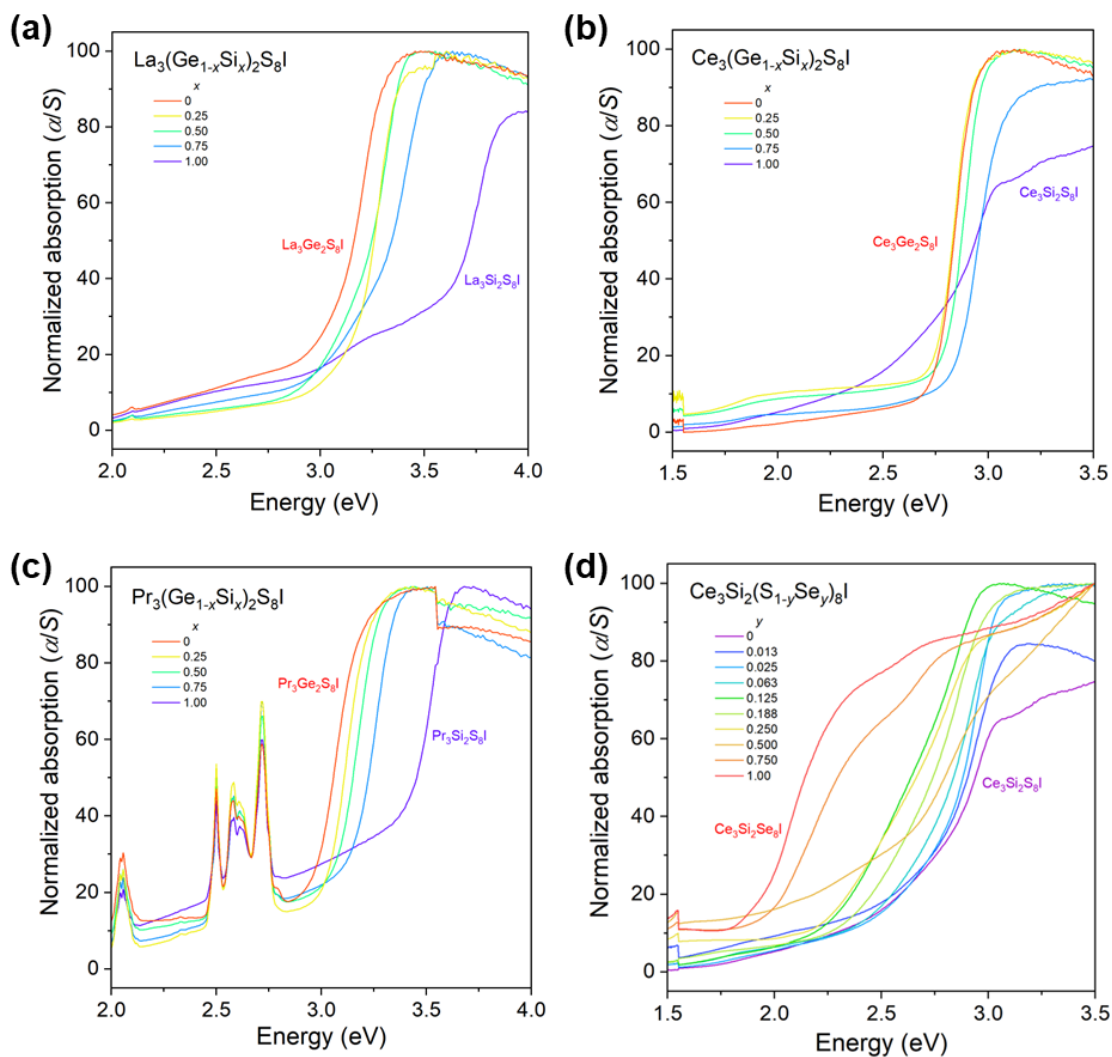


**Figure 3-4.** Normalized diffuse reflectance spectra for selected members of solid solutions  $RE_3(\text{Ge}_{1-x}\text{Si}_x)_2\text{S}_8\text{I}$  ( $RE = \text{La}, \text{Ce}, \text{Pr}$ ) and  $\text{Ce}_3\text{Si}_2(\text{S}_{1-y}\text{Se}_y)_8\text{I}$ .

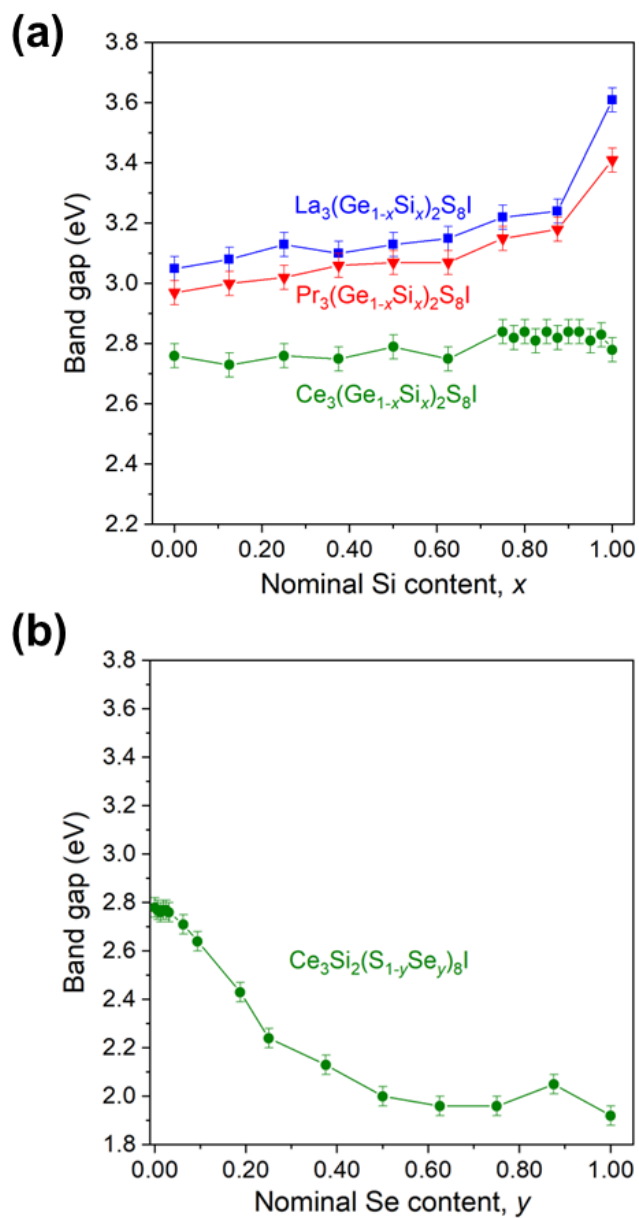


**Figure 3-5.** Optical band gaps for (a)  $RE_3(\text{Ge}_{1-x}\text{Si}_x)_2\text{S}_8\text{I}$  ( $RE = \text{La}, \text{Ce}, \text{Pr}$ ) and (b)  $\text{Ce}_3\text{Si}_2(\text{S}_{1-y}\text{Se}_y)_8\text{I}$ .

### 3.3.3. Electronic Structure

To gain further insight on the experimental results above, DFT calculations were performed on models of  $\text{Ce}_3(\text{Ge}_{1-x}\text{Si}_x)_2\text{S}_8\text{I}$  ( $x = 0-1$ ) and  $\text{Ce}_3\text{Si}_2(\text{S}_{1-y}\text{Se}_y)_8\text{I}$  ( $y = 0-0.25$ ). The band dispersion diagrams show the presence of a direct band gap, with valence band maxima and conduction band

minima at the Brillouin zone centre ( $\Gamma$ ), for  $\text{Ce}_3(\text{Ge}_{1-x}\text{Si}_x)_2\text{S}_8\text{I}$  (**Figure 3-6(a)**). The extrema do not quite coincide at the  $\Gamma$ -point, but the band gap remains essentially direct for  $\text{Ce}_3\text{Si}_2(\text{S}_{1-y}\text{Se}_y)_8\text{I}$  (**Figure 3-6(b)**). Although the cerium f-electrons are frozen as core states in these calculations, the general trends in the calculated band gaps can be related to the shift in absorption edges, caused by cerium 4f-to-5d transitions, in the experimental optical spectra. The calculated band gap increases from 2.05 to 2.61 eV on progressing from  $\text{Ce}_3\text{Ge}_2\text{S}_8\text{I}$  to  $\text{Ce}_3\text{Si}_2\text{S}_8\text{I}$ , and it decreases from 2.61 to 2.38 eV on progressing from  $\text{Ce}_3\text{Si}_2\text{S}_8\text{I}$  to  $\text{Ce}_3\text{Si}_2\text{S}_6\text{Se}_2\text{I}$ . Although the magnitudes of band gaps calculated from DFT are recognized to be inaccurate without appropriate corrections applied, the trends are in good agreement with the shift in the observed optical absorption edges.

The contributions to bonding were evaluated from the DOS, COHP, and COBI curves (**Figure A1-8** and **Figure A1-9**). The valence band is dominated by the nonmetal states, with contributions from iodine highest near the top, and results from mixing with the metal states to form metal-nonmetal (Ce–Ch, Ce–I, Tt–Ch) bonding interactions. The conduction band is dominated by the metal states, particularly cerium d-states near the bottom, and is characterized by cerium-chalcogen and tetrel-chalcogen antibonding interactions. The integrated values of COBI serve as a means to quantify the degree of covalent vs. ionic character in bonds (**Table A1-7**). In agreement with expectations, the bonds to cerium atoms are more ionic (ICOBI in units of eV/bond of 0.11–0.43 for Ce–S, 0.27–0.51 for Ce–Se, 0.16–0.57 for Ce–I) whereas the bonds to tetrel atoms are highly covalent (ICOBI of 0.85–0.93 for Ge–S, 0.86–0.97 for Si–S, 0.84–0.93 for Si–Se). The ELF plots emphasize this distinction in bonding character, in which the localized electron density around the cerium atoms can be contrasted with the shared electron density between the tetrel and chalcogen atoms (**Figure A1-10**). The Bader charges also tend to be less extreme around Ge (0.24+ to 0.75+) compared to Si atoms

(0.36+ to 1.09+), and around Se (0.43– to 0.72–) compared to S atoms (0.57– to 1.03–), corroborating expectations noted above for the relative covalent character of bonds to these atoms.

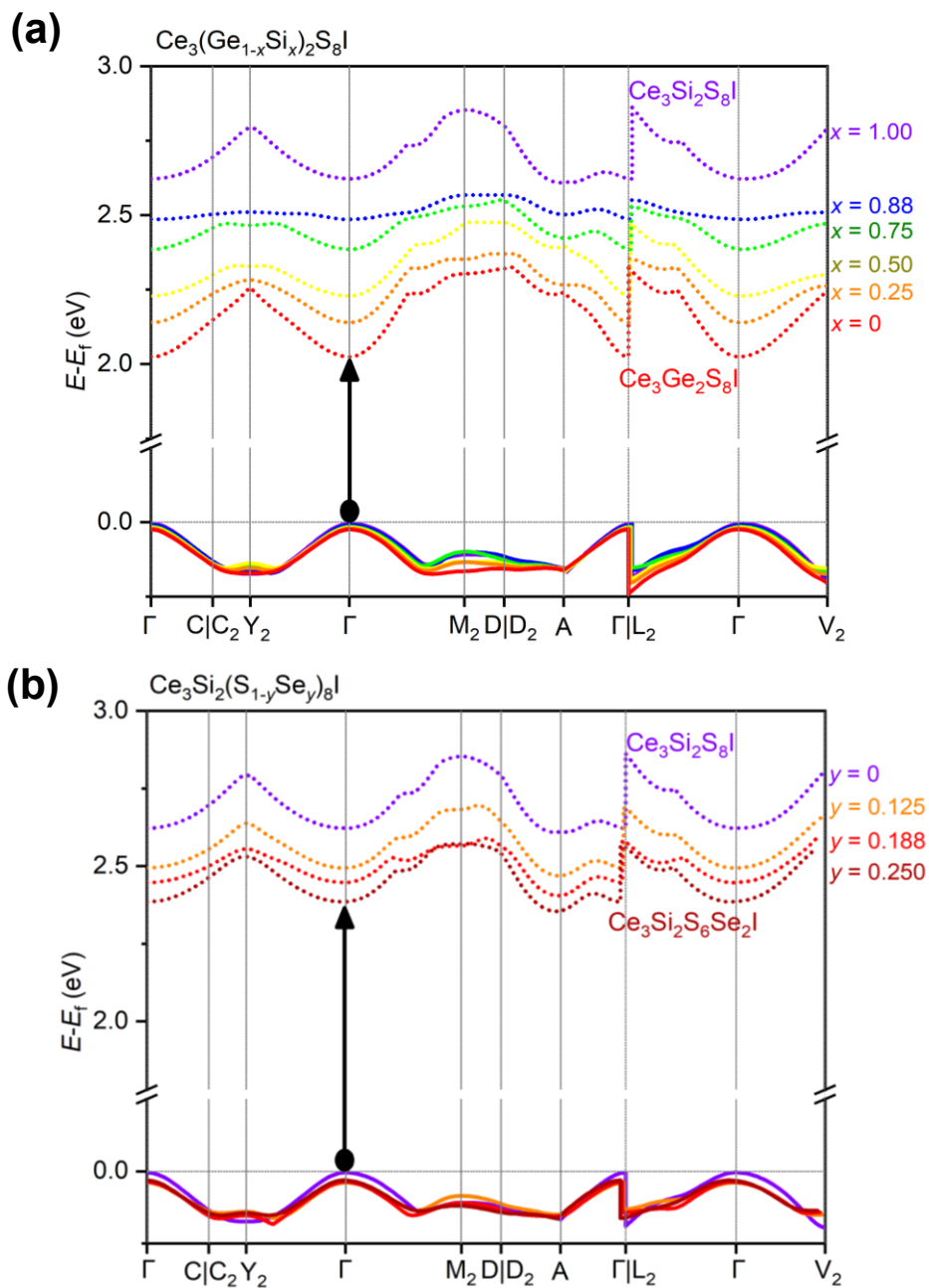


**Figure 3-6.** Band dispersion for (a)  $\text{Ce}_3(\text{Ge}_{1-x}\text{Si}_x)_2\text{S}_8\text{I}$  and (b)  $\text{Ce}_3\text{Si}_2(\text{S}_{1-y}\text{Se}_y)_8\text{I}$ .

### 3.3.4. Photoluminescence

Initial excitation and emission spectra were collected for some of the Si-rich members of  $\text{Ce}_3(\text{Ge}_{1-x}\text{Si}_x)_2\text{S}_8\text{I}$  (**Figure A1-11**). All subsequent spectra were collected using an ultraviolet Ar-ion laser source with excitation at 365+352 nm (combined UV lines), for various members of  $\text{Ce}_3(\text{Ge}_{1-x}\text{Si}_x)_2\text{S}_8\text{I}$  and  $\text{Ce}_3\text{Si}_2(\text{S}_{1-y}\text{Se}_y)_8\text{I}$  (**Figure 3-7**). The parent compound  $\text{Ce}_3\text{Si}_2\text{S}_8\text{I}$  shows strong luminescence in the blue region, assigned to the parity-allowed electronic transition from the 5d to 4f orbitals of the cerium atoms. In accordance with a similar treatment for  $(\text{La}_{0.90}\text{Ce}_{0.10})_3\text{Si}_2\text{S}_8\text{Br}$ ,<sup>16</sup> the spectrum can be fitted to four Gaussian components, arising from spin-orbit coupling ( $^2F_{5/2}$  and  $^2F_{7/2}$ ) of the  $4f^1$  ground state for the two Ce sites (at 8f and 4e), which experience different environments; the splitting of 0.26 eV is typical of spin-orbit coupling interactions for  $\text{Ce}^{3+}$  ions (**Figure A1-12**).

Because the 5d orbitals are not well shielded, the expectation is that the emission spectra may be significantly influenced by the changes in the local environment around the Ce atoms. For  $\text{Ce}_3(\text{Ge}_{1-x}\text{Si}_x)_2\text{S}_8\text{I}$ , the photoluminescence intensity is rapidly quenched with greater concentration of Ge (**Figure 3-7(a)**). As indicated in the normalized spectra, the two peaks do not shift significantly in wavelength, but the component at shorter wavelength (near 450 nm) decreases in intensity relatively faster than the one at longer wavelength (near 490 nm). For  $\text{Ce}_3\text{Si}_2(\text{S}_{1-y}\text{Se}_y)_8\text{I}$  (**Figure 3-7(b)**), the photoluminescence intensity quenches with greater concentration of Se, but the peaks shift to longer wavelength, the spectral maximum increasing from 462 nm in  $\text{Ce}_3\text{Si}_2\text{S}_8\text{I}$  to 504 nm in  $\text{Ce}_3\text{Si}_2\text{S}_{6.5}\text{Se}_{1.5}\text{I}$ . This wavelength shift is consistent with the trend in the optical absorption edges found earlier in the diffuse reflectance spectra, in which the substitution of S by Se leads to a lowering of the 5d levels in the conduction band and a narrower energy gap. At a maximum concentration of 25% Ge (corresponding to  $\text{Ce}_3\text{Ge}_{0.5}\text{Si}_{1.5}\text{S}_8\text{I}$ ) or 19% Se (corresponding to  $\text{Ce}_3\text{Si}_2\text{S}_{6.5}\text{Se}_{1.5}\text{I}$ ), the photoluminescence intensity is less than 1% that of the parent compound  $\text{Ce}_3\text{Si}_2\text{S}_8\text{I}$ .

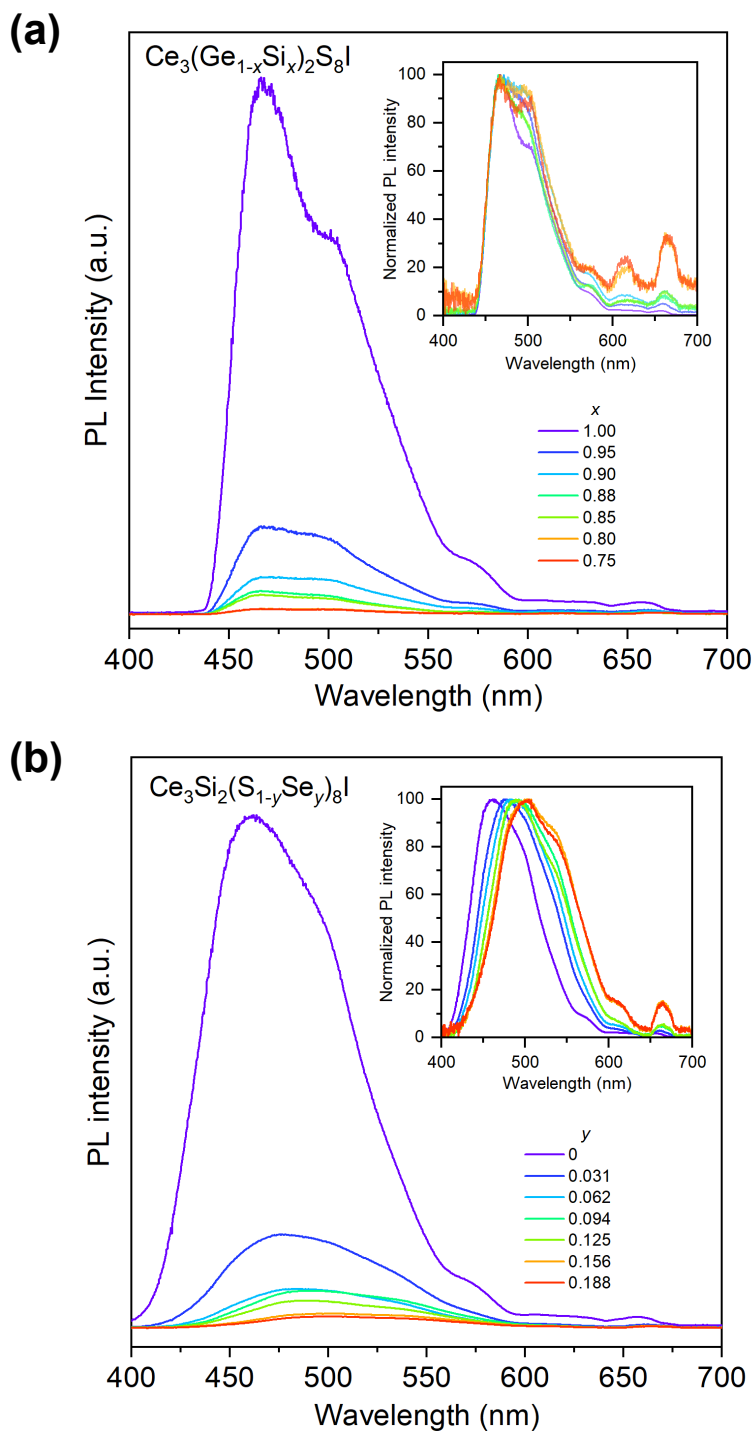


**Figure 3-7.** Photoluminescence emission spectra for [ $\lambda_{\text{ex}} = 365+352$  nm (combined UV lines)] (a)  $\text{Ce}_3(\text{Ge}_{1-x}\text{Si}_x)_2\text{S}_8\text{I}$  (with filters applied to sharpen the peaks) and (b)  $\text{Ce}_3\text{Si}_2(\text{S}_{1-y}\text{Se}_y)_8\text{I}$ . Normalized spectra are shown in the insets.

The colour changes were quantified by extracting the chromaticity coordinates from the photoluminescence emission spectra. These coordinates were mapped onto the CIE 1931 colour space (**Table A1-8 and Figure 3-8**). For  $\text{Ce}_3(\text{Ge}_{1-x}\text{Si}_x)_2\text{S}_8\text{I}$ , the shifts in the colour coordinates are small, with the Ge-richer members appearing slightly blue-green, compared to the blue colour of  $\text{Ce}_3\text{Si}_2\text{S}_8\text{I}$ , because the intensity of the emission peak component at shorter wavelength (near 450 nm) decreases faster relatively one at longer wavelength (near 489 nm). For  $\text{Ce}_3\text{Si}_2(\text{S}_{1-y}\text{Se}_y)_8\text{I}$ , there is a definite shift from blue to green with greater Se concentrations, clearly perceptible in the photographs of samples exposed to ultraviolet light. The samples do not degrade after repeated excitation (with an irradiation time around 2 min); for example, the powder XRD patterns for  $\text{Ce}_3\text{Si}_2\text{S}_8\text{I}$  appear identical before and after the laser photoluminescence experiments (**Figure A1-13**).

Time-resolved photoluminescence (TRPL) experiments were performed for various members of  $\text{Ce}_3(\text{Ge}_{1-x}\text{Si}_x)_2\text{S}_8\text{I}$  and  $\text{Ce}_3\text{Si}_2(\text{S}_{1-y}\text{Se}_y)_8\text{I}$ . The decay lifetimes could not be adequately fit by a single or double exponential function, as expected on the basis of the curvature of the photoluminescence decay data on a semilog plot; instead, the curves were modeled with reasonably good results by fitting them to a lifetime distribution function (**Figure 3-9 and Table A1-9**).<sup>40</sup> The observation that the photoluminescence decay functions appear to follow a distribution suggests that there are a range of emissive centres, consistent with the presence of two *RE* sites and the slightly different environments they experience due to the disorder of S and Se atoms immediately surrounding them or of Ge and Si atoms further away. The mean lifetime is longest for  $\text{Ce}_3\text{Si}_2\text{S}_8\text{I}$  (6.99 ns), and it becomes monotonically shorter as Si is substituted by Ge (1.81 ns for  $\text{Ce}_3\text{Ge}_{0.50}\text{Si}_{1.50}\text{S}_8\text{I}$ ) or as S is substituted by Se (3.77 ns for  $\text{Ce}_3\text{Si}_2\text{S}_{6.50}\text{Se}_{1.50}\text{I}$ ).

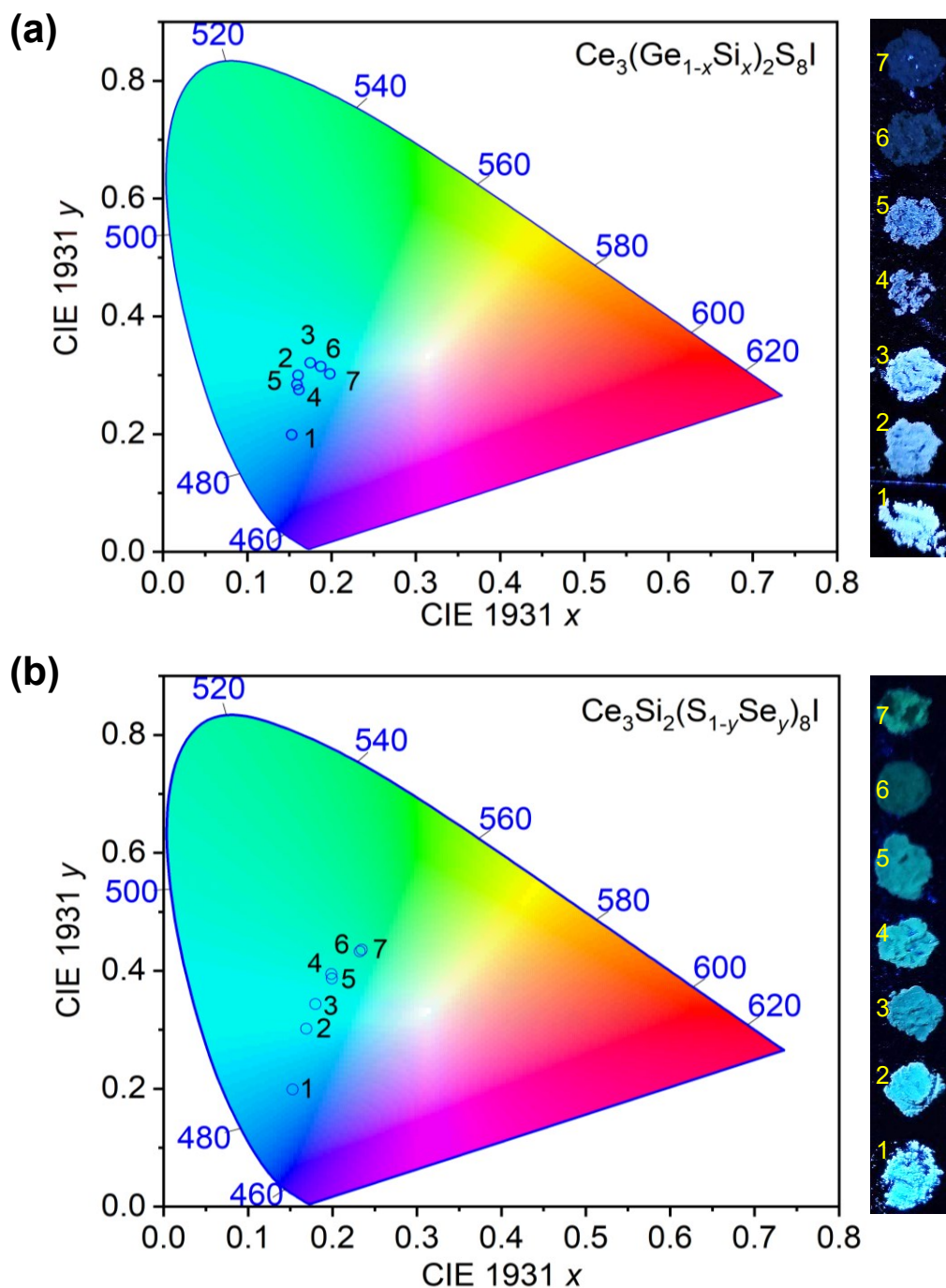


**Figure 3-8.** CIE 1931 colour coordinates for various members of (a)  $Ce_3(Ge_{1-x}Si_x)_2S_8I$  and (b)  $Ce_3Si_2(S_{1-y}Se_y)_8I$ . The samples were exposed to ultraviolet light with wavelength of 365 nm. The brightness was adjusted to 40% and the contrast to -20% to improve visibility in the photos.

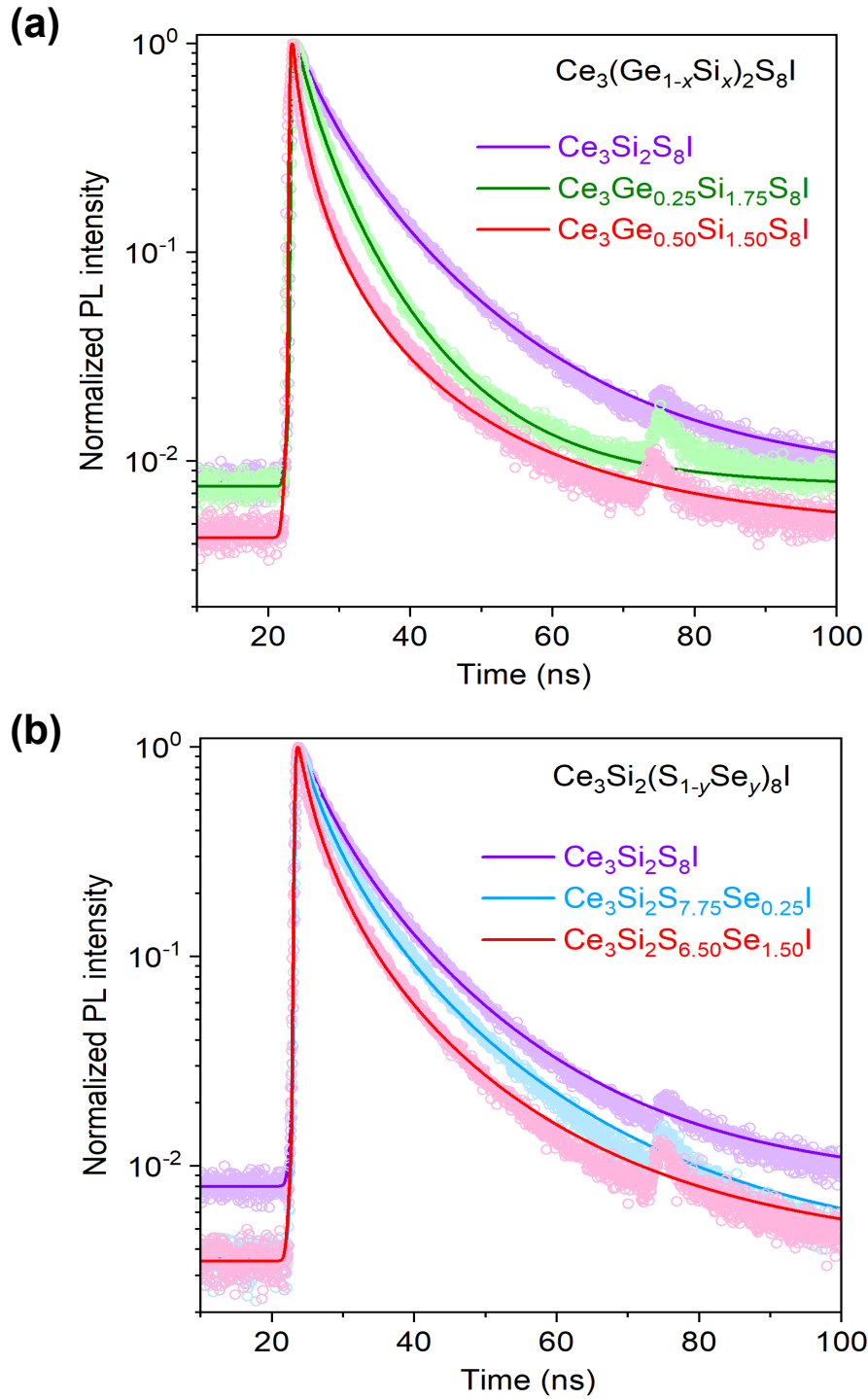


**Figure 3-9.** Photoluminescence decay curve ( $\lambda_{\text{ex}} = 405 \text{ nm}$ ) for (a)  $\text{Ce}_3(\text{Ge}_{1-x}\text{Si}_x)_2\text{S}_8\text{I}$  and (b)  $\text{Ce}_3\text{Si}_2(\text{S}_{1-y}\text{Se}_y)_8\text{I}$ . The small bump near 75 ns is a reflection in the 5-meter long optical fibers.

Next, to assess the thermal quenching properties, which are important for applications in white light emitting diodes, the temperature dependence of the photoluminescence emission for  $\text{Ce}_3\text{Si}_2\text{S}_8\text{I}$  was examined. As the temperature increases from 30 to 200 °C, the emission becomes less intense. Vibrational levels within both ground and excited electronic states become increasingly populated, so that non-radiative relaxation processes become more probable (**Figure 3-10(a)**). The relative integrated intensity of the emission peaks is assumed to follow the relationship  $I(T) = I_0/[1 + c \exp(-E_a/kT)]$ , where  $I_0$  is the initial room-temperature intensity,  $E_a$  is an activation energy for thermal quenching and  $k$  is Boltzmann's constant.<sup>41</sup> Fitting the data to this relationship gives an activation energy  $E_a = 0.68$  eV for  $\text{Ce}_3\text{Si}_2\text{S}_8\text{I}$  (**Figure 3-10(b)**). This value is higher than  $(\text{La}_{0.90}\text{Ce}_{0.10})_3(\text{SiS}_4)_2\text{Br}$  ( $E_a = 0.29$  eV).<sup>16</sup> The thermal quenching temperature, at which the emission intensity has been reduced to half that at room temperature, is  $T_{1/2} = 85$  °C. At typical working temperature in LEDs (420 K), the emission intensity remains ~ 20 % of that measured at room temperature, which suggests that the phosphor does not have good thermal-quenching properties. Preliminary experiments indicate that the photoluminescent quantum yield is 3% for  $\text{Ce}_3\text{Si}_2\text{S}_8\text{I}$ , suggesting significant migration to defect traps.

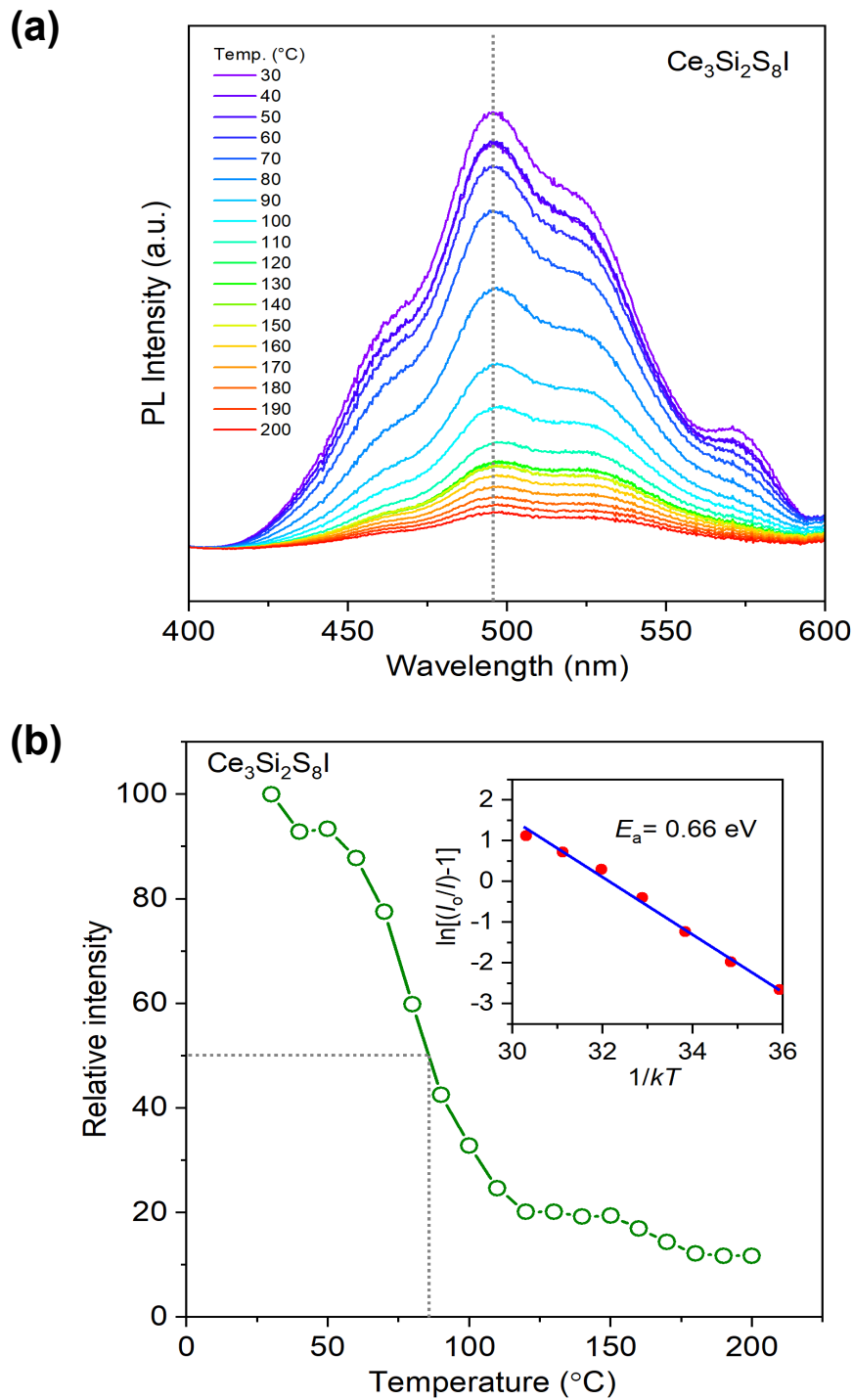


**Figure 3-10.** (a) Temperature-dependent photoluminescence emission spectra ( $\lambda_{\text{ex}} = 365 \text{ nm}$ ) for  $\text{Ce}_3\text{Si}_2\text{S}_8\text{I}$ . (b) Plot of relative integrated intensity of emission peaks. The inset shows an Arrhenius fitting to extract the activation energy.

Several hypotheses may be considered for the quenching of photoluminescence at higher concentrations of Ge or Se, relative to  $\text{Ce}_3\text{Si}_2\text{S}_8\text{I}$ . The electronic structure calculations presented earlier indicate that the band gap remains essentially direct for all members of  $\text{Ce}_3(\text{Ge}_{1-x}\text{Si}_x)_2\text{S}_8\text{I}$  and  $\text{Ce}_3\text{Si}_2(\text{S}_{1-y}\text{Se}_y)_8\text{I}$ , so a change in the nature of the band gap can be largely ruled out. Because the cerium atoms are the only possible activator centres, a change in their oxidation states could potentially promote quenching. High-resolution cerium XPS spectra collected for several members of  $\text{Ce}_3(\text{Ge}_{1-x}\text{Si}_x)_2\text{S}_8\text{I}$  and  $\text{Ce}_3\text{Si}_2(\text{S}_{1-y}\text{Se}_y)_8\text{I}$  reveal the presence of  $\text{Ce}^{3+}$ , in accordance with expectations, but also a not-insignificant amount of  $\text{Ce}^{4+}$  (**Table A1-10 and Figure A1-14**). Quantification of the component peaks, fit to Gaussian profiles, leads to a ratio of 75:25 of  $\text{Ce}^{3+}:\text{Ce}^{4+}$ . Given that the presence of  $\text{Ce}^{4+}$  species is highly improbable in a sulfide, we suggest that they may have formed from oxidation or decomposition processes over time. The more important observation is that the XPS spectra are identical for different members of  $\text{Ce}_3(\text{Ge}_{1-x}\text{Si}_x)_2\text{S}_8\text{I}$  (**Figure 3-11**), indicating no change in cerium oxidation states. Thus, the most likely origin for quenching in these compounds is site disorder, which would lead to more disparate coordination environments around the cerium atoms in their excited states. Inspection of the bond distances obtained from the structure determinations (**Figure 3-3**) shows that Ge substitution does lead to wider ranges of Ce–S distances, whereas Se substitution necessarily leads to a mixture of Ce–S and Ce–Se bonds around the cerium atoms.

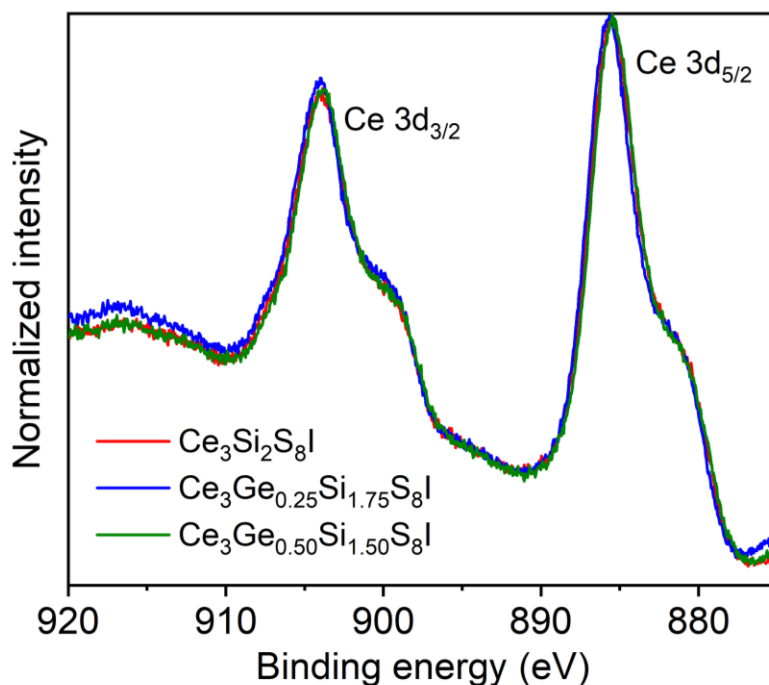


**Figure 3-11.** High-resolution cerium XPS spectra for various members of  $Ce_3(Ge_{1-x}Si_x)_2S_8I$ .

### 3.4. Conclusions

The successful preparation of complete solid solutions  $RE_3(Ge_{1-x}Si_x)_2S_8I$  ( $RE = La, Ce, Pr$ ) and  $Ce_3Si_2(S_{1-y}Se_y)_8I$  led to several observations about the effects of composition on the structures and properties, especially pertaining to the potential emissive centres in these compounds. Substituting Si for Ge atoms in  $RE_3(Ge_{1-x}Si_x)_2S_8I$  leads to less distorted coordination environments around one of the two  $RE$  sites, with a narrower range of distances to the surrounding chalcogen atoms. Substituting a small amount of Se for S atoms in  $Ce_3Si_2(S_{1-y}Se_y)_8I$  leads surprisingly to only a partially disordered environment around the  $RE$  centres, with one of the four  $Ch$  sites being preferentially occupied; at higher levels of substitution, the Se atoms tend to occupy the more distant sites to the Si atoms first. The optical band gaps evolve smoothly, generally increasing upon substitution of Si for Ge in  $RE_3(Ge_{1-x}Si_x)_2S_8I$  and decreasing upon substitution of Se for S in

$\text{Ce}_3\text{Si}_2(\text{S}_{1-y}\text{Se}_y)_8\text{I}$ . The Ce-containing compounds  $\text{Ce}_3(\text{Ge}_{1-x}\text{Si}_x)_2\text{S}_8\text{I}$  and  $\text{Ce}_3\text{Si}_2(\text{S}_{1-y}\text{Se}_y)_8\text{I}$  act as phosphors, excitable over the range of 280 to 400 nm. The colours emitted by  $\text{Ce}_3(\text{Ge}_{1-x}\text{Si}_x)_2\text{S}_8\text{I}$  are relatively insensitive to Ge substitution, shifting slightly from blue to blue-green, but quenching occurs rapidly with small amounts of Ge. In contrast, the emission wavelengths are highly tunable in  $\text{Ce}_3\text{Si}_2(\text{S}_{1-y}\text{Se}_y)_8\text{I}$ , shifting from blue to green by substituting with small amounts of Se. This tunability may be useful for phosphor-converted white LED applications where there is a need for phosphors in the cyan-to-green region. Given that mixing of S and Se atoms has been demonstrated to be feasible in these compounds, the next steps would entail investigation of the La-containing series  $\text{La}_3\text{Si}_2(\text{S}_{1-y}\text{Se}_y)_8\text{I}$  as host materials, with doped  $\text{Ce}^{3+}$  and  $\text{Eu}^{2+}$  ions acting as activator centres.

### 3.4.1. References

- (1) Kageyama, H.; Hayashi, K.; Maeda, K.; Attfield, J. P.; Hiroi, Z.; Rondinelli, J. M.; Poeppelmeier, K. R. *Nat. Commun.* **2018**, *9*, 772-1–772-15.
- (2) Harada, J. K.; Charles, N.; Poeppelmeier, K. R.; Rondinelli, J. M. *Adv. Mater.* **2019**, *31*, 1805295.
- (3) Kageyama, H.; Yajima, T.; Tsujimoto, Y.; Yamamoto, T.; Tassel, C.; Kobayashi, Y. *Bull. Chem. Soc. Jpn.* **2019**, *92*, 1349–1357.
- (4) Li, Y.-Y.; Wang, W.-J.; Wang, H.; Lin, H.; Wu, L.-M. *Cryst. Growth Des.* **2019**, *19*, 4172–4192.
- (5) Tripathi, T. S.; Karppinen, M. *Adv. Mater. Interfaces* **2021**, *8*, 2100146.
- (6) Maeda, K.; Takeiri, F.; Kobayashi, G.; Matsuishi, S.; Ogino, H.; Ida, S.; Mori, T.; Uchimoto, Y.; Tanabe, S.; Hasegawa, T.; Imanaka, N.; Kageyama, H. *Bull. Chem. Soc. Jpn.* **2022**, *95*, 26–37.
- (7) Ghorpade, U. V.; Suryawanshi, M. P.; Green, M. A.; Wu, T.; Hao, X.; Ryan, K. M. *Chem. Rev.* **2023**, *123*, 327–378.
- (8) Xiao, J.-R.; Yang, S.-H.; Feng, F.; Xue, H.-G.; Guo, S.-P. *Coord. Chem. Rev.* **2017**, *347*, 23–47.
- (9) Gauthier, G.; Kawasaki, S.; Jobic, S.; Macaudière, P.; Brec, R.; Rouxel, J. *J. Mater. Chem.* **1998**, *8*, 179–186.
- (10) Gauthier, G.; Kawasaki, S.; Jobic, S.; Macaudière, P.; Brec, R.; Rouxel, J. *J. Alloys Compd.* **1998**, *275–277*, 46–49.
- (11) Riccardi, R.; Gout, D.; Gauthier, G.; Guillen, F.; Jobic, S.; Garcia, A.; Huguenin, D.; Macaudière, P.; Fouassier, C.; Brec, R. *J. Solid State Chem.* **1999**, *147*, 259–268.

- (12) Hatscher, S. T.; Umland, W. *Z. Anorg. Allg. Chem.* **2001**, *627*, 2198–2200.
- (13) Hatscher, S. T.; Umland, W. *Mater. Res. Bull.* **2002**, *37*, 1239–1247.
- (14) Hatscher, S. T.; Umland, W. *Z. Anorg. Allg. Chem.* **2002**, *628*, 608–611.
- (15) Hatscher, S. T.; Umland, W. *Acta Crystallogr., Sect. E* **2002**, *58*, i100–i102.
- (16) Lee, S.-P.; Liu, S.-D.; Chan, T.-S.; Chen, T.-M. *Appl. Mater. Interfaces* **2016**, *8*, 9218–9223.
- (17) Ye, S.; Xiao, F.; Pan, Y. X.; Ma, Y. Y.; Zhang, Q. Y. *Mater. Sci. Eng. R* **2010**, *71*, 1–34.
- (18) Smet, P. F.; Moreels, I.; Hens, Z.; Poelman, D. *Materials* **2010**, *3*, 2834–2883.
- (19) Qin, X.; Liu, X.; Huang, W.; Bettinelli, M.; Liu, X. *Chem. Rev.* **2017**, *117*, 4488–4527.
- (20) Mumbaraddi, D.; Iyer, A. K.; Üzer, E.; Mishra, V.; Oliynyk, A. O.; Nilges, T.; Mar, A. *J. Solid State Chem.* **2019**, *274*, 162–167.
- (21) Coelho, A. A. *TOPAS-Academic, version 6*; Coelho Software: Brisbane, Australia, 2007.
- (22) Sheldrick, G. M. *Acta Crystallogr., Sect. A* **2008**, *64*, 112–122.
- (23) Gravereau, P.; Es-Sakhi, B.; Fouassier, C. *Acta Crystallogr., Sect. C* **1988**, *44*, 1884–1887.
- (24) Gelato, L. M.; Parthé, E. *J. Appl. Crystallogr.* **1987**, *20*, 139–143.
- (25) Spek, A. L. *Acta Crystallogr., Sect. D* **2009**, *65*, 148–155.
- (26) Kortüm, G. *Reflectance Spectroscopy*; Springer: New York, 1969; pp 103–169.
- (27) Fairley, N.; Fernandez, V.; Richard-Plouet, M.; Guillot-Deudon, C.; Walton, J.; Smith, E.; Flahaut, D.; Grenier, M.; Biesinger, M.; Tougaard, S.; Morgan, D.; Baltrusaitis, J. *Appl. Surf. Sci. Adv.* **2021**, *5*, 100112.
- (28) Okhotnikov, K.; Charpentier, T.; Cadars, S. *J. Cheminform.* **2016**, *8*, 17.
- (29) Hafner, J. *J. Comput. Chem.* **2008**, *29*, 2044–2078.
- (30) Perdew, J. P.; Burke, K.; Ernzerhof, M. *Phys. Rev. Lett.* **1996**, *77*, 3865–3868.

- (31) Grin, Y.; Savin, A.; Silvi, B. The ELF perspective of chemical bonding. In *The Chemical Bond: Fundamental Aspects of Chemical Bonding*; Frenking, G.; Shaik, S., Eds.; Wiley-VCH: Weinheim, 2014; pp 345–382.
- (32) Momma, K.; Izumi, F. *J. Appl. Crystallogr.* **2011**, *44*, 1272–1276.
- (33) Yu, M.; Trinkle, R. *J. Chem. Phys.* **2011**, *134*, 064111.
- (34) Deringer, V. L.; Tchougréeff, A. L.; Dronskowski, R. *J. Phys. Chem. A* **2011**, *115*, 5461–5466.
- (35) Müller, P. C.; Ertural, C.; Hempelmann, J.; Dronskowski, R. *J. Phys. Chem. C* **2021**, *125*, 7959–7970.
- (36) Maintz, S.; Deringer, V. L.; Tchougréeff, A. L.; Dronskowski, R. *J. Comput. Chem.* **2016**, *37*, 1030–1035.
- (37) Guo, G.-C.; Wang, Y.-G.; Zhuang, J.-N.; Chen, J.-T.; Huang, J.-S.; Zhang, Q. E. *Acta Crystallogr., Sect. C* **1995**, *51*, 2471–2473.
- (38) Sieke, C.; Hartenbach, I.; Schleid, T. *Z. Anorg. Allg. Chem.* **2000**, *626*, 2235–2239.
- (39) Shannon, R. D. *Acta Crystallogr., Sect. A* **1976**, *32*, 751–767.
- (40) Zhi, Y.; Feng, Z.; Mehreen, T.; Liu, X.; Gardner, K.; Li, X.; Guan, B.-O.; Zhang, L.; Vagin, S. I.; Rieger, B.; Meldrum, A. *Inorganics* **2022**, *10*, 101.
- (41) Hariyani, S.; Brgoch, J. *Chem. Mater.* **2020**, *32*, 6640–6649.

## Chapter 4.

### Minority report: Structure and bonding of $\text{YbNi}_3\text{Ga}_9$ and $\text{YbCu}_3\text{Ga}_8$ obtained in gallium flux

*A version of this chapter has been published. Mumbaraddi, D.; Mishra, V.; Lidin, S.; Mar, A. J. Solid State Chem. 2022, 311, 123157. Copyright (2022) by Elsevier.*

#### 4.1. Introduction

Intermetallic compounds containing rare-earth, transition-metal, and main-group metals  $RE-M-X$  comprise an enormous class of materials that often exhibit unusual physical properties resulting from the interplay of localized f and delocalized d electrons. Among these, Ce- and Yb-containing intermetallics are especially sought because they are prone to revealing complex electronic structures arising from the possibility of intermediate valence and different competing magnetic ground states. However, Yb-containing intermetallics are more difficult to prepare by conventional synthetic routes, such as arc-melting, because of the relatively high volatility of ytterbium metal. To contend with this problem, reactions in metal fluxes that are low melting (e.g., Al, Ga, In, Sn, Pb) may offer alternatives to preparing intermetallics that would otherwise be inaccessible by normal routes.<sup>1-3</sup> Flux methods have led to the discovery of numerous intermetallics, but the outcomes can seem to be frustratingly aleatory, depending on subtle changes in conditions (e.g., form of starting materials, heating and cooling profiles) and likely other unknown factors. Although efforts are now underway to probe the mechanisms of flux growth reactions by in situ measurements, these experiments require careful design to overcome many technical complications.<sup>4</sup> The appearance of beautiful crystals in the products of metal flux reactions can also be deceiving, as these often turn out to be known binary phases instead of the desired new ternary phases. In an early thought-provoking

proposal, Westerveld et al. developed a simple stability diagram based on empirical observations and hypothesized that ternary intermetallic phases are more likely to crystallize if the melting temperatures of the pure components are similar and if the atomic radii are disparate.<sup>5</sup>

As a test of this hypothesis, we wish to target the preparation of ternary gallides  $RE-M-Ga$  because the very low melting temperature of gallium (30 °C) provides an extreme scenario to probe the limits of the Westerveld stability diagram. As reported herein, many of these reactions failed to yield ternary gallides, illustrating that significant challenges remain. However, crystals of two Yb-containing gallides,  $YbNi_3Ga_9$  and  $YbCu_3Ga_8$ , were obtained and deserving of further attention. The first compound,  $YbNi_3Ga_9$ , has been previously reported to exhibit intermediate valence and undergo pressure-induced valence fluctuations.<sup>6–10</sup> It has been proposed to be a chiral magnetic material<sup>9</sup>, and on the basis of powder X-ray diffraction analysis, its crystal structure was assigned to be the  $ErNi_3Al_9$ -type,<sup>6</sup> which differs subtly from the  $DyNi_3Al_9$ -type (both in space group  $R32$ ) through the occurrence of additional partially occupied sites in the latter.<sup>11</sup> Contradicting this assignment, an unpublished report of the single-crystal structure of  $YbNi_3Ga_9$  appearing in a Ph.D. thesis argues for the  $DyNi_3Al_9$ -type structure.<sup>12</sup> To resolve this disagreement, it would be worthwhile to redetermine the structure of  $YbNi_3Ga_9$ . The second compound,  $YbCu_3Ga_8$ , is new and does not correspond to any existing ones in the Yb–Cu–Ga phase diagram.<sup>13</sup>

We report here investigations of flux growth of gallides  $Yb-M-Ga$ . Because related gallides are frequently susceptible to undergo structural transitions,<sup>14,15</sup> temperature-dependent single-crystal structure determinations of  $YbNi_3Ga_9$  and  $YbCu_3Ga_8$  were carried out. Given that rare-earth gallides are considered to be typical examples of polar intermetallics, in which a substantial electron transfer is assumed to take place, the electronic structures of these two compounds were also calculated and

a bonding analysis was applied using the recently developed concept of crystal orbital bond index (COBI) to test this assumption.<sup>16</sup>

## 4.2. Experimental

### 4.2.1. Synthesis

Starting materials were selected *RE* metals (La, Ce, and Yb pieces; 99.9%, Hefa), various transition metals *M* (Cr pieces, 99.99%, Alfa-Aesar; Mn powder, 99.6%, Alfa-Aesar; Fe powder, 99.9+%, Alfa-Aesar; Co powder, 99.8%, Cerac; Ni powder, 99.9%, Cerac; Cu powder, 99.5%, Alfa-Aesar; Ru sponge, 99.98%, Onyxmet), and Ga ingots (99.99%, Alfa-Aesar). The *RE* pieces were freshly filed before use. Reactions were performed following similar conditions as those reported for many related ternary gallides.<sup>14,17-19</sup> The elements were combined in fixed stoichiometric amounts of  $RE:M:Ga = 1:2:20$  (mole ratio), with a total mass of 1.6-1.8 g. They were loaded into thimble-shaped alumina crucibles, covered with quartz wool to serve as a filter, and placed in turn inside fused-silica tubes, which were evacuated and sealed. The tubes were placed in a furnace where they were heated to 1050 °C in 9 h, kept there for 10 h, cooled to 600 °C in 4 h, slowly cooled to 300 °C in 168 h, and then cooled to room temperature in 4 h. The tubes were reheated to 300 °C in 4 h and centrifuged to remove the majority of excess gallium flux. Initial attempts were made to remove residual gallium flux from the surfaces of single crystals by soaking them in a 3 M solution of I<sub>2</sub> in DMF, but visual inspection with an optical microscope indicated sluggish reaction. Instead, the single crystals were placed into vials to which 2 mL of 5% HCl was added, and they were sonicated for 15 min. The process was repeated until the surfaces were visually clean. The samples were then soaked overnight in HCl for 12 h, washed with distilled water and acetone, and dried in air.

Single crystals were examined on a JEOL JSM-6010LA InTouchScope scanning electron microscope operated with an accelerating voltage of 15 kV. Their compositions were determined by energy-dispersive X-ray (EDX) analyses, performed on several points on these single crystals, with acquisition times of 120 s each. Powder X-ray diffraction (XRD) patterns on ground samples were collected on a Bruker D8 Advance diffractometer equipped with a Cu  $K\alpha$  radiation source operated at 40 kV and 40 mA.

#### 4.2.2. Structure determination

Although crystals of YbNi<sub>3</sub>Ga<sub>9</sub> were plentiful, finding specimens that led to a reasonable structure determination proved to be challenging, as discussed later. Conversely, crystals of YbCu<sub>3</sub>Ga<sub>8</sub> were few, but they were of good quality and led to straightforward structure determination.

Intensity data were collected on suitable crystals of YbNi<sub>3</sub>Ga<sub>9</sub> and YbCu<sub>3</sub>Ga<sub>8</sub> at 100, 200, and 300 K on a Bruker D8 diffractometer equipped with a SMART APEX II CCD area detector and a graphite-monochromated Mo  $K\alpha$  radiation source, using  $\omega$  scans at various  $\phi$  angles with a frame width of 0.3° and an exposure time of 10 s per frame. Face-indexed numerical absorption corrections were applied. Structure solution and refinement were carried out with use of the SHELXTL (version 2018/3) program package.<sup>20</sup>

Structural models were proposed using direct methods in trigonal space group  $R\bar{3}2$  for YbNi<sub>3</sub>Ga<sub>9</sub> and in cubic space group  $Pm\bar{3}m$  for YbCu<sub>3</sub>Ga<sub>8</sub>. Disorder between Ni or Cu with Ga atoms was considered in the structure refinements, which included anisotropic displacement parameters. Atomic positions were standardized with the program STRUCTURE TIDY.<sup>21</sup> Full structural results are listed in **Table A2-1** to **Table A2-6** and the room-temperature results are listed in **Table 4-1** to **Table 4-3**.

**Table 4-1.** Crystallographic data for YbNi<sub>3</sub>Ga<sub>9</sub> and YbCu<sub>3</sub>Ga<sub>8</sub>.

formula	YbNi <sub>3</sub> Ga <sub>9</sub>	YbCu <sub>3</sub> Ga <sub>8</sub>
formula mass (amu)	976.65	921.42
space group	<i>R</i> 32 (No. 155)	<i>Pm</i> $\bar{3}$ <i>m</i> (No. 221)
<i>a</i> (Å)	7.2294(7)	8.2818(13)
<i>c</i> (Å)	27.513(3)	
<i>V</i> (Å <sup>3</sup> )	1245.3(3)	568.0(3)
<i>Z</i>	6	3
<i>T</i> (K)	298(2)	296(2)
$\rho_{\text{calcd}}$ (g cm <sup>-3</sup> )	7.814	8.081
crystal dimensions (mm)	0.09 × 0.08 × 0.05	0.11 × 0.08 × 0.08
$\mu$ (Mo <i>K</i> α) (mm <sup>-1</sup> )	46.36	48.29
transmission factors	0.049–0.205	0.065–0.132
2 $\theta$ limits	4.44–63.05°	4.92–63.41°
data collected	–6 ≤ <i>h</i> ≤ 10, –10 ≤ <i>k</i> ≤ 10, –25 ≤ <i>l</i> ≤ 40	–12 ≤ <i>h</i> ≤ 12, –12 ≤ <i>k</i> ≤ 12, –12 ≤ <i>l</i> ≤ 12
no. of data collected	3297	7600
no. of unique data, including $F_o^2 < 0$	938 ( $R_{\text{int}} = 0.045$ )	243 ( $R_{\text{int}} = 0.057$ )
no. of unique data, with $F_o^2 > 2\sigma(F_o^2)$	829	216
no. of variables	43	16
Flack parameter	0.14(6)	
$R(F)$ for $F_o^2 > 2\sigma(F_o^2)$ <sup>a</sup>	0.033	0.048
$R_w(F_o^2)$ <sup>b</sup>	0.070	0.127
goodness of fit	1.02	1.13
( $\Delta\rho$ ) <sub>max</sub> , ( $\Delta\rho$ ) <sub>min</sub> (e Å <sup>-3</sup> )	2.12, –2.13	3.49, –5.08

<sup>a</sup>  $R(F) = \sum ||F_o| - |F_c|| / \sum |F_o|$ . <sup>b</sup>  $R_w(F_o^2) = [\sum [w(F_o^2 - F_c^2)^2] / \sum wF_o^4]^{1/2}$ ;  $w^{-1} = [\sigma^2(F_o^2) + (Ap)^2 + Bp]$ , where  $p = [\max(F_o^2, 0) + 2F_c^2] / 3$ .

**Table 4-2.** Atomic coordinates and equivalent isotropic displacement parameters for YbNi<sub>3</sub>Ga<sub>9</sub> and YbCu<sub>3</sub>Ga<sub>8</sub>.

Atom	Wyckoff position	<i>x</i>	<i>y</i>	<i>z</i>	<i>U</i> <sub>eq</sub> (Å <sup>2</sup> ) <sup>a</sup>
YbNi <sub>3</sub> Ga <sub>9</sub>					
Yb	6 <i>c</i>	0	0	0.16692(2)	0.0088(2)
Ni	18 <i>f</i>	0.3335(3)	0.3273(3)	0.08475(6)	0.0083(3)
Ga1	9 <i>e</i>	0.0032(2)	0.3365(2)	0.10070(7)	0.0101(3)
Ga2	9 <i>d</i>	0.7901(2)	0	½	0.0094(4)
Ga3	6 <i>c</i>	0	0	0.05094(7)	0.0102(4)
Ga4	6 <i>c</i>	0	0	0.28317(8)	0.0100(4)
Ga5	6 <i>c</i>	0	0	0.38508(8)	0.0112(4)
YbCu <sub>3</sub> Ga <sub>8</sub> <sup>b</sup>					
Yb	3 <i>c</i>	0	½	½	0.0158(5)
X1	12 <i>j</i>	½	0.1531(2)	0.1531(2)	0.0169(5)
X2	12 <i>i</i>	0	0.2318(2)	0.2318(2)	0.0194(5)
X3	8 <i>g</i>	0.3391(3)	0.3391(3)	0.3391(3)	0.0329(8)
X4	1 <i>a</i>	0	0	0	0.0231(15)

<sup>a</sup> *U*<sub>eq</sub> is defined as one-third of the trace of the orthogonalized *U*<sub>*ij*</sub> tensor.

<sup>b</sup> Each *X* site contains a disordered mixture of 0.27 Cu and 0.73 Ga.

**Table 4-3.** Interatomic distances (Å) in YbNi<sub>3</sub>Ga<sub>9</sub> and YbCu<sub>3</sub>Ga<sub>8</sub>.

YbNi <sub>3</sub> Ga <sub>9</sub>			
Yb–Ga2 (×3)	2.959(1)	Ni–Ga5	2.570(2)
Yb–Ga1 (×3)	3.022(2)	Ni–Ga6	2.617(2)
Yb–Ga1 (×3)	3.030(2)	Ga1–Ga6	2.741(2)
Yb–Ga4	3.191(2)	Ga1–Ga2	2.770(2)
Yb–Ga5	3.198(2)	Ga1–Ga2	2.770(2)
Yb–Ni (×3)	3.278(2)	Ga1–Ga4	2.782(2)
Yb–Ni (×3)	3.289(2)	Ga1–Ga5	2.792(2)
Ni–Ga3	2.332(2)	Ga2–Ga2 (×2)	2.629(3)
Ni–Ga1	2.429(2)	Ga3–Ga5 (×2)	2.779(1)
Ni–Ga2	2.441(2)	Ga3–Ga4 (×2)	2.785(2)
Ni–Ga1	2.460(2)	Ga3–Ga6 (×2)	2.800(1)
Ni–Ga1	2.462(2)	Ga4–Ga4	2.803(4)
Ni–Ga4	2.564(2)	Ga5–Ga6	2.804(3)
YbCu <sub>3</sub> Ga <sub>8</sub>			
Yb–X1 (×8)	3.140(1)	X1–X2 (×4)	2.639(1)
Yb–X2 (×4)	3.141(2)	X2–X2 (×4)	2.715(2)
Yb–X3 (×8)	3.382(1)	X2–X4	2.715(2)
X1–X1 (×2)	2.536(3)	X2–X3 (×2)	3.076(3)
X1–X3 (×2)	2.554(2)	X3–X3 (×3)	2.665(4)

#### 4.2.3. Electronic structure calculations

First-principles calculations were performed using the projected augmented wave (PAW) method as implemented in the Vienna ab initio simulation package (VASP) to determine the electronic structure and density of states (DOS) of YbNi<sub>3</sub>Ga<sub>9</sub> and YbCu<sub>3</sub>Ga<sub>8</sub>.<sup>22–24</sup> Exchange and correlation were treated in this density functional theory (DFT) method by the generalized gradient approximation, as parameterized by Perdew, Burke, and Ernzerhof (PBE).<sup>25–27</sup> For simplicity, an ordered model was used for YbCu<sub>3</sub>Ga<sub>8</sub>, with Cu atoms placed at 8g and 1a sites, and Ga atoms placed at 12j and 12i sites. The recommended standard PAW potentials (Yb\_2, Cu, Ni, Ga\_d) were used, with the plane-wave basis cutoff energy set to 400 eV. The first Brillouin zone was sampled by a

Monkhorst-Pack  $k$ -mesh for YbNi<sub>3</sub>Ga<sub>9</sub> ( $18 \times 18 \times 4$ ) and YbCu<sub>3</sub>Ga<sub>8</sub> ( $12 \times 12 \times 12$ ). The convergence criteria were set to  $10^{-8}$  eV for electronic optimization, and  $|-2 \times 10^{-2}|$  eV for ionic relaxation. Chemical bonding was examined by evaluating projected crystal orbital Hamilton populations ( $-p$ COHP), electron localization functions (ELF), Löwdin charges, and COBI using the program LOBSTER (version 4.1.0).<sup>16,28–30</sup>

### 4.3. Results and discussion

#### 4.3.1. Flux growth

Mixtures of Yb and various transition metals  $M$  in a large excess of Ga, serving as a flux, were reacted at 1050 °C, followed by slow cooling. Crystals of binary or ternary gallides were obtained after the flux was removed, as determined by EDX analyses of samples examined on a scanning electron microscope (**Table 4-4** and **Figure A2-1**) and powder XRD patterns of the ground crystals (**Figure A2-2**). The composition from EDX agreed with the expected results within a 2-3% standard deviation. The Yb–Ni–Ga reaction yielded exclusively crystals of YbNi<sub>3</sub>Ga<sub>9</sub>. The majority of the crystals resulting from the Yb–Cu–Ga reaction correspond to a tetragonal Yb(Cu,Ga)<sub>12</sub> phase (space group  $I4/mmm$ ), which has been reported to adopt partially disordered ThMn<sub>12</sub>-type structures for YbCu<sub>5.4</sub>Ga<sub>6.6</sub> and YbCu<sub>5</sub>Ga<sub>7</sub>, or an ordered CeMn<sub>4</sub>Al<sub>8</sub>-type structure for YbCu<sub>4</sub>Ga<sub>8</sub>.<sup>17,31,32</sup> The observed EDX composition matches closely with YbCu<sub>~5</sub>Ga<sub>~7</sub>. However, embedded within this collection of mostly YbCu<sub>~5</sub>Ga<sub>~7</sub> crystals, there were other crystals that tended to have cubic habits (**Figure 4-1a**). These minority crystals exhibit a Cu-poorer and Ga-richer composition, close to YbCu<sub>3</sub>Ga<sub>8</sub>. SEM images of YbNi<sub>3</sub>Ga<sub>9</sub> and YbCu<sub>3</sub>Ga<sub>8</sub> are shown (**Figure 4-1b**). The powder XRD patterns of ground crystals of YbNi<sub>3</sub>Ga<sub>9</sub> and YbCu<sub>3</sub>Ga<sub>8</sub> agree well with patterns simulated from the structure determinations, discussed later, of these compounds (**Figure 4-2**).

**Table 4-4.** Compositions, as determined by EDX analyses, of crystals obtained in Ga flux reactions.

Loading composition	Crystals obtained	Composition (mol%) from EDX analysis
YbCr <sub>2</sub> Ga <sub>20</sub>	CrGa <sub>4</sub>	17.2% Cr, 82.8% Ga (expected 20.0% Cr, 80.0% Ga)
YbMn <sub>2</sub> Ga <sub>20</sub>	MnGa <sub>4</sub>	20.2% Mn, 79.8% Ga (expected 20.0% Mn, 80.0% Ga)
YbFe <sub>2</sub> Ga <sub>20</sub>	FeGa <sub>3</sub>	23.9% Fe, 76.1% Ga (expected 25.0% Fe, 75.0% Ga)
YbCo <sub>2</sub> Ga <sub>20</sub>	YbCo <sub>2</sub> Ga <sub>8</sub>	11.7% Yb, 17.8% Co, 70.4% Ga (expected 9.1% Yb, 18.2% Co, 72.7% Ga)
YbNi <sub>2</sub> Ga <sub>20</sub>	YbNi <sub>3</sub> Ga <sub>9</sub>	7.2% Yb, 22.8% Ni, 70.0% Ga (expected 7.7% Yb, 23.1% Ni, 69.2% Ga)
YbCu <sub>2</sub> Ga <sub>20</sub>	YbCu <sub>~.5</sub> Ga <sub>~.7</sub> (major)	6.4% Yb, 40.8% Cu, 52.8% Ga (expected 7.7% Yb, 38.5% Cu, 53.8% Ga)
	YbCu <sub>3</sub> Ga <sub>8</sub> (minor)	7.9% Yb, 28.6% Cu, 63.4% Ga (expected 8.3% Yb, 25.0% Cu, 66.7% Ga)
YbRu <sub>2</sub> Ga <sub>20</sub>	RuGa <sub>3</sub>	26.0% Ru, 74.0% Ga (expected 25.0% Ru, 75.0% Ga)

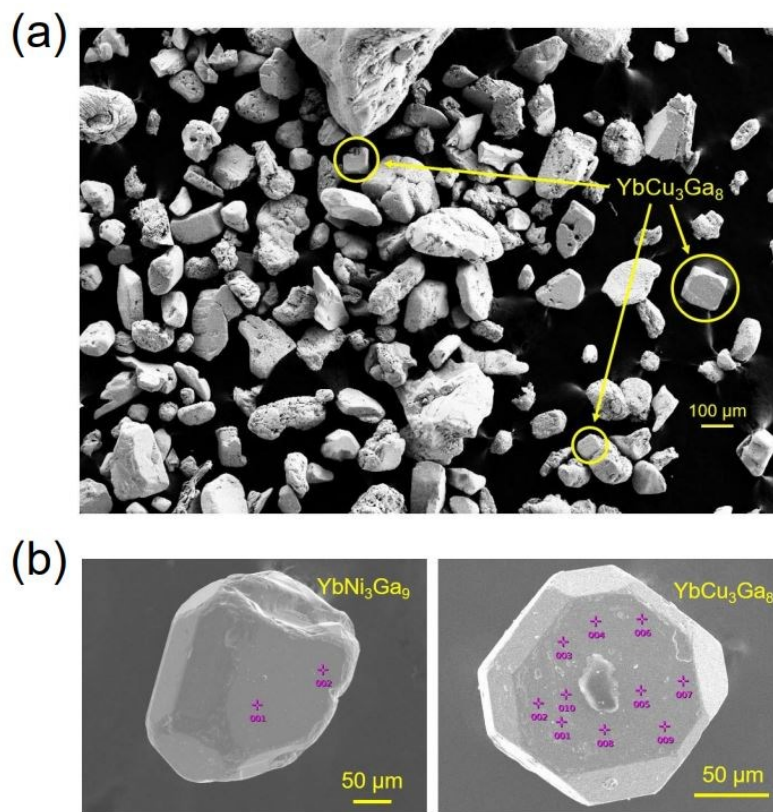


**Figure 4-1.** SEM images: (a) YbCu<sub>3</sub>Ga<sub>8</sub> crystals (circled) within a larger collection of mostly Yb(Cu,Ga)<sub>12</sub> crystals grown in gallium flux. (b) Single crystals of YbNi<sub>3</sub>Ga<sub>9</sub> and YbCu<sub>3</sub>Ga<sub>8</sub>.

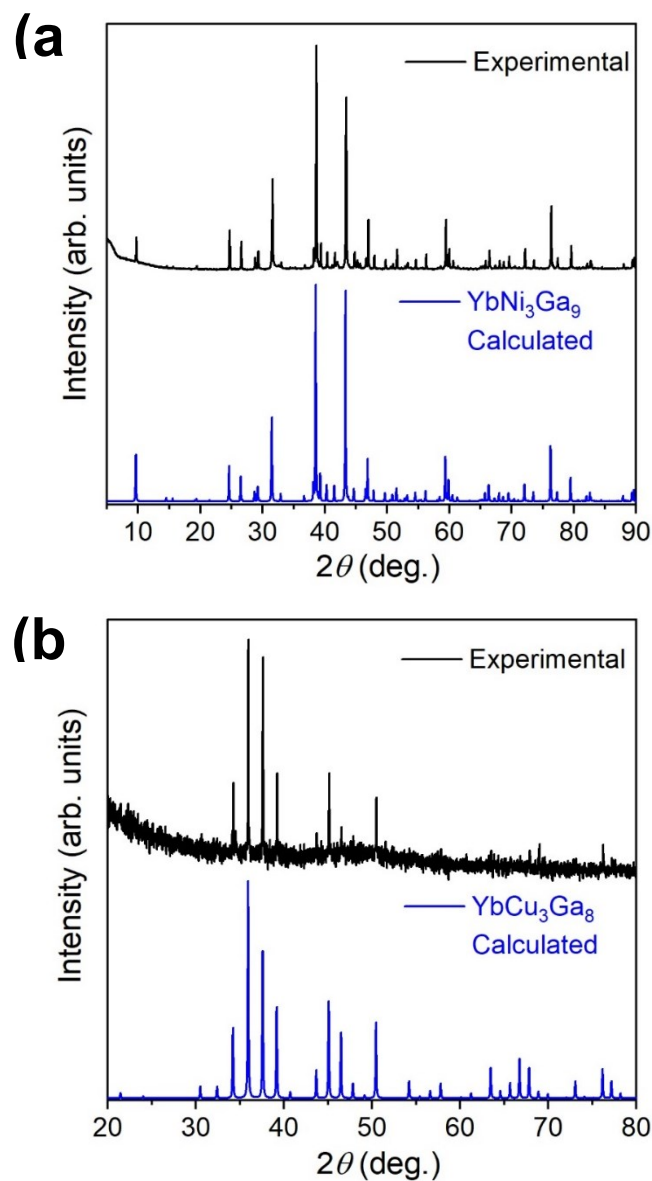


**Figure 4-2.** Powder XRD patterns of ground crystals of (a) YbNi<sub>3</sub>Ga<sub>9</sub> and (b) YbCu<sub>3</sub>Ga<sub>8</sub> grown by gallium flux.

It is interesting to evaluate the outcomes of these flux-growth experiments in the context of a previously developed stability diagram which attempts to classify whether a ternary, quasi-ternary, or binary phase will crystallize when two metals A and B are combined in the presence of excess metal flux C (selected among Ga, In, Sn, Pb).<sup>5</sup> This diagram is based on two parameters that relate

to disparities in radii,  $|\Delta R_{AB}| + |\Delta R_{AC}| + |\Delta R_{BC}|$ , and in melting temperatures of the components,  $T_A/T_B + T_A/T_C + T_B/T_C$  (**Figure 4-3**). The general trend is that crystals of ternary intermetallic compounds are most likely to be obtained when the radii are not too similar and when the melting temperatures are not too different. In addition to the Yb-containing reactions as described above, three other reactions were performed with La and Ce, with the same nominal compositions of  $REM_2Ga_{20}$  and an identical heat treatment as before. These reactions yielded crystals of binary phases ( $Ni_2Ga_3$  from La–Ni–Ga) and ternary phases ( $Ce_2NiGa_{10}$  and  $Ce_2NiGa_{12}$  from Ce–Ni–Ga;  $Cu_2CuGa_{12}$  from Ce–Cu–Ga). When plotted on the diagram, the new results give mixed agreement. The violations seen for the Yb–*M*–Ga systems could be rectified if the critical value for the melting temperature parameter is not fixed at 14, but allowed to vary with the radius parameter (i.e., the boundary indicated by the dashed line is not vertical, but sloping).

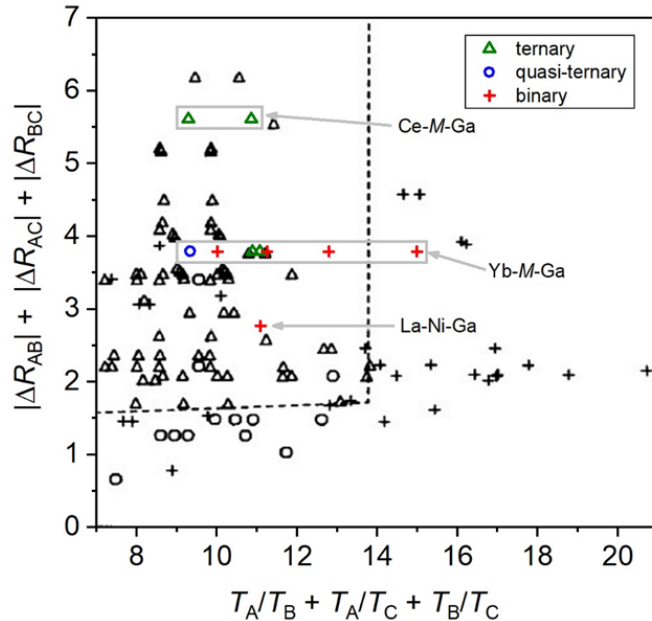


**Figure 4-3.** Stability diagram showing the crystal growth of ternary, quasi-ternary, or binary phases as promoted by metal fluxes within intermetallic systems A–B–C, with new results overlaid on the plot previously reported by Westerveld et al.<sup>5</sup>

### 4.3.2. YbNi<sub>3</sub>Ga<sub>9</sub>

Many crystals of YbNi<sub>3</sub>Ga<sub>9</sub> were screened for single-crystal X-ray diffraction analysis. All of them gave diffraction patterns exhibiting broad reflections and diffuse scattering. The apparently hexagonal symmetry in the intensity pattern was suspected to arise from twinning of the crystals, with the true symmetry assumed to be trigonal and the possible space groups being  $R3$ ,  $R\bar{3}$ ,  $R32$ ,  $R3m$ , or  $R\bar{3}m$ . Initial attempts were made to analyze these data based on a rhombohedral superstructure in  $R3$  with twinning (see discussion in Appendix 2). After significant efforts were made to synthesize new batches of this compound and to ensure that only small fragments of crystals were selected for screening, a good data set was eventually obtained on an untwinned crystal.

The structure of YbNi<sub>3</sub>Ga<sub>9</sub>, which was successfully refined in the noncentrosymmetric space group  $R32$ , contains one Yb, one Ni, and five Ga sites. Typical of intermetallic compounds, the structure consists of densely packed atoms, but it can be built up in terms of three types of nets, with compositions of Yb<sub>2</sub>Ga<sub>3</sub>, Ni<sub>3</sub>Ga<sub>6</sub>, and Ga<sub>3</sub>, stacked along the  $c$ -direction in a 12-layer sequence (**Figure 4-4**). All of these nets can be derived from close-packed arrangements of atoms ( $3^6$  in Schläfli notation). The Yb<sub>2</sub>Ga<sub>3</sub> nets are formed by replacing one-third of the nodes in a close-packed arrangement of Yb atoms by Ga<sub>3</sub> triangles. Similarly, in the Ni<sub>3</sub>Ga<sub>6</sub> nets, which are highly puckered, Ni atoms occupy one-third and Ga atoms occupy two-thirds of these close-packed arrangements. The Ga<sub>3</sub> nets are half as dense and are almost flat. The 12-layer stacking sequence results from a tripling of a basic four-layer sequence, (Ga<sub>3</sub>–Ni<sub>3</sub>Ga<sub>6</sub>–Yb<sub>2</sub>Ga<sub>3</sub>–Ni<sub>3</sub>Ga<sub>6</sub>)<sub>3</sub>, in which the Yb<sub>2</sub>Ga<sub>3</sub> nets are successively shifted in their relative orientation parallel to the  $ab$ -plane, in accordance with rhombohedral centring. The interatomic distances of 2.9–3.2 Å for Yb–Ga, 3.2–3.3 Å for Yb–Ni, 2.3–2.6 Å for Ni–Ga, and 2.6–2.8 Å for Ga–Ga contacts agree well with typical ranges found in Pearson's Crystal Data.<sup>33</sup> If distances up to a cutoff of 3.5 Å are considered, the local environments

around atoms have high coordination numbers (CN) and irregular geometries: CN17 for Yb, CN10 for Ni, and CN8–11 for Ga atoms (**Figure A2-3**).

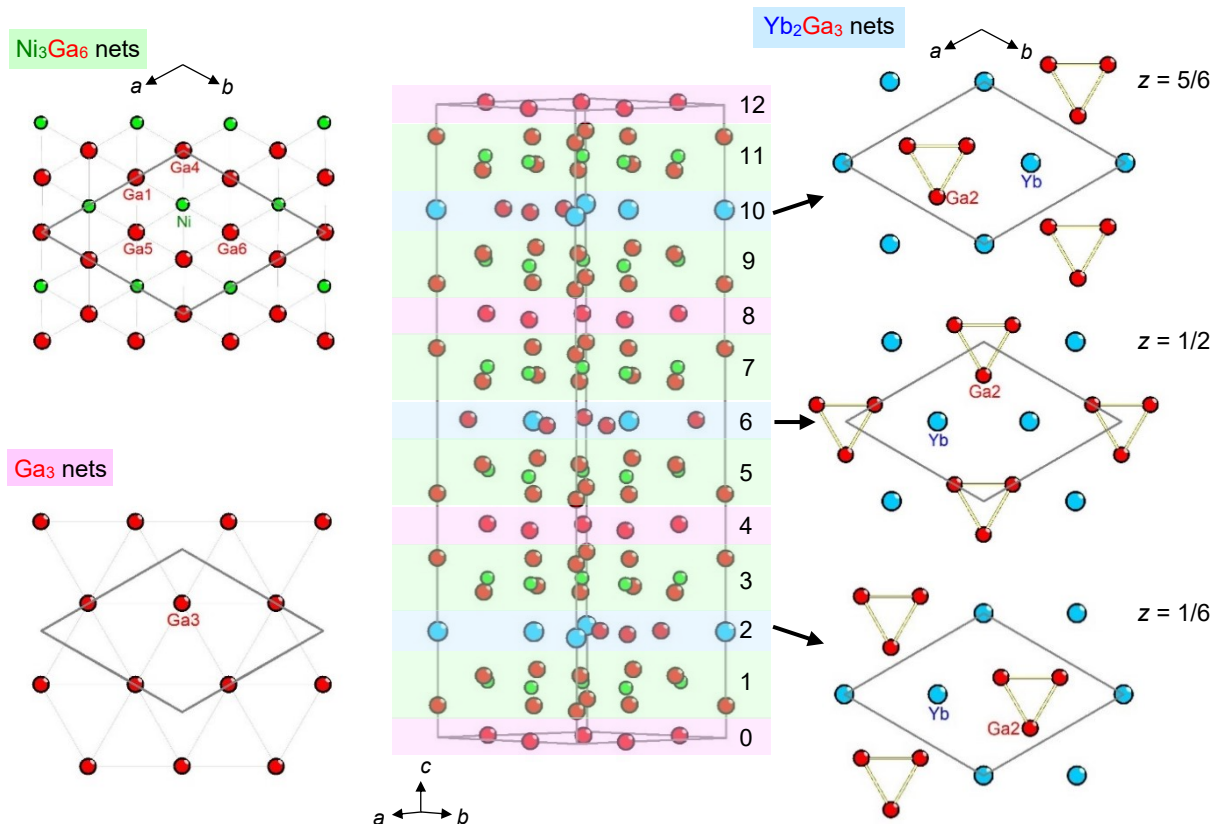


**Figure 4-4.** Structure of  $\text{YbNi}_3\text{Ga}_9$  in terms of nets.

These results support the proposal that  $\text{YbNi}_3\text{Ga}_9$  adopts the ordered  $\text{ErNi}_3\text{Al}_9$ -type structure instead of the partially disordered  $\text{DyNi}_3\text{Al}_9$ -type structure. In retrospect, the discrepancies reported previously are perhaps unsurprising given that related ternary rare-earth nickel aluminides and gallides  $\text{RENi}_3\text{Tr}_9$  ( $\text{Tr} = \text{Al}, \text{Ga}$ ) are prone to exhibit stacking faults of the  $\text{RE}_2\text{Tr}_3$  nets, manifested as disorder and partial occupancy of the  $\text{RE}$  sites and  $\text{Tr}_3$  triangles, which gives rise to apparently unphysical short distances between sites. Complete disorder leads to the  $\text{Yb}_{0.67}\text{Ni}_2\text{Al}_6$ -type structure ( $P\bar{6}m2$ ,  $a = 4.2 \text{ \AA}$ ,  $c = 9.1 \text{ \AA}$ ),<sup>34</sup> partial disorder to the  $\text{DyNi}_3\text{Al}_9$ -type structure ( $R32$ ,  $a = 7.3 \text{ \AA}$ ,  $c = 27.4 \text{ \AA}$ ),<sup>11,35</sup> and complete order to the  $\text{ErNi}_3\text{Al}_9$ -type structure ( $R32$ ,  $a = 7.3 \text{ \AA}$ ,  $c = 27.3 \text{ \AA}$ ).<sup>11,15,36–38</sup>

Many of the structural assignments were inferred on the basis of powder XRD patterns, but it is likely that most of these compounds exhibit the same problems of diffuse scattering as observed in the present study, as well as in previous reports of quaternary intermetallics  $RE-Ni-Ga-(Si \text{ or } Ge)$ .<sup>39</sup>

$YbNi_3Ga_9$  has been previously shown by magnetic susceptibility measurements and X-ray photoemission spectroscopy to exhibit intermediate Yb valence, which evolves to a greater proportion of the divalent state upon cooling.<sup>6-10</sup> Because  $Yb^{2+}$  has a nominally larger radius than  $Yb^{3+}$ , it is worthwhile to see if this change in valence state will be reflected in the structural data. Temperature-dependent measurements of the cell parameters, refined from single-crystal diffraction data from 200 to 100 K (**Table A2-7**), reveal a gradual contraction of the unit cell (**Figure 4-5**). However, this contraction is quite weak, the cell lengths changing by only 0.1%. Moreover, single-crystal structure refinements show that while the Ni-Ga and Ga-Ga bonds generally shorten on proceeding from 300 to 100 K, most of the Yb-Ga and Yb-Ni bonds are little changed (**Table A2-3**). These observations can be understood in terms of the competing trends in which cell expansion arising from greater proportions of divalent Yb is counteracted by cell contraction due to diminished thermal vibration effects.

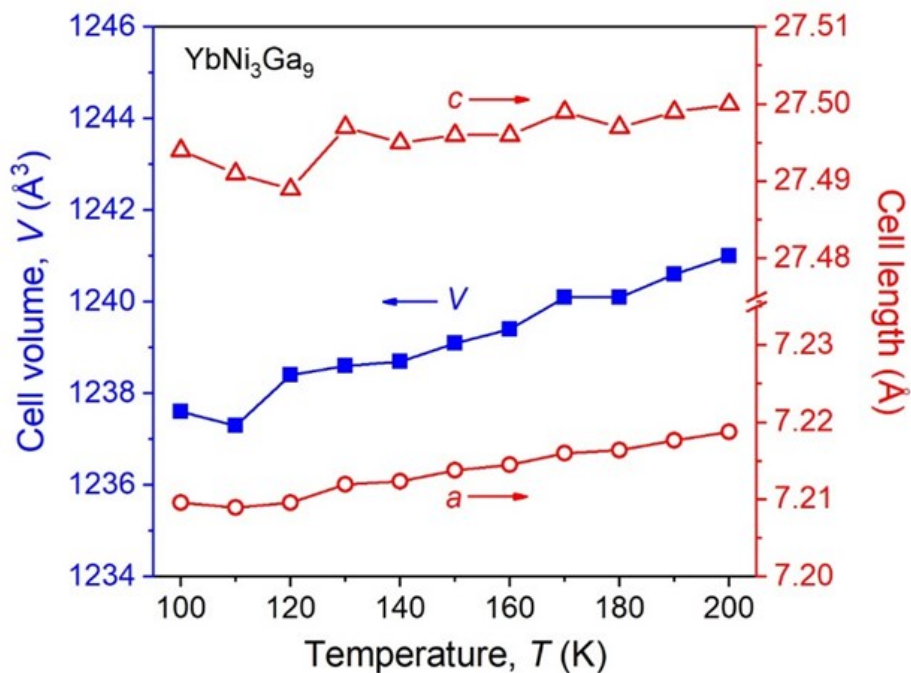


**Figure 4-5.** Cell parameters of  $\text{YbNi}_3\text{Ga}_9$  as a function of temperature.

### 4.3.3. $\text{YbCu}_3\text{Ga}_8$

The structure of the cubic crystals of  $\text{YbCu}_3\text{Ga}_8$ , which constituted the minority of the Yb–Cu–Ga reaction product, was determined in space group  $Pm\bar{3}m$  and corresponds to the  $\text{BaHg}_{11}$ -type.<sup>40</sup> In the structural model, the Yb atoms occupy the  $3c$  sites, and the Cu and Ga atoms are assumed to be disordered within four sites ( $12j$ ,  $12i$ ,  $8g$ ,  $1a$ ) because they cannot be distinguished based on their similar X-ray scattering factors (**Table 4-2**). Although it is possible to propose ordered models that are consistent with the formula  $\text{YbCu}_3\text{Ga}_8$  (Cu in  $8g$  and  $1a$ ; Ga in  $12j$  and  $12i$ ), there were no statistically meaningful improvements in the refinement results.

The  $\text{BaHg}_{11}$ -type structure of  $\text{YbCu}_3\text{Ga}_8$  can be described in terms of three types of polyhedra:  $X_{12}$  cuboctahedra centred by  $X$  atoms, empty  $X_8$  cubes, and large  $X_{20}$  polyhedra centred by Yb atoms, where  $X$  represents the disordered mixture of Cu and Ga atoms (**Figure 4-6**). Within the cubic unit

cell, the  $X@X_{12}$  cuboctahedra are located at the corners, the  $Yb@X_{20}$  polyhedra at the faces, and the empty  $X_8$  cubes at the centre, analogous to the arrangement of atoms in a perovskite structure. The  $Yb-X$  distances are 3.1–3.4 Å and the  $X-X$  distances are 2.5–3.1 Å within these polyhedra. Characteristic of this structure type, there are also kagome nets formed by the Yb atoms, but at rather long distances (5.86 Å).

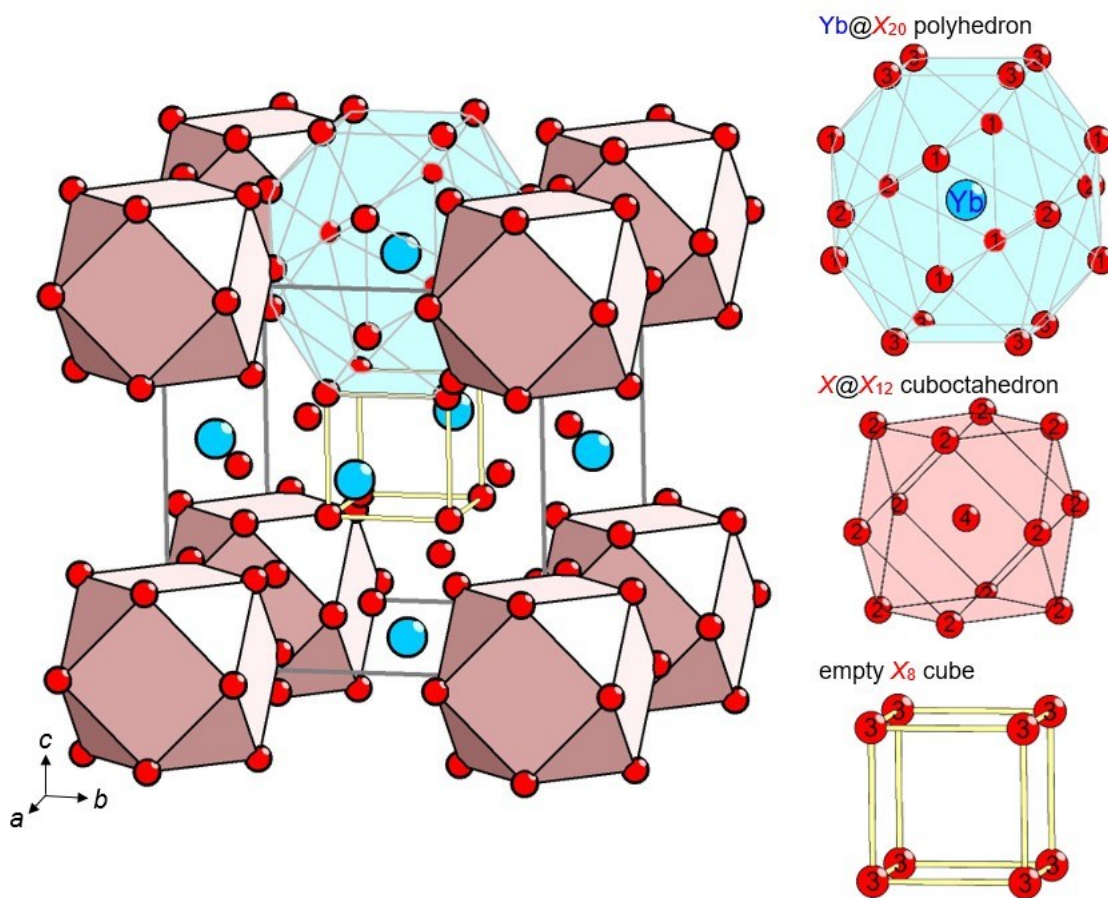


**Figure 4-6.** Structure of  $YbCu_3Ga_8$  in terms of polyhedra. The Cu and Ga atoms are disordered within sites labelled  $X$ .

Although many Ga-rich phases in the Yb–Cu–Ga system have been previously reported,<sup>17,19,31,32</sup>  $YbCu_3Ga_8$  appears to be a new ternary phase. The cubic  $BaHg_{11}$ -type structure of  $YbCu_3Ga_8$  contrasts with the tetragonal  $BaCd_{11}$ -type structure adopted by ternary  $RE(Cu,Ga)_{11}$  phases

known for  $RE = \text{Ce-Nd, Sm, Gd-Dy, Y}$ .<sup>31</sup> The two structure types formed by these ternary derivatives compete with each other, with the  $\text{BaHg}_{11}$ -type favoured at higher electron concentrations than the  $\text{BaCd}_{11}$ -type in order to optimize heteroatomic contacts.<sup>41</sup> If divalent Yb is assumed, the electron concentration for  $\text{YbCu}_3\text{Ga}_8$  is  $29/11 = 2.6 e^-$  per electronegative metal atom, within the ranges of  $2.3\text{--}2.7 e^-$  found for other ternary aluminides  $A\text{Ag}_{3-4}\text{Al}_{8-7}$  ( $A = \text{Ca, Ce, Eu, Yb}$ ) and gallides  $\text{YbPd}_{2.1-3.4}\text{Ga}_{8.9-7.6}$  adopting the  $\text{BaHg}_{11}$ -type structure. In contrast, the electron concentration is  $2.0 e^-$  for gallides  $RE\text{Cu}_7\text{Ga}_4$  ( $RE = \text{Sm, Gd, Dy}$ ) adopting the  $\text{BaCd}_{11}$ -type structure, where a composition has been estimated.<sup>33</sup>

Given that other  $\text{BaHg}_{11}$ -type structures have been observed to undergo temperature-dependent distortions,<sup>14,18</sup> the structure of  $\text{YbCu}_3\text{Ga}_8$  was also examined at lower temperatures below 300 K (**Table A2-4** to **Table A2-6**). No low-temperature transitions were observed down to 100 K (near the limits of the variable temperature capability of the diffractometer) although this does not preclude that they do not occur at higher temperatures above 300 K. For example,  $\text{CePd}_{3+x}\text{Ga}_{8-x}$  has been shown to undergoes complex transitions at high temperature, including a transition at  $640^\circ\text{C}$  from orthorhombic to cubic structure.<sup>14</sup>

#### 4.3.4. Electronic structure

Rare-earth gallides are classified as polar intermetallics in which the electronegativity differences are sufficiently large to impart polar character in the bonds, although such pronouncements are often made without quantitative support. An intuitive assessment of the bonding in  $\text{YbNi}_3\text{Ga}_9$  and  $\text{YbCu}_3\text{Ga}_8$  suggests that electron transfer takes place from electropositive Yb to electronegative Ga atoms. However, this expectation is not obvious given that the electronegativity of Ni and Cu is greater than Ga in some scales (Pauling, Allred-Rochow) and not in others (Mulliken).

DFT calculations were performed on  $\text{YbNi}_3\text{Ga}_9$  and an ordered model of  $\text{YbCu}_3\text{Ga}_8$ , and plots of the DOS,  $-\text{pCOHP}$ , and COBI curves are shown (**Figure 4-7**). Metallic behaviour is confirmed by the absence of an energy gap in the DOS at the Fermi level, where the main contributions are Ga 4p states. Filled Ni or Cu 3d states are found below the Fermi level and dominate the DOS (down to  $-4$  eV). The  $-\text{pCOHP}$  and COBI curves reveal that the Ga–Ga contacts are the critical bonding interactions in both compounds, given the prominent crossover from bonding to antibonding states at the Fermi level. Optimization of these homoatomic Ga–Ga bonds, which are the strongest in both structures as gauged by the integrated  $-\text{pCOHP}$  values ( $-\text{IpCOHP}$ ), prevails over the heteroatomic Ni–Ga or Cu–Ga bonds, for which some antibonding interactions are present. The degree of covalency in these bonds can be quantified using the concept of COBI. Values of COBI range from 0 for fully ionic to 1 for fully covalent character, but will be scaled down when multicentre interactions are present, as occurs in many extended inorganic solids, including intermetallic compounds.<sup>42</sup> With this caution in mind, it is reassuring that the homoatomic Ga–Ga bonds, which would be expected to be the most covalent, do show the highest COBI values (0.3–0.4) compared to the heteroatomic Ni–Ga (0.2–0.3) or Cu–Ga (0.1–0.2) contacts. The COBI values for Yb–Ni, Yb–Cu, and Yb–Ga contacts are all less than 0.1, but this could be a reflection of high electronic delocalization (which is an extreme expression of multicentre bonding) just as much as greater ionicity.

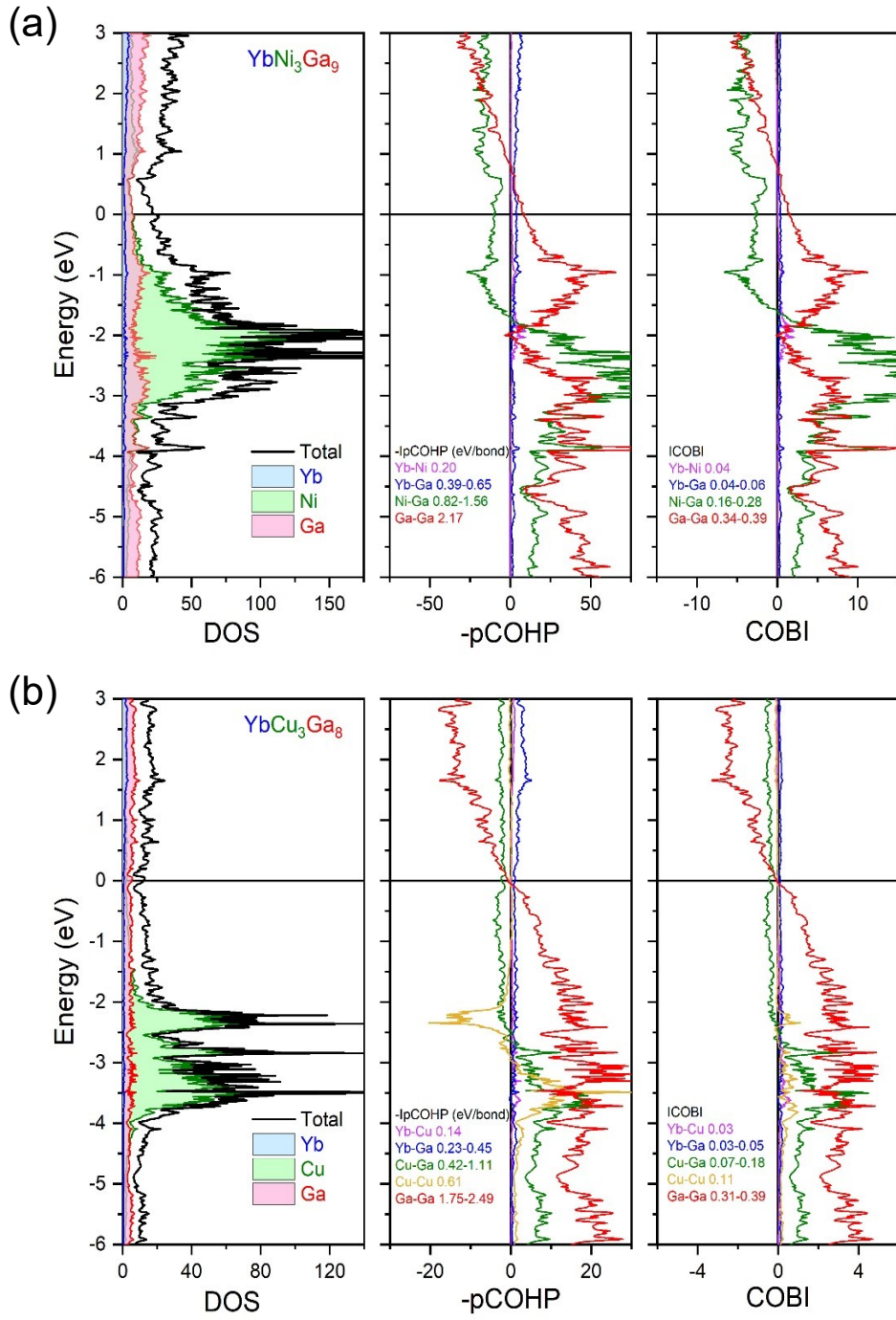


**Figure 4-7.** Density of states (DOS), projected crystal orbital Hamilton population ( $-p\text{COHP}$ ), and crystal orbital bond index (COBI) for (a)  $\text{YbNi}_3\text{Ga}_9$  and (b) ordered model of  $\text{YbCu}_3\text{Ga}_8$ .

To visualize the bonding in more detail, ELF plots were extracted from the electronic structure calculations, and Löwdin charges were calculated for the atoms in  $\text{YbNi}_3\text{Ga}_9$  and  $\text{YbCu}_3\text{Ga}_8$  (**Figure 4-8**). The most striking feature is the presence of intermediate electron density (green colours) defining the multicentre bonding network of Ga atoms. Greater electron density (yellow colours) builds up between these atoms, indicative of the covalent bonding character and consistent with the higher COBI values for Ga–Ga contacts described above. These bonding networks are anionic, as indicated by the negative charges on the Ga atoms (0.1– to 0.5– in  $\text{YbNi}_3\text{Ga}_9$ ; 0.2– to 0.5– in  $\text{YbCu}_3\text{Ga}_8$ ). Interestingly, the charges around the Ni (0.6+) or Cu atoms (0.5+) remain positive, so that the direction of electron transfer is from these transition metal atoms to the Ga atoms. The buildup of electron density between Ni or Cu and Ga atoms is not as prominent, implying more ionic character in the Ni–Ga and Cu–Ga bonds than in the Ga–Ga bonds. On the other hand, the electron density is highly localized around the Yb atoms, which have high positive charges of 1.3+ in both compounds, corroborating expectations for significantly greater ionic character in the bonds to these atoms.

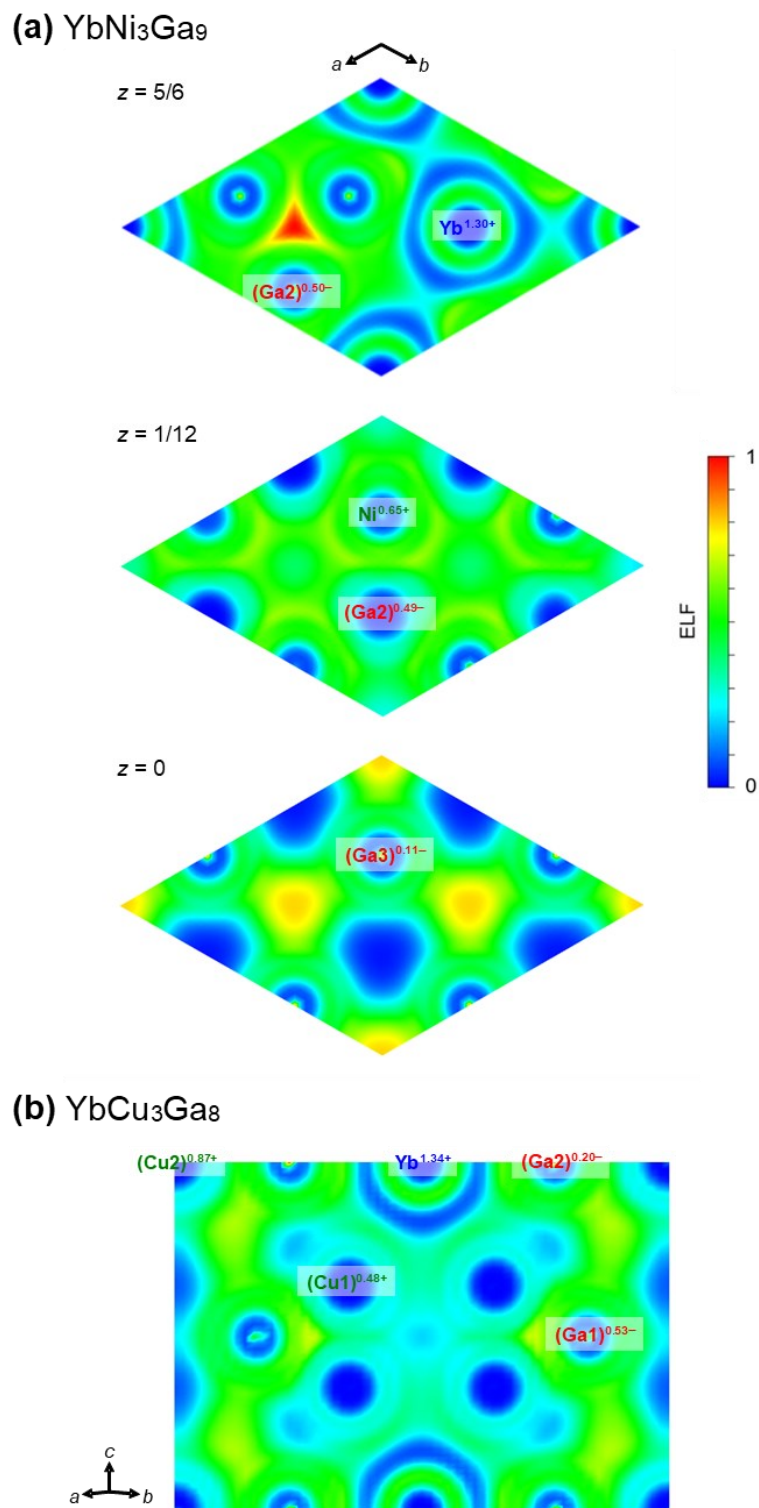


**Figure 4-8.** ELF plots and Löwdin charges for (a) YbNi<sub>3</sub>Ga<sub>9</sub> (projected parallel to (001) plane at  $z = 0, 1/12,$  and  $5/6$ ) and (b) ordered model of YbCu<sub>3</sub>Ga<sub>8</sub> projected on (110) plane.

#### 4.4. Conclusions

To test the hypothesis that the crystal growth of ternary intermetallic phases in flux reactions can be related to simple descriptors of the components, Yb–*M*–Ga reactions were performed. The results were not entirely conclusive, because there were several violations within the stability diagram, but the general trends suggest that melting temperatures and atomic radii are certainly important factors. Nevertheless, it would be worthwhile to apply more modern machine-learning approaches, such as the sure independence screening and sparsifying operator (SISSO) method,<sup>43</sup> to develop a more accurate and unbiased descriptor that would be able to predict the results of such flux growth experiments. YbNi<sub>3</sub>Ga<sub>9</sub> was confirmed to adopt the ordered ErNi<sub>3</sub>Al<sub>9</sub>-type structure, but the significant effort required to find an untwinned crystal suggests that stacking faults are likely an inherent feature of related aluminides and gallides *RE*Ni<sub>3</sub>*Tr*<sub>9</sub> (*Tr* = Al, Ga). This may have important implications for the interpretation of chiral magnetism in these compounds, for which helical magnetic ordering has been proposed,<sup>8,9,37</sup> given that the noncentrosymmetry in this structure depends on the occurrence of long-range ordering of the *RE*<sub>2</sub>*Tr*<sub>3</sub> nets. YbCu<sub>3</sub>Ga<sub>8</sub> was discovered as a new phase in the Yb–Cu–Ga system from the flux growth reactions, but in small amounts, suggesting that it is probably metastable. Efforts to prepare this phase through other methods, such as induction heating and direct reaction, have so far been unsuccessful. As confirmed by DFT calculations, the bonding in both YbNi<sub>3</sub>Ga<sub>9</sub> and YbCu<sub>3</sub>Ga<sub>8</sub>, which are Ga-rich phases, can be viewed in terms of electron transfer from Yb to Ga atoms, which then participate in multicentre bonding with significant covalent character.

#### 4.5. References

- (1) Kanatzidis, M. G.; Pöttgen, R.; Jeitschko, W. *Angew. Chem. Int. Ed.* **2005**, *44*, 6996–7029.
- (2) Phelan, W. A.; Menard, M. C.; Kangas, M. J.; McCandless, G. T.; Drake, B. L.; Chan, J. Y. *Chem. Mater.* **2012**, *24*, 409–420.
- (3) Latturmer, S. E. *Acc. Chem. Res.* **2018**, *51*, 40–48.
- (4) Weiland, A.; Frith, M. G.; Lapidus, S. H.; Chan, J. Y. *Chem. Mater.* **2021**, *33*, 7657–7664.
- (5) Westerveld, J. P. A.; Lo Cascio, D. M. R.; Doornik, M. O.; Loeff, P. I.; Bakker, H.; Heijligers, H. J. M.; Bastin, G. F. *J. Less-Common Met.* **1989**, *146*, 189–195.
- (6) Yamashita, T.; Miyazaki, R.; Aoki, Y.; Ohara, S. *J. Phys. Soc. Jpn.* **2012**, *81*, 034705.
- (7) Utsumi, Y.; Sato, H.; Ohara, S.; Yamashita, T.; Mimura, K.; Motonami, S.; Shimada, K.; Ueda, S.; Kobayashi, K.; Yamaoka, H.; Tsujii, N.; Hiraoka, N.; Namatame, H.; Taniguchi, M. *Phys. Rev. B* **2012**, *86*, 115114.
- (8) Matsubayashi, K.; Hirayama, T.; Yamashita, T.; Ohara, S.; Kawamura, N.; Mizumaki, M.; Ishimatsu, N.; Watanabe, S.; Kitagawa, K.; Uwatoko, Y. *Phys. Rev Lett.* **2015**, *114*, 086401.
- (9) Umeo, K.; Otaki, T.; Arai, Y.; Ohara, S.; Takabatake, T. *Phys. Rev. B* **2018**, *98*, 024420.
- (10) Okamura, H.; Takigawa, A.; Yamasaki, T.; Bauer, E. D.; Ohara, S.; Ikemoto, Y.; Moriwaki, T. *Phys. Rev. B* **2019**, *100*, 195112.
- (11) Gladyshevskii, R. E.; Cenzual, K.; Flack, H. D.; Parthé, E. *Acta Crystallogr. B* **1993**, *49*, 468–474.
- (12) Thomas, K. R. Synthesis and characterization of rare earth-nickel-gallium ternary intermetallics, Ph.D. thesis, Louisiana State University, Louisiana, USA, 2010.
- (13) Shevchenko, I. P.; Markiv, V. Ya. *Metally* **1993**, *6*, 183–189.

- (14) Francisco, M. C.; Malliakas, C. D.; Macaluso, R. T.; Prestigiacomo, J.; Haldolaarachchige, N.; Adams, P. W.; Young, D. P.; Jia, Y.; Claus, H.; Gray, K. E.; Kanatzidis, M. G. *J. Am. Chem. Soc.* **2012**, *134*, 12998–13009.
- (15) Mercena, S. G.; Duque, J. G. S.; Silva, L. S.; Lora-Serrano, R.; Amaral, R. P.; Cadogan, J. M.; Garcia, D. J. *J. Alloys Compd.* **2019**, *785*, 105–109.
- (16) Müller, P. C.; Ertural, C.; Hempelmann, J.; Dronskowski, R. *J. Phys. Chem. C* **2021**, *125*, 7959–7970.
- (17) Drake, B. L.; Capan, C.; Cho, J. Y.; Nambu, Y.; Kuga, K.; Xiong, Y. M.; Karki, A. B.; Nakatsuji, S.; Adams, P. W.; Young, D. P.; Chan, J. Y. *J. Phys.: Condens. Matter* **2010**, *22*, 066001.
- (18) Macaluso, R. T.; Francisco, M.; Young, D. P.; Stadler, S.; Mitchell, J. F.; Geiser, U.; Hong, H.-Y.; Kanatzidis, M. G. *J. Solid State Chem.* **2011**, *184*, 3185–3189.
- (19) Mishra, V.; Oliynyk, A. O.; Subbarao, U.; Sarma, S. Ch.; Mumbaraddi, D.; Roy, S.; Peter, S. C. *Cryst. Growth Des.* **2018**, *18*, 6091–6099.
- (20) Sheldrick, G. M. *Acta Crystallogr. A: Found. Crystallogr.* **2008**, *64*, 112–122.
- (21) Gelato, L. M.; Parthé, E. *J. Appl. Crystallogr.* **1987**, *20*, 139–143.
- (22) Kresse, G.; Furthmüller, J. *Phys. Rev. B* **1996**, *54*, 11169–11186.
- (23) Kresse, G.; Joubert, D. *Phys. Rev. B* **1999**, *59*, 1758–1775.
- (24) Blöchl, P. E. *Phys. Rev. B* **1994**, *50*, 17953–17979.
- (25) Perdew, J. P.; Burke, K.; Ernzerhof, M. *Phys. Rev. Lett.* **1996**, *77*, 3865–3868.
- (26) Hohenberg, P.; Kohn, W. *Phys. Rev.* **1964**, *136*, B864–B871.
- (27) Kohn, W.; Sham, L. J. *Phys. Rev.* **1965**, *140*, A1133–A1138.

- (28) Deringer, V. L.; Tchougréeff, A. L.; Dronskowski, R. *J. Phys. Chem. A* **2011**, *115*, 5461–5466.
- (29) Grin, Y.; Savin, A.; Silvi, B., The ELF perspective of chemical bonding. In *The Chemical Bond: Fundamental Aspects of Chemical Bonding*, Frenking, G.; Shaik, S., Eds.; Wiley-VCH: Weinheim, **2014**; pp. 345–382.
- (30) Maintz, S.; Deringer, V. L.; Tchougréeff, A. L.; Dronskowski, R. *J. Comput. Chem.* **2016**, *37*, 1030–1035.
- (31) Verbovytskyy, Yu.; Pereira Gonçalves, A. *Chem. Met. Alloys* **2012**, *5*, 129–135.
- (32) Subbarao, U.; Gutmann, M. J.; Peter, S. C. *Inorg. Chem.* **2013**, *52*, 2219–2227.
- (33) Villars, P.; Cenzual, K. *Pearson's Crystal Data – Crystal Structure Database for Inorganic Compounds*, Release 2021/22, ASM International, Materials Park, OH, USA.
- (34) Matselko, O.; Pukas, S.; Lutsyshyn, Yu.; Gladyshevskii, R.; Kaczorowski, D. *J. Solid State Chem.* **2013**, *198*, 50–56.
- (35) Topertser, V.; Martyniak, R.-I.; Muts, N.; Tokaychuk, Ya.; Gladyshevskii, R. *Chem. Met. Alloys* **2019**, *12*, 21–28.
- (36) Lutsyshyn, Yu.; Tokaychuk, Ya.; Davydov, V.; Gladyshevskii, R. *Chem. Met. Alloys* **2008**, *1*, 303–316.
- (37) Ninomiya, H.; Matsumoto, Y.; Nakamura, S.; Kono, Y.; Kittaka, S.; Sakakibara, T.; Inoue, K.; Ohara, S. *J. Phys. Soc. Jpn.* **2017**, *86*, 124704.
- (38) Silva, L. S.; Mercena, S. G.; Garcia, D. J.; Bittar, E. M.; Jesus, C. B. R.; Pagliuso, P. G.; Lora-Serrano, R.; Meneses, C. T.; Duque, J. G. S. *Phys. Rev. B* **2017**, *95*, 134434.
- (39) Zhuravleva, M. A.; Chen, X. Z.; Wang, X.; Schultz, A. J.; Ireland, J.; Kannewurf, C. K.; Kanatzidis, M. G. *Chem. Mater.* **2002**, *14*, 3066–3081.

- (40) Biehl, E.; Deiseroth, H. J. *Z. Anorg. Allg. Chem.* **1999**, *625*, 1073–1080.
- (41) Wang, F.; Pearson, K. N.; Straszheim, W. E.; Miller, G. J. *Chem. Mater.* **2010**, *22*, 1798–1806.
- (42) Simons, J.; Hempelmann, J.; Fries, K. S.; Müller, P. C.; Dronskowski, R.; Steinberg, S. *RSC Adv.* **2021**, *11*, 20679–20686.
- (43) Ouyang, R.; Curtarolo, S.; Ahmetcik, E.; Scheffler, M.; Ghiringelli, L. M. *Phys. Rev. Mater.* **2018**, *2*, 083802.

## Chapter 5.

### Crystal growth of Ce, Eu, and Yb-containing germanides in metal flux

#### 5.1. Introduction

Intermetallic compounds containing Ce, Eu, and Yb possess diverse structures and physical properties, some of which suggest intermediate valence.<sup>1-5</sup> It is desirable to obtain single crystals of these compounds to enable more detailed measurements of magnetic and transport properties. Unfortunately, such crystals are often challenging to grow using conventional synthetic methods such as arc melting, inducting heating, and direct reactions. Fluxes of low-melting metals (Al, Ga, In, Sn, Pb, Bi) can aid in crystal growth of intermetallic compounds by lowering the reaction temperatures and sometimes by promoting the formation of phases that may be metastable or kinetically stable compared to the thermodynamically favoured phase at high temperatures.<sup>6</sup> In some cases, the flux may be incorporated into the desired product, so it acts a reactive flux.

Among ternary rare-earth transition-metal germanides  $RE-M-Ge$ , two of the most commonly occurring types of phases have the composition  $REM_2Ge_2$ , adopting the closely related tetragonal  $ThCr_2Si_2$ -type (space group  $I4/mmm$ ) and  $CaBe_2Ge_2$ -type (space group  $P4/nmm$ ) structures, both of which are derived from the  $BaAl_4$ -type structure.<sup>7</sup> Some examples of  $REM_2Ge_2$  crystals grown by metal fluxes have been previously reported:  $CeRh_2Ge_2$  showing an antiferromagnetic transition at 15 K (Bi flux),<sup>8</sup>  $CeAu_2Ge_2$  showing magnetic anisotropy (Sn flux),<sup>9</sup>  $EuCu_2Ge_2$  showing intermediate Eu valence (In flux),<sup>10</sup>  $EuZn_2Ge_2$  showing two low-temperature antiferromagnetic transitions (Pb flux),<sup>11</sup> and  $YbCu_2Ge_2$  (Sn flux) and  $YbZn_2Ge_2$  (Zn flux).<sup>12,13</sup>

In early investigations of these germanides, an empirical classification model for  $RE-M-Ge$  phases was developed to predict which of three closely related  $U_4Re_7Si_6$ -,  $ThCr_2Si_2$ -, and  $CaBe_2Ge_2$ -

type structures were likely to form based on the simple radius ratio  $r_{RE}/r_M$ .<sup>14</sup> If  $r_{RE}/r_M \leq 1.3$ , the  $U_4Re_7Si_6$ -type structure is favoured, whereas if  $r_{RE}/r_M \geq 1.3$ , the  $ThCr_2Si_2$ - and  $CaBe_2Ge_2$ -type structures are favoured. It is surprising that, nearly 40 years later, the existence of many of these ternary germanides remains inconclusive.

Here, some of the missing  $REM_2Ge_2$  phases were targeted, focusing on the Ce-, Eu-, and Yb-containing members, with the intent of using In as a nonreactive flux. Ultimately, the hypothesis failed, but in the course of the investigation, crystals of various other ternary germanides were obtained and characterized, including the previously unknown compound  $CeIrGe_2$ , and several previously known compounds  $RECo_2Ge_2$  ( $RE = Eu, Yb$ ),  $CeCoGe_2$ ,  $CeIr_2Ge_2$ ,  $Yb_4Ir_7Ge_6$ , and  $Yb_5Ir_4Ge_{10}$ .

## 5.2. Experimental

### 5.2.1. Synthesis

In a typical procedure, mixtures of  $RE$  metals (Ce, Eu, and Yb pieces; 99.9%, Hefa), transition metals (Cr pieces, 99.99%, Alfa-Aesar; Fe powder, 99+%, Alfa Aesar; Co powder, 99.5%, Alfa-Aesar; Zn powder, 99.8%, Onyxmet; Pd powder, 99.95%, Alfa-Aesar; Ag powder, 99.9%, Sigma-Aldrich; Pt sponge, 99.99%, Alfa-Aesar), Ge ingot crushed into powder (99.9999%, Alfa-Aesar) and In shot (99.9%, Alfa Aesar) were loaded with different ratios into alumina crucibles. Each crucible was placed within a fused silica tube, with quartz wool on top of the crucible. The tubes were evacuated and sealed. The tubes were heated to 1000 °C over 12 h, kept there for 12 h, cooled to 550 °C over 48 h, kept there for 48 h, removed from the furnace, and immediately centrifuged to filter the In flux while molten. The samples were transferred to vials, to which 2 mL of 5% HCl(aq) was added. The samples were sonicated for 10 min and soaked in HCl over 12 h to ensure that all excess In was

removed from the surface of crystals. The crystals were washed with water and acetone, and then dried in air. These processes were performed in a fume hood.

Chemical compositions of selected single crystals were determined by EDX analysis on a Zeiss Sigma 300 VP field emission scanning electron microscope operated with an accelerating voltage of 15 kV and equipped with a Bruker Quantax 600 system with dual X-Flash 6/60 detectors. In general, these compositions are within 3% of expected values. Powder XRD patterns of crushed crystals were collected on a Bruker D8 Advance diffractometer equipped with a Cu K $\alpha$  radiation source operated at 40 kV and 40 mA.

### 5.2.2. Structure determination

Crystals of EuCo<sub>2</sub>Ge<sub>2</sub>, YbCo<sub>2</sub>Ge<sub>2</sub>, CeCoGe<sub>2</sub>, CeIrGe<sub>2</sub>, Yb<sub>4</sub>Ir<sub>7</sub>Ge<sub>6</sub>, and Yb<sub>5</sub>Ir<sub>4</sub>Ge<sub>10</sub> were obtained. They were mounted on quartz fibres, attached with epoxy. Intensity data were collected at 296 and 193 K on a Bruker PLATFORM diffractometer equipped with a graphite-monochromated Mo K $\alpha$  radiation source and a SMART APEX II CCD detector, using  $\omega$  scans at 6–8 different  $\phi$  angles with a frame width of 0.3° and an exposure time of 10–15 s per frame. Face-indexed numerical absorption corrections were applied. Structures solution and refinement were carried out using the SHELXTL (version2018/3) program package.<sup>15</sup> All anisotropic displacement parameters were well-behaved, and all occupancy factors were 0.98–0.99 when refined. Atomic coordinates were standardized using the program STRUCTURE TIDY.<sup>16</sup> The ADDSYM routine within the PLATON suite of programs revealed no additional symmetry. Crystal data are listed in **Table A3-3** to **Table A3-8**, atomic positions and displacement parameters are listed in **Table A3-9** to **Table A3-11**, and selected bond distances are listed in **Table A3-12** to **Table A3-12**.

### 5.3. Results and discussion

#### 5.3.1. Flux growth

Many reactions to prepare ternary germanides  $RE-M-Ge$  in the presence of In flux were attempted, but in most cases, they were unsuccessful. Only a few reactions led to formation of crystals of ternary germanides, and in one case, a quaternary germanide containing In was obtained (**Table 5-1**).

**Table 5-1.** Compositions of crystals obtained in indium flux reactions.

Loading composition	Crystal obtained	Composition (mol%) from EDX analysis
CeCoGeIn <sub>30</sub>	CeCo <sub>2</sub> Ge <sub>2</sub>	22% Ce, 41% Co, 37% Ge
EuCoGeIn <sub>30</sub>	EuCo <sub>2</sub> Ge <sub>2</sub>	18% Eu, 40% Co, 42% Ge
YbCoGeIn <sub>30</sub>	YbCo <sub>2</sub> Ge <sub>2</sub>	22% Yb, 42% Co, 36% Ge
CeCo <sub>2</sub> Ge <sub>2</sub> In <sub>30</sub>	CeCo <sub>2</sub> Ge <sub>2</sub>	22% Ce, 41% Co, 37% Ge
	CeCo <sub>0.93</sub> Ge <sub>2</sub>	22% Ce, 24% Co, 53% Ge
YbCo <sub>2</sub> Ge <sub>2</sub> In <sub>30</sub>	YbCo <sub>2</sub> Ge <sub>2</sub>	19% Yb, 41% Co, 40% Ge
YbPtGe <sub>2</sub> In <sub>30</sub>	YbPtGe	31 % Yb, 34 % Pt, 35 % Ge
CeIrGe <sub>2</sub> In <sub>28</sub>	CeIr <sub>2</sub> Ge <sub>2</sub>	21% Ce, 40% Ir, 39% Ge
	CeIrGe <sub>2</sub>	27% Ce, 29% Ir, 44% Ge
EuIrGe <sub>2</sub> In <sub>28</sub>	EuIr <sub>4</sub> In <sub>2</sub> Ge <sub>4</sub>	11% Eu, 33% Ir, 23% In, 34% Ge
	EuIrGe <sub>3</sub>	26% Eu, 20% Ir, 53% Ge
YbIrGe <sub>2</sub> In <sub>28</sub>	Yb <sub>4</sub> Ir <sub>7</sub> Ge <sub>6</sub>	24% Yb, 39% Ir, 37% Ge
	Yb <sub>5</sub> Ir <sub>4</sub> Ge <sub>10</sub>	26% Yb, 19% Ir, 54% Ge

Most of the crystals obtained were prismatic (**Figure 5-1**). The  $RE-Co-Ge-In$  ( $RE = Ce, Eu, Yb$ ) reactions yielded crystals of CeCo<sub>2</sub>Ge<sub>2</sub>, CeCoGe<sub>2</sub>, EuCo<sub>2</sub>Ge<sub>2</sub> and YbCo<sub>2</sub>Ge<sub>2</sub>, all with prismatic morphology. The Ce-Ir-Ge-In reactions led to prismatic crystals of CeIr<sub>2</sub>Ge<sub>2</sub> and plate-shaped crystals of CeIrGe<sub>2</sub>. The Yb-Ir-Ge-In reactions led to prismatic crystals of Yb<sub>4</sub>Ir<sub>7</sub>Ge<sub>6</sub> and needle-shaped crystals of Yb<sub>5</sub>Ir<sub>4</sub>Ge<sub>10</sub>. Although most of these crystals are relatively small, with typical

dimensions of about 0.1–0.2 mm, they are suitable for single-crystal diffraction analysis and are much larger than would be achievable in conventional syntheses such as arc-melting.

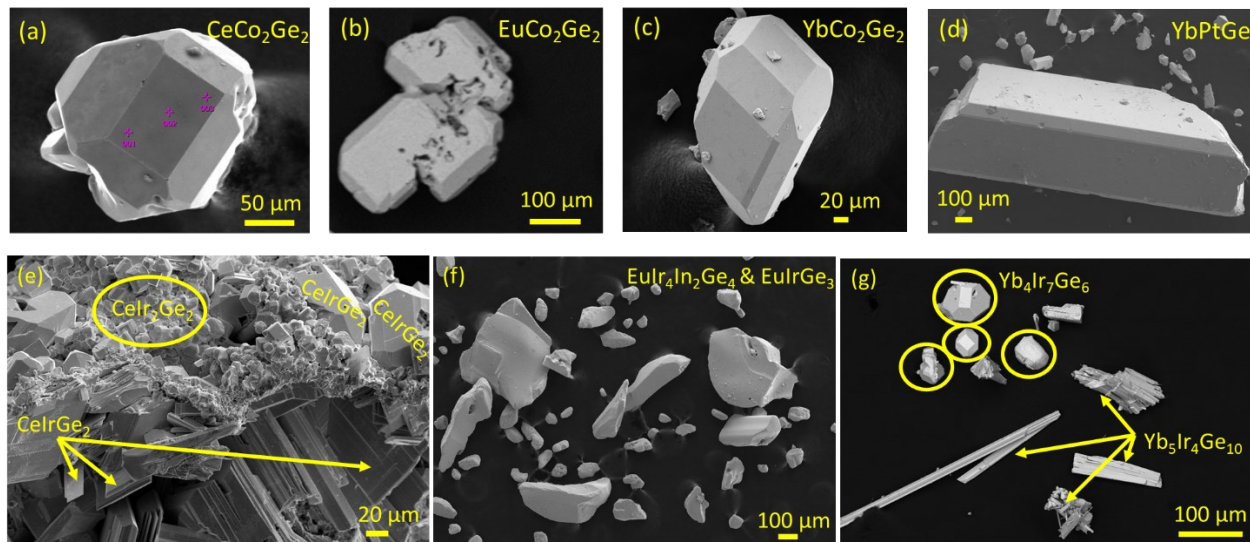


**Figure 5-1.** SEM images of single crystals obtained from In flux.

Analysis of the powder XRD patterns of the samples of ground crystals enabled identification of their phase composition (**Figure A3-1** to **Figure A3-2**). The structure map of  $RE-M-Ge$  phases based on the radius ratio  $r_{RE}/r_M$  has been updated to include new results since it was first proposed (**Figure 5-2**). In general, the  $U_4Re_7Si_6$ -type phase is favoured by smaller  $RE$  atoms ( $r_{RE}/r_M \leq 1.3$ ). The  $ThCr_2Si_2$ -type phase is overwhelmingly dominant, but note that in a few cases ( $RE-Rh-Ge$ ), the  $U_4Re_7Si_6$ -type phase can be formed as an alternative polymorph, near the threshold radius ratio of  $r_{RE}/r_M = 1.3$ .

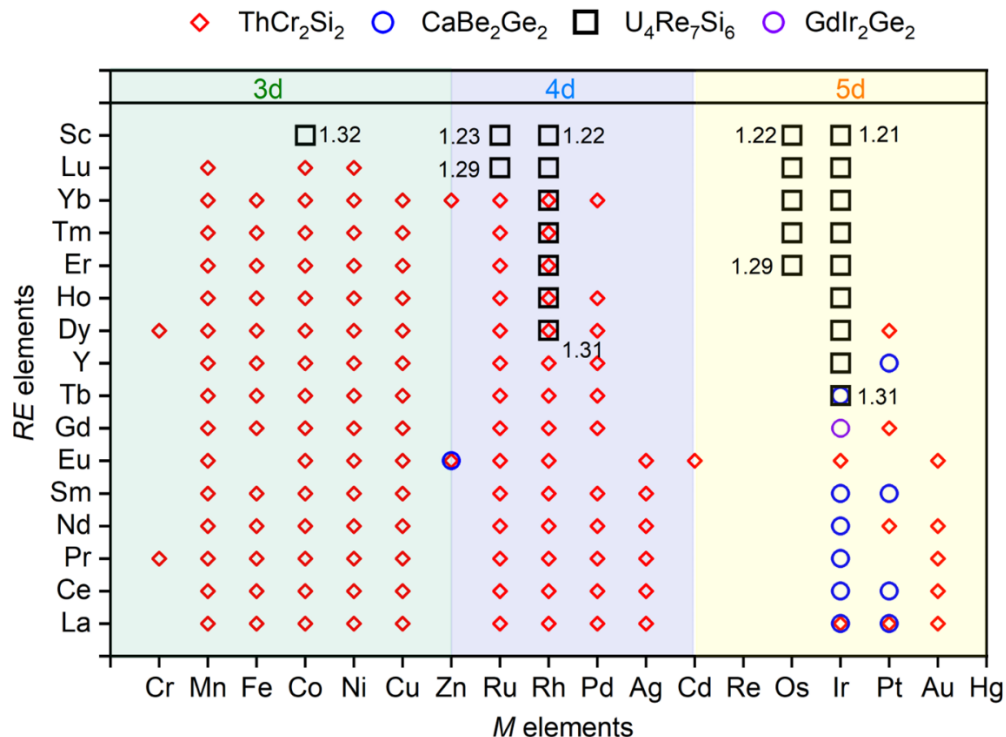


**Figure 5-2.** Structure map of  $RE-M-Ge$  phases based on radius ratios  $r_{RE}/r_M$ .

The  $RE-Ir-Ge$  systems are interesting because they exhibit the most diverse structures depending on the  $RE$  component. The flux reactions confirm the assignments expected from this structure map.  $\text{CeIr}_2\text{Ge}_2$  was found to adopt the  $\text{CaBe}_2\text{Ge}_2$ -type structure.<sup>17–19</sup>  $\text{EuIr}_2\text{Ge}_2$  was not obtained from the flux reaction, which resulted in  $\text{EuIr}_4\text{Ge}_3$  and  $\text{EuIr}_4\text{In}_2\text{Ge}_4$  instead.  $\text{Yb}_4\text{Ir}_7\text{Ge}_6$  was formed, in agreement with expectations, but in the presence of  $\text{Yb}_5\text{Ir}_4\text{Ge}_{10}$  crystals.<sup>20,21</sup> Single-crystal X-ray diffraction data were collected on  $\text{Yb}_4\text{Ir}_7\text{Ge}_6$  at various temperatures down to 193 K, but no unusual effects were observed and the cell lengths simply contract.

### 5.3.2. Structures

The compounds  $\text{EuCo}_2\text{Ge}_2$  and  $\text{YbCo}_2\text{Ge}_2$  have been previously reported to adopt  $\text{ThCr}_2\text{Si}_2$ -type structures, based on powder XRD data.<sup>22</sup> Because only cell parameters were reported, full single-crystal structure determinations for them have been undertaken here (**Table A3-3**, **Table A3-**

4, Table A3-9, Table A3-12). Temperature-dependent data show no unusual transitions down to 193 K. The structure consists of [CoGe] layers, built from edge-sharing Co-centred tetrahedra; these layers are connected by Ge–Ge bonds to form a framework with the intervening spaces occupied by RE atoms (Figure 5-3). These Ge–Ge bonds are relatively long for  $\text{EuCo}_2\text{Ge}_2$  (2.76 Å) but significantly shorter and within a single-bond distance for  $\text{YbCo}_2\text{Ge}_2$  (2.51 Å).<sup>23</sup>

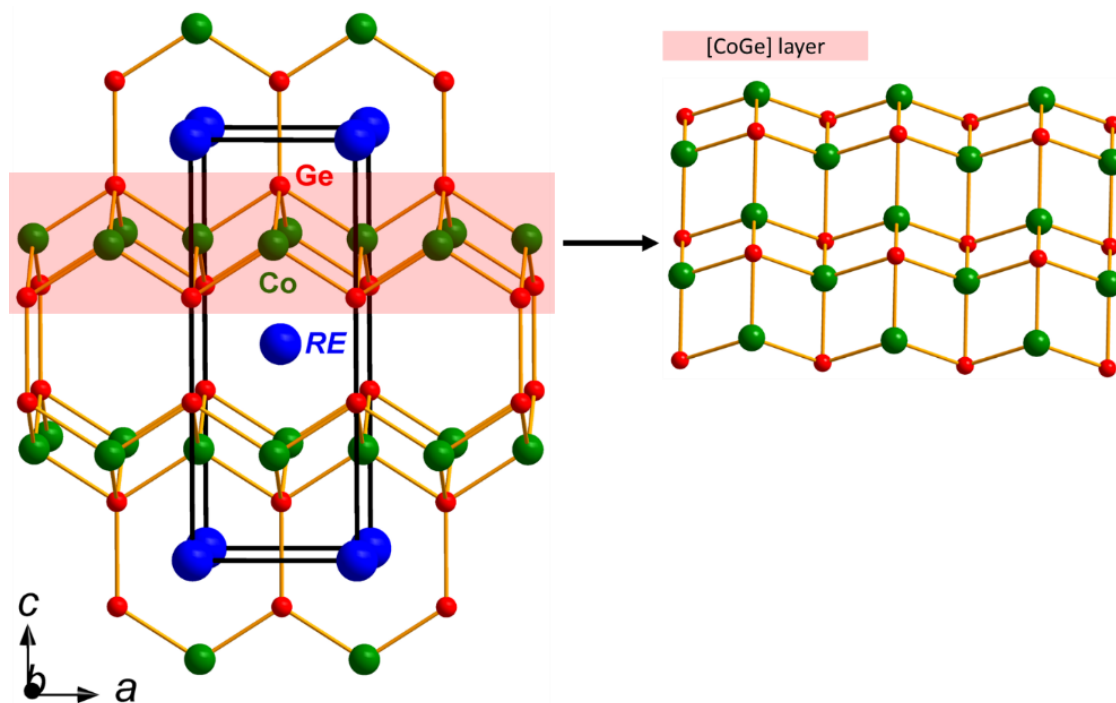
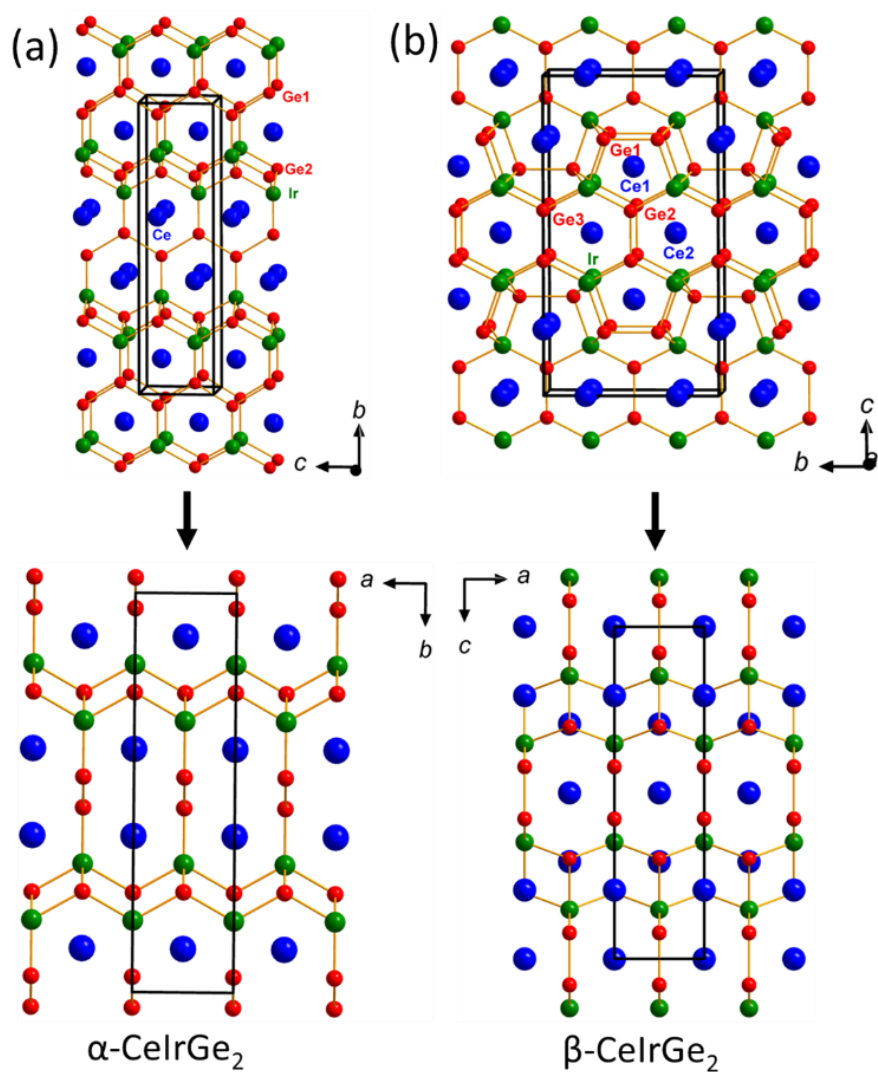


Figure 5-3. Structure of  $\text{RECo}_2\text{Ge}_2$  ( $\text{RE} = \text{Eu}, \text{Yb}$ ).

The Ce–Ir–Ge–In reactions gave crystals with compositions of  $\text{CeIr}_2\text{Ge}_2$  and  $\text{CeIrGe}_2$ . The latter actually occur in two orthorhombic polymorphs, occurring as a result of a peritectoid reaction:  $\text{CeIr}_2\text{Ge}_2 + \alpha\text{-CeIrGe}_2$  (CeNiSi<sub>2</sub>-type,  $Cmcm$ )  $\rightarrow$   $\beta\text{-CeIrGe}_2$  (YIrGe<sub>2</sub>-type,  $Immm$ ). A similar peritectoid reaction was observed in Er–Ni–Ge system.<sup>24</sup> Single-crystal structure determinations were performed here for both forms of  $\text{CeIrGe}_2$ , given that prior analyses were limited to powder XRD data for  $\alpha\text{-CeIrGe}_2$ . Moreover, previously reported determinations of YIrGe<sub>2</sub>-type phases

tended to exhibit high displacement parameters for one of the Ge atoms, suggesting that twinning may be occurring. However, a temperature-dependent study of  $\beta$ -CeIrGe<sub>2</sub> carried out here shows no anomalies down to 193 K. The structures of  $\alpha$ - and  $\beta$ -CeIrGe<sub>2</sub> are closely related (**Figure 5-4**). Both contain Ir-centred square pyramids linked to form a framework within which Ce atoms lie. A key difference is that  $\alpha$ -CeIrGe<sub>2</sub> contains isolated Ge atoms and zigzag Ge chains, whereas  $\beta$ -CeIrGe<sub>2</sub> contains Ge–Ge dimers.



**Figure 5-4.** Structures of  $\alpha$ - and  $\beta$ -CeIrGe<sub>2</sub>.

The structures can be conceptually converted to each other by breaking the bonds within the Ge–Ge dimers in  $\beta$ -CeIrGe<sub>2</sub>, shearing the resulting slabs, and then reassembling them to form Ge zigzag chains in  $\alpha$ -CeIrGe<sub>2</sub> (**Figure 5-5**).

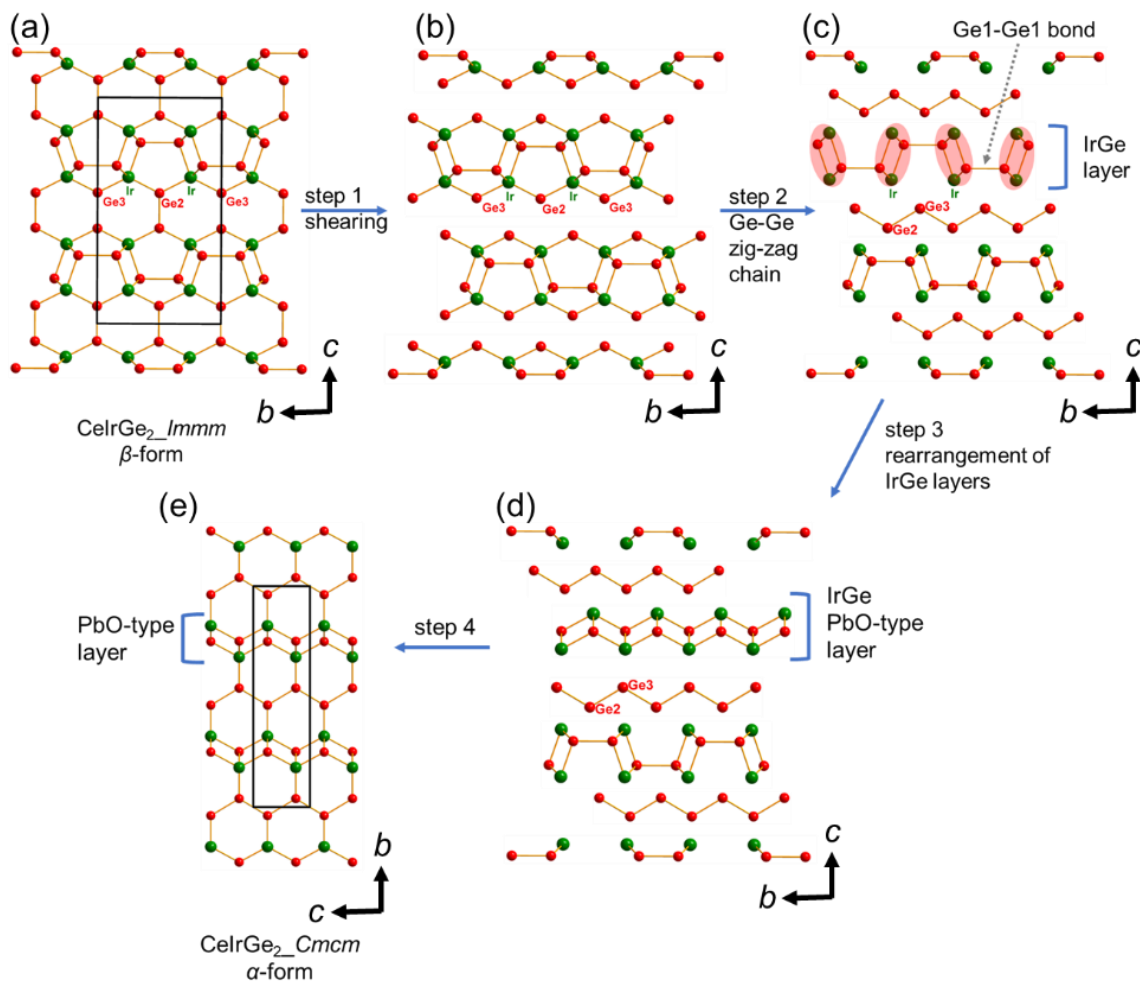


**Figure 5-5.** Conceptual structural conversion between  $\alpha$ - and  $\beta$ -CeIrGe<sub>2</sub>.

Yb<sub>5</sub>Ir<sub>4</sub>Ge<sub>10</sub> was previously characterized by powder XRD data alone, and assigned to have a tetragonal Sc<sub>5</sub>Co<sub>4</sub>Si<sub>10</sub>-type structure.<sup>25,26</sup> This is a relatively complicated structure for which single-crystal diffraction is worthwhile performing. Compared to other members of the RE<sub>5</sub>Ir<sub>4</sub>Ge<sub>10</sub> series, the *c/a* ratio for Yb<sub>5</sub>Ir<sub>4</sub>Ge<sub>10</sub> is anomalously large (**Table A3-2** and **Figure A3-3**). Temperature

dependent single-crystal studies reveal that the cell parameters actually increase on cooling down from room temperature to 193 K. These observations do seem to support the presence of divalent Yb, but further magnetic characterization will be required to confirm this proposal.<sup>27</sup> The structure consists of an  $[\text{Ir}_4\text{Ge}_{10}]$  framework defining three types of tunnels, with pentagonal, hexagonal, and octagonal cross-sections, that propagate along the  $c$ -direction and are filled with Yb atoms (**Figure 5-6**). Ge–Ge dimers with distances of 2.42 to 2.53 Å are also present in the structure. Given that the Rh-containing analogue exhibits strong magnetic anisotropy, as is evident from the tunnel structure, it would be interesting to perform single-crystal magnetization experiments on  $\text{Yb}_5\text{Ir}_4\text{Ge}_{10}$ .

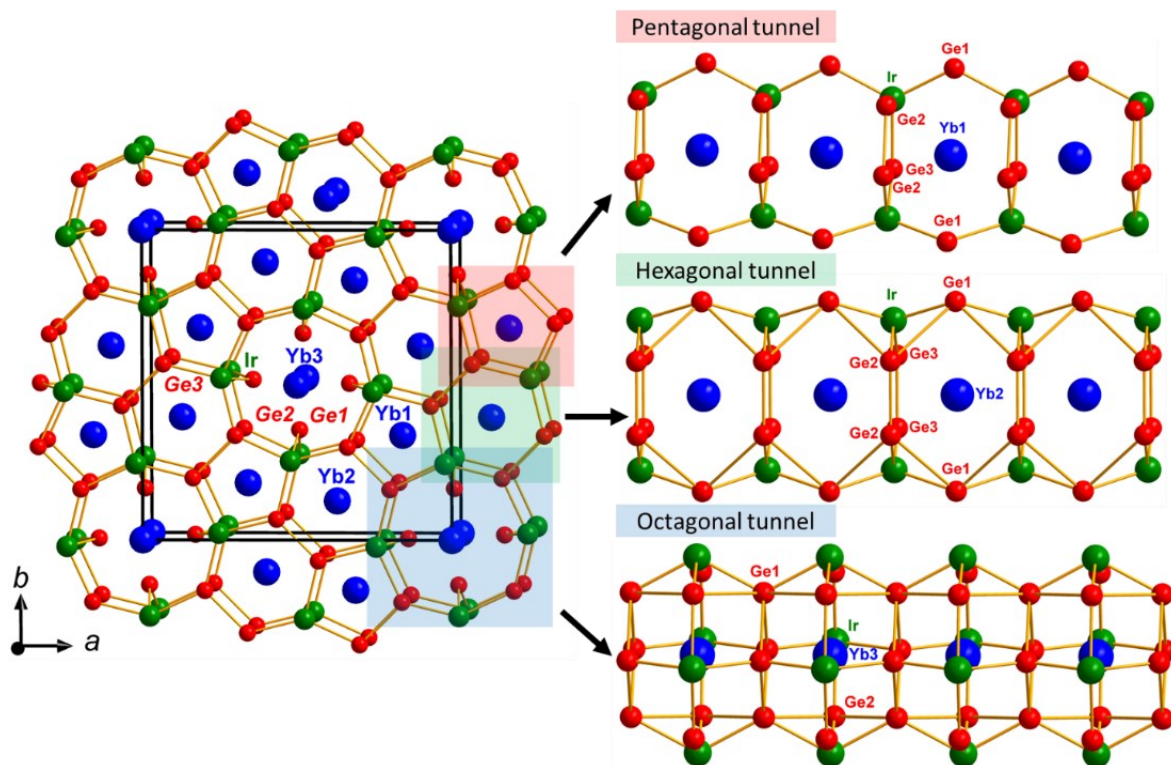


**Figure 5-6.** Structure of  $\text{Yb}_5\text{Ir}_4\text{Ge}_{10}$ , with tunnels propagating along the  $c$ -direction.

## 5.4. Conclusions

Many synthetic attempts were made to prepare crystals of ternary rare-earth germanides within an In flux. Crystals of  $RECo_2Ge_2$  ( $RE = Ce, Eu, Yb$ ),  $CeIr_2Ge_2$ ,  $CeCoGe_2$ ,  $CeIrGe_2$ ,  $EuIr_4In_2Ge_4$ ,  $EuIrGe_3$ ,  $Yb_4Ir_7Ge_6$ , and  $Yb_5Ir_4Ge_{10}$  were obtained. Although many of these compounds were previously known, their structural characterization had been limited to powder XRD data. The availability of good quality crystals thus enabled single-crystal structures to be determined accurately.  $CeIrGe_2$  was obtained as two orthorhombic polymorphs, with a clear structural relationship between them in which Ge–Ge dimers are converted to zigzag Ge chains.  $Yb_5Ir_4Ge_{10}$  exhibits a complex tunnel structure with indications from temperature-dependent data that Yb may be divalent.

## 5.5. References

- (1) Mishra, V.; Subbarao, U.; Roy, S.; Sarma, S. Ch.; Mumbaraddi, D.; Sarkar, S.; Peter, S. C. *Inorg. Chem.* **2018**, *57*, 12576–12587.
- (2) Sarkar, S.; Mumbaraddi, D.; Halappa, P.; Kalsi, D.; Rayaprol, S.; Peter, S. C. *J. Solid State Chem.* **2015**, *229*, 287–295.
- (3) Lattur, S. E.; Bilc, D.; Ireland, J. R.; Kannewurf, C. R.; Mahanti, S. D.; Kanatzidis, M. G. *J. Solid State Chem.* **2003**, *170*, 48–57.
- (4) Salvador, J. R.; Bilc, D.; Gour, J. R.; Mahanti, S. D.; Kanatzidis, M. G. *Inorg. Chem.* **2005**, *44*, 8670–8679.
- (5) Salvador, J. R.; Malliakas, C.; Gour, J. R.; Kanatzidis, M. G. *Chem. Mater.* **2005**, *17*, 1636–1645.
- (6) Kanatzidis, M. G.; Pöttgen, R.; Jeitschko, W. *Angew. Chem.* **2005**, *44*, 6996–7029.
- (7) Villars, P.; Cenzual, K., *Pearson's Crystal Data – Structure Database for Inorganic Compounds*, Release 2021/22, ASM International: Materials Park, OH, USA.
- (8) Voßwinkel, D.; Niehaus, O.; Rodewald, U. Ch; Pöttgen, R. *Z. Naturforsch.* **2012**, *67b*, 1241–1247.
- (9) Fritsch, V.; Pfundstein, P.; Schweiss, P.; Kampert, E.; Pilawa, B.; Löhneysen, H. V. *Phys. Rev. B* **2011**, *84*, 104446.
- (10) Subbarao, U.; Roy, S.; Sarma, S. Ch.; Sarkar, S.; Mishra, V.; Khulbe, Y.; Peter, S. C. *Inorg. Chem.* **2016**, *55*, 10351–10360.
- (11) Kosaka, M.; Michimura, S.; Hirabayashi, H.; Numakura, R.; Iizuka, R.; Kuwahara, K.; Uwatoko, Y. *J. Phys. Soc. Jpn.* **2020**, *89*, 054704.

- (12) Dung, D. N.; Matsuda, T. D.; Haga, Y.; Ikeda, S.; Yamamoto, E.; Ishikura, T.; Endo, T.; Tatsuoka, S.; Aoki, Y.; Sato, H.; Takeuchi, T.; Settai, R.; Harima, H.; Ōnuki, Y. *J. Phys. Soc. Jpn.* **2009**, *78*, 084711.
- (13) Grytsiv, A.; Leithe-Jasper, A.; Flandorfer, H.; Rogl, P.; Hiebl, K.; Godart, C.; Velikanova, T. *J. Alloys Compd.* **1998**, *266*, 7–12.
- (14) Francois, M.; Venturini, G.; Marêché, J. F.; Malaman, et B. B; Roques, B. *J. Less-Common Met.* **1985**, *113*, 231–237.
- (15) Sheldrick, G. M. *Acta Crystallogr., Sect. A: Found. Crystallogr.* **2008**, *64*, 112–122.
- (16) Gelato, L. M.; Parthé, E. *J. Appl. Crystallogr.* **1987**, *20*, 139–143.
- (17) Mallik, R.; Sampathkumaran, E. V.; Paulose, P. L.; Dumschat, J.; Wortmann, G. *Phys. Rev. B* **1997**, *55*, 3627–3630.
- (18) Mathur, N. D.; Frost, C. D. *J. Alloys Compd.* **1994**, *215*, 325–328.
- (19) Niepmann, D.; Pöttgen, R. *Intermetallics* **2001**, *9*, 313–318.
- (20) Heying, B.; Katoh, K.; Niide, Y.; Ochiai, A.; Pöttgen, R. *Z. Anorg. Allg. Chem.* **2004**, *630*, 1423–1426.
- (21) Katoh, K.; Abe, H.; Negishi, D.; Terui, G.; Niide, Y.; Ochiai, A. *J. Magn. Magn. Mater.* **2004**, *279*, 118–124.
- (22) McCall, W. M.; Narasimhan, K. S. V. L.; Butera, R. A. *J. Appl. Cryst.* **1973**, *6*, 301–303.
- (23) Pauling, L.; Kamb, B. *Proc. Nati. Acad. Sci.* **1986**, *83*, 3569–3571.
- (24) Oleksyn, O, Ya.; Bodak, O. I. *Mater. Sci. Forum* **1993**, *133–136*, 529–536.
- (25) Katoh, K.; Tsutsumi, T.; Yamada, K.; Terui, G.; Niide, Y.; Ochiai, A. *Physica B Condens.* **2006**, *373*, 111–119.

- (26) Venturini, G.; Méot-Meyer, M.; Rae, E. Mc.; Marêché, J. F.; Roques, B. *Mat. Res. Bull.* **1984**, *19*, 1647–1652.
- (27) Qiao, Y.; Song, Y.; Sanson, A.; Fan, L.; Sun, Q.; Hu, S.; He, L.; Zhang, H.; Xing, X.; Chen, J. *npj Quantum Materials*. **2021**, *6*, 49.

## Chapter 6.

### Conclusions

This thesis set out to investigate two broad classes of rare-earth compounds, chalcogenides and intermetallics. In the first part, the aims were to expand the number of examples of rare-earth chalcogenides because doing so offers greater possibilities to vary both cations and anions, allowing physical properties to be controlled more finely. In the second part, the aims were to develop ways to grow larger single crystals of rare-earth intermetallics because they are not easily obtained by conventional methods.

Chapters 2 and 3 described efforts to expand a nascent series of chalcogenides,  $RE_3Tt_2Ch_8X$  ( $Tt = Si, Ge$ ;  $Ch = S, Se$ ;  $X = Cl, Br, I$ ). The Si-containing series was known previously, and here, the Ge-containing series was prepared in conjunction with early *RE* metals (La–Nd). These compounds are semiconductors with band gaps ranging from 2.7 to 3.6 eV. Because  $Ce_3Si_2S_8I$  was previously noted to be photoluminescent, a systematic study was made to understand how cation and anion substitutions affect the optical properties. The solid solutions  $RE_3(Ge_{1-x}Si_x)_2S_8I$  and  $Ce_3Si_2(S_{1-y}Se_y)_8I$  were prepared. Substitution with Ge tended to quench the photoluminescence, whereas substitution with Se shifted the emission from blue to green. Because  $Ce^{3+}$  ions are the source of the photoemission, a more realistic system to investigate to avoid self-quenching would be to use  $La_3Si_2(S_{1-y}Se_y)_8I$  as a host material that can be gradually doped with  $Ce^{3+}$  as activator ions.

Chapters 4 and 5 described efforts to exploit metal fluxes to grow single crystals of ternary rare-earth gallides and germanides. In particular, some rare-earth metals, such as Eu and Yb, are not easily amenable to conventional methods of synthesis because of their high volatility during arc-melting or high reactivity with containers. Reactions in the Yb–*M*–Ga systems were performed using

excess Ga as a self or reactive flux. Most of these reactions lead to frequently encountered binary gallides, but a few were successful in giving ternary gallides, including  $\text{YbNi}_3\text{Ga}_9$  and  $\text{YbCu}_3\text{Ga}_8$ . A somewhat well hidden paper had suggested that crystal growth of ternary intermetallic phases in flux reactions can be related to simple descriptors of the components, as summarized in a stability diagram. The results obtained here tend to support the suggestion that melting temperatures and atomic radii are important factors, but it is probably too early to generalize given the limited breadth of reactions examined.  $\text{YbNi}_3\text{Ga}_9$  was confirmed to adopt the ordered  $\text{ErNi}_3\text{Al}_9$ -type structure, but the significant effort required to find an untwinned crystal suggests that stacking faults are likely an inherent feature of related aluminides and gallides  $\text{RENi}_3\text{Tr}_9$  ( $\text{Tr} = \text{Al}, \text{Ga}$ ). This may have important implications for the interpretation of chiral magnetism in these compounds, for which helical magnetic ordering has been proposed, given that the noncentrosymmetry in this structure depends on the occurrence of the long-range ordering of the  $\text{RE}_2\text{Tr}_3$  nets.  $\text{YbCu}_3\text{Ga}_8$  was discovered as a new phase but in small amounts, suggesting that it is probably metastable. Efforts to prepare this phase through other methods, such as induction heating and direct reaction, have so far been unsuccessful. As confirmed by DFT calculations, the bonding in both  $\text{YbNi}_3\text{Ga}_9$  and  $\text{YbCu}_3\text{Ga}_8$ , which are Ga-rich phases, can be viewed in terms of electron transfer from Yb to Ga atoms, which then participate in multicentre bonding with significant covalent character.

Similar reactions in the germanide systems  $\text{RE}-\text{M}-\text{Ge}$  were performed in In fluxes for the much the same reason that crystals are not easily obtained by conventional methods. There is strong interest in preparing crystals because many of these compounds have been implicated as quantum materials, some of which are expected to display anisotropic behaviour given their low-dimensional arrangement of  $\text{RE}$  atoms. Moreover, many of the presumed structures of these ternary germanides are assigned on the basis of powder XRD patterns, so it is desirable to confirm these structures through

more reliable single-crystal XRD studies. Most of these reactions yielded crystals of binary germanides, but a few were successful in leading to reasonably sized crystals of  $RECo_2Ge_2$  ( $RE = Ce, Eu, Yb$ ),  $CeCoGe_2$ ,  $CeIrGe_2$ ,  $Yb_4Ir_7Ge_6$ , and  $Yb_5Ir_4Ge_{10}$ , for which full structure determinations were performed. An unusual peritectoid reaction was observed in which two different polymorphs of  $CeIrGe_2$  were observed. Most of these compounds did not show structural transitions or unusual behaviour when cooled to low temperature, but the unit cell of  $Yb_5Ir_4Ge_{10}$  was found to actually expand slightly, suggesting perhaps a valence change.

Although most of these ternary rare-earth gallides and germanides have no immediately useful technological applications, they are of intense interest to the condensed matter physics community, given the highly correlated electron behaviour that they often exhibit. Preparing suitable samples remains challenging. Many of the physical property measurements are made on powder samples, for which a nagging concern is that secondary or minor phases may obscure conclusions, or worse, mislead. Measurements made on single crystals can help alleviate these concerns because they are, by necessity, single phase. The conditions for crystal growth depends on a case-by-case basis on the particular compound being studied, and it is still not easy to make generalizations on which conditions are best. The work presented in this thesis serve as the first tentative steps to understanding how to optimize these conditions. It would be beneficial to apply techniques, such as in situ X-ray diffraction, to examine more closely what is happening during crystal growth, but these remain very challenging experiments to conduct.

## Bibliography

- (1) Ma, Z.; Mohapatra, J.; Wei, K.; Liu, J. P.; Sun, S. *Chem. Rev.* **2021**, *in Press*.
- (2) Geusic, J. E.; Marcos, H. M.; Van Uitert, L. G. *Appl. Phys. Lett.* **1964**, *4*, 182–184.
- (3) Zheng, B.; Fan, J.; Chen, B.; Qin, X.; Wang, J.; Wang, F.; Deng, R.; Liu, X. *Chem. Rev.* **2022**, *122*, 5519–5603.
- (4) Fang, M.-H.; Bao, Z.; Huang, W.-T.; Liu, R.-S. *Chem. Rev.* **2022**, *122*, 11474–11513.
- (5) Minagawa, K.; Nishiguchi, Y.; Oka, R.; Masui, T. *ACS Omega* **2021**, *6*, 3411–3417.
- (6) Smith, A. E.; Mizoguchi, H.; Delaney, K.; Spaldin, N. A.; Sleight, A. W.; Subramanian, M. *A. J. Am. Chem. Soc.* **2009**, *131*, 17084–17086.
- (7) Kageyama, H.; Hayashi, K.; Maeda, K.; Attfield, J. P.; Hiroi, Z.; Rondinelli, J. M.; Poeppelmeier, K. R. *Nat. Commun.* **2018**, *9*, 772-1–772-15.
- (8) Doussier, C.; Moëlo, Y.; Meerschaut, A.; Léone, P.; Guillot-Deudon, C. *J. Solid State Chem.* **2008**, *181*, 920–934.
- (9) Kumar, R. S.; Hamlin, J. J.; Maple, M. B.; Zhang, Y.; Chen, C.; Baker, J.; Cornelius, A. L.; Zhao, Y.; Xiao, Y.; Sinogeikin, S.; Chow, P. *Appl. Phys. Lett.* **2014**, *105*, 251902.
- (10) Yang, X.; Li, Y.; Shen, C.; Si, B.; Sun, Y.; Tao, Q.; Cao, G.; Xu, Z.; Zhang, F. *Appl. Phys. Lett.* **2013**, *103*, 022410.
- (11) Villars, P.; Cenzual, K., *Pearson's Crystal Data – Crystal Structure Database for Inorganic Compounds*. Release 2022/23, ASM International, Materials Park: Ohio, USA,.
- (12) Johnsen, S.; Liu, Z.; Peters, J. A.; Song, J.-H.; Nguyen, S.; Malliakas, C. D.; Jin, H.; Freeman, A. J.; Wessels, B. W.; Kanatzidis, M. G. *J. Am. Chem. Soc.* **2011**, *133*, 10030–10033.

- (13) Minafra, N.; Kraft, M. A.; Bernges, T.; Li, C.; Schlem, R.; Morgan, B. J.; Zeier, W. G. *Inorg. Chem.* **2020**, *59*, 11009–11019.
- (14) Kavanagh, S. R.; Savory, C. N.; Scanlon, D. O.; Walsh, A. *Mater. Horiz.* **2021**, *8*, 2709–2716.
- (15) Kulbachinskii, V. A.; Kytin, V. G.; Kudryashov, A. A.; Kuznetsov, A. N.; Shevelkov, A. V. *J Solid State Chem.* **2012**, *193*, 154–160.
- (16) Liu, P. -F.; Li, Y. -Y.; Zheng, Y. -J.; Yu, J. -S.; Duan, R. -H.; Chen, H.; Lin, H.; Chen, L.; Wu, L. -M. *Dalton Trans.* **2017**, *46*, 2715–2721.
- (17) Puff, H.; Lorbacher, G.; Heine, D. *Naturwissenschaften* **1969**, *56*, 461.
- (18) Pfitzner, A.; Preitschaft, C.; Rau, F. *Z. Anorg. Allg. Chem.* **2004**, *630*, 75–79.
- (19) Pfitzner, A. *Chem. Eur. J.* **1997**, *3*, 2032–2038.
- (20) Nilges, T.; Reiser, S.; Hong, J. H.; Gaudin, E.; Pfitzner, A. *Phys. Chem. Chem. Phys.* **2002**, *4*, 5888–5894.
- (21) Heerwig, A.; Merkle, R.; Maier, J.; Ruck, M. *J. Solid State Chem.* **2011**, *184*, 191–198.
- (22) Belin, R.; Aldon, L.; Zerouale, A.; Belin, C.; Ribes, M. *Solid State Sci.* **2001**, *3*, 251–265.
- (23) Moro'oka, M.; Ohki, H.; Yamada, K.; Okuda, T. *Bull. Chem. Soc. Jpn.* **2004**, *77*, 975–980.
- (24) Sedlmaier, S. J.; Indris, S.; Dietrich, C.; Yavuz, M.; Dräger, C.; Seggern, F. V.; Sommer, H.; Janek, J. *Chem. Mater.* **2017**, *29*, 1830–1835.
- (25) Liu, Z.; Zinkevich, T.; Indris, S.; He, X.; Liu, J.; Xu, W.; Bai, J.; Xiong, S.; Mo, Y.; Chen, H. *Inorg. Chem.* **2020**, *59*, 226–234.
- (26) Tougait, O.; Ibers, J. A.; Mar, A. *Acta Crystallogr. C* **2003**, *59*, i77–i78.
- (27) Doussier, C.; Léone, P.; Moëlo, Y. *Solid State Sci.* **2004**, *6*, 1387–1391.

- (28) Rosenthal, T.; Döblinger, M.; Wagatha, P.; Gold, C.; Scheidt, E. -W.; Scherer, W.; Oeckler, O. *Z. Anorg. Allg. Chem* **2011**, *637*, 2239–2245.
- (29) Kabbour, H.; Cario, L.; Danot, M.; Meerschaut, A. *Inorg. Chem.* **2006**, *45*, 917–922.
- (30) Jörgens, S.; Mewis, A. *Solid State Sci.* **2007**, *9*, 213–217.
- (31) Pilet, G.; Perrin, A. *Solid State Sci* **2004**, *6*, 109–116.
- (32) Sturza, M.; Allred, J. M.; Malliakas, C. D.; Bugaris, D. E.; Han, F.; Chung, D. Y.; Kanatzidis, M. G. *Chem. Mater.* **2015**, *27*, 3280–3290.
- (33) Lin, H.; Chen, H.; Lin, Z. -X.; Zhao, H. -J.; Liu, P. -F.; Yu, J. -S.; Chen, L. *Inorg. Chem.* **2016**, *55*, 1014–1016.
- (34) Poudeu, P. F.; Söhnle, T.; Ruck, M. *Z. Anorg. Allg. Chem.* **2004**, *630*, 1276–1285.
- (35) Poudeu, P. F.; Ruck, M. *J. Solid State Chem.* **2006**, *179*, 3636–3644.
- (36) Motomitsu, E.; Yanagi, H.; Kamiya, T.; Hirano, M.; Hosono, H. *J. Solid State Chem.* **2006**, *179*, 1668–1673.
- (37) Janka, O.; Schleid, T. *Z. Anorg. Allg. Chem.* **2008**, *634*, 2048.
- (38) Grossholz, H.; Schleid, T. *Z. Anorg. Allg. Chem.* **2002**, *628*, 2169.
- (39) Kang, D. -H.; Ledderboge, F.; Kleinke, H.; Schleid, T. *Z. Anorg. Allg. Chem.* **2015**, *641*, 322–326.
- (40) Sugimoto, T.; Paris, E.; Terashima, K.; Barinov, A.; Giampietri, A.; Wakita, T.; Yokoya, T.; Kajitani, J.; Higashinaka, R.; Matsuda, T. D.; Aoki, Y.; Mizokawa, T.; Saini, N. L. *Phys. Rev. B* **2019**, *100*, 064520.
- (41) Higashinaka, R.; Endo, H.; Kajitani, J.; Matsuda, T. D.; Aoki, Y. *Physica. B Condens. Matter* **2018**, *536*, 824–826.

- (42) Zhai, H. -F.; Zhang, P.; Wu, S. -Q.; He, C. -Y.; Tang, Z. -T.; Jiang, H.; Sun, Y. -L.; Bao, J. -K.; Nowik, I.; Felner, I.; Zeng, Y. -W.; Li, Y. -K.; Xu, X. -F.; Tao, Q.; Xu, Z. -A.; Cao, G. *H. J. Am. Chem. Soc.* **2014**, *136*, 15386–15393.
- (43) Gout, D.; Jobic, S.; Evain, M.; Brec, R. *J. Solid State Chem.* **2001**, *158*, 218–226.
- (44) Gout, D.; Jobic, S.; Evain, M.; Brec, R. *Solid State Sci.* **2001**, *3*, 223–234.
- (45) Mills, A. M.; Ruck, M. *Inorg. Chem.* **2006**, *45*, 5172–5178.
- (46) Bräunling, D.; Leoni, S.; Mills, A. M.; Ruck, M. *Z. Anorg. Allg. Chem* **2008**, *634*, 107–114.
- (47) Tougait, O.; Ibers, J. A. *Inorg. Chem.* **2000**, *39*, 6136–6138.
- (48) Lin, H.; Li, L. H.; Chen, L. *Inorg. Chem.* **2012**, *51*, 4588–4596.
- (49) Hatscher, S. T.; Umland, W. *Mater. Res. Bull.* **2003**, *38*, 99–112.
- (50) Hatscher, S. T.; Umland, W. *Acta Crystallogr., Sect. E , Struct. Rep. Online* **2002**, *58*, i124–i126.
- (51) Hatscher, S. T.; Umland, W. *Z. Anorg. Allg. Chem.* **2002**, *628*, 608–611.
- (52) Riccardi, R.; Gout, D.; Gauthier, G.; Guillen, F.; Jobic, S.; Garcia, A.; Huguenin, D.; Macaudière, P.; Fouassier, C.; Brec, R. *J. Solid State Chem.* **1999**, *147*, 259–268.
- (53) Mumbaraddi, D.; Iyer, A. K.; Üzer, E.; Mishra, V.; Oliynyk, A. O.; Nilges, T.; Mar, A. *J. Solid State Chem.* **2019**, *274*, 162–167.
- (54) Gauthier, G.; Kawasaki, S.; Jobic, S.; Macaudière, P.; Brec, R.; Rouxel, J. *J. Alloys Compd.* **1998**, *275–277*, 46–49.
- (55) Gauthier, G.; Kawasaki, S.; Jobic, S.; Macaudière, P.; Brec, R.; Rouxel, J. *J. Mater. Chem.* **1998**, *8*, 179–186.
- (56) Hatscher, S. T.; Umland, W. *Acta Crystallogr., Sect. E, Struct. Rep. Online* **2002**, *58*, i100–i102.

- (57) Hatscher, S. T.; Umland, W. Z. *Anorg. Allg. Chem.* **2001**, *627*, 2198–2200.
- (58) Charkin, D. O.; Urmanov, A. V.; Kazakov, S. M. *J. Alloys Compd.* **2012**, *516*, 134–138.
- (59) Zhu, W. J.; Huang, Y. Z.; Wu, F.; Dong, C.; Chen, H.; Zhao, Z. X. *Mater. Res. Bull.* **1994**, *29*, 505–508.
- (60) Park, C. -H.; Kykyneshi, R.; Yokochi, A.; Tate, J.; Keszler, D. A. *J. Solid State Chem.* **2007**, *180*, 1672–1677.
- (61) Chen, H.; McClain, R.; He, J.; Zhang, C.; Olding, J. N.; Reis, R.; Bao, J. -K.; Hadar, I.; Spanopoulos, I.; Malliakas, C. D.; He, Y.; Chung, D. Y.; Kwok, W. -K.; Weiss, E. A.; Dravid, V. P.; Wolverton, C.; Kanatzidis, M. G. *J. Am. Chem. Soc.* **2019**, *141*, 17421–17430.
- (62) Stoloff, N. S.; Liu, C. T.; Deevi, S. C. *Intermetallics* **2000**, *8*, 1313–1320.
- (63) Lee, H. -T.; Chen, M. -H. *Mater. Sci. Eng. A* **2002**, *333*, 24–34.
- (64) Pantsyrny, V.; Shikov, A.; Vorobieva, A. *Cryogenics* **2008**, *48*, 354–370.
- (65) Sauthoff, G., *Intermetallics*. VCH: Weinheim, New York, 1995.
- (66) Lys, A.; Fadonougbo, J. O.; Faisal, M.; Suh, J. -Y.; Lee, Y. -S.; Shim, J. -H.; Park, J.; Cho, Y. W. *Hydrogen* **2020**, *1*, 38–63.
- (67) Belo, J. H.; Pereira, A. M.; Ventura, J.; Oliveira, G. N. P.; Araújo, J. P.; Tavares, P. B.; Fernandes, L.; Algarabel, P. A.; Magen, C.; Morellon, L.; Ibarra, M. R. *J. Alloys Compd.* **2012**, *529*, 89–95.
- (68) Kumar, N.; Guin, S. N.; Manna, K.; Shekhar, C.; Felser, C. *Chem. Rev.* **2021**, *121*, 2780–2815.
- (69) Gille, P.; Grin, Y., *Crystal Growth of Intermetallics*. Walter de Gruyter: Berlin, 2019.
- (70) Kanatzidis, M. G.; Pöttgen, R.; Jeitschko, W. *Angew. Chem. Int. Ed.* **2005**, *44*, 6996–7023.

- (71) Chen, X. Z.; Sportouch, S.; Sieve, B.; Brazis, P.; Kannewurf, C. R.; Cowen, J. A.; Patschke, R.; Kanatzidis, M. G. *Chem. Mater.* **1998**, *10*, 3202–3211.
- (72) Sieve, B.; Gray, D. L.; Henning, R.; Bakas, T.; Schultz, A. J.; Kanatzidis, M. G. *Chem. Mater.* **2008**, *20*, 6107–6115.
- (73) Sieve, B.; Chen, X. Z.; Henning, R.; Brazis, P.; Kannewurf, C. R.; Cowen, J. A.; Schultz, A. J.; Kanatzidis, M. G. *J. Am. Chem. Soc.* **2001**, *123*, 7040–7047.
- (74) Kangas, M. J.; Treadwell, L. J.; Haldolaarachchige, N.; McAlpin, J. D.; Young, D. P.; Chan, J. Y. *J. Solid State Chem.* **2013**, *197*, 523–531.
- (75) Zhuravleva, M. A.; Evain, M.; Petricek, V.; Kanatzidis, M. G. *J. Am. Chem. Soc.* **2007**, *129*, 3082–3083.
- (76) Mishra, V.; Subbarao, U.; Roy, S.; Sarma, S. Ch.; Mumbaraddi, D.; Sarkar, S.; Peter, S. C. *Inorg. Chem.* **2018**, *57*, 12576–12587.
- (77) Mishra, V.; Oliynyk, A. O.; Subbarao, U.; Sarma, S. Ch.; Mumbaraddi, D.; Roy, S.; Peter, S. C. *Cryst. Growth Des.* **2018**, *18*, 6091–6099.
- (78) Bugaris, D. E.; Malliakas, C. D.; Bud'ko, S. L.; Calta, N. P.; Chung, D. Y.; Kanatzidis, M. G. *Inorg. Chem.* **2017**, *56*, 14584–14595.
- (79) Peter, S. C.; Subbarao, U.; Sarkar, S.; Vaitheeswaran, G.; Svane, A.; Kanatzidis, M. G. *J. Alloys Compds.* **2014**, *589*, 405–411.
- (80) Subbarao, U.; Roy, S.; Sarma, S. Ch.; Sarkar, S.; Mishra, V.; Khulbe, Y.; Peter, S. C. *Inorg. Chem.* **2016**, *55*, 10351–10360.
- (81) Peter, S. C.; Chondroudi, M.; Malliakas, C. D.; Balasubramanian, M.; Kanatzidis, M. G. *J. Am. Chem. Soc.* **2011**, *133*, 13840–13843.

- (82) Calta, N. P.; Im, J.; Rodriguez, A. P.; Fang, L.; Bugaris, D. E.; Chasapis, T. C.; Freeman, A. J.; Kanatzidis, M. G. *Angew. Chem. Int. Ed.* **2015**, *54*, 9186–9191.
- (83) Bao, J.-K.; Bugaris, D. E.; Zheng, H.; Willa, K.; Welp, U.; Chung, D. Y.; Kanatzidis, M. G. *Phys. Rev. Materials* **2019**, *3*, 024802.
- (84) Chondroudi, M.; Balasubramanian, M.; Welp, U.; Kwok, W. -K.; Kanatzidis, M. G. *Chem. Mater.* **2007**, *19*, 4769–4775.
- (85) Subbarao, U.; Jana, R.; Chondroudi, M.; Balasubramanian, M.; Kanatzidis, M. G.; Peter, S. *C. Dalton Trans.* **2015**, *44*, 5797–5804.
- (86) Chondroudi, M.; Peter, S. C.; Malliakas, C. D.; Balasubramanian, M.; Li, Q.; Kanatzidis, M. G. *Inorg. Chem.* **2011**, *50*, 1184–1193.
- (87) Han, F.; Malliakas, C. D.; Stoumpos, C. C.; Sturza, M.; Claus, H.; Chung, D. Y.; Kanatzidis, M. G. *Phys. Rev. B Condens. Matter* **2013**, *88*, 144511.
- (88) Pfannenschmidt, U.; Pöttgen, R. *Z. Naturforsch.* **2013**, *68b*, 1185–1190.
- (89) Niehaus, O.; Hoffmann, R.-D.; Pöttgen, R. *Z. Naturforsch.* **2016**, *71(8)b*, 919–923.
- (90) Mumbaraddi, D.; Mishra, V.; Lidin, S.; Mar, A. *J. Solid State Chem.* **2022**, *311*, 123157.
- (91) Kubelka, P.; Munk, F., *Z. Tech. Phys* **1931**, *12*, 259–274.
- (92) Makuła, P.; Pacia, M.; Macyk, W. *J. Phys. Chem. Lett.* **2018**, *9*, 6814–6817.
- (93) Hoffmann, R. *Angew. Chem., Int. Ed. Engl.* **1987**, *26*, 846–878.
- (94) Blasse, G.; Bril, A. *Appl. Phys. Lett.* **1967**, *11*, 53–55.
- (95) Hariyani, S.; Brgoch, J. *ACS Appl. Mater. Interfaces* **2021**, *13*, 16669–16676.
- (96) Uheda, K.; Hirosaki, N.; Yamamoto, Y.; Naito, A.; Nakajima, T.; Yamamoto, H. *Electrochem. Solid-State Lett.* **2006**, *9*, H22–H25.

- (97) Kominami, H.; Mjakin, S. V.; Sychov, M. M.; Korsakov, V. G.; Bakhmetjev, V. V.; Sidorova, A. A.; Sosnov, E. A.; Nakanishi, Y.; Hara, K.; Mimura, H. *Opt. Mater.* **2013**, *35*, 1109–1111.
- (98) Yin, L. -J.; Dong, J.; Wang, Y.; Zhang, B.; Zhou, Z. -Y.; Jian, X.; Wu, M.; Xu, X.; Ommen, J. R.; Hintzen, H. T. *J. Phys. Chem. C* **2016**, *120*, 2355–2361.
- (99) Laing, C. C.; Shen, J.; Chica, D. G.; Cuthriell, S. A.; Schaller, R. D.; Wolverton, C.; Kanatzidis, M. G. *Chem. Mater.* **2021**, *33*, 5780–5789.
- (100) Wang, R.; Zhang, X.; He, J.; Bu, K.; Zheng, C.; Lin, J.; Huang, F. *Inorg. Chem.* **2018**, *57*, 1449–1454.
- (101) Yu, P.; Zhou, L.-J.; Chen, L. *J. Am. Chem. Soc.* **2012**, *134*, 2227–2235.
- (102) Lee, S. -P.; Liu, S. -D.; Chan, T. -S.; Chen, T. -M. *ACS Appl. Mater. Interfaces* **2016**, *8*, 9218–9223.
- (103) Kageyama, H.; Hayashi, K.; Maeda, K.; Attfield, J. P.; Hiroi, Z.; Rondinelli, J. M.; Poeppelmeier, K. R. *Nat. Commun.* **2018**, *9*, 772-1–772-15.
- (104) Recham, N.; Chotard, J.-N.; Dupont, L.; Delacourt, C.; Walker, W.; Armand, M.; Tarascon, J.-M. *Nat. Mater.* **2010**, *9*, 68–74.
- (105) Ueda, K.; Inoue, S.; Hirose, S.; Kawazoe, H.; Hosono, H. *Appl. Phys. Lett.* **2000**, *77*, 2701–2703.
- (106) Jansen, M.; Letschert, H. P. *Nature* **2000**, *404*, 980–982.
- (107) Kamihara, Y.; Watanabe, T.; Hirano, M.; Hosono, H. *J. Am. Chem. Soc.* **2008**, *130*, 3296–3297.
- (108) Xiao, J.-R.; Yang, S.-H.; Feng, F.; Xue, H.-G.; Guo, S.-P. *Coord. Chem. Rev.* **2017**, *347*, 23–47.

- (109) Nilges, T.; Nilges, S.; Pfitzner, A.; Doert, T.; Böttcher, P. *Chem. Mater.* **2004**, *16*, 806–812.
- (110) Shi, H.; Ming, W.; Du, M.-H. *Phys. Rev. B* **2016**, *93*, 104108-1–104108-7.
- (111) Li, Y.-Y.; Liu, P.-F.; Hu, L.; Chen, L.; Lin, H.; Zhou, L.-J.; Wu, L.-M. *Adv. Opt. Mater.* **2015**, *3*, 957–966.
- (112) Gauthier, G.; Kawasaki, S.; Jobic, S.; Macaudière, P.; Brec, R.; Rouxel, J. *J. Alloys Compd.* **1998**, *275–277*, 46–49.
- (113) Gauthier, G.; Kawasaki, S.; Jobic, S.; Macaudière, P.; Brec, R.; Rouxel, J. *J. Mater. Chem.* **1998**, *8*, 179–186.
- (114) Riccardi, R.; Gout, D.; Gauthier, G.; Guillen, F.; Jobic, S.; Garcia, A.; Huguenin, D.; Macaudière, P.; Fouassier, C.; Brec, R. *J. Solid State Chem.* **1999**, *147*, 259–268.
- (115) Hatscher, S. T.; Umland, W. *Z. Anorg. Allg. Chem.* **2001**, *627*, 2198–2200.
- (116) Hatscher, S. T.; Umland, W. *Acta Crystallogr., Sect. E, Struct. Rep. Online* **2002**, *58*, i100–i102.
- (117) Hatscher, S. T.; Umland, W. *Z. Anorg. Allg. Chem.* **2002**, *628*, 608–611.
- (118) Hatscher, S. T.; Umland, W. *Mater. Res. Bull.* **2002**, *37*, 1239–1247.
- (119) Hatscher, S. T.; Umland, W. *Acta Crystallogr., Sect. E, Struct. Rep. Online* **2002**, *58*, i124–i126.
- (120) Hatscher, S. T.; Umland, W. *Mater. Res. Bull.* **2003**, *38*, 99–112.
- (121) Coelho, A. A. TOPAS-Academic, version 6, Coelho Software, Brisbane, Australia, 2007.
- (122) Sheldrick, G. M. SHELXTL, version 6.12, Bruker AXS Inc., Madison, WI, 2001.
- (123) Gelato, L. M.; Parthé, E. *J. Appl. Crystallogr.* **1987**, *20*, 139–143.
- (124) Tank, R.; Jepsen, O.; Burkhardt, A.; Andersen, O. K. TB-LMTO-ASA Program, version 4.7, Max Planck Institut für Festkörperforschung, Stuttgart, Germany, 1998.

- (125) Dronskowski, R.; Blöchl, P. E. *J. Phys. Chem.* **1993**, *97*, 8617–8624.
- (126) Kortüm, G. *Reflectance Spectroscopy*, Springer, New York, 1969.
- (127) Gravereau, P.; Es-Sakhi, B.; Fouassier, C. *Acta Crystallogr., Sect. C: Cryst. Struct. Commun.* **1988**, *44*, 1884–1887.
- (128) Villars, P.; Cenzual, K. *Pearson's Crystal Data – Crystal Structure Database for Inorganic Compounds (on DVD)*, Release 2016/17, ASM International, Materials Park, OH, USA.
- (129) Shannon, R. D. *Acta Crystallogr., Sect. A: Cryst. Phys., Diffr., Theor. Gen. Crystallogr.* **1976**, *32*, 751–767.
- (130) Brese, N. E. O'Keeffe, M. *Acta Crystallogr., Sect. B: Struct. Sci.* **1991**, *47*, 192–197.
- (131) Kageyama, H.; Hayashi, K.; Maeda, K.; Attfield, J. P.; Hiroi, Z.; Rondinelli, J. M.; Poeppelmeier, K. R. *Nat. Commun.* **2018**, *9*, 772-1–772-15.
- (132) Harada, J. K.; Charles, N.; Poeppelmeier, K. R.; Rondinelli, J. M. *Adv. Mater.* **2019**, *31*, 1805295.
- (133) Kageyama, H.; Yajima, T.; Tsujimoto, Y.; Yamamoto, T.; Tassel, C.; Kobayashi, Y. *Bull. Chem. Soc. Jpn.* **2019**, *92*, 1349–1357.
- (134) Li, Y.-Y.; Wang, W.-J.; Wang, H.; Lin, H.; Wu, L.-M. *Cryst. Growth Des.* **2019**, *19*, 4172–4192.
- (135) Tripathi, T. S.; Karppinen, M. *Adv. Mater. Interfaces* **2021**, *8*, 2100146.
- (136) Maeda, K.; Takeiri, F.; Kobayashi, G.; Matsuishi, S.; Ogino, H.; Ida, S.; Mori, T.; Uchimoto, Y.; Tanabe, S.; Hasegawa, T.; Imanaka, N.; Kageyama, H. *Bull. Chem. Soc. Jpn.* **2022**, *95*, 26–37.
- (137) Ghorpade, U. V.; Suryawanshi, M. P.; Green, M. A.; Wu, T.; Hao, X.; Ryan, K. M. *Chem. Rev.* **2023**, *123*, 327–378.

- (138) Xiao, J.-R.; Yang, S.-H.; Feng, F.; Xue, H.-G.; Guo, S.-P. *Coord. Chem. Rev.* **2017**, *347*, 23–47.
- (139) Gauthier, G.; Kawasaki, S.; Jobic, S.; Macaudière, P.; Brec, R.; Rouxel, J. *J. Mater. Chem.* **1998**, *8*, 179–186.
- (140) Gauthier, G.; Kawasaki, S.; Jobic, S.; Macaudière, P.; Brec, R.; Rouxel, J. *J. Alloys Compd.* **1998**, *275–277*, 46–49.
- (141) Riccardi, R.; Gout, D.; Gauthier, G.; Guillen, F.; Jobic, S.; Garcia, A.; Huguenin, D.; Macaudière, P.; Fouassier, C.; Brec, R. *J. Solid State Chem.* **1999**, *147*, 259–268.
- (142) Hatscher, S. T.; Urland, W. *Z. Anorg. Allg. Chem.* **2001**, *627*, 2198–2200.
- (143) Hatscher, S. T.; Urland, W. *Mater. Res. Bull.* **2002**, *37*, 1239–1247.
- (144) Hatscher, S. T.; Urland, W. *Z. Anorg. Allg. Chem.* **2002**, *628*, 608–611.
- (145) Hatscher, S. T.; Urland, W. *Acta Crystallogr., Sect. E* **2002**, *58*, i100–i102.
- (146) Lee, S.-P.; Liu, S.-D.; Chan, T.-S.; Chen, T.-M. *Appl. Mater. Interfaces* **2016**, *8*, 9218–9223.
- (147) Ye, S.; Xiao, F.; Pan, Y. X.; Ma, Y. Y.; Zhang, Q. Y. *Mater. Sci. Eng. R* **2010**, *71*, 1–34.
- (148) Smet, P. F.; Moreels, I.; Hens, Z.; Poelman, D. *Materials* **2010**, *3*, 2834–2883.
- (149) Qin, X.; Liu, X.; Huang, W.; Bettinelli, M.; Liu, X. *Chem. Rev.* **2017**, *117*, 4488–4527.
- (150) Mumbaraddi, D.; Iyer, A. K.; Üzer, E.; Mishra, V.; Oliynyk, A. O.; Nilges, T.; Mar, A. *J. Solid State Chem.* **2019**, *274*, 162–167.
- (151) Coelho, A. A. *TOPAS-Academic, version 6*; Coelho Software: Brisbane, Australia, 2007.
- (152) Sheldrick, G. M. *Acta Crystallogr., Sect. A* **2008**, *64*, 112–122.
- (153) Graveriau, P.; Es-Sakhi, B.; Fouassier, C. *Acta Crystallogr., Sect. C* **1988**, *44*, 1884–1887.
- (154) Gelato, L. M.; Parthé, E. *J. Appl. Crystallogr.* **1987**, *20*, 139–143.
- (155) Spek, A. L. *Acta Crystallogr., Sect. D* **2009**, *65*, 148–155.

- (156) Kortüm, G. *Reflectance Spectroscopy*; Springer: New York, 1969; pp 103–169.
- (157) Fairley, N.; Fernandez, V.; Richard-Plouet, M.; Guillot-Deudon, C.; Walton, J.; Smith, E.; Flahaut, D.; Grenier, M.; Biesinger, M.; Tougaard, S.; Morgan, D.; Baltrusaitis, J. *Appl. Surf. Sci. Adv.* **2021**, *5*, 100112.
- (158) Okhotnikov, K.; Charpentier, T.; Cadars, S. *J. Cheminform.* **2016**, *8*, 17.
- (159) Hafner, J. *J. Comput. Chem.* **2008**, *29*, 2044–2078.
- (160) Perdew, J. P.; Burke, K.; Ernzerhof, M. *Phys. Rev. Lett.* **1996**, *77*, 3865–3868.
- (161) Grin, Y.; Savin, A.; Silvi, B. The ELF perspective of chemical bonding. In *The Chemical Bond: Fundamental Aspects of Chemical Bonding*; Frenking, G.; Shaik, S., Eds.; Wiley-VCH: Weinheim, 2014; pp 345–382.
- (162) Momma, K.; Izumi, F. *J. Appl. Crystallogr.* **2011**, *44*, 1272–1276.
- (163) Yu, M.; Trinkle, R. *J. Chem. Phys.* **2011**, *134*, 064111.
- (164) Deringer, V. L.; Tchougréeff, A. L.; Dronskowski, R. *J. Phys. Chem. A* **2011**, *115*, 5461–5466.
- (165) Müller, P. C.; Ertural, C.; Hempelmann, J.; Dronskowski, R. *J. Phys. Chem. C* **2021**, *125*, 7959–7970.
- (166) Maintz, S.; Deringer, V. L.; Tchougréeff, A. L.; Dronskowski, R. *J. Comput. Chem.* **2016**, *37*, 1030–1035.
- (167) Guo, G.-C.; Wang, Y.-G.; Zhuang, J.-N.; Chen, J.-T.; Huang, J.-S.; Zhang, Q. E. *Acta Crystallogr., Sect. C* **1995**, *51*, 2471–2473.
- (168) Sieke, C.; Hartenbach, I.; Schleid, T. *Z. Anorg. Allg. Chem.* **2000**, *626*, 2235–2239.
- (169) Shannon, R. D. *Acta Crystallogr., Sect. A* **1976**, *32*, 751–767.

- (170) Zhi, Y.; Feng, Z.; Mehreen, T.; Liu, X.; Gardner, K.; Li, X.; Guan, B.-O.; Zhang, L.; Vagin, S. I.; Rieger, B.; Meldrum, A. *Inorganics* **2022**, *10*, 101.
- (171) Hariyani, S.; Brgoch, J. *Chem. Mater.* **2020**, *32*, 6640–6649.
- (172) Kanatzidis, M. G.; Pöttgen, R.; Jeitschko, W. *Angew. Chem. Int. Ed.* **2005**, *44*, 6996–7029.
- (173) Phelan, W. A.; Menard, M. C.; Kangas, M. J.; McCandless, G. T.; Drake, B. L.; Chan, J. Y. *Chem. Mater.* **2012**, *24*, 409–420.
- (174) Latturner, S. E. *Acc. Chem. Res.* **2018**, *51*, 40–48.
- (175) Weiland, A.; Frith, M. G.; Lapidus, S. H.; Chan, J. Y. *Chem. Mater.* **2021**, *33*, 7657–7664.
- (176) Westerveld, J. P. A.; Lo Cascio, D. M. R.; Doornik, M. O.; Loeff, P. I.; Bakker, H.; Heijligers, H. J. M.; Bastin, G. F. *J. Less-Common Met.* **1989**, *146*, 189–195.
- (177) Yamashita, T.; Miyazaki, R.; Aoki, Y.; Ohara, S. *J. Phys. Soc. Jpn.* **2012**, *81*, 034705.
- (178) Utsumi, Y.; Sato, H.; Ohara, S.; Yamashita, T.; Mimura, K.; Motonami, S.; Shimada, K.; Ueda, S.; Kobayashi, K.; Yamaoka, H.; Tsujii, N.; Hiraoka, N.; Namatame, H.; Taniguchi, M. *Phys. Rev. B* **2012**, *86*, 115114.
- (179) Matsubayashi, K.; Hirayama, T.; Yamashita, T.; Ohara, S.; Kawamura, N.; Mizumaki, M.; Ishimatsu, N.; Watanabe, S.; Kitagawa, K.; Uwatoko, Y. *Phys. Rev Lett.* **2015**, *114*, 086401.
- (180) Umeo, K.; Otaki, T.; Arai, Y.; Ohara, S.; Takabatake, T. *Phys. Rev. B* **2018**, *98*, 024420.
- (181) Okamura, H.; Takigawa, A.; Yamasaki, T.; Bauer, E. D.; Ohara, S.; Ikemoto, Y.; Moriwaki, T. *Phys. Rev. B* **2019**, *100*, 195112.
- (182) Gladyshevskii, R. E.; Cenzual, K.; Flack, H. D.; Parthé, E. *Acta Crystallogr. B* **1993**, *49*, 468–474.
- (183) Thomas, K. R. Synthesis and characterization of rare earth-nickel-gallium ternary intermetallics, Ph.D. thesis, Louisiana State University, Louisiana, USA, 2010.

- (184) Shevchenko, I. P.; Markiv, V. Ya. *Metally* **1993**, *6*, 183–189.
- (185) Francisco, M. C.; Malliakas, C. D.; Macaluso, R. T.; Prestigiacomo, J.; Haldolaarachchige, N.; Adams, P. W.; Young, D. P.; Jia, Y.; Claus, H.; Gray, K. E.; Kanatzidis, M. G. *J. Am. Chem. Soc.* **2012**, *134*, 12998–13009.
- (186) Mercena, S. G.; Duque, J. G. S.; Silva, L. S.; Lora-Serrano, R.; Amaral, R. P.; Cadogan, J. M.; Garcia, D. J. *J. Alloys Compd.* **2019**, *785*, 105–109.
- (187) Müller, P. C.; Ertural, C.; Hempelmann, J.; Dronskowski, R. *J. Phys. Chem. C* **2021**, *125*, 7959–7970.
- (188) Drake, B. L.; Capan, C.; Cho, J. Y.; Nambu, Y.; Kuga, K.; Xiong, Y. M.; Karki, A. B.; Nakatsuji, S.; Adams, P. W.; Young, D. P.; Chan, J. Y. *J. Phys.: Condens. Matter* **2010**, *22*, 066001.
- (189) Macaluso, R. T.; Francisco, M.; Young, D. P.; Stadler, S.; Mitchell, J. F.; Geiser, U.; Hong, H.-Y.; Kanatzidis, M. G. *J. Solid State Chem.* **2011**, *184*, 3185–3189.
- (190) Mishra, V.; Oliynyk, A. O.; Subbarao, U.; Sarma, S. Ch.; Mumbaraddi, D.; Roy, S.; Peter, S. C. *Cryst. Growth Des.* **2018**, *18*, 6091–6099.
- (191) Sheldrick, G. M. *Acta Crystallogr. A: Found. Crystallogr.* **2008**, *64*, 112–122.
- (192) Gelato, L. M.; Parthé, E. *J. Appl. Crystallogr.* **1987**, *20*, 139–143.
- (193) Kresse, G.; Furthmüller, J. *Phys. Rev. B* **1996**, *54*, 11169–11186.
- (194) Kresse, G.; Joubert, D. *Phys. Rev. B* **1999**, *59*, 1758–1775.
- (195) Blöchl, P. E. *Phys. Rev. B* **1994**, *50*, 17953–17979.
- (196) Perdew, J. P.; Burke, K.; Ernzerhof, M. *Phys. Rev. Lett.* **1996**, *77*, 3865–3868.
- (197) Hohenberg, P.; Kohn, W. *Phys. Rev.* **1964**, *136*, B864–B871.
- (198) Kohn, W.; Sham, L. J. *Phys. Rev.* **1965**, *140*, A1133–A1138.

- (199) Deringer, V. L.; Tchougréeff, A. L.; Dronskowski, R. *J. Phys. Chem. A* **2011**, *115*, 5461–5466.
- (200) Grin, Y.; Savin, A.; Silvi, B., The ELF perspective of chemical bonding. In *The Chemical Bond: Fundamental Aspects of Chemical Bonding*, Frenking, G.; Shaik, S., Eds.; Wiley-VCH: Weinheim, **2014**; pp. 345–382.
- (201) Maintz, S.; Deringer, V. L.; Tchougréeff, A. L.; Dronskowski, R. *J. Comput. Chem.* **2016**, *37*, 1030–1035.
- (202) Verbovytskyy, Yu.; Pereira Gonçalves, A. *Chem. Met. Alloys* **2012**, *5*, 129–135.
- (203) Subbarao, U.; Gutmann, M. J.; Peter, S. C. *Inorg. Chem.* **2013**, *52*, 2219–2227.
- (204) Villars, P.; Cenzual, K. *Pearson's Crystal Data – Crystal Structure Database for Inorganic Compounds*, Release 2021/22, ASM International, Materials Park, OH, USA.
- (205) Matselko, O.; Pukas, S.; Lutsyshyn, Yu.; Gladyshevskii, R.; Kaczorowski, D. *J. Solid State Chem.* **2013**, *198*, 50–56.
- (206) Topertser, V.; Martyniak, R.-I.; Muts, N.; Tokaychuk, Ya.; Gladyshevskii, R. *Chem. Met. Alloys* **2019**, *12*, 21–28.
- (207) Lutsyshyn, Yu.; Tokaychuk, Ya.; Davydov, V.; Gladyshevskii, R. *Chem. Met. Alloys* **2008**, *1*, 303–316.
- (208) Ninomiya, H.; Matsumoto, Y.; Nakamura, S.; Kono, Y.; Kittaka, S.; Sakakibara, T.; Inoue, K.; Ohara, S. *J. Phys. Soc. Jpn.* **2017**, *86*, 124704.
- (209) Silva, L. S.; Mercena, S. G.; Garcia, D. J.; Bittar, E. M.; Jesus, C. B. R.; Pagliuso, P. G.; Lora-Serrano, R.; Meneses, C. T.; Duque, J. G. S. *Phys. Rev. B* **2017**, *95*, 134434.
- (210) Zhuravleva, M. A.; Chen, X. Z.; Wang, X.; Schultz, A. J.; Ireland, J.; Kannewurf, C. K.; Kanatzidis, M. G. *Chem. Mater.* **2002**, *14*, 3066–3081.

- (211) Biehl, E.; Deiseroth, H. J. *Z. Anorg. Allg. Chem.* **1999**, *625*, 1073–1080.
- (212) Wang, F.; Pearson, K. N.; Straszheim, W. E.; Miller, G. J. *Chem. Mater.* **2010**, *22*, 1798–1806.
- (213) Simons, J.; Hempelmann, J.; Fries, K. S.; Müller, P. C.; Dronskowski, R.; Steinberg, S. *RSC Adv.* **2021**, *11*, 20679–20686.
- (214) Ouyang, R.; Curtarolo, S.; Ahmetcik, E.; Scheffler, M.; Ghiringelli, L. M. *Phys. Rev. Mater.* **2018**, *2*, 083802.
- (215) Mishra, V.; Subbarao, U.; Roy, S.; Sarma, S. Ch.; Mumbaraddi, D.; Sarkar, S.; Peter, S. C. *Inorg. Chem.* **2018**, *57*, 12576–12587.
- (216) Sarkar, S.; Mumbaraddi, D.; Halappa, P.; Kalsi, D.; Rayaprol, S.; Peter, S. C. *J. Solid State Chem.* **2015**, *229*, 287–295.
- (217) Lattner, S. E.; Bilc, D.; Ireland, J. R.; Kannewurf, C. R.; Mahanti, S. D.; Kanatzidis, M. *G. J. Solid State Chem.* **2003**, *170*, 48–57.
- (218) Salvador, J. R.; Bilc, D.; Gour, J. R.; Mahanti, S. D.; Kanatzidis, M. G. *Inorg. Chem.* **2005**, *44*, 8670–8679.
- (219) Salvador, J. R.; Malliakas, C.; Gour, J. R.; Kanatzidis, M. G. *Chem. Mater.* **2005**, *17*, 1636–1645.
- (220) Kanatzidis, M. G.; Pöttgen, R.; Jeitschko, W. *Angew. Chem.* **2005**, *44*, 6996–7029.
- (221) Villars, P.; Cenzual, K., *Pearson's Crystal Data – Structure Database for Inorganic Compounds*, Release 2021/22, ASM International: Materials Park, OH, USA.
- (222) Voßwinkel, D.; Niehaus, O.; Rodewald, U. Ch; Pöttgen, R. *Z. Naturforsch.* **2012**, *67b*, 1241–1247.

- (223) Fritsch, V.; Pfundstein, P.; Schweiss, P.; Kampert, E.; Pilawa, B.; Löhneysen, H. V. *Phys. Rev. B* **2011**, *84*, 104446.
- (224) Subbarao, U.; Roy, S.; Sarma, S. Ch.; Sarkar, S.; Mishra, V.; Khulbe, Y.; Peter, S. C. *Inorg. Chem.* **2016**, *55*, 10351–10360.
- (225) Kosaka, M.; Michimura, S.; Hirabayashi, H.; Numakura, R.; Iizuka, R.; Kuwahara, K.; Uwatoko, Y. *J. Phys. Soc. Jpn.* **2020**, *89*, 054704.
- (226) Dung, D. N.; Matsuda, T. D.; Haga, Y.; Ikeda, S.; Yamamoto, E.; Ishikura, T.; Endo, T.; Tatsuoka, S.; Aoki, Y.; Sato, H.; Takeuchi, T.; Settai, R.; Harima, H.; Ōnuki, Y. *J. Phys. Soc. Jpn.* **2009**, *78*, 084711.
- (227) Grytsiv, A.; Leithe-Jasper, A.; Flandorfer, H.; Rogl, P.; Hiebl, K.; Godart, C.; Velikanova, T. *J. Alloys Compd.* **1998**, *266*, 7–12.
- (228) Francois, M.; Venturini, G.; Marêché, J. F.; Malaman, et B. B; Roques, B. *J. Less-Common Met.* **1985**, *113*, 231–237.
- (229) Sheldrick, G. M. *Acta Crystallogr., Sect. A: Found. Crystallogr.* **2008**, *64*, 112–122.
- (230) Gelato, L. M.; Parthé, E. *J. Appl. Crystallogr.* **1987**, *20*, 139–143.
- (231) Mallik, R.; Sampathkumaran, E. V.; Paulose, P. L.; Dumschat, J.; Wortmann, G. *Phys. Rev. B* **1997**, *55*, 3627–3630.
- (232) Mathur, N. D.; Frost, C. D. *J. Alloys Compd.* **1994**, *215*, 325–328.
- (233) Niepmann, D.; Pöttgen, R. *Intermetallics* **2001**, *9*, 313–318.
- (234) Heying, B.; Katoh, K.; Niide, Y.; Ochiai, A.; Pöttgen, R. *Z. Anorg. Allg. Chem.* **2004**, *630*, 1423–1426.
- (235) Katoh, K.; Abe, H.; Negishi, D.; Terui, G.; Niide, Y.; Ochiai, A. *J. Magn. Magn. Mater.* **2004**, *279*, 118–124.

- (236) McCall, W. M.; Narasimhan, K. S. V. L.; Butera, R. A. *J. Appl. Cryst.* **1973**, *6*, 301–303.
- (237) Pauling, L.; Kamb, B. *Proc. Nati. Acad. Sci.* **1986**, *83*, 3569–3571.
- (238) Oleksyn, O. Ya.; Bodak, O. I. *Mater. Sci. Forum* **1993**, *133–136*, 529–536.
- (239) Katoh, K.; Tsutsumi, T.; Yamada, K.; Terui, G.; Niide, Y.; Ochiai, A. *Physica B Condens.* **2006**, *373*, 111–119.
- (240) Venturini, G.; Méot-Meyer, M.; Rae, E. Mc.; Marêché, J. F.; Roques, B. *Mat. Res. Bull.* **1984**, *19*, 1647–1652.
- (241) Qiao, Y.; Song, Y.; Sanson, A.; Fan, L.; Sun, Q.; Hu, S.; He, L.; Zhang, H.; Xing, X.; Chen, J. *npj Quantum Materials.* **2021**, *6*, 49.

## Appendix 1.

### Supplementary Data for Chapter 3

**Table A1-1.** Cell Parameters and Refinement Agreement Factors for  $\text{RE}_3(\text{Ge}_{1-x}\text{Si}_x)_2\text{S}_8\text{I}$  and  $\text{Ce}_3\text{Si}_2(\text{S}_{1-y}\text{Se}_y)_8\text{I}$

nominal composition	$x$ or $y$	$a$ (Å)	$b$ (Å)	$c$ (Å)	$\beta$ (deg.)	$R_p$	$R_{wp}$
<b><math>\text{La}_3(\text{Ge}_{1-x}\text{Si}_x)_2\text{S}_8\text{I}</math></b>							
$\text{La}_3\text{Ge}_2\text{S}_8\text{I}$	0	16.1616(1)	7.9812(1)	11.0259(1)	98.17(1)	0.095	0.146
$\text{La}_3\text{Ge}_{1.50}\text{Si}_{0.50}\text{S}_8\text{I}$	0.250	16.1523(2)	7.9691(2)	11.0086(2)	98.11(1)	0.088	0.134
$\text{La}_3\text{Ge}_{1.00}\text{Si}_{1.00}\text{S}_8\text{I}$	0.500	16.1229(2)	7.9458(2)	10.9770(2)	98.04(1)	0.101	0.155
$\text{La}_3\text{Ge}_{0.50}\text{Si}_{1.50}\text{S}_8\text{I}$	0.750	16.1112(1)	7.9312(1)	10.9563(1)	97.99(1)	0.084	0.120
$\text{La}_3\text{Si}_2\text{S}_8\text{I}$	1.000	16.0917(1)	7.9130(1)	10.9292(1)	97.96(1)	0.067	0.095
<b><math>\text{Ce}_3(\text{Ge}_{1-x}\text{Si}_x)_2\text{S}_8\text{I}</math></b>							
$\text{Ce}_3\text{Ge}_2\text{S}_8\text{I}$	0	16.0436(1)	7.9184(1)	10.9640(1)	98.27(1)	0.087	0.126
$\text{Ce}_3\text{Ge}_{1.50}\text{Si}_{0.50}\text{S}_8\text{I}$	0.250	16.0272(1)	7.9040(1)	10.9439(1)	98.16(1)	0.095	0.155
$\text{Ce}_3\text{Ge}_{1.00}\text{Si}_{1.00}\text{S}_8\text{I}$	0.500	16.0077(1)	7.8869(1)	10.9192(1)	98.06(1)	0.099	0.150
$\text{Ce}_3\text{Ge}_{0.50}\text{Si}_{1.50}\text{S}_8\text{I}$	0.750	15.9870(1)	7.8693(1)	10.8937(1)	97.98(1)	0.072	0.109
$\text{Ce}_3\text{Si}_2\text{S}_8\text{I}$	1.000	15.9739(1)	7.8574(1)	10.8744(1)	97.94(1)	0.061	0.081
<b><math>\text{Ce}_3\text{Si}_2(\text{S}_{1-y}\text{Se}_y)_8\text{I}</math></b>							
$\text{Ce}_3\text{Si}_2\text{S}_8\text{I}$	0	15.9739(1)	7.8574(1)	10.8744(1)	97.94(1)	0.061	0.081
$\text{Ce}_3\text{Si}_2\text{S}_{7.75}\text{Se}_{0.25}\text{I}$	0.031	15.9657(1)	7.8520(1)	10.8654(1)	97.86(1)	0.052	0.076
$\text{Ce}_3\text{Si}_2\text{S}_{7.50}\text{Se}_{0.50}\text{I}$	0.062	16.0102(1)	7.8734(1)	10.8947(1)	97.80(1)	0.044	0.066
$\text{Ce}_3\text{Si}_2\text{S}_{7.25}\text{Se}_{0.75}\text{I}$	0.094	16.0317(1)	7.8838(1)	10.9071(1)	97.72(1)	0.050	0.076
$\text{Ce}_3\text{Si}_2\text{S}_{7.00}\text{Se}_{1.00}\text{I}$	0.125	16.0413(1)	7.8882(1)	10.9120(1)	97.67(1)	0.050	0.076
$\text{Ce}_3\text{Si}_2\text{S}_{6.50}\text{Se}_{1.50}\text{I}$	0.188	16.0666(1)	7.9017(1)	10.9308(1)	97.61(1)	0.071	0.102
$\text{Ce}_3\text{Si}_2\text{S}_{6.00}\text{Se}_{2.00}\text{I}$	0.250	16.0929(3)	7.9146(2)	10.9484(2)	97.56(1)	0.051	0.075
$\text{Ce}_3\text{Si}_2\text{S}_{5.00}\text{Se}_{3.00}\text{I}$	0.375	16.1394(4)	7.9415(3)	10.9885(4)	97.48(1)	0.057	0.077
$\text{Ce}_3\text{Si}_2\text{S}_{4.00}\text{Se}_{4.00}\text{I}$	0.500	16.2308(3)	8.0005(2)	11.0896(3)	97.45(1)	0.063	0.091
$\text{Ce}_3\text{Si}_2\text{S}_{3.00}\text{Se}_{5.00}\text{I}$	0.625	16.2955(4)	8.0403(3)	11.1708(4)	97.47(1)	0.070	0.098
$\text{Ce}_3\text{Si}_2\text{S}_{2.00}\text{Se}_{6.00}\text{I}$	0.750	16.3643(3)	8.0774(2)	11.2539(2)	97.54(1)	0.064	0.090
$\text{Ce}_3\text{Si}_2\text{S}_{1.00}\text{Se}_{7.00}\text{I}$	0.875	16.4218(2)	8.1028(2)	11.3232(2)	97.67(1)	0.069	0.092
$\text{Ce}_3\text{Si}_2\text{Se}_8\text{I}$	1	16.5277(7)	8.1430(5)	11.4193(7)	98.06(1)	0.064	0.091
<b><math>\text{Pr}_3(\text{Ge}_{1-x}\text{Si}_x)_2\text{S}_8\text{I}</math></b>							
$\text{Pr}_3\text{Ge}_2\text{S}_8\text{I}$	0	15.9810(5)	7.8786(3)	10.9272(5)	98.47(1)	0.059	0.092
$\text{Pr}_3\text{Ge}_{1.50}\text{Si}_{0.50}\text{S}_8\text{I}$	0.250	15.9533(2)	7.8577(1)	10.8986(2)	98.30(1)	0.111	0.160
$\text{Pr}_3\text{Ge}_{1.00}\text{Si}_{1.00}\text{S}_8\text{I}$	0.500	15.9329(3)	7.8426(2)	10.8730(3)	98.17(1)	0.082	0.124
$\text{Pr}_3\text{Ge}_{0.50}\text{Si}_{1.50}\text{S}_8\text{I}$	0.750	15.9116(4)	7.8260(3)	10.8495(4)	98.06(1)	0.111	0.172
$\text{Pr}_3\text{Si}_2\text{S}_8\text{I}$	1.000	15.8956(1)	7.8131(1)	10.8281(1)	97.99(1)	0.107	0.166

**Table A1-2.** EDX Analyses (mol. %) for  $RE_3(\text{Ge}_{1-x}\text{Si}_x)_2\text{S}_8\text{I}$  and  $\text{Ce}_3\text{Si}_2(\text{S}_{1-y}\text{Se}_y)_8\text{I}$ 

nominal composition	$x$ or $y$	$RE$	Ge	Si	S	Se	I
<b><math>\text{La}_3(\text{Ge}_{1-x}\text{Si}_x)_2\text{S}_8\text{I}</math></b>							
$\text{La}_3\text{Ge}_2\text{S}_8\text{I}$	0	22.0	14.1	0	54.6	0	9.3
$\text{La}_3\text{Ge}_{1.75}\text{Si}_{0.25}\text{S}_8\text{I}$	0.125	23.9	13.2	3.5	42.4	0	17.1
$\text{La}_3\text{Ge}_{1.50}\text{Si}_{0.50}\text{S}_8\text{I}$	0.250	25.3	11.8	5.4	39.7	0	17.8
$\text{La}_3\text{Ge}_{1.25}\text{Si}_{0.75}\text{S}_8\text{I}$	0.375	22.1	8.3	6.2	44.4	0	18.9
$\text{La}_3\text{Ge}_{1.00}\text{Si}_{1.00}\text{S}_8\text{I}$	0.500	24.5	7.8	8.0	43.4	0	16.3
$\text{La}_3\text{Ge}_{0.75}\text{Si}_{1.25}\text{S}_8\text{I}$	0.625	24.1	6.3	10.6	45.6	0	13.3
$\text{La}_3\text{Ge}_{0.50}\text{Si}_{1.50}\text{S}_8\text{I}$	0.750	25.2	4.7	13.0	43.6	0	13.4
$\text{La}_3\text{Ge}_{0.25}\text{Si}_{1.75}\text{S}_8\text{I}$	0.875	24.3	2.5	14.5	44.8	0	13.8
$\text{La}_3\text{Si}_2\text{S}_8\text{I}$	1.000	23.2	0	15.5	53.6	0	7.7
<b><math>\text{Ce}_3(\text{Ge}_{1-x}\text{Si}_x)_2\text{S}_8\text{I}</math></b>							
$\text{Ce}_3\text{Ge}_2\text{S}_8\text{I}$	0	23.0	16.0	0	50.9	0	10.1
$\text{Ce}_3\text{Ge}_{1.75}\text{Si}_{0.25}\text{S}_8\text{I}$	0.125	25.5	13.8	3.6	50.0	0	7.0
$\text{Ce}_3\text{Ge}_{1.50}\text{Si}_{0.50}\text{S}_8\text{I}$	0.250	27.6	13.4	4.2	45.2	0	9.6
$\text{Ce}_3\text{Ge}_{1.25}\text{Si}_{0.75}\text{S}_8\text{I}$	0.375	23.1	11.9	7.4	44.0	0	13.6
$\text{Ce}_3\text{Ge}_{1.00}\text{Si}_{1.00}\text{S}_8\text{I}$	0.500	31.6	8.5	8.2	43.8	0	7.8
$\text{Ce}_3\text{Ge}_{0.75}\text{Si}_{1.25}\text{S}_8\text{I}$	0.625	25.0	6.8	10.5	49.7	0	8.0
$\text{Ce}_3\text{Ge}_{0.50}\text{Si}_{1.50}\text{S}_8\text{I}$	0.750	26.3	2.9	10.1	53.5	0	7.2
$\text{Ce}_3\text{Ge}_{0.45}\text{Si}_{1.55}\text{S}_8\text{I}$	0.775	26.2	2.8	13.0	50.5	0	7.5
$\text{Ce}_3\text{Ge}_{0.40}\text{Si}_{1.60}\text{S}_8\text{I}$	0.800	26.6	2.5	13.7	49.0	0	8.2
$\text{Ce}_3\text{Ge}_{0.35}\text{Si}_{1.65}\text{S}_8\text{I}$	0.825	25.7	2.8	13.2	49.7	0	8.6
$\text{Ce}_3\text{Ge}_{0.30}\text{Si}_{1.70}\text{S}_8\text{I}$	0.850	27.1	3.2	16.4	45.3	0	8.0
$\text{Ce}_3\text{Ge}_{0.25}\text{Si}_{1.75}\text{S}_8\text{I}$	0.875	27.1	1.4	12.1	51.4	0	8.1
$\text{Ce}_3\text{Ge}_{0.20}\text{Si}_{1.80}\text{S}_8\text{I}$	0.900	26.1	2.5	14.7	49.3	0	7.5
$\text{Ce}_3\text{Ge}_{0.15}\text{Si}_{1.85}\text{S}_8\text{I}$	0.925	25.0	1.1	15.1	50.6	0	8.3
$\text{Ce}_3\text{Ge}_{0.10}\text{Si}_{1.90}\text{S}_8\text{I}$	0.950	24.8	1.7	16.0	49.6	0	7.8
$\text{Ce}_3\text{Ge}_{0.05}\text{Si}_{1.95}\text{S}_8\text{I}$	0.975	24.3	1.0	17.0	50.3	0	7.4
$\text{Ce}_3\text{Si}_2\text{S}_8\text{I}$	1.000	25.2	0	15.2	52.3	0	7.3
<b><math>\text{Ce}_3\text{Si}_2(\text{S}_{1-y}\text{Se}_y)_8\text{I}</math></b>							
$\text{Ce}_3\text{Si}_2\text{S}_8\text{I}$	0	25.2	0	15.2	52.3	0	7.2
$\text{Ce}_3\text{Si}_2\text{S}_{7.95}\text{Se}_{0.05}\text{I}$	0.006	24.0	0	13.6	51.6	0.1	10.6
$\text{Ce}_3\text{Si}_2\text{S}_{7.90}\text{Se}_{0.10}\text{I}$	0.012	24.7	0	17.9	47.0	0.2	10.2
$\text{Ce}_3\text{Si}_2\text{S}_{7.85}\text{Se}_{0.15}\text{I}$	0.019	23.8	0	15.2	52.2	0.5	8.4
$\text{Ce}_3\text{Si}_2\text{S}_{7.80}\text{Se}_{0.20}\text{I}$	0.025	23.9	0	15.2	48.2	2.2	10.5
$\text{Ce}_3\text{Si}_2\text{S}_{7.75}\text{Se}_{0.25}\text{I}$	0.031	24.3	0	15.4	51.3	1.1	7.9

Ce <sub>3</sub> Si <sub>2</sub> S <sub>7.50</sub> Se <sub>0.50</sub> I	0.062	26.6	0	15.4	42.7	4.0	11.2
Ce <sub>3</sub> Si <sub>2</sub> S <sub>7.25</sub> Se <sub>0.75</sub> I	0.094	25.4	0	16.0	42.9	6.5	9.2
Ce <sub>3</sub> Si <sub>2</sub> S <sub>7.00</sub> Se <sub>1.00</sub> I	0.125	26.4	0	17.8	38.1	8.5	9.3
Ce <sub>3</sub> Si <sub>2</sub> S <sub>6.75</sub> Se <sub>1.25</sub> I	0.156	26.9	0	16.6	39.6	6.8	10.2
Ce <sub>3</sub> Si <sub>2</sub> S <sub>6.50</sub> Se <sub>1.50</sub> I	0.188	25.0	0	17.2	39.8	9.0	9.0
Ce <sub>3</sub> Si <sub>2</sub> S <sub>6.00</sub> Se <sub>2.00</sub> I	0.250	19.4	0	16.3	36.2	12.4	15.7
Ce <sub>3</sub> Si <sub>2</sub> S <sub>5.00</sub> Se <sub>3.00</sub> I	0.375	19.6	0	22.1	27.7	18.3	12.3
Ce <sub>3</sub> Si <sub>2</sub> S <sub>4.00</sub> Se <sub>4.00</sub> I	0.500	17.6	0	18.0	25.7	29.8	8.6
Ce <sub>3</sub> Si <sub>2</sub> S <sub>3.00</sub> Se <sub>5.00</sub> I	0.625	17.9	0	15.2	22.1	34.7	10.0
Ce <sub>3</sub> Si <sub>2</sub> S <sub>2.00</sub> Se <sub>6.00</sub> I	0.750	18.6	0	15.5	13.8	44.6	7.5
Ce <sub>3</sub> Si <sub>2</sub> S <sub>1.00</sub> Se <sub>7.00</sub> I	0.875	20.2	0	14.8	5.9	43.0	16.1
Ce <sub>3</sub> Si <sub>2</sub> Se <sub>8</sub> I	1.000	18.8	0	14.9	0	54.4	11.8
<b>Pr<sub>3</sub>(Ge<sub>1-x</sub>Si<sub>x</sub>)<sub>2</sub>S<sub>8</sub>I</b>							
Pr <sub>3</sub> Ge <sub>2</sub> S <sub>8</sub> I	0	20.0	13.8	0	48.2	0	18.0
Pr <sub>3</sub> Ge <sub>1.75</sub> Si <sub>0.25</sub> S <sub>8</sub> I	0.125	16.2	18.0	3.8	51.8	0	10.2
Pr <sub>3</sub> Ge <sub>1.50</sub> Si <sub>0.50</sub> S <sub>8</sub> I	0.250	22.8	15.8	6.6	37.9	0	16.8
Pr <sub>3</sub> Ge <sub>1.25</sub> Si <sub>0.75</sub> S <sub>8</sub> I	0.375	17.4	12.4	7.4	52.2	0	10.5
Pr <sub>3</sub> Ge <sub>1.00</sub> Si <sub>1.00</sub> S <sub>8</sub> I	0.500	23.2	7.4	9.2	44.8	0	15.4
Pr <sub>3</sub> Ge <sub>0.75</sub> Si <sub>1.25</sub> S <sub>8</sub> I	0.625	21.2	5.5	13.0	44.0	0	16.3
Pr <sub>3</sub> Ge <sub>0.50</sub> Si <sub>1.50</sub> S <sub>8</sub> I	0.750	22.4	3.9	12.2	41.4	0	20.1
Pr <sub>3</sub> Ge <sub>0.25</sub> Si <sub>1.75</sub> S <sub>8</sub> I	0.875	23.0	1.6	16.2	45.9	0	13.2
Pr <sub>3</sub> Si <sub>2</sub> S <sub>8</sub> I	1.000	17.6	0	16.0	57.8	0	8.6

**Table A1-3.** Crystallographic Data for  $RE_3(\text{Ge}_{1-x}\text{Si}_x)_2\text{S}_8\text{I}$  and  $\text{Ce}_3\text{Si}_2(\text{S}_{1-y}\text{Se}_y)_8\text{I}$ 

nominal composition	$\text{La}_3\text{Ge}_{1.5}\text{Si}_{0.5}\text{S}_8\text{I}$	$\text{La}_3\text{GeSiS}_8\text{I}$	$\text{La}_3\text{Ge}_{0.5}\text{Si}_{1.5}\text{S}_8\text{I}$	$\text{Ce}_3\text{Ge}_{1.5}\text{Si}_{0.5}\text{S}_8\text{I}$	$\text{Ce}_3\text{GeSiS}_8\text{I}$
refined composition	$\text{La}_3\text{Ge}_{1.55(1)}\text{Si}_{0.45(1)}\text{S}_8\text{I}$	$\text{La}_3\text{Ge}_{0.98(2)}\text{Si}_{1.02(2)}\text{S}_8\text{I}$	$\text{La}_3\text{Ge}_{0.52(1)}\text{Si}_{1.48(1)}\text{S}_8\text{I}$	$\text{Ce}_3\text{Ge}_{1.55(1)}\text{Si}_{0.45(1)}\text{S}_8\text{I}$	$\text{Ce}_3\text{Ge}_{0.96(2)}\text{Si}_{1.04(2)}\text{S}_8\text{I}$
formula mass (amu)	923.04	900.79	878.54	926.67	908.42
space group	$C2/c$ (No. 15)				
$a$ (Å)	16.1274(13)	16.127(2)	16.137(16)	16.0237(10)	16.014(2)
$b$ (Å)	7.9621(6)	7.9458(11)	7.921(8)	7.8998(5)	7.8845(11)
$c$ (Å)	10.9988(9)	10.9756(15)	10.959(11)	10.9439(7)	10.9249(15)
$\beta$ (deg.)	98.0961(15)	98.019(3)	97.957(18)	98.1716(10)	98.063(3)
$V$ (Å <sup>3</sup> )	1398.26(19)	1392.7(3)	1387(2)	1371.26(15)	1365.8(3)
$Z$	4	4	4	4	4
$T$ (K)	296(2)	296(2)	296(2)	296(2)	296(2)
$\rho_{\text{calcd}}$ (g cm <sup>-3</sup> )	4.385	4.296	4.206	4.489	4.398
crystal dimensions (mm)	$0.09 \times 0.08 \times 0.04$	$0.10 \times 0.10 \times 0.07$	$0.14 \times 0.10 \times 0.08$	$0.16 \times 0.10 \times 0.06$	$0.13 \times 0.10 \times 0.06$
$\mu$ (Mo $K\alpha$ ) (mm <sup>-1</sup> )	15.56	14.61	13.65	16.48	15.52
transmission factors	0.384–0.628	0.446–0.515	0.422–0.494	0.231–0.464	0.347–0.460
$2\theta$ limits	5.10–57.83°	5.10–61.84°	5.10–61.70°	5.14–61.26°	5.14–61.37°
data collected	$-21 \leq h \leq 21, -10 \leq k \leq 10, -14 \leq l \leq 14$	$-23 \leq h \leq 23, -11 \leq k \leq 11, -15 \leq l \leq 15$	$-23 \leq h \leq 23, -11 \leq k \leq 11, -15 \leq l \leq 15$	$-22 \leq h \leq 22, -11 \leq k \leq 11, -15 \leq l \leq 15$	$-22 \leq h \leq 22, -11 \leq k \leq 11, -15 \leq l \leq 15$
no. of data collected	7078	8412	8281	8154	8155
no. of unique data, including $F_o^2 < 0$	1848 ( $R_{\text{int}} = 0.057$ )	2189 ( $R_{\text{int}} = 0.093$ )	2174 ( $R_{\text{int}} = 0.066$ )	2122 ( $R_{\text{int}} = 0.040$ )	2121 ( $R_{\text{int}} = 0.094$ )
no. of unique data, with $F_o^2 > 2\sigma(F_o^2)$	1431	1512	1689	1806	1484
no. of variables	67	66	66	66	66
$R(F)$ for $F_o^2 > 2\sigma(F_o^2)$ <sup>a</sup>	0.037	0.052	0.044	0.026	0.047
$R_w(F_o^2)$ <sup>b</sup>	0.084	0.141	0.113	0.054	0.124
goodness of fit	1.12	1.03	1.12	1.11	1.06
$(\Delta\rho)_{\text{max}}, (\Delta\rho)_{\text{min}}$ (e Å <sup>-3</sup> )	2.39, -1.66	3.35, -2.45	2.75, -2.66	1.52, -1.35	3.00, -2.36

**Table A1-3.** (Cont.)

nominal composition	Ce <sub>3</sub> Ge <sub>0.5</sub> Si <sub>1.5</sub> S <sub>8</sub> I	Ce <sub>3</sub> Si <sub>2</sub> S <sub>7.5</sub> Se <sub>0.5</sub> I	Ce <sub>3</sub> Si <sub>2</sub> S <sub>7</sub> SeI	Ce <sub>3</sub> Si <sub>2</sub> S <sub>4</sub> Se <sub>4</sub> I	Ce <sub>3</sub> Si <sub>2</sub> Se <sub>8</sub> I
refined composition	Ce <sub>3</sub> Ge <sub>0.43(1)</sub> Si <sub>1.57(1)</sub> S <sub>8</sub> I	Ce <sub>3</sub> Si <sub>2</sub> S <sub>7.55(1)</sub> Se <sub>0.45(1)</sub> I	Ce <sub>3</sub> Si <sub>2</sub> S <sub>7.00(2)</sub> Se <sub>1.00(2)</sub> I	Ce <sub>3</sub> Si <sub>2</sub> S <sub>4.21(1)</sub> Se <sub>3.79(1)</sub> I	Ce <sub>3</sub> Si <sub>2</sub> Se <sub>8</sub> I
formula mass (amu)	882.17	883.37	906.82	1047.52	1235.12
space group	<i>C2/c</i> (No. 15)	<i>C2/c</i> (No. 15)	<i>C2/c</i> (No. 15)	<i>C2/c</i> (No. 15)	<i>C2/c</i> (No. 15)
<i>a</i> (Å)	15.9844(11)	15.9941(12)	16.046(2)	16.2256(8)	16.5161(18)
<i>b</i> (Å)	7.8676(6)	7.8706(6)	7.8872(11)	7.9960(4)	8.1336(9)
<i>c</i> (Å)	10.8912(8)	10.8909(8)	10.9161(16)	11.0865(5)	11.4124(12)
$\beta$ (deg.)	98.0066(14)	97.8085(13)	97.689(3)	97.4601(7)	98.100(2)
<i>V</i> (Å <sup>3</sup> )	1356.31(17)	1358.27(18)	1369.1(3)	1426.19(12)	1517.8(3)
<i>Z</i>	4	4	4	4	4
<i>T</i> (K)	296(2)	296(2)	296(2)	296(2)	296(2)
$\rho_{\text{calcd}}$ (g cm <sup>-3</sup> )	4.320	4.320	4.399	4.879	5.405
crystal dimensions (mm)	0.08 × 0.08 × 0.06	0.10 × 0.09 × 0.05	0.12 × 0.07 × 0.07	0.14 × 0.11 × 0.10	0.07 × 0.06 × 0.05
$\mu$ (Mo <i>K</i> $\alpha$ ) (mm <sup>-1</sup> )	14.58	14.78	15.92	22.50	30.18
transmission factors	0.446–0.569	0.312–0.634	0.378–0.491	0.133–0.252	0.266–0.457
$2\theta$ limits	5.15–63.63°	5.14–57.83°	5.12–61.60°	5.06–63.33°	4.98–63.66°
data collected	$-23 \leq h \leq 23, -11 \leq k \leq 11, -16 \leq l \leq 16$	$-21 \leq h \leq 21, -10 \leq k \leq 10, -14 \leq l \leq 14$	$-22 \leq h \leq 23, -11 \leq k \leq 11, -15 \leq l \leq 15$	$-23 \leq h \leq 23, -11 \leq k \leq 11, -16 \leq l \leq 16$	$-24 \leq h \leq 24, -12 \leq k \leq 12, -16 \leq l \leq 16$
no. of data collected	8916	6861	8223	9254	9919
no. of unique data, including $F_o^2 < 0$	2322 ( $R_{\text{int}} = 0.060$ )	1789 ( $R_{\text{int}} = 0.031$ )	2144 ( $R_{\text{int}} = 0.116$ )	2404 ( $R_{\text{int}} = 0.026$ )	2596 ( $R_{\text{int}} = 0.082$ )
no. of unique data, with $F_o^2 > 2\sigma(F_o^2)$	1786	1599	1399	2190	1834
no. of variables	66	70	69	70	66
$R(F)$ for $F_o^2 > 2\sigma(F_o^2)$ <sup>a</sup>	0.040	0.025	0.055	0.018	0.047
$R_w(F_o^2)$ <sup>b</sup>	0.098	0.052	0.155	0.039	0.120
goodness of fit	1.10	1.13	1.04	1.11	1.04
$(\Delta\rho)_{\text{max}}, (\Delta\rho)_{\text{min}}$ (e Å <sup>-3</sup> )	3.72, -1.73	1.70, -1.05	3.49, -2.75	1.01, -0.84	2.56, -2.11

**Table A1-3.** (Cont.)

nominal composition	Pr <sub>3</sub> GeSiS <sub>8</sub> I
refined composition	Pr <sub>3</sub> Ge <sub>1.01(2)</sub> Si <sub>0.99(2)</sub> S <sub>8</sub> I
formula mass (amu)	906.79
space group	C2/c (No. 15)
<i>a</i> (Å)	15.908(4)
<i>b</i> (Å)	7.8343(19)
<i>c</i> (Å)	10.864(3)
$\beta$ (deg.)	98.191(5)
<i>V</i> (Å <sup>3</sup> )	1340.1(6)
<i>Z</i>	4
<i>T</i> (K)	296(2)
$\rho_{\text{calcd}}$ (g cm <sup>-3</sup> )	4.494
crystal dimensions (mm)	0.06 × 0.06 × 0.06
$\mu$ (Mo <i>K</i> $\alpha$ ) (mm <sup>-1</sup> )	16.53
transmission factors	0.485–0.604
2 $\theta$ limits	5.17–56.30°
data collected	–21 ≤ <i>h</i> ≤ 20, –10 ≤ <i>k</i> ≤ 10, – 14 ≤ <i>l</i> ≤ 14
no. of data collected	6304
no. of unique data, including $F_o^2 < 0$	1646 ( $R_{\text{int}} = 0.073$ )
no. of unique data, with $F_o^2 > 2\sigma(F_o^2)$	1209
no. of variables	66
$R(F)$ for $F_o^2 > 2\sigma(F_o^2)$ <sup>a</sup>	0.042
$R_w(F_o^2)$ <sup>b</sup>	0.108
goodness of fit	1.07
$(\Delta\rho)_{\text{max}}, (\Delta\rho)_{\text{min}}$ (e Å <sup>-3</sup> )	2.98, –1.64

<sup>a</sup>  $R(F) = \sum ||F_o| - |F_c|| / \sum |F_o|$ . <sup>b</sup>  $R_w(F_o^2) = [\sum [w(F_o^2 - F_c^2)^2] / \sum wF_o^4]^{1/2}$ ;  $w^{-1} = [\sigma^2(F_o^2) + (Ap)^2 + Bp]$ , where  $p = [\max(F_o^2, 0) + 2F_c^2] / 3$ .

**Table A1-4.** Atomic Coordinates and Equivalent Isotropic Displacement Parameters for  $RE_3(\text{Ge}_{1-x}\text{Si}_x)_2\text{S}_8\text{I}$  and  $\text{Ce}_3\text{Si}_2(\text{S}_{1-y}\text{Se}_y)_8\text{I}$ .

atom	Wyckoff position	occupancy	x	y	z	$U_{\text{eq}} (\text{\AA}^2)^a$
<b><math>\text{La}_3\text{Ge}_{1.55(1)}\text{Si}_{0.45(1)}\text{S}_8\text{I}</math></b>						
La1	8f	1	0.30362(3)	0.12033(6)	0.32070(4)	0.01348(15)
La2	4e	1	0	0.10071(9)	¼	0.01595(18)
Tt	8f	0.777(6) Ge, 0.223(6) Si	0.15880(6)	0.03898(13)	0.02779(8)	0.0134(3)
S1	8f	1	0.06590(13)	0.1564(3)	0.54088(19)	0.0170(4)
S2	8f	1	0.14491(13)	0.2489(3)	0.1489(2)	0.0169(4)
S3	8f	1	0.21673(12)	0.4298(3)	0.41356(18)	0.0148(4)
S4	8f	1	0.35054(13)	0.4006(3)	0.16631(19)	0.0151(4)
I	4e	1	0	0.51776(10)	¼	0.0266(2)
<b><math>\text{La}_3\text{Ge}_{0.98(2)}\text{Si}_{1.02(2)}\text{S}_8\text{I}</math></b>						
La1	8f	1	0.30365(4)	0.12004(7)	0.32042(5)	0.01805(17)
La2	4e	1	0	0.09876(11)	¼	0.0207(2)
Tt	8f	0.488(8) Ge, 0.512(8) Si	0.15911(9)	0.0383(2)	0.02850(13)	0.0164(5)
S1	8f	1	0.06671(16)	0.1544(3)	0.5417(2)	0.0227(5)
S2	8f	1	0.14474(16)	0.2472(3)	0.1483(2)	0.0205(5)
S3	8f	1	0.21783(16)	0.4307(3)	0.4141(2)	0.0194(5)
S4	8f	1	0.35017(16)	0.3999(3)	0.1638(2)	0.0198(5)
I	4e	1	0	0.51693(13)	¼	0.0316(3)
<b><math>\text{La}_3\text{Ge}_{0.52(1)}\text{Si}_{1.48(1)}\text{S}_8\text{I}</math></b>						
La1	8f	1	0.30361(3)	0.11979(6)	0.32033(4)	0.01409(13)
La2	4e	1	0	0.09689(8)	¼	0.01662(16)
Tt	8f	0.260(6) Ge, 0.740(6) Si	0.15929(9)	0.0379(2)	0.02908(13)	0.0136(5)
S1	8f	1	0.06758(12)	0.1530(3)	0.54198(19)	0.0177(4)
S2	8f	1	0.14488(12)	0.2451(2)	0.14756(18)	0.0164(4)
S3	8f	1	0.21855(12)	0.4305(3)	0.41452(17)	0.0155(4)
S4	8f	1	0.34991(12)	0.3994(2)	0.16171(18)	0.0154(4)
I	4e	1	0	0.51631(10)	¼	0.0274(2)
<b><math>\text{Ce}_3\text{Ge}_{1.55(1)}\text{Si}_{0.45(1)}\text{S}_8\text{I}</math></b>						
Ce1	8f	1	0.30317(2)	0.12106(3)	0.32060(2)	0.01185(7)
Ce2	4e	1	0	0.10296(5)	¼	0.01448(9)
Tt	8f	0.775(4) Ge, 0.225(4) Si	0.15862(3)	0.03890(7)	0.02716(5)	0.01112(17)
S1	8f	1	0.06563(7)	0.15873(15)	0.54033(11)	0.0155(2)
S2	8f	1	0.14444(8)	0.25031(15)	0.14893(11)	0.0150(2)
S3	8f	1	0.21603(7)	0.43015(15)	0.41366(11)	0.0133(2)
S4	8f	1	0.35086(7)	0.40105(15)	0.16808(11)	0.0137(2)
I	4e	1	0	0.51841(6)	¼	0.02387(12)
<b><math>\text{Ce}_3\text{Ge}_{0.96(2)}\text{Si}_{1.04(2)}\text{S}_8\text{I}</math></b>						
Ce1	8f	1	0.30316(3)	0.12078(7)	0.32035(5)	0.01589(16)
Ce2	4e	1	0	0.10061(10)	¼	0.0183(2)
Tt	8f	0.480(8) Ge, 0.520(8) Si	0.15892(9)	0.03847(19)	0.02778(13)	0.0147(5)
S1	8f	1	0.06644(16)	0.1563(3)	0.5412(2)	0.0199(5)
S2	8f	1	0.14456(16)	0.2480(3)	0.1476(2)	0.0184(5)
S3	8f	1	0.21709(16)	0.4309(3)	0.4143(2)	0.0166(5)
S4	8f	1	0.35037(16)	0.4005(3)	0.1655(2)	0.0175(5)
I	4e	1	0	0.51727(12)	¼	0.0285(3)

**Table A1-4.** (Cont.)

atom	Wyckoff position	occupancy	<i>x</i>	<i>y</i>	<i>z</i>	<i>U</i> <sub>eq</sub> (Å <sup>2</sup> ) <sup>a</sup>
<b>Ce<sub>3</sub>Ge<sub>0.43(1)</sub>Si<sub>1.57(1)</sub>S<sub>8</sub>I</b>						
Ce1	8 <i>f</i>	1	0.30315(2)	0.12043(5)	0.32000(3)	0.01335(11)
Ce2	4 <i>e</i>	1	0	0.09819(7)	¼	0.01582(13)
<i>Tt</i>	8 <i>f</i>	0.216(6) Ge, 0.784(6) Si	0.15909(9)	0.03785(18)	0.02843(12)	0.0133(4)
S1	8 <i>f</i>	1	0.06748(11)	0.1544(2)	0.54204(16)	0.0164(3)
S2	8 <i>f</i>	1	0.14466(11)	0.2459(2)	0.14744(16)	0.0158(3)
S3	8 <i>f</i>	1	0.21794(11)	0.4311(2)	0.41437(15)	0.0144(3)
S4	8 <i>f</i>	1	0.35021(11)	0.3995(2)	0.16246(15)	0.0142(3)
I	4 <i>e</i>	1	0	0.51649(9)	¼	0.02550(18)
<b>Ce<sub>3</sub>Si<sub>2</sub>S<sub>7.55(1)</sub>Se<sub>0.45(1)</sub>I</b>						
Ce1	8 <i>f</i>	1	0.30275(2)	0.11983(3)	0.31899(2)	0.01166(9)
Ce2	4 <i>e</i>	1	0	0.09622(5)	¼	0.01370(10)
Si	8 <i>f</i>	1	0.15990(8)	0.03695(16)	0.02887(12)	0.0103(2)
<i>Ch</i> 1	8 <i>f</i>	0.829(4) S, 0.171(4) Se	0.06648(6)	0.15703(13)	0.54235(9)	0.0152(3)
<i>Ch</i> 2	8 <i>f</i>	0.973(4) S, 0.027(4) Se	0.14478(7)	0.24476(14)	0.14665(11)	0.0138(4)
<i>Ch</i> 3	8 <i>f</i>	0.973(4) S, 0.027(4) Se	0.21820(7)	0.43108(14)	0.41467(10)	0.0127(4)
<i>Ch</i> 4	8 <i>f</i>	1.000(4) S, 0.001(4) Se	0.34982(7)	0.39936(15)	0.16059(11)	0.0120(4)
I	4 <i>e</i>	1	0	0.51479(6)	¼	0.02421(13)
<b>Ce<sub>3</sub>Si<sub>2</sub>S<sub>7.00(2)</sub>Se<sub>1.00(2)</sub>I</b>						
Ce1	8 <i>f</i>	1	0.30228(4)	0.11952(9)	0.31829(6)	0.0202(2)
Ce2	4 <i>e</i>	1	0	0.09609(13)	¼	0.0220(3)
Si	8 <i>f</i>	1	0.1600(2)	0.0371(4)	0.0283(3)	0.0184(7)
<i>Ch</i> 1	8 <i>f</i>	0.661(11) S, 0.339(11) Se	0.06552(14)	0.1584(3)	0.5422(2)	0.0241(7)
<i>Ch</i> 2	8 <i>f</i>	0.932(10) S, 0.068(10) Se	0.14463(18)	0.2448(4)	0.1460(3)	0.0220(9)
<i>Ch</i> 3	8 <i>f</i>	0.932(10) S, 0.068(10) Se	0.21776(18)	0.4307(4)	0.4149(3)	0.0208(9)
<i>Ch</i> 4	8 <i>f</i>	0.976(10) S, 0.024(10) Se	0.35006(19)	0.3988(4)	0.1605(3)	0.0206(10)
I	4 <i>e</i>	1	0	0.51384(16)	¼	0.0328(3)
<b>Ce<sub>3</sub>Si<sub>2</sub>S<sub>4.21(1)</sub>Se<sub>3.79(1)</sub>I</b>						
Ce1	8 <i>f</i>	1	0.30106(2)	0.12193(2)	0.31574(2)	0.01393(5)
Ce2	4 <i>e</i>	1	0	0.09876(3)	¼	0.01557(6)
Si	8 <i>f</i>	1	0.16046(5)	0.03706(10)	0.02729(7)	0.01237(15)
<i>Ch</i> 1	8 <i>f</i>	0.181(3) S, 0.819(3) Se	0.06470(2)	0.16151(4)	0.54365(3)	0.01443(11)
<i>Ch</i> 2	8 <i>f</i>	0.565(3) S, 0.435(3) Se	0.14373(3)	0.25007(6)	0.14425(4)	0.01521(15)
<i>Ch</i> 3	8 <i>f</i>	0.558(3) S, 0.442(3) Se	0.21435(3)	0.43059(6)	0.41589(4)	0.01426(14)
<i>Ch</i> 4	8 <i>f</i>	0.800(3) S, 0.200(3) Se	0.35105(4)	0.40115(7)	0.16273(5)	0.01404(18)
I	4 <i>e</i>	1	0	0.51283(4)	¼	0.02671(8)
<b>Ce<sub>3</sub>Si<sub>2</sub>Se<sub>8</sub>I</b>						
Ce1	8 <i>f</i>	1	0.30051(3)	0.12342(6)	0.31798(5)	0.01615(15)
Ce2	4 <i>e</i>	1	0	0.11068(10)	¼	0.01857(19)
Si	8 <i>f</i>	1	0.15966(15)	0.0352(3)	0.0280(2)	0.0150(5)
Se1	8 <i>f</i>	1	0.06555(6)	0.16154(13)	0.54327(9)	0.0183(2)
Se2	8 <i>f</i>	1	0.14351(6)	0.25245(12)	0.14392(9)	0.0177(2)

Se3	8 <i>f</i>	1	0.21342(6)	0.43079(12)	0.41399(8)	0.0166(2)
Se4	8 <i>f</i>	1	0.35310(6)	0.40140(12)	0.16580(8)	0.0167(2)
I	4 <i>e</i>	1	0	0.51431(12)	¼	0.0276(2)
<b>Pr<sub>3</sub>Ge<sub>1.01(2)</sub>Si<sub>0.99(2)</sub>S<sub>8</sub>I</b>						
Pr1	8 <i>f</i>	1	0.30274(4)	0.12134(8)	0.32031(6)	0.01578(18)
Pr2	4 <i>e</i>	1	0	0.10301(11)	¼	0.0187(2)
<i>Tt</i>	8 <i>f</i>	0.506(9) Ge, 0.494(9) Si	0.15865(10)	0.0386(2)	0.02736(15)	0.0159(6)
S1	8 <i>f</i>	1	0.06610(17)	0.1584(4)	0.5405(3)	0.0197(6)
S2	8 <i>f</i>	1	0.14399(17)	0.2493(4)	0.1478(3)	0.0185(6)
S3	8 <i>f</i>	1	0.21642(17)	0.4310(4)	0.4140(2)	0.0164(5)
S4	8 <i>f</i>	1	0.35072(17)	0.4008(4)	0.1668(3)	0.0173(6)
I	4 <i>e</i>	1	0	0.51802(14)	¼	0.0275(3)

<sup>a</sup>  $U_{eq}$  is defined as one-third of the trace of the orthogonalized  $U_{ij}$  tensor. <sup>b</sup> Fixed during refinement.

**Table A1-5.** Interatomic Distances (Å) for  $RE_3(\text{Ge}_{1-x}\text{Si}_x)_2\text{S}_8\text{I}$  and  $\text{Ce}_3\text{Si}_2(\text{S}_{1-y}\text{Se}_y)_8\text{I}$ .

	$\text{La}_3\text{Ge}_{1.55(1)}\text{Si}_{0.45(1)}\text{S}_8\text{I}$	$\text{La}_3\text{Ge}_{0.98(2)}\text{Si}_{1.02(2)}\text{S}_8\text{I}$	$\text{La}_3\text{Ge}_{0.52(1)}\text{Si}_{1.48(1)}\text{S}_8\text{I}$
La1-S3	2.968(2)	2.960(3)	2.957(3)
La1-S4	2.966(2)	2.970(3)	2.974(3)
La1-S1	3.000(2)	2.998(3)	2.995(3)
La1-S3	3.013(2)	3.009(3)	3.003(3)
La1-S4	3.060(2)	3.060(3)	3.059(3)
La1-S3	3.079(2)	3.076(3)	3.066(3)
La1-S2	3.077(2)	3.083(3)	3.089(3)
La1-S2	3.131(2)	3.131(3)	3.129(3)
La1-I	3.4636(5)	3.4610(8)	3.462(3)
La2-S4 (×2)	2.928(2)	2.931(3)	2.933(3)
La2-S2 (×2)	2.970(2)	2.968(3)	2.972(3)
La2-S1 (×2)	3.256(2)	3.262(3)	3.265(4)
La2-S1 (×2)	3.362(2)	3.334(3)	3.316(3)
La2-I	3.3206(11)	3.3227(14)	3.322(3)
Tt-S2	2.169(2)	2.150(3)	2.125(3)
Tt-S4	2.173(2)	2.152(3)	2.134(3)
Tt-S1	2.179(2)	2.156(3)	2.134(3)
Tt-S3	2.199(2)	2.172(3)	2.157(3)
	$\text{Ce}_3\text{Ge}_{1.55(1)}\text{Si}_{0.45(1)}\text{S}_8\text{I}$	$\text{Ce}_3\text{Ge}_{0.96(2)}\text{Si}_{1.04(2)}\text{S}_8\text{I}$	$\text{Ce}_3\text{Ge}_{0.43(1)}\text{Si}_{1.57(1)}\text{S}_8\text{I}$
Ce1-S3	2.9526(12)	2.947(2)	2.9341(17)
Ce1-S4	2.9368(12)	2.942(3)	2.9478(17)
Ce1-S1	2.9753(12)	2.975(3)	2.9675(18)
Ce1-S3	2.9951(12)	2.990(3)	2.9864(17)
Ce1-S4	3.0356(12)	3.032(3)	3.0328(17)
Ce1-S3	3.0582(12)	3.054(3)	3.0456(18)
Ce1-S2	3.0520(12)	3.063(3)	3.0694(18)
Ce1-S2	3.1118(13)	3.110(3)	3.0982(18)
Ce1-I	3.4489(3)	3.4457(7)	3.4379(5)
Ce2-S4 (×2)	2.9069(12)	2.909(3)	2.9068(17)
Ce2-S2 (×2)	2.9433(12)	2.947(3)	2.9436(17)
Ce2-S1 (×2)	3.2320(12)	3.240(3)	3.2434(18)
Ce2-S1 (×2)	3.3661(13)	3.334(3)	3.3051(18)
Ce2-I	3.2820(6)	3.2852(13)	3.2910(9)
Tt-S2	2.1686(13)	2.140(3)	2.120(2)
Tt-S4	2.1728(13)	2.150(3)	2.122(2)
Tt-S1	2.1771(13)	2.153(3)	2.125(2)
Tt-S3	2.1958(13)	2.170(3)	2.149(2)
	$\text{Ce}_3\text{Si}_2\text{S}_{7.55(1)}\text{Se}_{0.45(1)}\text{I}$	$\text{Ce}_3\text{Si}_2\text{S}_{7.00(2)}\text{Se}_{1.00(2)}\text{I}$	$\text{Ce}_3\text{Si}_2\text{S}_{4.21(1)}\text{Se}_{3.79(1)}\text{I}$
Ce1-Ch3	2.9263(12)	2.929(3)	2.9717(5)
Ce1-Ch4	2.9557(12)	2.960(3)	2.9795(6)
Ce1-Ch1	2.9803(10)	3.004(2)	3.0481(4)
Ce1-Ch3	2.9917(12)	2.999(3)	3.0471(5)
Ce1-Ch4	3.0268(12)	3.035(3)	3.0689(6)

Ce1–Ch3	3.0494(12)	3.059(3)	3.1160(5)
Ce1–Ch2	3.0779(12)	3.086(3)	3.1204(5)
Ce1–Ch2	3.0958(12)	3.104(3)	3.1498(5)
Ce1–I	3.4418(4)	3.4567(9)	3.5103(2)
Ce2–Ch4 (×2)	2.9126(12)	2.922(3)	2.9438(6)
Ce2–Ch2 (×2)	2.9503(11)	2.959(3)	2.9978(5)
Ce2–Ch1 (×2)	3.2522(10)	3.259(2)	3.3264(4)
Ce2–Ch1 (×2)	3.2972(10)	3.304(2)	3.3601(4)
Ce2–I	3.2944(7)	3.2948(17)	3.3109(4)
Si–Ch4	2.1085(17)	2.108(4)	2.1483(10)
Si–Ch2	2.1126(17)	2.116(4)	2.1789(9)
Si–Ch3	2.1325(17)	2.148(4)	2.2170(9)
Si–Ch1	2.1552(16)	2.182(4)	2.2453(9)

Ce<sub>3</sub>Si<sub>2</sub>Se<sub>8</sub>I

Ce1–Se4	3.0508(11)
Ce1–Se3	3.0568(11)
Ce1–Se1	3.0778(11)
Ce1–Se3	3.1309(11)
Ce1–Se4	3.1407(11)
Ce1–Se3	3.1566(11)
Ce1–Se2	3.1678(11)
Ce1–Se2	3.2124(12)
Ce1–I	3.6007(7)
Ce2–Se4 (×2)	3.0084(11)
Ce2–Se2 (×2)	3.0367(10)
Ce2–Se1 (×2)	3.3947(10)
Ce2–Se1 (×2)	3.5157(11)
Ce2–I	3.2830(13)
Si–Se2	2.245(3)
Si–Se4	2.252(3)
Si–Se1	2.254(3)
Si–Se3	2.272(3)

Pr<sub>3</sub>Ge<sub>1.01(2)</sub>Si<sub>0.99(2)</sub>S<sub>8</sub>I

Pr1–S4	2.919(3)
Pr1–S3	2.928(3)
Pr1–S1	2.953(3)
Pr1–S3	2.974(3)
Pr1–S4	3.010(3)
Pr1–S3	3.034(3)
Pr1–S2	3.042(3)
Pr1–S2	3.090(3)
Pr1–I	3.4306(9)
Pr2–S4 (×2)	2.891(3)
Pr2–S2 (×2)	2.918(3)
Pr2–S1 (×2)	3.210(3)

Pr2-S1 ( $\times 2$ )	3.342(3)
Pr2-I	3.2513(16)
<i>Tt</i> -S2	2.139(3)
<i>Tt</i> -S4	2.147(3)
<i>Tt</i> -S1	2.152(3)
<i>Tt</i> -S3	2.169(3)

---

**Table A1-6.** Optical Band Gaps (eV) for  $RE_3(\text{Ge}_{1-x}\text{Si}_x)_2\text{S}_8\text{I}$  and  $\text{Ce}_3\text{Si}_2(\text{S}_{1-y}\text{Se}_y)_8\text{I}$ .

nominal composition	$x$	$\text{La}_3(\text{Ge}_{1-x}\text{Si}_x)_2\text{S}_8\text{I}$	$\text{Ce}_3(\text{Ge}_{1-x}\text{Si}_x)_2\text{S}_8\text{I}$	$\text{Pr}_3(\text{Ge}_{1-x}\text{Si}_x)_2\text{S}_8\text{I}$
$RE_3\text{Ge}_2\text{S}_8\text{I}$	0	3.05	2.76	2.97
$RE_3\text{Ge}_{1.75}\text{Si}_{0.25}\text{S}_8\text{I}$	0.125	3.08	2.73	3.00
$RE_3\text{Ge}_{1.50}\text{Si}_{0.50}\text{S}_8\text{I}$	0.250	3.13	2.76	3.02
$RE_3\text{Ge}_{1.25}\text{Si}_{0.75}\text{S}_8\text{I}$	0.375	3.10	2.75	3.06
$RE_3\text{Ge}_{1.00}\text{Si}_{1.00}\text{S}_8\text{I}$	0.500	3.13	2.79	3.07
$RE_3\text{Ge}_{0.75}\text{Si}_{1.25}\text{S}_8\text{I}$	0.625	3.15	2.75	3.07
$RE_3\text{Ge}_{0.50}\text{Si}_{1.50}\text{S}_8\text{I}$	0.750	3.22	2.84	3.15
$RE_3\text{Ge}_{0.45}\text{Si}_{1.55}\text{S}_8\text{I}$	0.775		2.82	
$RE_3\text{Ge}_{0.40}\text{Si}_{1.60}\text{S}_8\text{I}$	0.800		2.84	
$RE_3\text{Ge}_{0.35}\text{Si}_{1.65}\text{S}_8\text{I}$	0.825		2.81	
$RE_3\text{Ge}_{0.30}\text{Si}_{1.70}\text{S}_8\text{I}$	0.850		2.84	
$RE_3\text{Ge}_{0.25}\text{Si}_{1.75}\text{S}_8\text{I}$	0.875	3.24	2.82	3.18
$RE_3\text{Ge}_{0.20}\text{Si}_{1.80}\text{S}_8\text{I}$	0.900		2.84	
$RE_3\text{Ge}_{0.15}\text{Si}_{1.85}\text{S}_8\text{I}$	0.925		2.84	
$RE_3\text{Ge}_{0.10}\text{Si}_{1.90}\text{S}_8\text{I}$	0.950		2.81	
$RE_3\text{Ge}_{0.05}\text{Si}_{1.95}\text{S}_8\text{I}$	0.975		2.83	
$RE_3\text{Si}_2\text{S}_8\text{I}$	1.000	3.61	2.78	3.41
nominal composition	$y$	$\text{Ce}_3\text{Si}_2(\text{S}_{1-y}\text{Se}_y)_8\text{I}$		
$\text{Ce}_3\text{Si}_2\text{S}_8\text{I}$	0	2.78		
$\text{Ce}_3\text{Si}_2\text{S}_{7.95}\text{Se}_{0.05}\text{I}$	0.006	2.77		
$\text{Ce}_3\text{Si}_2\text{S}_{7.90}\text{Se}_{0.10}\text{I}$	0.012	2.76		
$\text{Ce}_3\text{Si}_2\text{S}_{7.85}\text{Se}_{0.15}\text{I}$	0.019	2.77		
$\text{Ce}_3\text{Si}_2\text{S}_{7.80}\text{Se}_{0.20}\text{I}$	0.025	2.77		
$\text{Ce}_3\text{Si}_2\text{S}_{7.75}\text{Se}_{0.25}\text{I}$	0.031	2.76		
$\text{Ce}_3\text{Si}_2\text{S}_{7.50}\text{Se}_{0.50}\text{I}$	0.062	2.71		
$\text{Ce}_3\text{Si}_2\text{S}_{7.25}\text{Se}_{0.75}\text{I}$	0.094	2.64		
$\text{Ce}_3\text{Si}_2\text{S}_{7.00}\text{Se}_{1.00}\text{I}$	0.125	2.39		
$\text{Ce}_3\text{Si}_2\text{S}_{6.75}\text{Se}_{1.25}\text{I}$	0.156	2.42		
$\text{Ce}_3\text{Si}_2\text{S}_{6.50}\text{Se}_{1.50}\text{I}$	0.188	2.43		
$\text{Ce}_3\text{Si}_2\text{S}_6\text{Se}_2\text{I}$	0.250	2.24		
$\text{Ce}_3\text{Si}_2\text{S}_5\text{Se}_3\text{I}$	0.375	2.13		
$\text{Ce}_3\text{Si}_2\text{S}_4\text{Se}_4\text{I}$	0.500	2.00		
$\text{Ce}_3\text{Si}_2\text{S}_3\text{Se}_5\text{I}$	0.625	1.96		
$\text{Ce}_3\text{Si}_2\text{S}_2\text{Se}_6\text{I}$	0.750	1.96		
$\text{Ce}_3\text{Si}_2\text{SSe}_7\text{I}$	0.875	2.05		
$\text{Ce}_3\text{Si}_2\text{Se}_8\text{I}$	1.000	1.92		

**Table A1-7.** Integrated COBI (eV/bond) for Bonding Interactions in  $\text{Ce}_3(\text{Ge}_{1-x}\text{Si}_x)_2\text{S}_8\text{I}$  and  $\text{Ce}_3\text{Si}_2(\text{S}_{1-y}\text{Se}_y)_8\text{I}$ .

model	Ce-S	Ce-Se	Ce-I	Ge-S	Si-S	Si-Se
$\text{Ce}_3\text{Ge}_2\text{S}_8\text{I}$	0.22–0.40		0.30–0.55	0.85–0.93		
$\text{Ce}_3\text{Ge}_{1.5}\text{Si}_{0.5}\text{S}_8\text{I}$	0.21–0.42		0.29–0.56	0.85–0.93	0.87–0.95	
$\text{Ce}_3\text{GeSiS}_8\text{I}$	0.21–0.41		0.29–0.55	0.85–0.93	0.86–0.94	
$\text{Ce}_3\text{Ge}_{0.5}\text{Si}_{1.5}\text{S}_8\text{I}$	0.21–0.41		0.30–0.57	0.85–0.93	0.87–0.95	
$\text{Ce}_3\text{Ge}_{0.25}\text{Si}_{1.75}\text{S}_8\text{I}$	0.20–0.41		0.28–0.54	0.85–0.93	0.87–0.95	
$\text{Ce}_3\text{Si}_2\text{S}_8\text{I}$	0.22–0.41		0.31–0.53		0.87–0.94	
$\text{Ce}_3\text{Si}_2\text{S}_7\text{SeI}$	0.13–0.43	0.30–0.47	0.24–0.51		0.86–0.96	0.84–0.93
$\text{Ce}_3\text{Si}_2\text{S}_{6.5}\text{Se}_{0.5}\text{I}$	0.11–0.43	0.27–0.47	0.26–0.49		0.86–0.97	0.85–0.91
$\text{Ce}_3\text{Si}_2\text{S}_6\text{Se}_2\text{I}$	0.26–0.50	0.27–0.51	0.16–0.40		0.86–0.96	0.84–0.92

**Table A1-8.** CIE Coordinates for  $Ce_3(Ge_{1-x}Si_x)_2S_8I$  and  $Ce_3Si_2(S_{1-y}Se_y)_8I$ 

sample	composition	CIE 1931 $x$	CIE 1931 $y$
<b><math>Ce_3(Ge_{1-x}Si_x)_2S_8I</math></b>			
1	$Ce_3Si_2S_8I$	0.153	0.199
2	$Ce_3Ge_{0.1}Si_{1.9}S_8I$	0.160	0.300
3	$Ce_3Ge_{0.2}Si_{1.8}S_8I$	0.175	0.321
4	$Ce_3Ge_{0.25}Si_{1.75}S_8I$	0.161	0.276
5	$Ce_3Ge_{0.3}Si_{1.7}S_8I$	0.159	0.285
6	$Ce_3Ge_{0.4}Si_{1.6}S_8I$	0.187	0.315
7	$Ce_3Ge_{0.5}Si_{1.5}S_8I$	0.198	0.303
<b><math>Ce_3Si_2(S_{1-y}Se_y)_8I</math></b>			
1	$Ce_3Si_2S_8I$	0.153	0.199
2	$Ce_3Si_2S_{7.75}Se_{0.25}I$	0.169	0.302
3	$Ce_3Si_2S_{7.5}Se_{0.5}I$	0.180	0.344
4	$Ce_3Si_2S_{7.25}Se_{0.75}I$	0.199	0.395
5	$Ce_3Si_2S_7SeI$	0.199	0.387
6	$Ce_3Si_2S_{6.75}Se_{0.25}I$	0.232	0.433
7	$Ce_3Si_2S_{6.5}Se_{0.5}I$	0.235	0.436

**Table A1-9.** Fitting Parameters for Photoluminescent Decay for  $Ce_3(Ge_{1-x}Si_x)_2S_8I$  and  $Ce_3Si_2(S_{1-y}Se_y)_8I$  <sup>a</sup>

sample	k	sigma	mu	c1	decay lifetime (ns)
$Ce_3Si_2S_8I$	-1648	0.6791	1.714	0.008	6.99
$Ce_3Ge_{0.25}Si_{1.75}S_8I$	-1646	0.6745	1.167	0.008	4.03
$Ce_3Ge_{0.50}Si_{1.50}S_8I$	-1651	1.316	-0.272	0.005	1.81
$Ce_3Si_2S_{7.75}Se_{0.25}I$	-1646	0.8107	1.385	0.004	5.55
$Ce_3Si_2S_{6.50}Se_{1.50}I$	-1648	0.9969	0.831	0.004	3.77

<sup>a</sup> Decay curves were fit to lognormal functions.

**Table A1-10.** XPS peak position and % area.

sample	Peak position and % area										Ce <sup>3+</sup> :Ce <sup>4+</sup>
	v0 (Ce <sup>3+</sup> )	v (Ce <sup>4+</sup> )	v' (Ce <sup>3+</sup> )	v'' (Ce <sup>4+</sup> )	v''' (Ce <sup>4+</sup> )	u0 (Ce <sup>3+</sup> )	u (Ce <sup>4+</sup> )	u' (Ce <sup>3+</sup> )	u'' (Ce <sup>4+</sup> )	u''' (Ce <sup>4+</sup> )	
Ce <sub>3</sub> Si <sub>2</sub> S <sub>8</sub> I	880.88	883.04	885.33	886.71	896.82	899.37	901.57	903.91	906.38	915.24	75:25
	13.60	6.74	30.37	5.56	1.97	9.95	4.76	21.17	3.55	2.33	
Ce <sub>3</sub> Ge <sub>0.25</sub> Si <sub>1.75</sub> S <sub>8</sub> I	881.33	883.49	885.91	886.01	897.98	899.55	901.60	904.19	906.62	915.72	76:24
	12.99	6.63	31.95	4.13	5.46	8.49	4.76	22.19	3.05	1.86	
Ce <sub>3</sub> Ge <sub>0.50</sub> Si <sub>1.50</sub> S <sub>8</sub> I	881.02	883.42	885.66	886.19	898.63	899.48	901.83	904.08	906.57	915.68	74:26
	13.24	8.28	30.67	4.00	4.31	8.73	4.96	21.21	2.66	1.94	
Ce <sub>3</sub> Si <sub>2</sub> S <sub>7.75</sub> Se <sub>0.25</sub> I	880.45	882.65	884.22	886.05	897.50	899.03	902.81	902.56	905.18	914.86	73:27
	21.05	5.50	20.93	9.25	3.43	13.59	3.86	16.99	3.47	1.92	
Ce <sub>3</sub> Si <sub>2</sub> S <sub>6.50</sub> Se <sub>1.50</sub> I	880.74	883.19	884.67	886.46	899.00	898.48	902.90	903.04	905.87	915.12	76:24
	22.37	5.98	20.18	5.53	4.63	15.62	3.49	18.07	1.00	3.14	

<sup>a</sup> Refer to Figure. A1-13 for labels of the peak components in the spectra.

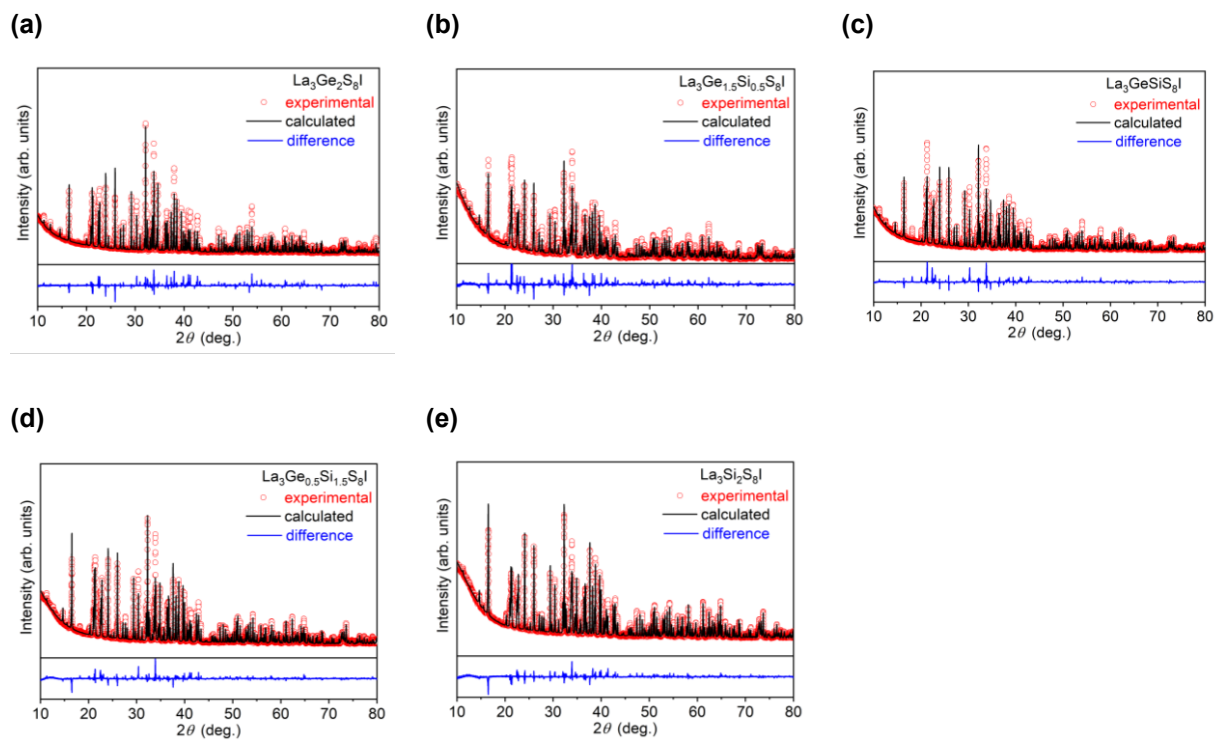


**Figure A1-1.** Powder XRD patterns for  $\text{La}_3(\text{Ge}_{1-x}\text{Si}_x)_2\text{S}_8\text{I}$ .

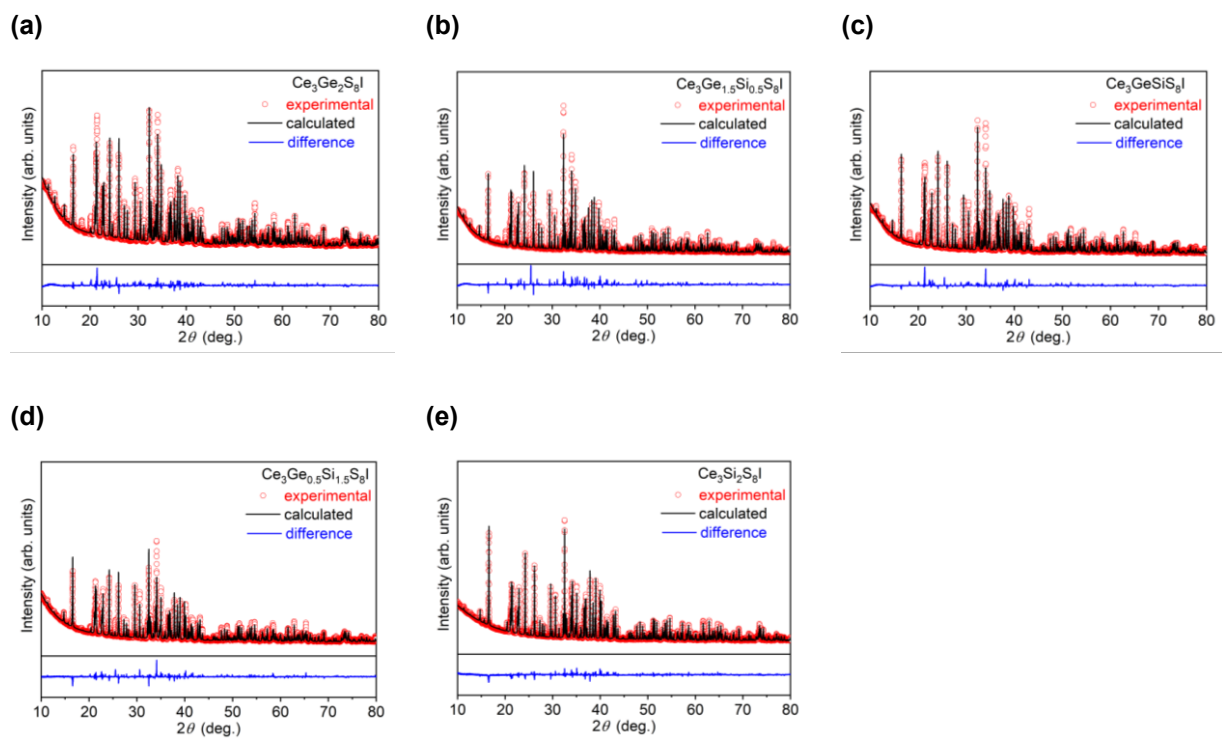


**Figure A1-2.** Powder XRD patterns for  $\text{Ce}_3(\text{Ge}_{1-x}\text{Si}_x)_2\text{S}_8\text{I}$ .

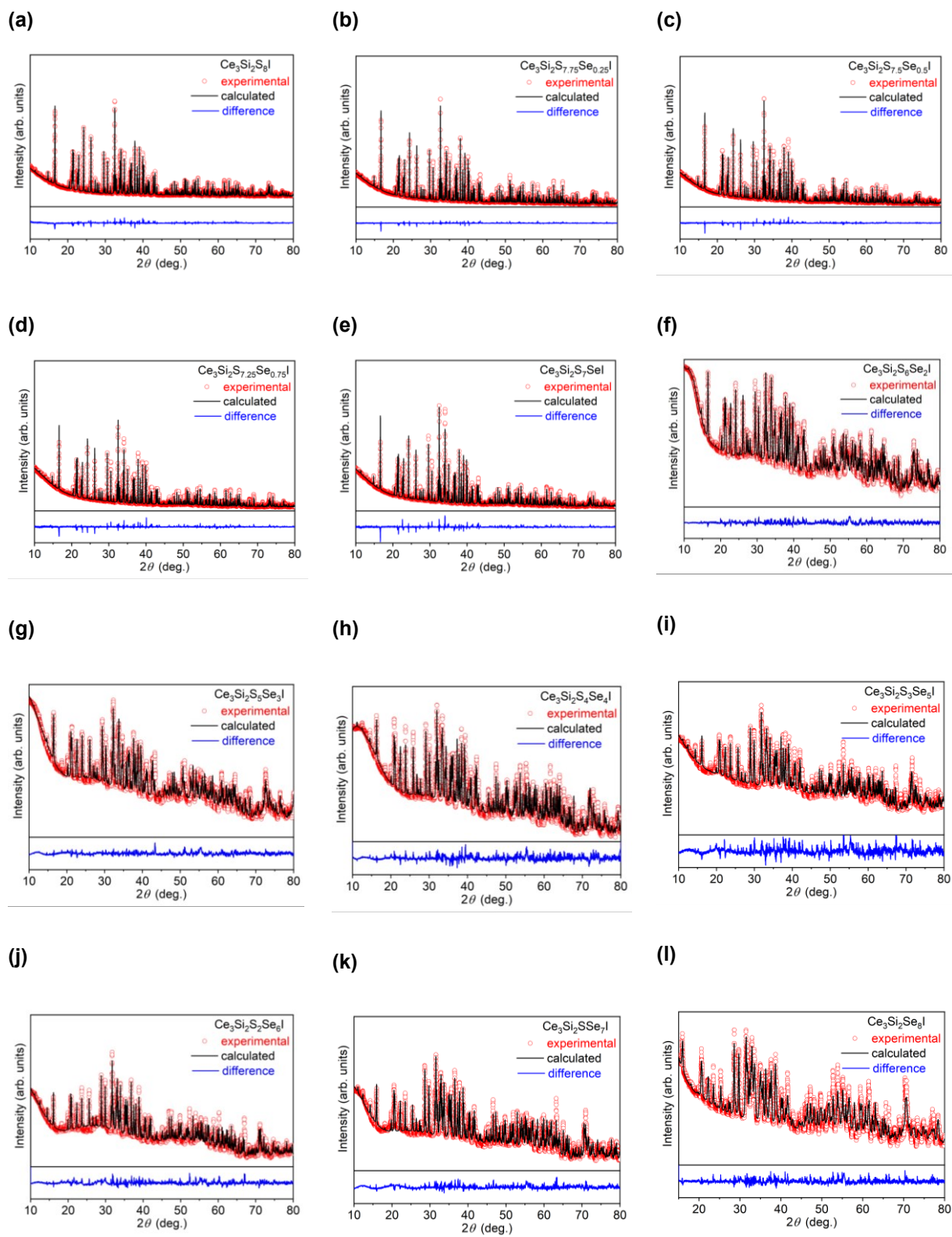


**Figure A1-3.** Powder XRD patterns for  $\text{Ce}_3\text{Si}_2(\text{S}_{1-y}\text{Se}_y)_8\text{I}$ .

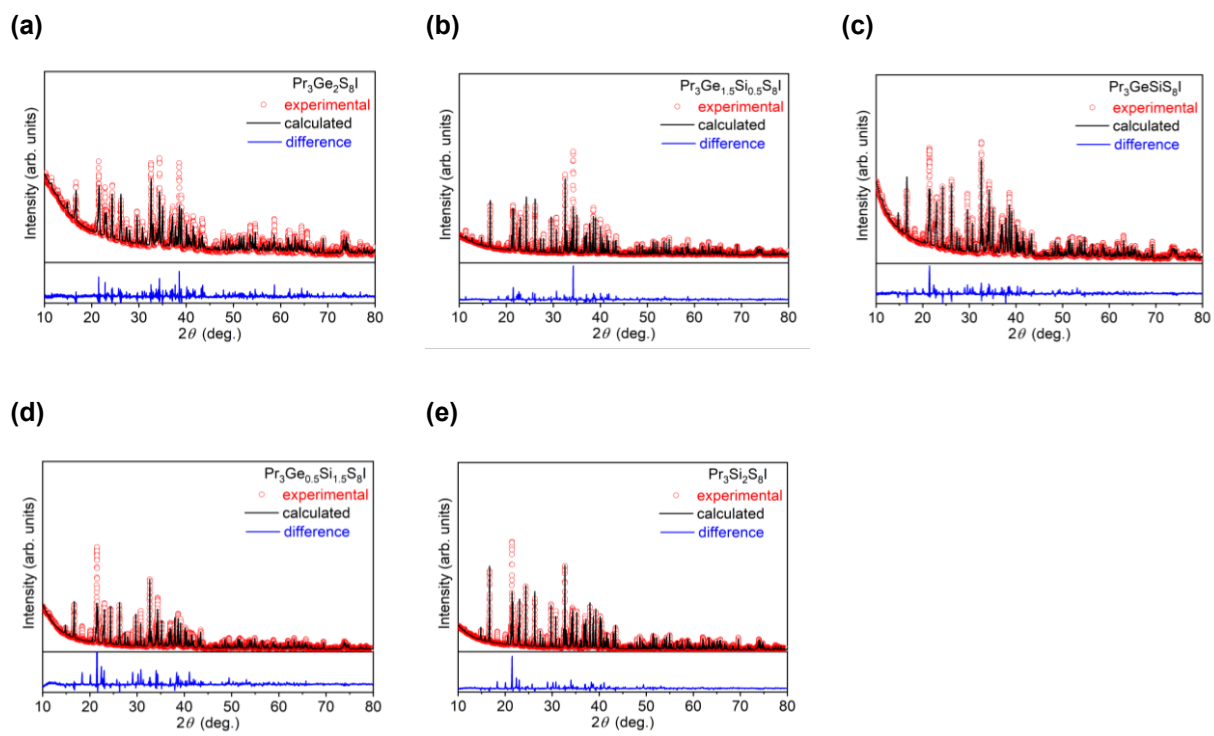


**Figure A1-4.** Powder XRD patterns for  $\text{Pr}_3(\text{Ge}_{1-x}\text{Si}_x)_2\text{S}_8\text{I}$ .

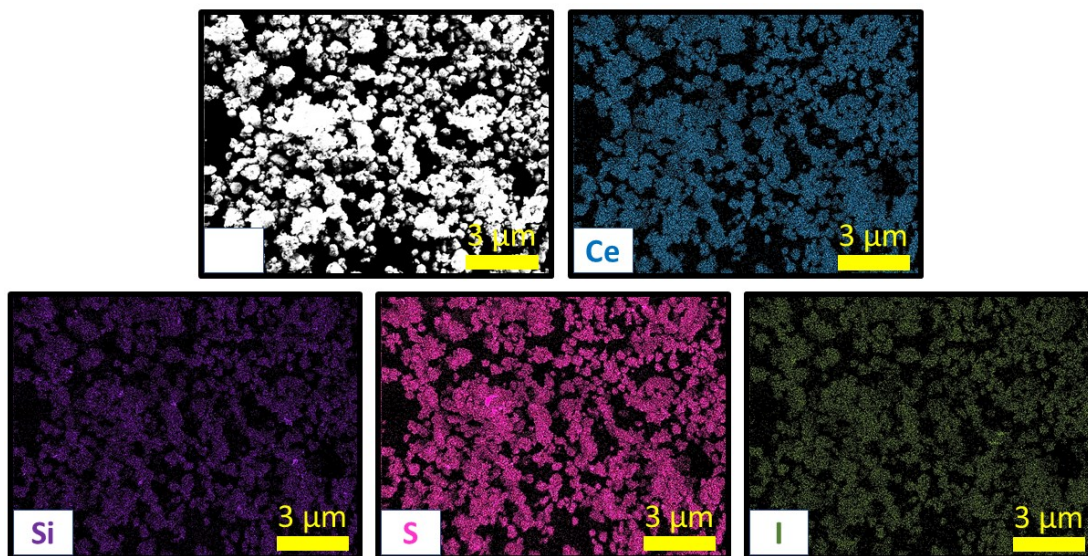


Figure A1-5. EDX elemental mapping for  $\text{Ce}_3\text{Si}_2\text{S}_8\text{I}$  sample

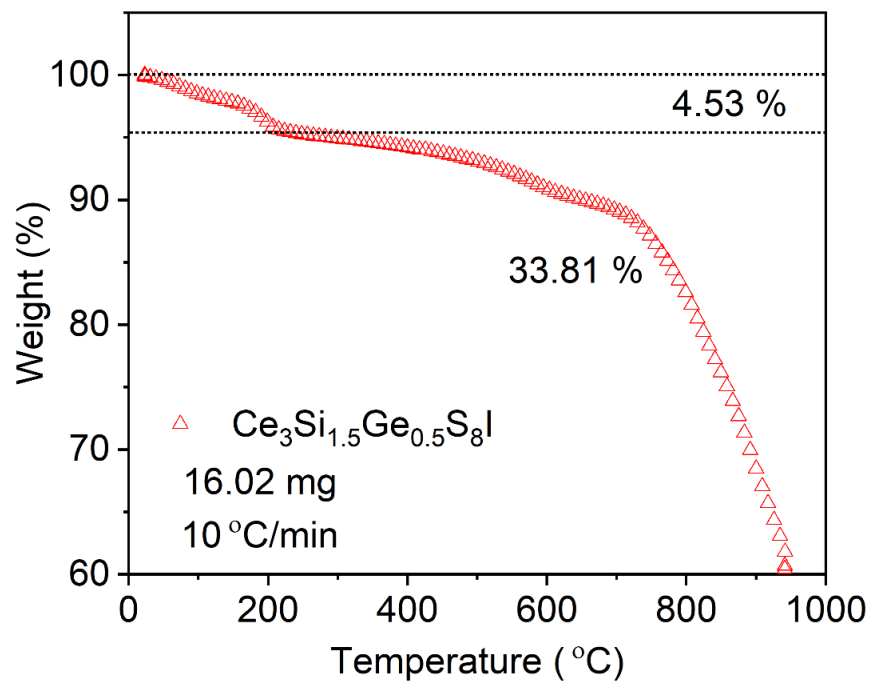
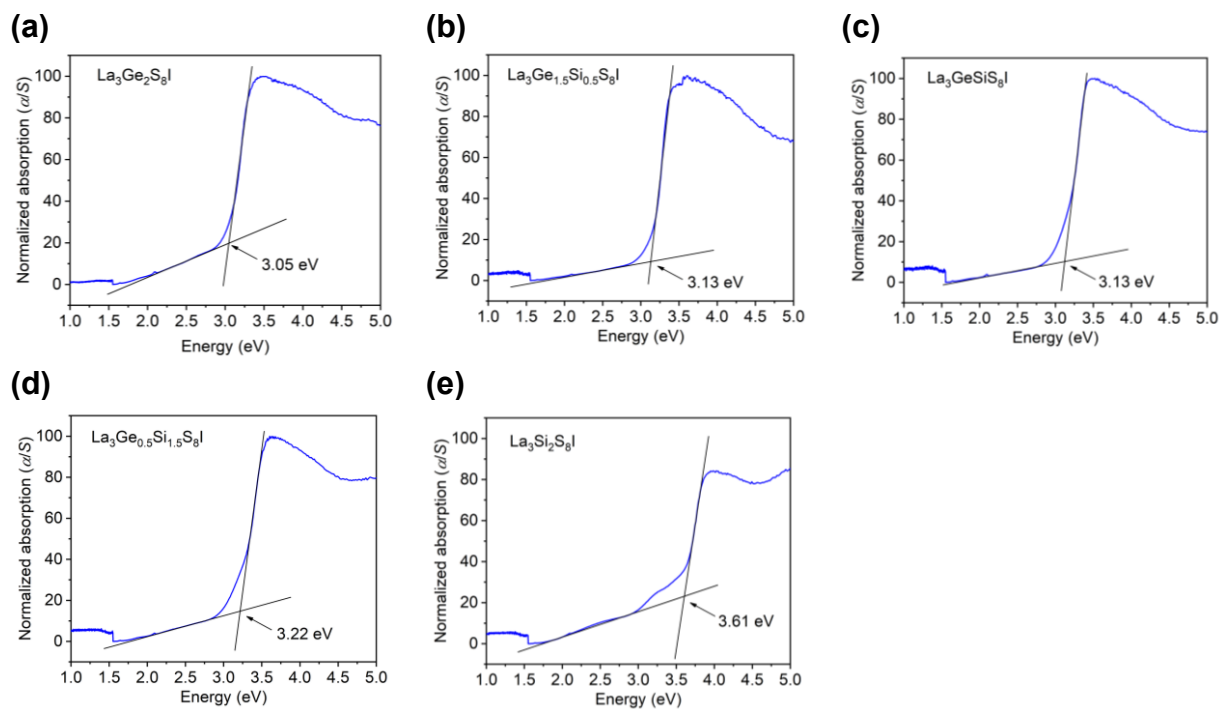
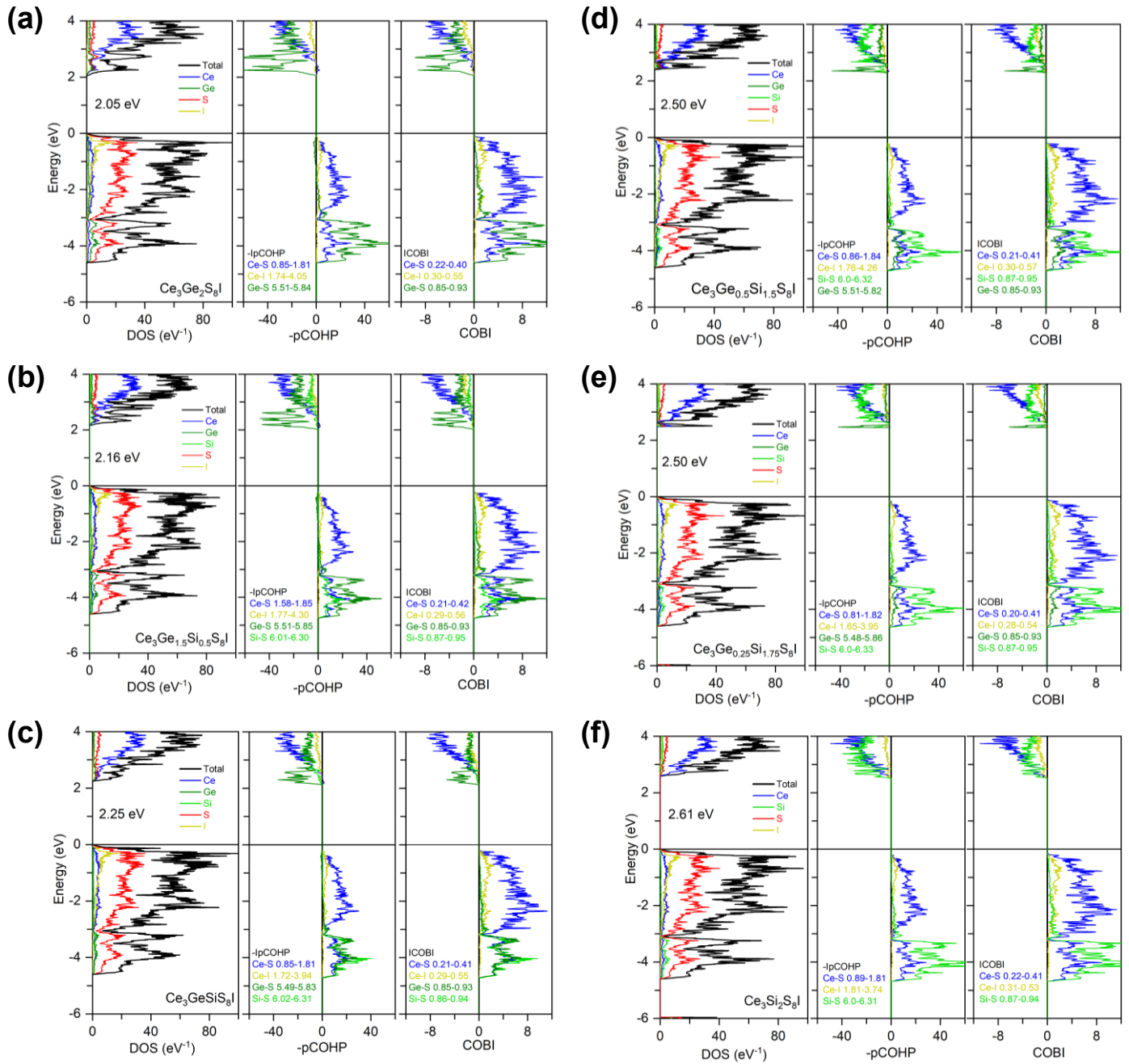


Figure A1-6. TGA analysis for sample of  $\text{Ce}_3\text{Si}_{1.5}\text{Ge}_{0.5}\text{S}_8\text{I}$ .



**Figure A1-7.** Normalized diffuse reflectance spectra for  $\text{La}_3(\text{Ge}_{1-x}\text{Si}_x)_2\text{S}_8\text{I}$ , showing fittings to extract band gaps.



**Figure A1-8.** Density of states (DOS), projected crystal orbital Hamilton populations (pCOHP), and crystal orbital bond index (COBI) for models within the solid solution  $\text{Ce}_3(\text{Ge}_{1-x}\text{Si}_x)_2\text{S}_8\text{I}$ .

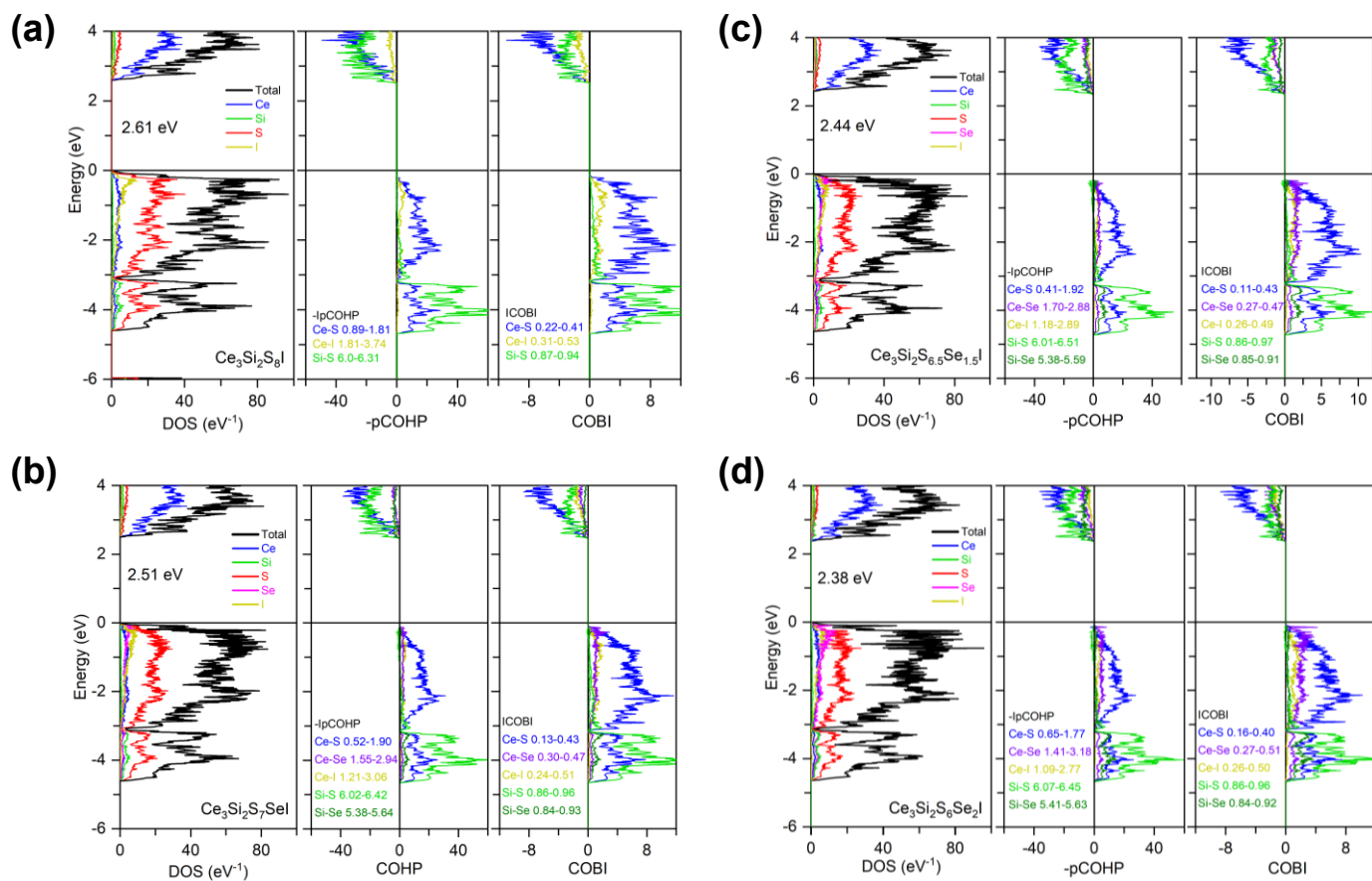


**Figure A1-9.** Density of states (DOS), projected crystal orbital Hamilton populations (pCOHP), and crystal orbital bond index (COBI) for models within the solid solution  $\text{Ce}_3\text{Si}_2(\text{S}_{1-y}\text{Se}_y)\text{I}$  (up to  $y = 0.25$ ).

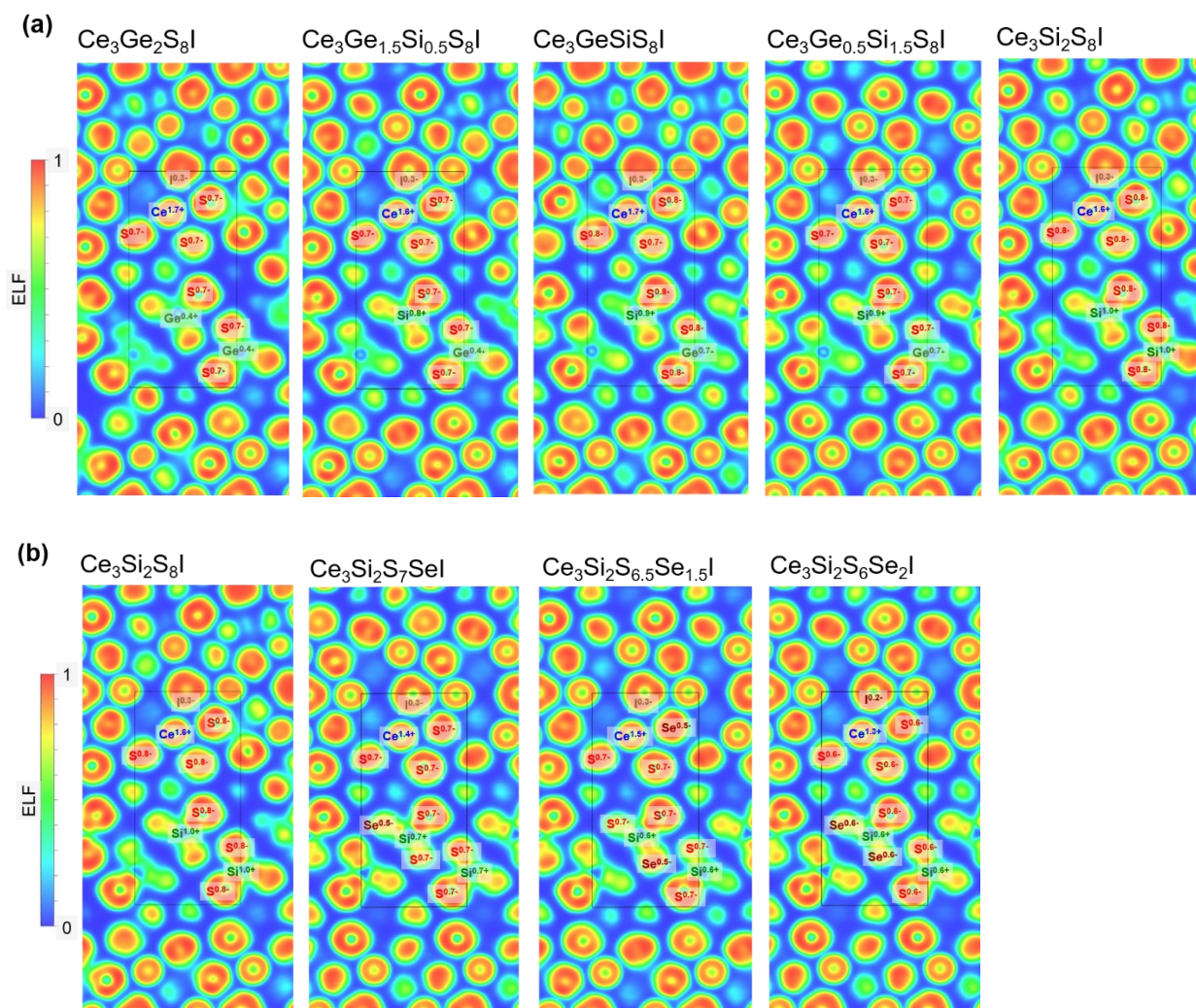


**Figure A1-10.** Electron localization function (ELF) plots, taken as slices parallel to (001), for (a)  $\text{Ce}_3(\text{Ge}_{1-x}\text{Si}_x)_2\text{S}_8\text{I}$  and (b)  $\text{Ce}_3\text{Si}_2(\text{S}_{1-y}\text{Se}_y)_8\text{I}$ . Bader charges are shown on selected atoms.

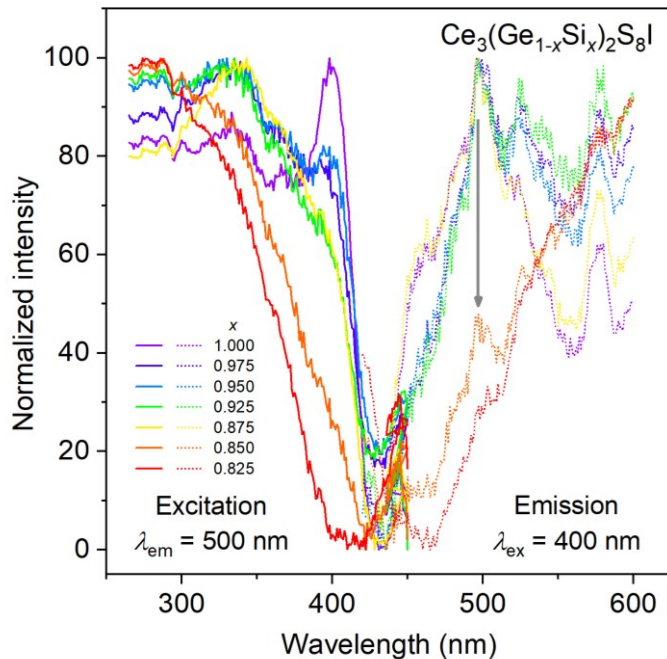


**Figure A1-11.** Excitation and emission spectra for Si-rich members of  $\text{Ce}_3(\text{Ge}_{1-x}\text{Si}_x)_2\text{S}_8\text{I}$ , measured on a Horiba PTI QM-8075-11 fluorescence system. The grey arrow shows quenching of the luminescence with lower Si concentrations.

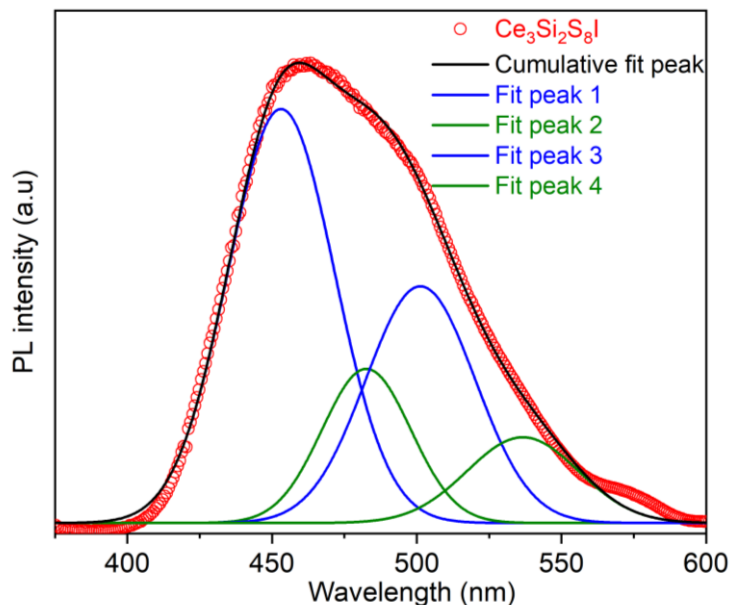


**Figure A1-12.** Emission spectrum of  $\text{Ce}_3\text{Si}_2\text{S}_8\text{I}$ , measured with an 365+351-nm Ar-ion laser source. The profile was fit to two sets of Gaussian peaks centred at 453 and 501 nm for the first sets (blue line) and 489 nm and 536 nm for the second set (green line).

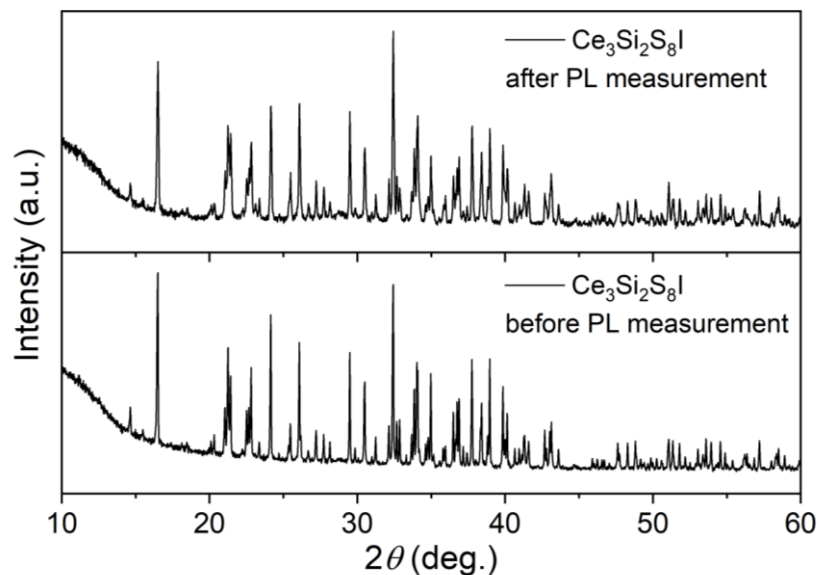


**Figure A1-13.** Powder XRD patterns of  $\text{Ce}_3\text{Si}_2\text{S}_8\text{I}$  sample before and after photoluminescence measurements made with a laser source.

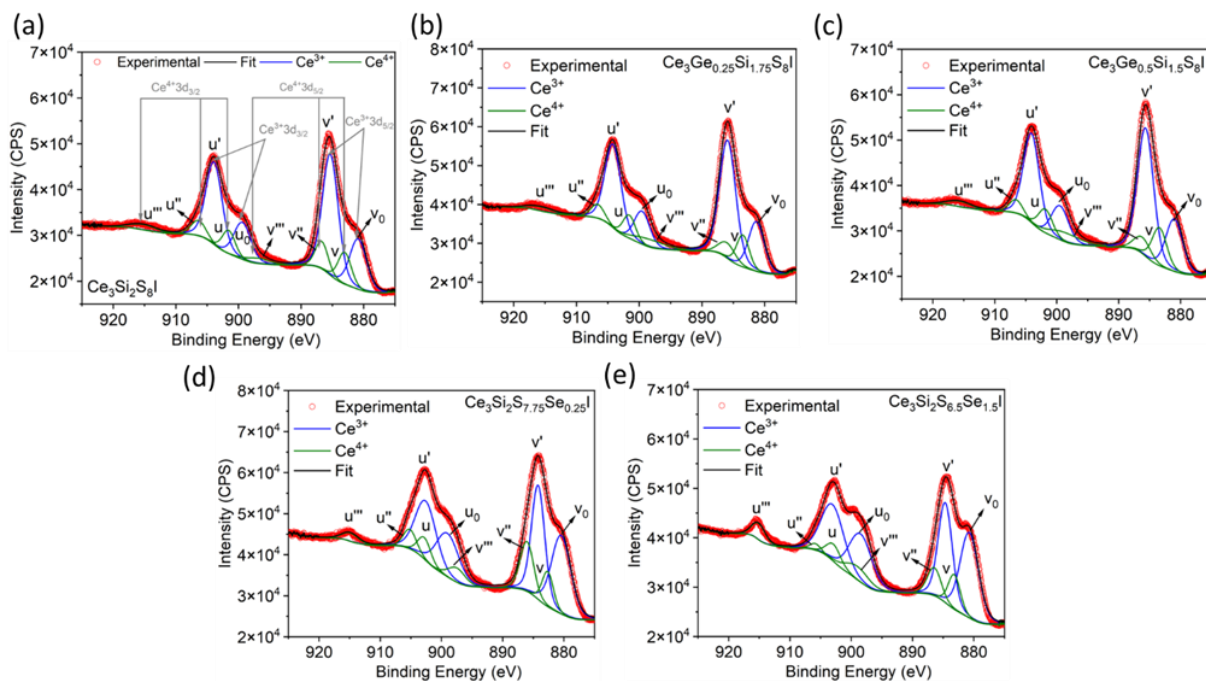


**Figure A1-14.** High-resolution cerium XPS spectra for (a)  $\text{Ce}_3\text{Si}_2\text{S}_8\text{I}$ , (b)  $\text{Ce}_3\text{Ge}_{0.25}\text{Si}_{1.75}\text{S}_8\text{I}$ , (c)  $\text{Ce}_3\text{Ge}_{0.5}\text{Si}_{1.5}\text{S}_8\text{I}$ , (d)  $\text{Ce}_3\text{Si}_2\text{S}_{7.75}\text{Se}_{0.25}\text{I}$  and (e)  $\text{Ce}_3\text{Si}_2\text{S}_{6.5}\text{Se}_{1.5}\text{I}$ .

## Appendix 2.

### Supplementary Data for Chapter 4

**Structure determination of twinned crystal of YbNi<sub>3</sub>Ga<sub>9</sub>.** Initial attempts were made to determine the crystal structure of YbNi<sub>3</sub>Ga<sub>9</sub> based on data collected on a twinned crystal. The diffraction pattern is characterized by the presence of diffuse lines of scattering containing strongly marked maxima (**Figure A2-1**). In a trigonal/hexagonal setting, these maxima lie on the positions  $\frac{1}{3}, \frac{2}{3}, l$  and  $\frac{2}{3}, \frac{1}{3}, l$ ; although the component along  $c^*$  is diffuse, there is a clear tendency for splitting of the main maxima, making these positions  $\frac{1}{3}, \frac{2}{3}, \frac{1}{3}$  and  $\frac{2}{3}, \frac{1}{3}, \frac{2}{3}$ . This is a strong indication of a rhombohedral superstructure with twinning. The diffuse scattering implies that there is significant disorder in the superstructure. The rhombohedral cell is not the only possibility, but it is the most prevalent.

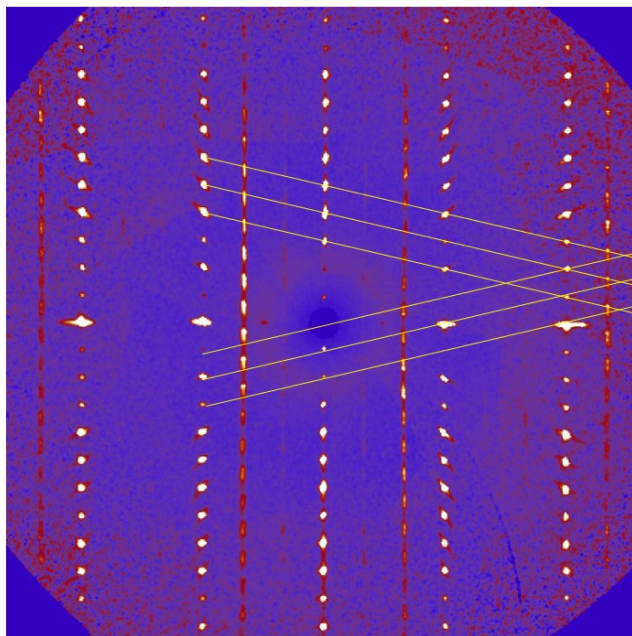


**Figure A2-1.** Reciprocal lattice section of YbNi<sub>3</sub>Ga<sub>9</sub> viewed on the *hhl* plane. Note how the reciprocal space diagonals go through the most prominent parts of the diffuse scattering.

An automatic indexing routine yields the expected supercell with lattice parameters of  $a = 7.2572 \text{ \AA}$ ,  $b = 7.2572 \text{ \AA}$ , and  $c = 27.6403 \text{ \AA}$  (hexagonal setting), but fails to pick up the rhombohedral centring because of the twinning. The twinning also leads to additional symmetry in the diffraction pattern, identified as  $P6/mmm$  from an automated routine. Imposing the rhombohedral centring reduces the expected (maximal) symmetry to  $R\bar{3}m$ . A structure solution in this space group leads to no refinable model (with  $R_w$  of 0.50). The model is nicely atomic, as indicated by the presence of strong main maxima in the electron density, but there are many unphysically short interatomic distances. Most prominently, one of the expected Yb positions lies close to, but not at, the unit cell origin, generating a forbidden self-contact (**Figure A2-2**).

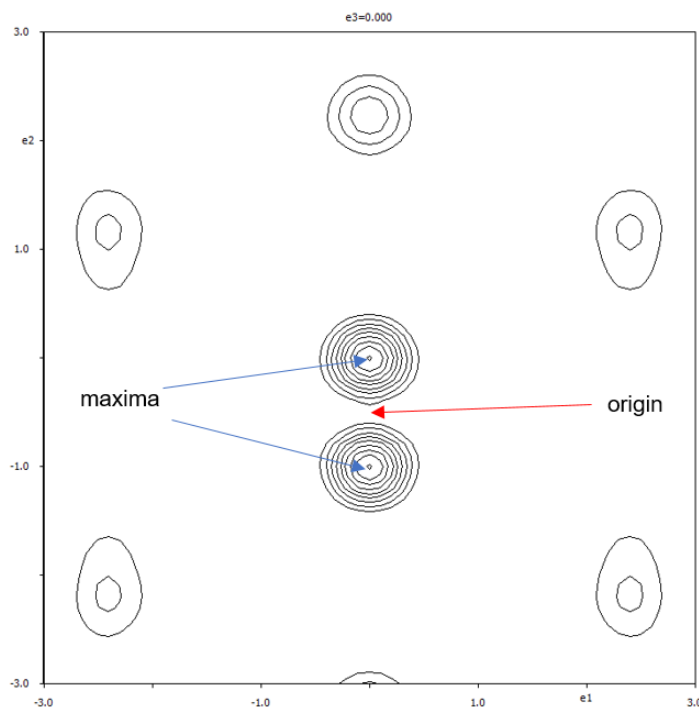


**Figure A2-2.** Note the twin maxima of electron density (blue arrows). The locus of their barycentres (red arrow) is the origin of the unit cell. The axes in the image are  $a$  (horizontal) and  $c$  (vertical).

These results clearly suggest a misassigned symmetry. The centre of symmetry and the twofold rotation axes along  $x$  and  $y$  all map the position  $0, 0, z$  onto  $0, 0, \bar{z}$ . The subgroup that removes these symmetry elements is  $R3m$  (and not  $R32$ ). The logical procedure is to recast the present solution (high  $R$ -value, many short interatomic distances, good atomicity) into this lower symmetry space group, and to remove one of the two copies of the Yb position to seed the lowering of symmetry. The refinement is promising, but far from good, with  $R_w$  of 0.25 and some problematic features (**Figure A2-3**).

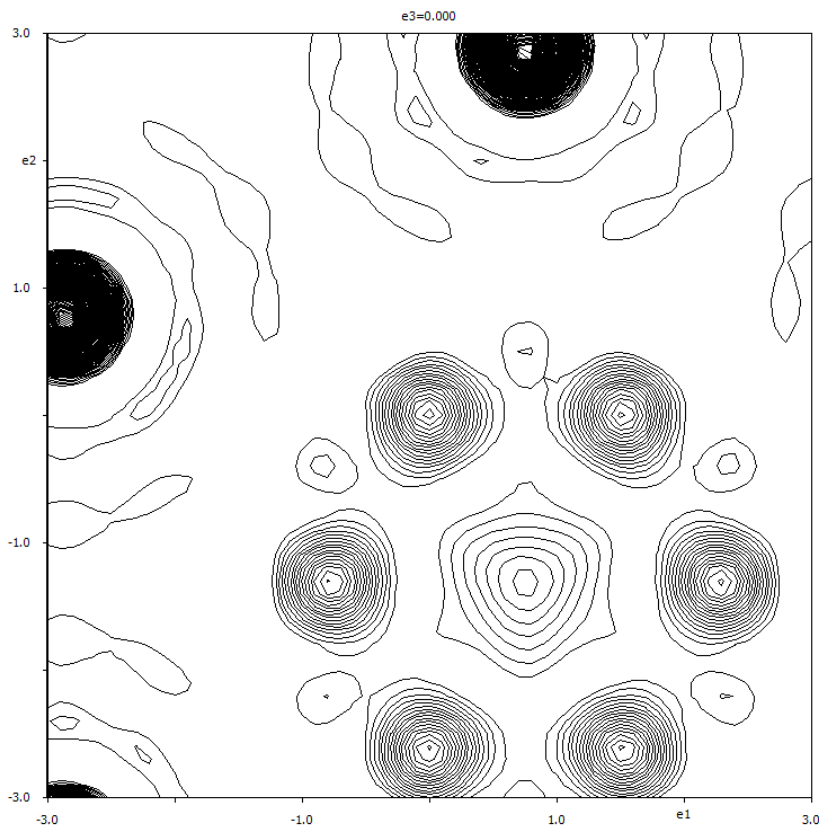


**Figure A2-3.** Electron density from the model in  $R3m$ . The section is the  $ab$ -plane and the  $a$ -axis is horizontal. The centre of the hexagon of electron density is at  $\frac{2}{3}, \frac{1}{3}, 0$ .

Again, this signals a symmetry that is too high. The mirror plane lies between the maxima, generating a hexagon rather than a triangle generated by the threefold axis alone. There are several other short interatomic distances in the model that can be resolved if the proper position is chosen after lower the symmetry to  $R3$ . This symmetry reduction resolves all short interatomic distances, but there remain challenges to assigning the proper identity of the atomic positions. The  $R$ -value is still high and many atomic positions are modeled by non-positive definite displacement parameters. The key to improving the refinement is to allow the sizes of the twin domains to be refined. In the present model, there are four domains. The first pair is the twinning, evident from the diffraction pattern, generated by obverse and reverse rhombohedral centring. The second pair is generated by removal of the mirror planes on proceeding from  $R3m$  to  $R3$ . These domains are initially all the same size. However, the strong diffuse scattering in the diffraction pattern is expected to be manifested as an imbalance in the intensity relationship between the superstructure reflections and the basic reflections. This can be modeled by freeing the twin domain sizes, or by refining the main reflections with a separate scale factor. All that remains is to distinguish between the Ni and Ga atoms. The simplest way to do this is to refine the occupancies of all non-Yb sites. If these non-Yb sites are initially assigned to be Ga atoms, those that have the lowest occupancies will be revealed to be Ni atoms. The resulting model corresponds to approximately the correct chemical composition of  $\text{YbNi}_3\text{Ga}_9$ . Anisotropic displacement parameters were not applied for atoms other than Yb, because the rather heavy twinning leads to correlations. The final  $R$ -values are reasonable ( $R_1 = 0.035$ ,  $R_w = 0.054$ ,  $\text{GOF} = 1.0$ ).

**Table A2-1.** Crystallographic data for YbNi<sub>3</sub>Ga<sub>9</sub>

formula	YbNi <sub>3</sub> Ga <sub>9</sub>	YbNi <sub>3</sub> Ga <sub>9</sub>	YbNi <sub>3</sub> Ga <sub>9</sub>
formula mass (amu)	976.65	976.65	976.65
space group	<i>R</i> 32 (No. 155)	<i>R</i> 32 (No. 155)	<i>R</i> 32 (No. 155)
<i>a</i> (Å)	7.2137(16)	7.2180(4)	7.2294(7)
<i>c</i> (Å)	27.509(6)	27.4975(15)	27.513(3)
<i>V</i> (Å <sup>3</sup> )	1239.7(6)	1240.67(15)	1245.3(3)
<i>Z</i>	6	6	6
<i>T</i> (K)	99(2)	199(2)	298(2)
$\rho_{\text{calcd}}$ (g cm <sup>-3</sup> )	7.849	7.843	7.814
crystal dimensions (mm)	0.07 × 0.06 × 0.04	0.08 × 0.07 × 0.04	0.09 × 0.08 × 0.05
$\mu(\text{Mo } K\alpha)$ (mm <sup>-1</sup> )	46.56	46.53	46.36
transmission factors	0.204–0.389	0.100–0.320	0.049–0.205
2 $\theta$ limits	4.44–63.14°	4.44–63.00°	4.44–63.05°
data collected	–10 ≤ <i>h</i> ≤ 10, –10 ≤ <i>k</i> ≤ 10, –40 ≤ <i>l</i> ≤ 40	–10 ≤ <i>h</i> ≤ 10, –10 ≤ <i>k</i> ≤ 10, –40 ≤ <i>l</i> ≤ 40	–6 ≤ <i>h</i> ≤ 10, –10 ≤ <i>k</i> ≤ 10, –25 ≤ <i>l</i> ≤ 40
no. of data collected	3570	5505	3297
no. of unique data, including $F_o^2 < 0$	938 ( $R_{\text{int}} = 0.040$ )	934 ( $R_{\text{int}} = 0.034$ )	938 ( $R_{\text{int}} = 0.045$ )
no. of unique data, with $F_o^2 > 2\sigma(F_o^2)$	840	880	829
no. of variables	43	43	43
Flack parameter	0.17(5)	0.13(3)	0.14(6)
$R(F)$ for $F_o^2 > 2\sigma(F_o^2)$ <sup>a</sup>	0.029	0.018	0.033
$R_w(F_o^2)$ <sup>b</sup>	0.059	0.038	0.070
goodness of fit	1.04	1.10	1.02
$(\Delta\rho)_{\text{max}}, (\Delta\rho)_{\text{min}}$ (e Å <sup>-3</sup> )	1.93, –1.59	2.19, –1.05	2.12, –2.13

<sup>a</sup>  $R(F) = \sum ||F_o| - |F_c|| / \sum |F_o|$ . <sup>b</sup>  $R_w(F_o^2) = [\sum [w(F_o^2 - F_c^2)^2] / \sum wF_o^4]^{1/2}$ ;  $w^{-1} = [\sigma^2(F_o^2) + (Ap)^2 + Bp]$ , where  $p = [\max(F_o^2, 0) + 2F_c^2] / 3$ .

**Table A2-2.** Atomic coordinates and equivalent isotropic displacement parameters for YbNi<sub>3</sub>Ga<sub>9</sub>.

Atom	Wyckoff position	<i>x</i>	<i>y</i>	<i>z</i>	$U_{\text{eq}} (\text{\AA}^2)$ <sup>a</sup>
<b>99 K</b>					
Yb	6 <i>c</i>	0	0	0.16689(2)	0.0039(2)
Ni	18 <i>f</i>	0.3335(2)	0.3274(2)	0.08457(5)	0.0040(3)
Ga1	18 <i>f</i>	0.0033(2)	0.3366(2)	0.10058(5)	0.0041(2)
Ga2	9 <i>e</i>	0.7902(2)	0	½	0.0044(3)
Ga3	9 <i>d</i>	0.6673(2)	0	0	0.0048(3)
Ga4	6 <i>c</i>	0	0	0.05082(6)	0.0041(3)
Ga5	6 <i>c</i>	0	0	0.28325(6)	0.0044(3)
Ga6	6 <i>c</i>	0	0	0.38479(6)	0.0042(3)
<b>199 K</b>					
Yb	6 <i>c</i>	0	0	0.16691(2)	0.0060(1)
Ni	18 <i>f</i>	0.3333(1)	0.3273(1)	0.08468(3)	0.0058(2)
Ga1	18 <i>f</i>	0.0033(1)	0.3366(1)	0.10068(3)	0.0066(2)
Ga2	9 <i>e</i>	0.7900(1)	0	½	0.0065(2)
Ga3	9 <i>d</i>	0.6671(1)	0	0	0.0085(2)
Ga4	6 <i>c</i>	0	0	0.05080(4)	0.0067(2)
Ga5	6 <i>c</i>	0	0	0.28325(4)	0.0066(2)
Ga6	6 <i>c</i>	0	0	0.38492(4)	0.0072(2)
<b>298 K</b>					
Yb	6 <i>c</i>	0	0	0.16692(2)	0.0088(2)
Ni	18 <i>f</i>	0.3335(3)	0.3273(3)	0.08475(6)	0.0083(3)
Ga1	9 <i>e</i>	0.0032(2)	0.3365(2)	0.10070(7)	0.0101(3)
Ga2	9 <i>d</i>	0.7901(2)	0	½	0.0094(4)
Ga3	6 <i>c</i>	0	0	0.05094(7)	0.0102(4)
Ga4	6 <i>c</i>	0	0	0.28317(8)	0.0100(4)
Ga5	6 <i>c</i>	0	0	0.38508(8)	0.0112(4)

<sup>a</sup>  $U_{\text{eq}}$  is defined as one-third of the trace of the orthogonalized  $U_{ij}$  tensor.

**Table A2-3.** Interatomic distances (Å) in YbNi<sub>3</sub>Ga<sub>9</sub>.

	99 K	199 K	298 K
Yb–Ga2 (×3)	2.953(1)	2.954(1)	2.959(1)
Yb–Ga1 (×3)	3.020(2)	3.019(1)	3.022(2)
Yb–Ga1 (×3)	3.028(2)	3.026(1)	3.030(2)
Yb–Ga4	3.193(2)	3.193(1)	3.191(2)
Yb–Ga5	3.201(2)	3.199(1)	3.198(2)
Yb–Ni (×3)	3.279(2)	3.277(1)	3.278(2)
Yb–Ni (×3)	3.288(2)	3.286(1)	3.289(2)
Ni–Ga3	2.327(1)	2.329(1)	2.332(2)
Ni–Ga1	2.425(2)	2.426(1)	2.429(2)
Ni–Ga2	2.444(2)	2.440(1)	2.441(2)
Ni–Ga1	2.454(2)	2.457(1)	2.460(2)
Ni–Ga1	2.456(2)	2.456(1)	2.462(2)
Ni–Ga4	2.558(2)	2.560(1)	2.564(2)
Ni–Ga5	2.564(2)	2.567(1)	2.570(2)
Ni–Ga6	2.612(2)	2.613(1)	2.617(2)
Ga1–Ga6	2.738(2)	2.738(1)	2.741(2)
Ga1–Ga2	2.768(2)	2.767(1)	2.770(2)
Ga1–Ga2	2.768(2)	2.766(1)	2.770(2)
Ga1–Ga4	2.778(2)	2.780(1)	2.782(2)
Ga1–Ga5	2.787(2)	2.790(1)	2.792(2)
Ga2–Ga2 (×2)	2.621(3)	2.625(2)	2.629(3)
Ga3–Ga5 (×2)	2.773(1)	2.774(1)	2.779(1)
Ga3–Ga4 (×2)	2.778(2)	2.779(1)	2.785(2)
Ga3–Ga6 (×2)	2.792(1)	2.794(1)	2.800(1)
Ga4–Ga4	2.796(3)	2.794(2)	2.803(4)
Ga5–Ga6	2.793(3)	2.796(2)	2.804(3)

**Table A2-4.** Crystallographic data for YbCu<sub>3</sub>Ga<sub>8</sub>.

formula	YbCu <sub>3</sub> Ga <sub>8</sub>	YbCu <sub>3</sub> Ga <sub>8</sub>	YbCu <sub>3</sub> Ga <sub>8</sub>
formula mass (amu)	921.42	921.42	921.42
space group	$Pm\bar{3}m$ (No. 221)	$Pm\bar{3}m$ (No. 221)	$Pm\bar{3}m$ (No. 221)
$a$ (Å)	8.2542(8)	8.2684(6)	8.2818(13)
$V$ (Å <sup>3</sup> )	562.37(16)	565.28(12)	568.0(3)
$Z$	3	3	3
$T$ (K)	100(2)	200(2)	296(2)
$\rho_{\text{calcd}}$ (g cm <sup>-3</sup> )	8.162	8.120	8.081
crystal dimensions (mm)	0.11 × 0.06 × 0.06	0.07 × 0.07 × 0.06	0.11 × 0.08 × 0.08
$\mu$ (Mo $K\alpha$ ) (mm <sup>-1</sup> )	48.78	48.53	48.29
transmission factors	0.060–0.181	0.112–0.216	0.065–0.132
$2\theta$ limits	4.93–63.17°	4.93–64.23°	4.92–63.41°
data collected	$-12 \leq h \leq 12,$ $-12 \leq k \leq 12,$ $-12 \leq l \leq 12$	$-12 \leq h \leq 12,$ $-12 \leq k \leq 12,$ $-12 \leq l \leq 12$	$-12 \leq h \leq 12,$ $-12 \leq k \leq 12,$ $-12 \leq l \leq 12$
no. of data collected	7487	7627	7600
no. of unique data, including $F_o^2 < 0$	236 ( $R_{\text{int}} = 0.031$ )	247 ( $R_{\text{int}} = 0.035$ )	243 ( $R_{\text{int}} = 0.057$ )
no. of unique data, with $F_o^2 > 2\sigma(F_o^2)$	230	233	216
no. of variables	16	16	16
$R(F)$ for $F_o^2 > 2\sigma(F_o^2)$ <sup>a</sup>	0.041	0.041	0.048
$R_w(F_o^2)$ <sup>b</sup>	0.076	0.076	0.127
goodness of fit	1.08	1.08	1.13
$(\Delta\rho)_{\text{max}}, (\Delta\rho)_{\text{min}}$ (e Å <sup>-3</sup> )	4.77, -5.52	4.54, -5.49	3.49, -5.08

<sup>a</sup>  $R(F) = \sum ||F_o| - |F_c|| / \sum |F_o|$ . <sup>b</sup>  $R_w(F_o^2) = [\sum [w(F_o^2 - F_c^2)^2] / \sum wF_o^4]^{1/2}$ ;  $w^{-1} = [\sigma^2(F_o^2) + (Ap)^2 + Bp]$ , where  $p = [\max(F_o^2, 0) + 2F_c^2] / 3$ .

**Table A2-5.** Atomic coordinates and equivalent isotropic displacement parameters for YbCu<sub>3</sub>Ga<sub>8</sub>.<sup>a</sup>

Atom	Wyckoff position	<i>x</i>	<i>y</i>	<i>z</i>	$U_{\text{eq}}$ (Å <sup>2</sup> ) <sup>b</sup>
<b>100 K</b>					
Yb	3 <i>c</i>	0	½	½	0.0057(3)
X1	12 <i>j</i>	½	0.1530(1)	0.1530(1)	0.0079(4)
X2	12 <i>i</i>	0	0.2318(2)	0.2318(2)	0.0092(4)
X3	8 <i>g</i>	0.3389(2)	0.3389(2)	0.3389(2)	0.0227(6)
X4	1 <i>a</i>	0	0	0	0.0179(15)
<b>200 K</b>					
Yb	3 <i>c</i>	0	½	½	0.0081(3)
X1	12 <i>j</i>	½	0.1529(1)	0.1529(1)	0.0100(4)
X2	12 <i>i</i>	0	0.2319(1)	0.2319(1)	0.0114(4)
X3	8 <i>g</i>	0.3390(2)	0.3390(2)	0.3390(2)	0.0255(6)
X4	1 <i>a</i>	0	0	0	0.0193(14)
<b>296 K</b>					
Yb	3 <i>c</i>	0	½	½	0.0158(5)
X1	12 <i>j</i>	½	0.1531(2)	0.1531(2)	0.0169(5)
X2	12 <i>i</i>	0	0.2318(2)	0.2318(2)	0.0194(5)
X3	8 <i>g</i>	0.3391(3)	0.3391(3)	0.3391(3)	0.0329(8)
X4	1 <i>a</i>	0	0	0	0.0231(15)

<sup>a</sup> Each *X* site contains a disordered mixture of 0.27 Cu and 0.73 Ga.

<sup>b</sup>  $U_{\text{eq}}$  is defined as one-third of the trace of the orthogonalized  $U_{ij}$  tensor.

**Table A2-6.** Interatomic distances (Å) in YbCu<sub>3</sub>Ga<sub>8</sub>.

	100 K	200 K	296 K
Yb–X1 (×8)	3.130(1)	3.136(1)	3.140(1)
Yb–X2 (×4)	3.130(2)	3.135(2)	3.141(2)
Yb–X3 (×8)	3.371(1)	3.376(1)	3.382(1)
X1–X1 (×2)	2.526(2)	2.529(2)	2.536(3)
X1–X3 (×2)	2.545(2)	2.551(2)	2.554(2)
X1–X2 (×4)	2.630(1)	2.634(1)	2.639(1)
X2–X2 (×4)	2.706(2)	2.711(2)	2.715(2)
X2–X4	2.706(2)	2.711(2)	2.715(2)
X2–X3 (×2)	3.064(3)	3.070(3)	3.076(3)
X3–X3 (×3)	2.659(4)	2.662(4)	2.665(4)

**Table A2-7.** Cell parameters for YbNi<sub>3</sub>Ga<sub>9</sub> at different temperatures.

<i>T</i> (K)	<i>a</i> (Å)	<i>c</i> (Å)	<i>V</i> (Å <sup>3</sup> )
200	7.2188(6)	27.500(2)	1241.0(3)
190	7.2177(7)	27.499(3)	1240.6(3)
180	7.2164(7)	24.497(3)	1240.1(3)
170	7.2160(7)	24.499(3)	1240.1(3)
160	7.2145(7)	24.496(3)	1239.4(3)
150	7.2138(7)	27.496(3)	1239.1(3)
140	7.2124(7)	27.495(3)	1238.7(4)
130	7.2120(8)	27.497(3)	1238.6(4)
120	7.2096(9)	27.489(3)	1237.4(4)
110	7.2090(10)	27.491(3)	1237.3(5)
100	7.2096(10)	27.494(4)	1237.6(5)

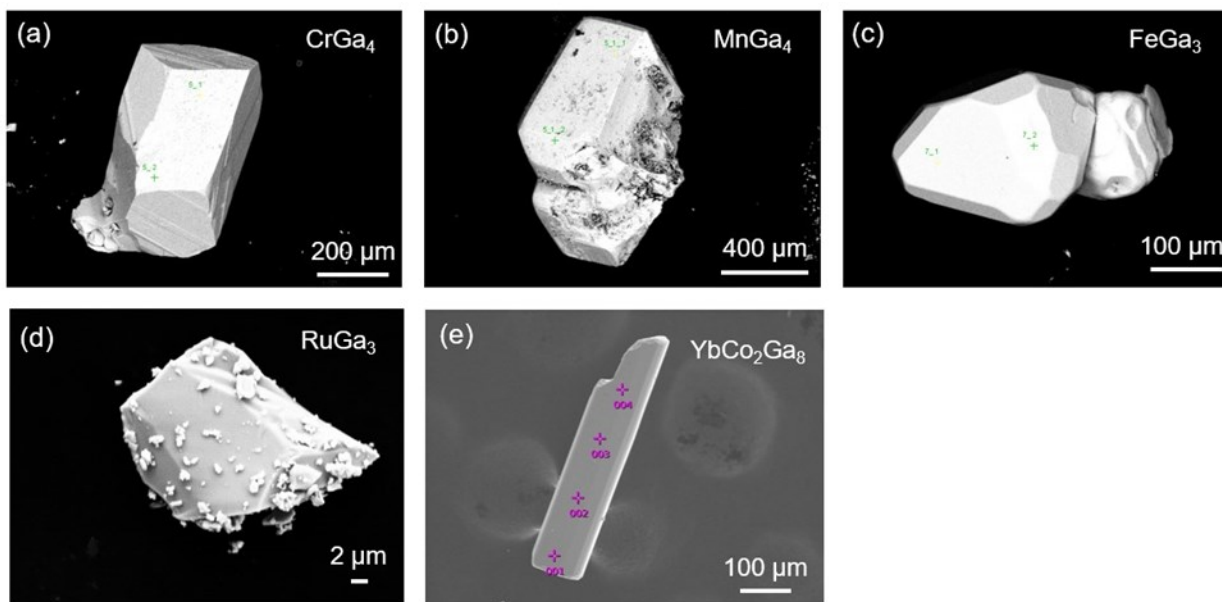


**Figure A2-4.** SEM images of crystals grown in gallium flux.

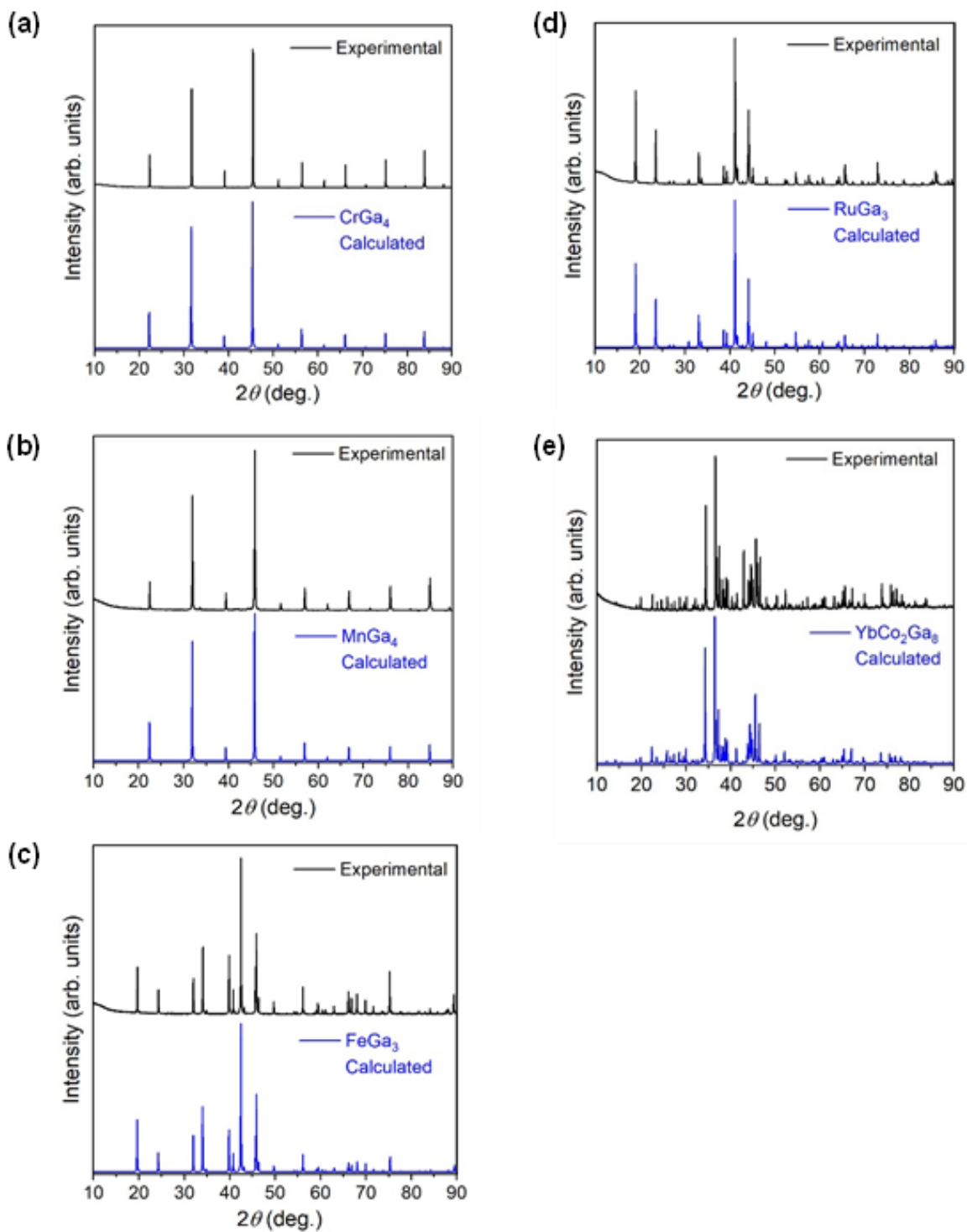


**Figure A2-5.** Powder XRD patterns of ground crystals grown in gallium flux.

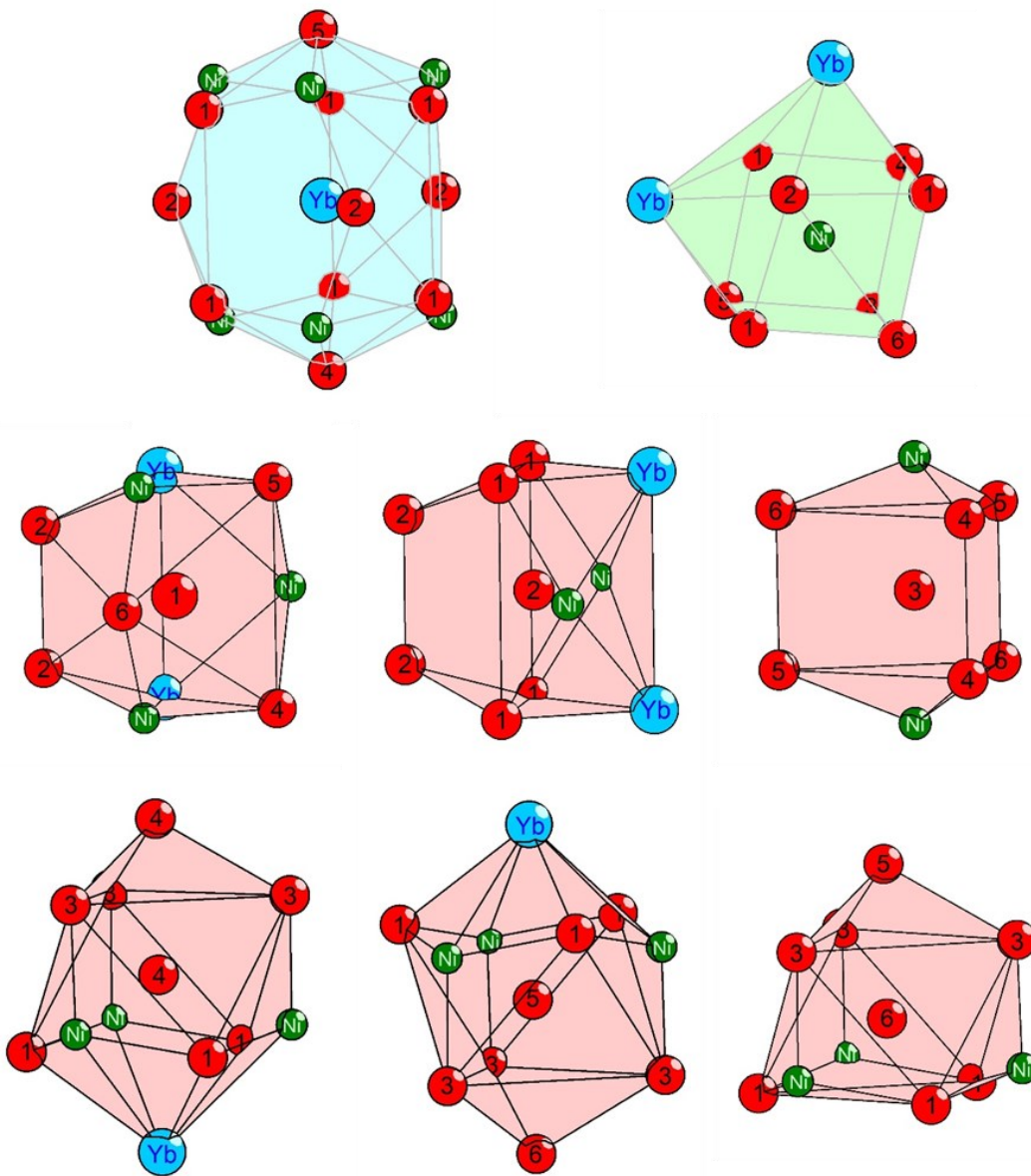


**Figure A2-6.** Coordination polyhedra around Yb (blue), Ni (green), and Ga (red) atoms in  $\text{YbNi}_3\text{Ga}_9$ .

## Appendix 3

### Supplementary Data for Chapter 5

**Table A3-1.** Ternary germanides with U<sub>4</sub>Re<sub>7</sub>Ge<sub>6</sub>-type structure.

<b>Compound</b>	<b><i>a</i> (Å)</b>	<b>Compound</b>	<b><i>a</i> (Å)</b>
Sc <sub>4</sub> Co <sub>7</sub> Ge <sub>6</sub>	7.850(1)	Mn <sub>4</sub> Ir <sub>7</sub> Ge <sub>6</sub>	8.0248(4)
Ti <sub>4</sub> Co <sub>7</sub> Ge <sub>6</sub>	7.673(4)	Tb <sub>4</sub> Ir <sub>7</sub> Ge <sub>6</sub>	8.345(5)
Zr <sub>4</sub> Co <sub>7</sub> Ge <sub>6</sub>	7.886(2)	Y <sub>4</sub> Ir <sub>7</sub> Ge <sub>6</sub>	8.324(7)
Hf <sub>4</sub> Co <sub>7</sub> Ge <sub>6</sub>	7.831(2)	Dy <sub>4</sub> Ir <sub>7</sub> Ge <sub>6</sub>	8.322(5)
		Ho <sub>4</sub> Ir <sub>7</sub> Ge <sub>6</sub>	8.311(7)
		Er <sub>4</sub> Ir <sub>7</sub> Ge <sub>6</sub>	8.295(8)
Lu <sub>4</sub> Ru <sub>7</sub> Ge <sub>6</sub>	8.239(1)	Tm <sub>4</sub> Ir <sub>7</sub> Ge <sub>6</sub>	8.273(6)
Sc <sub>4</sub> Ru <sub>7</sub> Ge <sub>6</sub>	8.129	Yb <sub>4</sub> Ir <sub>7</sub> Ge <sub>6</sub>	8.262(7)
		Lu <sub>4</sub> Ir <sub>7</sub> Ge <sub>6</sub>	8.258(5)
Dy <sub>4</sub> Rh <sub>7</sub> Ge <sub>6</sub>	8.326(7)	Sc <sub>4</sub> Ir <sub>7</sub> Ge <sub>6</sub>	8.136(2)
Ho <sub>4</sub> Rh <sub>7</sub> Ge <sub>6</sub>	8.305(7)		
Er <sub>4</sub> Rh <sub>7</sub> Ge <sub>6</sub>	8.296	Er <sub>4</sub> Os <sub>7</sub> Ge <sub>6</sub>	8.314(6)
Tm <sub>4</sub> Rh <sub>7</sub> Ge <sub>6</sub>	8.276(5)	Tm <sub>4</sub> Os <sub>7</sub> Ge <sub>6</sub>	8.297(6)
Yb <sub>4</sub> Rh <sub>7</sub> Ge <sub>6</sub>	8.253(1)	Yb <sub>4</sub> Os <sub>7</sub> Ge <sub>6</sub>	8.288(6)
Lu <sub>4</sub> Rh <sub>7</sub> Ge <sub>6</sub>	8.243	Lu <sub>4</sub> Os <sub>7</sub> Ge <sub>6</sub>	8.276(6)
Sc <sub>4</sub> Rh <sub>7</sub> Ge <sub>6</sub>	8.1255(8)	Sc <sub>4</sub> Os <sub>7</sub> Ge <sub>6</sub>	8.146(1)

**Table A3-2.** Ternary germanides with Sc<sub>5</sub>Co<sub>4</sub>Si<sub>10</sub>-type structure.

<b>Compound</b>	<b><i>a</i> (Å)</b>	<b><i>c</i> (Å)</b>	<b>Compound</b>	<b><i>a</i> (Å)</b>	<b><i>c</i> (Å)</b>
Y <sub>5</sub> Co <sub>4</sub> Ge <sub>10</sub>	12.944(9)	4.270(3)	Gd <sub>5</sub> Ir <sub>4</sub> Ge <sub>10</sub>	12.949(9)	4.333(3)
Tm <sub>5</sub> Co <sub>4</sub> Ge <sub>10</sub>	12.622(9)	4.139(4)	Tb <sub>5</sub> Ir <sub>4</sub> Ge <sub>10</sub>	12.935(9)	4.318(3)
Yb <sub>5</sub> Co <sub>4</sub> Ge <sub>10</sub>	12.6369(18)	4.1378(8)	Y <sub>5</sub> Ir <sub>4</sub> Ge <sub>10</sub>	12.927(5)	4.308(5)
Lu <sub>5</sub> Co <sub>4</sub> Ge <sub>10</sub>	12.606(8)	4.125(3)	Dy <sub>5</sub> Ir <sub>4</sub> Ge <sub>10</sub>	12.910(8)	4.304(3)
			Ho <sub>5</sub> Ir <sub>4</sub> Ge <sub>10</sub>	12.875(2)	4.283(1)
Yb <sub>5</sub> Ni <sub>4</sub> Ge <sub>10</sub>	12.6716(18)	4.1598(8)	Er <sub>5</sub> Ir <sub>4</sub> Ge <sub>10</sub>	12.865(9)	4.278(3)
			Tm <sub>5</sub> Ir <sub>4</sub> Ge <sub>10</sub>	12.846(8)	4.267
Gd <sub>5</sub> Rh <sub>4</sub> Ge <sub>10</sub>	12.984(5)	4.296(5)	Yb <sub>5</sub> Ir <sub>4</sub> Ge <sub>10</sub>	12.877(9)	4.285(3)
Tb <sub>5</sub> Rh <sub>4</sub> Ge <sub>10</sub>	12.954(5)	4.285(5)	Lu <sub>5</sub> Ir <sub>4</sub> Ge <sub>10</sub>	12.831	4.252(3)
Y <sub>5</sub> Rh <sub>4</sub> Ge <sub>10</sub>	12.953(3)	4.272(2)			
Dy <sub>5</sub> Rh <sub>4</sub> Ge <sub>10</sub>	12.944(9)	4.270(3)	Y <sub>5</sub> Os <sub>4</sub> Ge <sub>10</sub>	13.006(8)	4.297(5)
Ho <sub>5</sub> Rh <sub>4</sub> Ge <sub>10</sub>	12.881(7)	4.240(2)	Dy <sub>5</sub> Os <sub>4</sub> Ge <sub>10</sub>	13.0340(4)	4.2950(4)
Er <sub>5</sub> Rh <sub>4</sub> Ge <sub>10</sub>	12.843(3)	4.225(1)	Ho <sub>5</sub> Os <sub>4</sub> Ge <sub>10</sub>	12.984(3)	4.2820(16)
Tm <sub>5</sub> Rh <sub>4</sub> Ge <sub>10</sub>	12.845(2)	4.2095(7)	Y <sub>4</sub> TmOs <sub>4</sub> Ge <sub>10</sub>	12.9126(63)	4.2613(23)
Yb <sub>5</sub> Rh <sub>4</sub> Ge <sub>10</sub>	12.886(9)	4.234(3)	Tm <sub>5</sub> Os <sub>4</sub> Ge <sub>10</sub>	12.929(6)	4.253(2)
Lu <sub>5</sub> Rh <sub>4</sub> Ge <sub>10</sub>	12.827(5)	4.209(5)	Y <sub>4</sub> TmOs <sub>4</sub> Ge <sub>10</sub>	12.9621(53)	4.2792(25)
Ca <sub>1.15</sub> Lu <sub>3.85</sub> Rh <sub>4</sub> Ge <sub>10</sub>	12.8567(35)	4.2279(13)	Y <sub>2</sub> Dy <sub>3</sub> Os <sub>4</sub> Ge <sub>10</sub>	13.0220(4)	4.2938(4)

**Table A3-3.** Crystallographic data for EuCo<sub>2</sub>Ge<sub>2</sub>.

formula	EuCo <sub>2</sub> Ge <sub>2</sub>	EuCo <sub>2</sub> Ge <sub>2</sub>
formula mass (amu)	415.00	415.00
space group	<i>I4/mmm</i>	<i>I4/mmm</i>
<i>a</i> (Å)	4.0377(7)	4.0313(6)
<i>b</i> (Å)	4.0377(7)	4.0313(6)
<i>c</i> (Å)	10.4780(19)	10.4624(17)
<i>V</i> (Å <sup>3</sup> )	170.82(7)	170.03(6)
<i>Z</i>	2	2
$\rho_{\text{calcd}}$ (g cm <sup>-3</sup> )	8.068	8.106
<i>T</i> (K)	296(2)	193(2)
crystal dimensions (mm)	0.116 × 0.079 × 0.065	0.081 × 0.038 × 0.033
$\mu$ (Mo K $\alpha$ ) (mm <sup>-1</sup> )	44.701	44.910
transmission factors	0.531–0.746	0.165–0.375
2 $\theta$ limits (°)	7.778–63.258	7.79–62.832
data collected	$-5 \leq h \leq 5,$ $-5 \leq k \leq 5,$ $-15 \leq l \leq 15$	$-5 \leq h \leq 5,$ $-5 \leq k \leq 5,$ $-15 \leq l \leq 15$
no. of data collected	2976	2220
no. of unique data, including $F_o^2 < 0$	110 ( $R_{\text{int}} = 0.169$ )	109 ( $R_{\text{int}} = 0.162$ )
no. of unique data, with $F_o^2 > 2\sigma(F_o^2)$	102	102
no. of variables	9	9
$R(F)$ for $F_o^2 > 2\sigma(F_o^2)$ <sup>a</sup>	0.031	0.0242
$R_w(F_o^2)$ <sup>b</sup>	0.076	0.0578
goodness of fit	1.149	1.249
$(\Delta\rho)_{\text{max}}, (\Delta\rho)_{\text{min}}$ (e·Å <sup>-3</sup> )	3.534, -3.014	2.187, -2.361

<sup>a</sup>  $R(F) = \sum ||F_o| - |F_c|| / \sum |F_o|$ . <sup>b</sup>  $R_w(F_o^2) = [\sum [w(F_o^2 - F_c^2)^2] / \sum wF_o^4]^{1/2}$ ;  $w^{-1} = [\sigma^2(F_o^2) + (Ap)^2 + Bp]$ , where  $p = [\max(F_o^2, 0) + 2F_c^2] / 3$ .

**Table A3-4.** Crystallographic data for YbCo<sub>2</sub>Ge<sub>2</sub>

formula	YbCo <sub>2</sub> Ge <sub>2</sub>	YbCo <sub>2</sub> Ge <sub>2</sub>
formula mass (amu)	436.08	436.08
space group	<i>I4/mmm</i>	<i>I4/mmm</i>
<i>a</i> (Å)	3.9378(4)	3.9317(6)
<i>b</i> (Å)	3.9378(4)	3.9317(6)
<i>c</i> (Å)	10.0655(10)	10.0641(16)
<i>V</i> (Å <sup>3</sup> )	156.08(4)	155.57(4)
<i>Z</i>	2	2
$\rho_{\text{calcd}}$ (g cm <sup>-3</sup> )	9.279	9.309
<i>T</i> (K)	296(2)	193(2)
crystal dimensions (mm)	0.068 × 0.041 × 0.032	0.087 × 0.068 × 0.055
$\mu$ (Mo K $\alpha$ ) (mm <sup>-1</sup> )	58.791	58.982
transmission factors	0.385–0.555	0.275–0.363
2 $\theta$ limits (°)	8.098–62.772	8.10–62.836
data collected	$-5 \leq h \leq 5,$ $-5 \leq k \leq 5,$ $-14 \leq l \leq 14$	$-5 \leq h \leq 5,$ $-5 \leq k \leq 5,$ $-14 \leq l \leq 14$
no. of data collected	2873	1425
no. of unique data, including $F_o^2 < 0$	101 [ $R_{\text{int}} = 0.1336$ ]	101 [ $R_{\text{int}} = 0.1287$ ]
no. of unique data, with $F_o^2 > 2\sigma(F_o^2)$	101	100
no. of variables	9	9
$R(F)$ for $F_o^2 > 2\sigma(F_o^2)$ <sup>a</sup>	0.018	0.017
$R_w(F_o^2)$ <sup>b</sup>	0.039	0.042
goodness-of-fit	1.299	1.188
$(\Delta\rho)_{\text{max}}, (\Delta\rho)_{\text{min}}$ (e·Å <sup>-3</sup> )	2.065, -1.980	2.127, -1.498

<sup>a</sup>  $R(F) = \sum ||F_o| - |F_c|| / \sum |F_o|$ . <sup>b</sup>  $R_w(F_o^2) = [\sum [w(F_o^2 - F_c^2)^2] / \sum wF_o^4]^{1/2}$ ;  $w^{-1} = [\sigma^2(F_o^2) + (Ap)^2 + Bp]$ , where  $p = [\max(F_o^2, 0) + 2F_c^2] / 3$ .

**Table A3-5.** Crystallographic data for CeTGe<sub>2</sub> (*T* = Co, Ir).

formula	CeCo <sub>0.94</sub> Ge <sub>2</sub>	CeIrGe <sub>2</sub>
formula mass (amu)	681.09	477.50
space group		<i>Cmcm</i>
<i>a</i> (Å)	4.2594(5)	4.3312(16)
<i>b</i> (Å)	16.7802(19)	17.101(6)
<i>c</i> (Å)	4.2114(5)	4.3803(16)
<i>V</i> (Å <sup>3</sup> )	301.00(6)	324.4(2)
<i>Z</i>	2	2
$\rho_{\text{calcd}}$ (g cm <sup>-3</sup> )	7.515	4.888
<i>T</i> (K)		296(2)
crystal dimensions (mm)	0.066 × 0.054 × 0.046	0.081 × 0.077 × 0.056
$\mu$ (Mo K $\alpha$ ) (mm <sup>-1</sup> )	39.361	36.345
transmission factors	0.577–0.746	0.3568–0.7462
2 $\theta$ limit	4.856 to 63.248°	4.764 to 63.462°
data collected	–6 ≤ <i>h</i> ≤ 6, –24 ≤ <i>k</i> ≤ 24, –6 ≤ <i>l</i> ≤ 6	–6 ≤ <i>h</i> ≤ 6, –25 ≤ <i>k</i> ≤ 23, –6 ≤ <i>l</i> ≤ 6
no. of data collected	2977	1965
no. of unique data, including $F_o^2 < 0$	319 [ $R_{\text{int}} = 0.0705$ ]	345 [ $R_{\text{int}} = 0.2168$ ]
no. of unique data, with $F_o^2 > 2\sigma(F_o^2)$	288	270
no. of variables	19	17
$R(F)$ for $F_o^2 > 2\sigma(F_o^2)$ <sup>a</sup>	0.022	0.062
$R_w(F_o^2)$ <sup>b</sup>	0.047	0.143
goodness-of-fit	1.118	0.992
$(\Delta\rho)_{\text{max}}, (\Delta\rho)_{\text{min}}$ (e·Å <sup>-3</sup> )	3.030, –2.198	9.859, –7.572

<sup>a</sup>  $R(F) = \sum ||F_o| - |F_c|| / \sum |F_o|$ . <sup>b</sup>  $R_w(F_o^2) = [\sum [w(F_o^2 - F_c^2)^2] / \sum wF_o^4]^{1/2}$ ;  $w^{-1} = [\sigma^2(F_o^2) + (Ap)^2 + Bp]$ , where  $p = [\max(F_o^2, 0) + 2F_c^2] / 3$ .

**Table A3-6.** Crystallographic data for CeIrGe<sub>2</sub>.

formula	CeIrGe <sub>2</sub>	CeIrGe <sub>2</sub>
formula mass (amu)	477.50	477.50
space group		<i>Immm</i>
<i>a</i> (Å)	4.3842(7)	4.3809(6)
<i>b</i> (Å)	8.8960(14)	8.8882(12)
<i>c</i> (Å)	16.258(3)	16.250(2)
<i>V</i> (Å <sup>3</sup> )	634.09(17)	632.77(15)
<i>Z</i>		8
$\rho_{\text{calcd}}$ (g cm <sup>-3</sup> )	10.004	10.025
<i>T</i> (K)	297(2)	193(2)
crystal dimensions (mm)	0.079 × 0.067 × 0.050	0.077 × 0.072 × 0.052
$\mu$ (Mo K $\alpha$ ) (mm <sup>-1</sup> )	74.387	74.542
transmission factors	0.162–0.265	0.190–0.270
2 $\theta$ limit	5.012–63.45	5.014–63.218
data collected	$-6 \leq h \leq 6,$ $-13 \leq k \leq 13,$ $-24 \leq l \leq 24$	$-6 \leq h \leq 6,$ $-12 \leq k \leq 13,$ $-23 \leq l \leq 23$
no. of data collected	11386	7339
no. of unique data, including $F_o^2 < 0$	653 [ $R_{\text{int}} = 0.1661$ ]	645 [ $R_{\text{int}} = 0.1468$ ]
no. of unique data, with $F_o^2 > 2\sigma(F_o^2)$	554	565
no. of variables	29	29
$R(F)$ for $F_o^2 > 2\sigma(F_o^2)$ <sup>a</sup>	0.0368	0.0305
$R_w(F_o^2)$ <sup>b</sup>	0.0854	0.0716
goodness-of-fit	1.151	1.101
$(\Delta\rho)_{\text{max}}, (\Delta\rho)_{\text{min}}$ (e·Å <sup>-3</sup> )	7.525, -5.338	6.517, -4.349

<sup>a</sup>  $R(F) = \sum ||F_o| - |F_c|| / \sum |F_o|$ . <sup>b</sup>  $R_w(F_o^2) = [\sum [w(F_o^2 - F_c^2)^2] / \sum wF_o^4]^{1/2}$ ;  $w^{-1} = [\sigma^2(F_o^2) + (Ap)^2 + Bp]$ , where  $p = [\max(F_o^2, 0) + 2F_c^2] / 3$ .

**Table A3-7.** Crystallographic data for Yb<sub>4</sub>Ir<sub>7</sub>Ge<sub>6</sub>.

formula	Yb <sub>4</sub> Ir <sub>7</sub> Ge <sub>6</sub>	Yb <sub>4</sub> Ir <sub>7</sub> Ge <sub>6</sub>
formula mass (amu)	2473.10	2473.10
space group		<i>Im-3m</i>
<i>a</i> (Å)	8.2709(16)	8.2677(15)
<i>V</i> (Å <sup>3</sup> )	565.8(3)	565.1(3)
<i>Z</i>		2
$\rho_{\text{calcd}}$ (g cm <sup>-3</sup> )	14.517	14.533
<i>T</i> (K)	296(2)	193(2)
crystal dimensions (mm)	0.171 × 0.167 × 0.061	0.060 × 0.056 × 0.053
$\mu$ (Mo K $\alpha$ ) (mm <sup>-1</sup> )	130.217	130.368
transmission factors	0.017–0.107	0.014–0.055
2 $\theta$ limit	6.968–63.028	6.97–63.054
data collected	–12 ≤ <i>h</i> ≤ 12, –12 ≤ <i>k</i> ≤ 12, –12 ≤ <i>l</i> ≤ 12	–12 ≤ <i>h</i> ≤ 12, –10 ≤ <i>k</i> ≤ 12, –11 ≤ <i>l</i> ≤ 11
no. of data collected	7398	2634
no. of unique data, including $F_o^2 < 0$	120 [ <i>R</i> <sub>int</sub> = 0.2173]	120 [ <i>R</i> <sub>int</sub> = 0.1568]
no. of Unique data, with $F_o^2 > 2\sigma(F_o^2)$	108	102
no. of Variables	10	10
<i>R</i> ( <i>F</i> ) for $F_o^2 > 2\sigma(F_o^2)$ <sup>a</sup>	0.0375	0.0415
<i>R</i> <sub>w</sub> ( $F_o^2$ ) <sup>b</sup>	0.0890	0.101
goodness-of-fit	1.105	1.178
( $\Delta\rho$ ) <sub>max</sub> , ( $\Delta\rho$ ) <sub>min</sub> (e·Å <sup>-3</sup> )	3.861, –5.529	4.262, –5.912

<sup>a</sup>  $R(F) = \sum ||F_o| - |F_c|| / \sum |F_o|$ . <sup>b</sup>  $R_w(F_o^2) = [\sum [w(F_o^2 - F_c^2)^2] / \sum wF_o^4]^{1/2}$ ;  $w^{-1} = [\sigma^2(F_o^2) + (Ap)^2 + Bp]$ , where  $p = [\max(F_o^2, 0) + 2F_c^2] / 3$ .

**Table A3-8.** Crystallographic data for Yb<sub>5</sub>Ir<sub>4</sub>Ge<sub>10</sub>.

formula	Yb <sub>5</sub> Ir <sub>4</sub> Ge <sub>10</sub>	Yb <sub>5</sub> Ir <sub>4</sub> Ge <sub>10</sub>
formula mass (amu)	2359.90	2359.90
space group		<i>P4/mbm</i>
<i>a</i> (Å)	12.867(3)	12.8754(17)
<i>b</i> (Å)	12.867(3)	12.8754(17)
<i>c</i> (Å)	4.2777(9)	4.2819(6)
<i>V</i> (Å <sup>3</sup> )	708.2(3)	709.8(2)
<i>Z</i>		2
$\rho_{\text{calcd}}$ (g cm <sup>-3</sup> )	11.067	11.041
<i>T</i> (K)	297(2)	193(2)
crystal dimensions (mm)	0.145 × 0.114 × 0.046	0.118 × 0.052 × 0.022
$\mu$ (Mo K $\alpha$ ) (mm <sup>-1</sup> )	90.852	90.641
transmission factors	0.027–0.314	0.029–0.216
2 $\theta$ limit	4.476–63.444	4.474–63.65
data collected	–19 ≤ <i>h</i> ≤ 18, –19 ≤ <i>k</i> ≤ 19, –6 ≤ <i>l</i> ≤ 6	–19 ≤ <i>h</i> ≤ 18, –19 ≤ <i>k</i> ≤ 19, –6 ≤ <i>l</i> ≤ 6
no. of data collected	17587	12779
no. of unique data, including $F_o^2 < 0$	711 [ $R_{\text{int}} = 0.2411$ ]	717 [ $R_{\text{int}} = 0.1687$ ]
no. of unique data, with $F_o^2 > 2\sigma(F_o^2)$	546	537
no. of variables	34	34
$R(F)$ for $F_o^2 > 2\sigma(F_o^2)$ <sup>a</sup>	0.039	0.042
$R_w(F_o^2)$ <sup>b</sup>	0.086	0.092
goodness-of-fit	1.026	1.042
$(\Delta\rho)_{\text{max}}, (\Delta\rho)_{\text{min}}$ (e·Å <sup>-3</sup> )	4.960, –6.432	4.940, –5.974

<sup>a</sup>  $R(F) = \sum ||F_o| - |F_c|| / \sum |F_o|$ . <sup>b</sup>  $R_w(F_o^2) = [\sum [w(F_o^2 - F_c^2)^2] / \sum wF_o^4]^{1/2}$ ;  $w^{-1} = [\sigma^2(F_o^2) + (Ap)^2 + Bp]$ , where  $p = [\max(F_o^2, 0) + 2F_c^2] / 3$ .

**Table A3-9.** Atomic coordinates and equivalent isotropic displacement parameters ( $\text{\AA}^2$ )<sup>a</sup> for  $R\text{Co}_2\text{Ge}_2$  ( $R = \text{Eu}, \text{Yb}$ ),  $\text{CeCoGe}_2$  and  $\text{CeIrGe}_2$  ( $Cmcm$ ).

Label	Wyckoff position	$x$	$y$	$z$	$occ$	$U_{eq}(\text{\AA}^2)^a$
<b>EuCo<sub>2</sub>Ge<sub>2</sub>_296 K</b>						
Eu	2 <i>a</i>	0	0	0	1	0.012(1)
Co	4 <i>d</i>	0	½	¼	1	0.011(1)
Ge	4 <i>e</i>	0	0	0.3682(2)	1	0.010(1)
<b>EuCo<sub>2</sub>Ge<sub>2</sub>_193 K</b>						
Eu	2 <i>a</i>	0	0	0	1	0.007(1)
Co	4 <i>d</i>	0	½	¼	1	0.006(1)
Ge	4 <i>e</i>	0	0	0.3681(2)	1	0.006(1)
<b>YbCo<sub>2</sub>Ge<sub>2</sub>_296 K</b>						
Yb	2 <i>a</i>	0	0	0	1	0.008(1)
Co	4 <i>d</i>	0	½	¼	1	0.007(1)
Ge	4 <i>e</i>	0	0	0.3751(1)	1	0.007(1)
<b>YbCo<sub>2</sub>Ge<sub>2</sub>_193 K</b>						
Yb	2 <i>a</i>	0	0	0	1	0.006(1)
Co	4 <i>d</i>	0	½	¼	1	0.005(1)
Ge	4 <i>e</i>	0	0	0.3752(1)	1	0.005(1)
<b>CeCo<sub>0.94</sub>Ge<sub>2</sub>_296 K</b>						
Ce	4 <i>c</i>	0	0.3917(1)	¼	1	0.008(1)
Co	4 <i>c</i>	0	0.1814(1)	¼	0.937(5)	0.011(1)
Ge1	4 <i>c</i>	0	0.0438(1)	¼	1	0.010(1)
Ge2	4 <i>c</i>	0	0.7499(1)	¼	1	0.010(1)
<b>CeIrGe<sub>2</sub>_296 K</b>						
Ce	4 <i>c</i>	0	0.3911(1)	¼	1	0.014(1)
Ir	4 <i>c</i>	0	0.1793(1)	¼	1	0.017(1)
Ge1	4 <i>c</i>	0	0.0385(2)	¼	1	0.019(1)
Ge2	4 <i>c</i>	0	0.7508(2)	¼	1	0.015(1)

<sup>a</sup> $U_{eq}$  is defined as one third of the trace of the orthogonalized  $U_{ij}$  tensor.

**Table A3-10.** Atomic coordinates and equivalent isotropic displacement parameters ( $\text{\AA}^2$ ) for  $\text{CeIrGe}_2$  ( $Immm$ ),  $\text{Yb}_4\text{Ir}_7\text{Ge}_6$ .

Label	Wyckoff position	$x$	$y$	$z$	$occ$	$U_{eq}(\text{\AA}^2)^a$
<b>CeIrGe<sub>2</sub>_296 K</b>						
Ce1	4 <i>i</i>	0	0	0.2073(1)	1	0.009(1)
Ce2	4 <i>g</i>	0	0.2394(1)	0	1	0.009(1)
Ir	8 <i>l</i>	0	0.2489(1)	0.3516(1)	1	0.008(1)
Ge1	8 <i>l</i>	0	0.3456(2)	0.1986(1)	1	0.010(1)
Ge2	4 <i>j</i>	1/2	0	0.0776(2)	1	0.010(1)
Ge3	4 <i>i</i>	0	0	0.4206(2)	1	0.012(1)
<b>CeIrGe<sub>2</sub>_193 K</b>						
Ce1	4 <i>i</i>	0	0	0.2073(1)	1	0.007(1)
Ce2	4 <i>g</i>	0	0.2390(1)	0	1	0.006(1)
Ir	8 <i>l</i>	0	0.2489(1)	0.3516(1)	1	0.006(1)
Ge1	8 <i>l</i>	0	0.3456(2)	0.1987(1)	1	0.007(1)
Ge2	4 <i>j</i>	1/2	0	0.0775(1)	1	0.007(1)
Ge3	4 <i>i</i>	0	0	0.4206(1)	1	0.008(1)
<b>Yb<sub>4</sub>Ir<sub>7</sub>Ge<sub>6</sub>_296 K</b>						
Yb	8 <i>c</i>	¼	¼	¼	1	0.009(1)
Ir1	2 <i>a</i>	0	0	0	1	0.005(1)
Ir2	12 <i>d</i>	¼	0	½	1	0.007(1)
Ge	12 <i>e</i>	0.03150(4)	0	0	1	0.007(1)
<b>Yb<sub>4</sub>Ir<sub>7</sub>Ge<sub>6</sub>_193 K</b>						
Yb	8 <i>c</i>	¼	¼	¼	1	0.009(1)
Ir1	2 <i>a</i>	0	0	0	1	0.006(1)
Ir2	12 <i>d</i>	¼	0	½	1	0.008(1)
Ge	12 <i>e</i>	0.03146(5)	0	0	1	0.009(1)

<sup>a</sup> $U_{eq}$  is defined as one third of the trace of the orthogonalized  $U_{ij}$  tensor.

**Table A3-11.** Atomic coordinates and equivalent isotropic displacement parameters ( $\text{\AA}^2$ ) for  $\text{Yb}_5\text{Ir}_4\text{Ge}_{10}$ .

Label	Wyckoff position	$x$	$y$	$z$	$occ$	$U_{eq}(\text{\AA}^2)^a$
<b><math>\text{Yb}_5\text{Ir}_4\text{Ge}_{10}</math>_296 K</b>						
Yb1	$4h$	0.01731(1)	0.6731(1)	$\frac{1}{2}$	1	0.011(1)
Yb2	$4h$	0.06148(1)	0.1148(1)	$\frac{1}{2}$	1	0.012(1)
Yb3	$2a$	0	0	0	1	0.011(1)
Ir	$8i$	0.2454(1)	0.0219(1)	0	1	0.009(1)
Ge1	$8j$	0.1556(2)	0.0062(2)	$\frac{1}{2}$	1	0.012(1)
Ge2	$8i$	0.1630(2)	0.2002(2)	0	1	0.013(1)
Ge3	$4g$	0.0672(2)	0.5672(2)	0	1	0.011(1)
<b><math>\text{Yb}_5\text{Ir}_4\text{Ge}_{10}</math>_193 K</b>						
Yb1	$4h$	0.01730(1)	0.6730(1)	$\frac{1}{2}$	1	0.010(1)
Yb2	$4h$	0.06148(1)	0.1148(1)	$\frac{1}{2}$	1	0.011(1)
Yb3	$2a$	0	0	0	1	0.010(1)
Ir	$8i$	0.2452(1)	0.0222(1)	0	1	0.009(1)
Ge1	$8j$	0.1554(2)	0.0063(2)	$\frac{1}{2}$	1	0.011(1)
Ge2	$8i$	0.1629(2)	0.2003(2)	0	1	0.012(1)
Ge3	$4g$	0.0672(2)	0.5672(2)	0	1	0.010(1)

<sup>a</sup> $U_{eq}$  is defined as one third of the trace of the orthogonalized  $U_{ij}$  tensor.

**Table A3-12.** Interatomic distances (Å) for  $R\text{Co}_2\text{Ge}_2$  ( $R = \text{Eu}, \text{Yb}$ ),  $\text{Ce}T\text{Ge}_2$  ( $T = \text{Co}, \text{Ir}$ ).

<b>Label</b>	<b>296 K</b>	<b>193 K</b>		<b>296 K</b>	<b>193 K</b>
<b>EuCo<sub>2</sub>Ge<sub>2</sub></b>			<b>YbCo<sub>2</sub>Ge<sub>2</sub></b>		
Eu–Ge (×8)	3.1718(8)	3.1672(6)	Yb–Ge (×8)	3.0551(5)	3.0509(6)
Eu–Co (×4)	3.3072(4)	3.3022(4)	Yb–Co (×4)	3.1951(2)	3.1930(4)
Ge–Co (×4)	2.3682(8)	2.3641(7)	Ge–Co (×4)	2.3371(5)	2.3348(6)
Ge–Ge	2.763(3)	2.761(2)	Ge–Ge	2.5144(19)	2.5129(19)
Co–Co (×4)	2.8551(5)	2.8506(4)	Co–Co (×4)	2.7844(3)	2.7801(4)
<b>Label</b>	<b>296 K</b>		<b>296 K</b>		
<b>CeCo<sub>0.94</sub>Ge<sub>2</sub></b>			<b>CeIr<sub>0.94</sub>Ge<sub>2</sub></b>		
Ce–Ge <sub>2</sub> (×2)	3.1754(7)		Ce–Ge <sub>2</sub> (×2)	3.231(2)	
Ce–Ge <sub>1</sub> (×4)	3.1842(4)		Ce–Ge <sub>1</sub> (×4)	3.3069(14)	
Ce–Ge <sub>2</sub> (×2)	3.1929(7)		Ce–Ge <sub>2</sub> (×2)	3.269(3)	
Ce–Co (×4)	3.2363(5)		Ce–Ir (×4)	3.3071(10)	
Ge <sub>1</sub> –Co	2.3080(15)		Ge <sub>1</sub> –Ir	2.408(3)	
Ge <sub>1</sub> –Ge <sub>1</sub> (×2)	2.5688(10)		Ge <sub>1</sub> –Ge <sub>1</sub> (×2)	2.556(3)	
Ge <sub>2</sub> –Co (×2)	2.4004(7)		Ge <sub>2</sub> –Ir (×2)	2.4870(17)	
Ge <sub>2</sub> –Co (×2)	2.4206(7)		Ge <sub>2</sub> –Ir (×2)	2.4945(16)	

**Table A3-13.** Interatomic distances (Å) for CeIrGe<sub>2</sub> (*Immm*), Yb<sub>4</sub>Ir<sub>7</sub>Ge<sub>6</sub> and Yb<sub>5</sub>Ir<sub>4</sub>Ge<sub>10</sub>.

<b>Label</b>	<b>296 K</b>	<b>193 K</b>	<b>Label</b>	<b>296 K</b>	<b>193 K</b>
<b>CeIrGe<sub>2</sub></b>			<b>Yb<sub>5</sub>Ir<sub>4</sub>Ge<sub>10</sub></b>		
Ce1–Ge1 (×4)	3.0050(11)	3.0025(9)	Yb1–Ge3 (×2)	2.879(2)	2.880(2)
Ce1–Ge2 (×2)	3.0418(16)	3.0403(14)	Yb1–Ge2 (×4)	3.0243(16)	3.0286(17)
Ce1–Ge1 (×2)	3.0780(14)	3.0748(12)	Yb1–Ir (×4)	3.0760(7)	3.0764(7)
Ce1–Ir (×2)	3.2257(9)	3.2240(8)	Yb1–Ge1 (×2)	3.077(2)	3.080(2)
Ce1–Ir (×2)	3.2731(6)	3.2702(5)	Yb2–Ge3 (×4)	3.2296(13)	3.2325(14)
Ce2–Ir (×4)	3.2613(5)	3.2597(4)	Yb2–Ge2 (×4)	3.2602(18)	3.2610(19)
Ce2–Ge2 (×4)	3.3066(10)	3.3012(9)	Yb2–Ir (×4)	3.3020(7)	3.3080(7)
Ce2–Ge1 (×2)	3.3642(15)	3.3654(13)	Yb3–Ge1 (×8)	2.9309(14)	2.9316(15)
Ce2–Ge3 (×2)	3.4417(11)	3.4414(9)	Yb3–Ir (×4)	3.1696(9)	3.1688(13)
Ir–Ge3	2.4824(10)	2.4807(9)	Ir–Ge1	2.4391(11)	2.4416(11)
Ir–Ge1 (×2)	2.4858(7)	2.4843(6)	Ir–Ge2	2.448(2)	2.452(2)
Ir–Ge2	2.5125(10)	2.5114(9)	Ir–Ge3	2.4813(17)	2.4845(18)
Ir–Ge1	2.6324(15)	2.6286(13)	Ir–Ge2	2.527(2)	2.527(2)
Ge1–Ge1	2.746(3)	2.745(2)	Ge1–Ge1 (×2)	2.834(3)	2.832(3)
Ge2–Ge2	2.524(4)	2.520(3)	Ge2–Ge2	2.490(4)	2.491(5)
Ge3–Ge3	2.581(4)	2.579(3)	Ge3–Ge3	2.445(6)	2.446(6)
<b>Label</b>	<b>296 K</b>	<b>193 K</b>			
<b>Yb<sub>4</sub>Ir<sub>7</sub>Ge<sub>6</sub></b>					
Yb–Ir2 (×6)	2.9242(6)	2.9231(5)			
Yb–Ge (×6)	2.9732(8)	2.9714(10)			
Ir1–Ge (×6)	2.605(3)	2.601(4)			
Ir2–Ge (×4)	2.572(2)	2.573(3)			
Ir2–Ir2 (×4)	2.9242(6)	2.9231(5)			

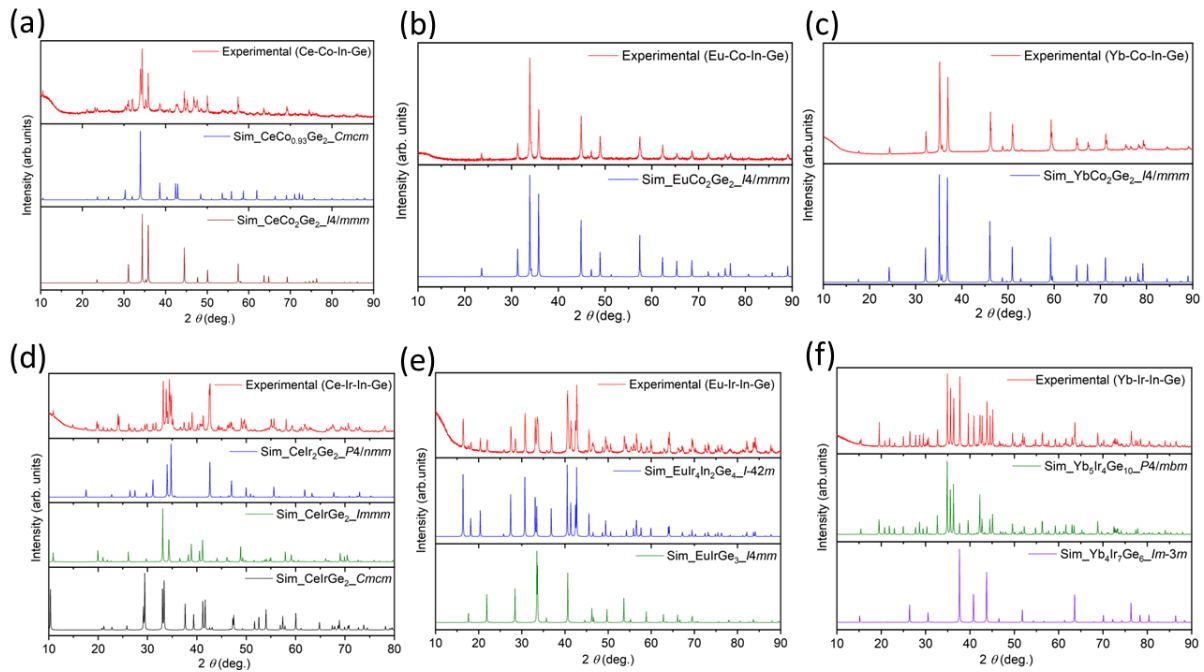


**Figure A3-1.** Powder X-ray diffraction patterns compared with simulated patterns.

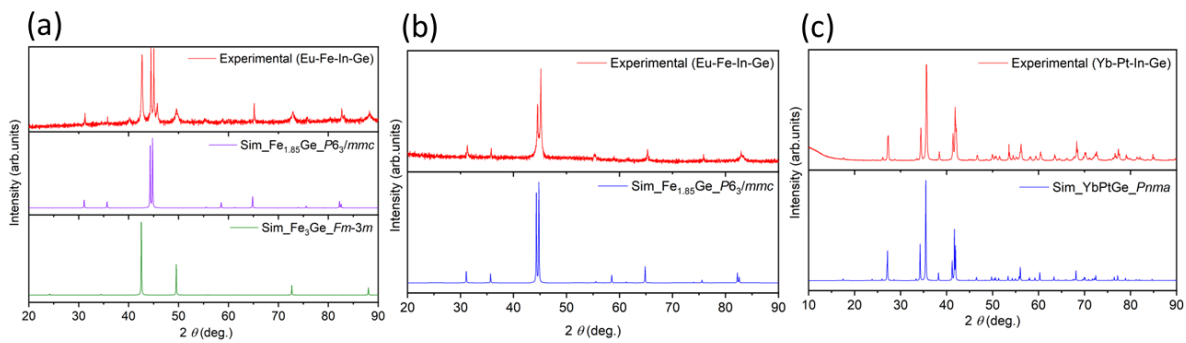


**Figure A3-2.** Powder X-ray diffraction patterns compared with simulated patterns.

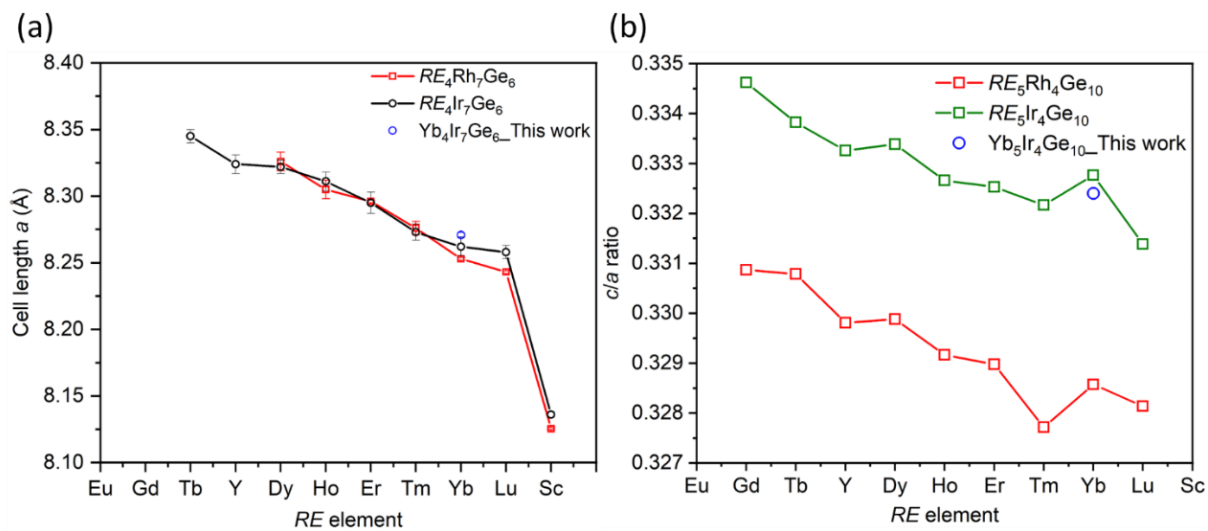


**Figure A3-3.** (a) Cell length of  $RE_4T_7Ge_6$  ( $T = Rh, Ir$ ) compounds, and (b)  $c/a$  ratio of  $RE_5T_4Ge_{10}$  ( $T = Rh, Ir$ ) compounds.